Development of Joint Systems Using SFRCC for Enhanced Seismic Performance of Steel Structures

September 2009

Yao CUI

TABLE OF CONTENTS

CHAPTER 4   Test on Shallowly Embedded Column Base with SFRCC Slab

ACKNOWLEDGEMENT

CHAPTER 1

Introduction

1.1 Background

Steel moment resisting frames are commonly used in seismic regions. Their connections have significant effects on the behavior and performance of these frames. In the structural system, beams are welded to columns, and the column bottoms are commonly connected to reinforced concrete foundation beams through base plates and anchor bolts. During the 1995 Hyogoken-Nanbu (Kobe) earthquake, a large number of steel frames buildings sustained cracks and brittle fracture at welded beam-to-column connections and some buildings suffered fracture of anchor bolts (for example, Nakashima et al. 1998; Reconnaissance 1995). Meanwhile, there was similar damage disclosed to steel frame buildings in the 1994 Northridge earthquake (for example, Bertero et al. 1994). After the events, much research was conducted, aiming at the reduction of earthquake hazards of steel moment frame structures. Design of improved connections and rehabilitation procedure to improve the seismic performance of steel connections and frames (Engelhardt et al. 1998; Recommended 2000; Recommendations 2001) was developed.

The column base plate connection is a potential vulnerable component under earthquake loading. It was observed by the post-earthquake field investigations that not a few buildings collapsed were severely damaged due to the fracture of anchor bolts. In addition, the behavior of this type of column bases is characterized by severely pinched hysteresis that has low capacity of energy dissipation. It is because plastic deformation is limited to the anchor bolts under lateral loading. After the 1995 Hyogoken-Nanbu earthquake, various modifications were proposed to increase the deformation capacity and energy dissipation (for example, Kutani et al. 2001; Kunioka et al. 2002). However, no major change has been made for the key connection details despite the shortcoming inherent in this type of connection. In view of this situation, a new type of ductile column base connection may be needed as a design alternative.

After the 1995 Hyogoken-Nanbu earthquake, fracture at welded beam-to-column connections has been one of the most serious concerns. The fractures may partly be attributed to weld defects and insufficient weld deposition. Various practical solutions have been suggested to ensure adequate plastic deformation capacity of welded connections. This includes improved welding practice, using high toughness material, geometrical modifications of welds access hole detail (Nakashima et al. 1998), plate-reinforced connections (Kim et al. 2002), welded haunches (Uang et al. 2000), reduced

beam sections (Engelhardt et al. 1998) among others. Although the modified connections have shown satisfactory performance in the laboratory, it is realized that the quality of welds is got not easy to control in practice as long as the structural fabrication relied on workmanship. How to ensure weld quality remains a key issue. To overcome the difficulty in the weld quality assurance, an innovative beam-column connection with the feature of "weld-free" may be needed.

In recent decades, material development in response to the call for more durable infrastructures has led to many advancements. Concrete and steel are by far the most widely used man-made construction materials in the world. Concrete can be cast to fit any structural shape from a cylindrical water storage tank to a rectangular beam or column in a high-rise building. It is readily available at relatively low cost. The advantages to using concrete include high compressive strength, good fire resistance, high water resistance, low maintenance, and long service life. The disadvantages to using concrete include small tensile strength, and formwork requirement. Steel is particularly dominant in the design and construction of larger structures and structures with unusual geometry because of its large strength to weight ratio and the ability to economically fabricate and erect complex structures. While structural steel is prone to corrosion, and the fire protection and weldability are also critical issues. A variety of more durable construction materials have been developed to supplement conventional concrete and steel.

Steel fiber reinforced cementitious composites (SFRCC) is one of the advanced concrete for use in structures. It was developed based on CRC (compact reinforced composite), one of ultra-high-strength concretes, which was invented in Denmark in 1980s by Bache (1987). This material is made with a very low water/binder ratio (0.16 or smaller), and contains from 2 to 6% steel fibers, providing matrix strengths of 140 to 400 MPa. The strength properties of SFRCC are comparable to those of conventional concrete, for example the tensile strength of SFRCC is approximately four times larger of that of conventional concrete (15MPa for SFRCC and 3MPa for conventional concrete). Because of the presence of steel fibers, the deformation and energy absorption capacities of SFRCC are significantly improved. Therefore, it is also combined with closely spaced steel rebars. Such advancement makes it possible to use SFRCC in increasingly wide applications.

1.2 Objectives

In many cases of actual practice for steel building construction, floor slabs are present on the beam top of the beam-column connection and on the base plate and anchor bolts of base plate connection. In this dissertation, contribution of the floor slabs to the enhancement of the seismic behavior of the connections is explored. Two new connections, one for the base plate connection and the other for the beam-column connection, are proposed by taking into account the effect of the floor slabs as illustrated in Fig. 1.1.

For the base plate connection, contribution of the floor slab to the resistance of the column base is ignored in current design provisions, with the assumption that the contribution is minimal. A preliminary study (Nakashima and Igarashi 1986; Morino et al. 2003), however, indicated that

contribution of such slab to the stiffness, strength, and energy dissipation is more than minimal and that particularly if the column base is properly reinforced in the slab a dramatic increase is likely in these properties. This leads us to a possibility of making the column base as strong as the fully embedded column base so that the column yielding and failure precedes the column base failure. Here, we call such a column base the "shallowly embedded column base", as shown in Fig.1.1 (a). It is noted that the thickness of the floor slab is not greater than that required for embedded column bases. Both SFRCC and conventional concrete are applied for the shallowly embedded column base. Based on the comparison between the specimens with SFRCC and with conventional concrete floor slab, the benefit of SFRCC will be proved.

For the beam-column connection, a new type beam-column connection with the feature of "weld-free" is proposed as illustrated in Fig. 1.2 (b). The welding between the column face and beam flange is removed. A portion of the floor slab around the column is casted by SFRCC. Through a group of headed studs, two SFRCC slabs (SFRCC diaphragms hereinafter) on both the top and bottom beam flange are adopted to connect the beam and column. The headed studs are closely welded on the beam flange to transfer the beam force to the SFRCC diaphragm. In this new beam-column connection, the beam hinge is expected to form at the edge of SFRCC diaphragm. It is difficult to apply conventional concrete in this system, since the small spacing of studs would cause trouble to cast concrete and slab crush in this region.
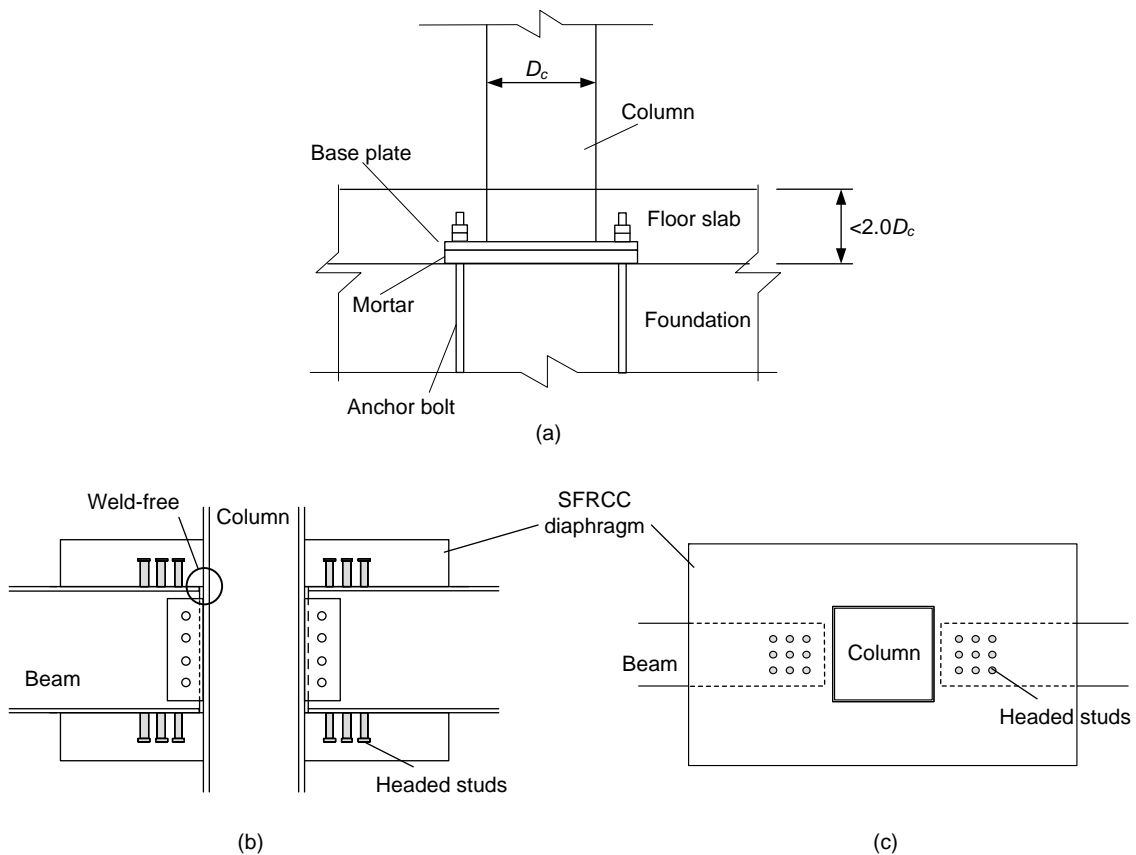

Fig. 1.1 Proposed connections: (a) shallowly embedded column base;
(b) elevation view of beam-column connection; and (c) plan view of beam-column connection

Based on the research of Kirikoshi et al. (2000), both the deformation and energy absorption capacities of SFRCC reach the maximum when 6% steel fibers in volume is adopted. To expect the largest contribution of SFRCC, 6% steel fibers in volume are used for SFRCC in this study.

To summarize, the objectives of this study are to explore the contribution of floor slabs to enhance the seismic behavior of connections, especially the base plate connection and the beam-column connection, and to demonstrate the benefit of applying SFRCC to the connections. A series of test was conducted to investigate the seismic behavior of the proposed connections (shallowly embedded column bases and the new beam-column connections) and provide information for engineers to facilitate the associated design.

1.3 Organization

This dissertation consists of seven chapters. Chapter 1 presents the background of this study, and Chapter 7 is the summary and conclusions. Chapters 2 through 6 constitute the main part of the dissertation: (1) test on shallowly embedded column bases with conventional concrete slab; (2) numerical analysis of shallowly embedded column bases with conventional concrete slab; (3) test on shallowly embedded column bases with SFRCC slab; (4) push-out test on shear stud connectors in solid SFRCC slab; and (5) beam-column connection of steel structures using SFRCC. The contents of the five chapters are outlined as follows.

In Chapter 2, the shallowly embedded column base system is proposed. In this column base system, a relatively thin floor slab is used to cover the base plate and anchor bolts. The test conducted on eight 2/3 scale specimens with conventional concrete slab is summarized. The important design parameters, i.e. the elastic stiffness, maximum strength, and energy dissipation are examined. The effects of the slab thickness, slab shape, and rebar on these properties are also investigated. Design procedure to estimate the elastic stiffness and strength of column base are proposed, and the obtained results are compared with the corresponding test results.

In Chapter 3, the specimens described in Chapter 2 are analyzed utilizing a numerical model. The model is developed to simulate the cyclic behavior of specimens by incorporating the contact model between the base plate and anchor bolts and adopting the damage plasticity model of concrete. The analytical hysteresis curves are compared with the curves obtained from the experiment. A parametric study on the effects of main variables in the seismic behavior of shallowly embedded column bases is also conducted. Investigation is given to the effects of three parameters, i.e. the thickness of concrete slab, the number of anchor bolts, and axial force ratio. Moreover, the design procedure to estimate the elastic stiffness and strength of specimens proposed in Chapter 2 is calibrated against the analysis results.

In Chapter 4, application of SFRCC to the slab of shallowly embedded column bases is explored. The test conducted on five 2/3 scale specimens is summarized. The seismic behavior of the specimens with SFRCC slab is compared with that of the specimens having conventional slab, in terms of the elastic stiffness, maximum strength, and energy dissipation. In addition, the matrix/rebars interaction is compared between the SFRCC and conventional concrete. The numerical model introduced in

Chapter 3 is adopted again to simulate the test results. The parametric study that is the same as described in Chapter 3 is conducted as well. The procedure to estimate the elastic stiffness and maximum strength of shallowly embedded column bases with conventional concrete is calibrated for its applicability to those with SFRCC slab.

In Chapter 5, behavior of shear stud connectors embedded in solid SFRCC slab is investigated both in physical test and numerical analysis. Push-out tests are conducted to provide a basis to understand the overall behavior of the headed stud connectors in the solid SFRCC slabs, e.g. the load-slip relationships, shear capacity, and failure mode. Four specimens are designed to investigate a group effect of the shear stud connectors. A detailed finite element model is developed to provide the insight into the stress and strain distributions in both the studs and slab. The results obtained from the analysis and experiment are compared in terms of the overall performance. A series of parametric analysis is also conducted to investigate the effects of the longitudinal spacing and transversal spacing on the stud behavior.

In Chapter 6, a new beam-column connection is proposed aiming at solving the difficulty in the weld quality assurance. Feasibility of the proposed beam-column connection is experimentally investigated by two full-scale beam-column connection specimens. Based on the measured shear stud strength described in Chapter 5, the two specimens are designed to fail by two distinct failure modes, i.e. the stud fracture and beam yielding at the end of SFRCC slab. Seismic behavior of the proposed beam-column connection is compared with that of the conventional bare steel beam-column connections in terms of the elastic stiffness, strength and energy dissipation. Furthermore, the behavior of studs in the proposed connections is compared with that in the push-out specimens.

REFERENCES

[1.1]   Aarup, B. (2004). "CRC – a special fiber reinforced high performance concrete." Advances in concrete through science and engineering, Bagneux, France, RILEM Publications, CD-ROM Paper 13, Hybrid-Fiber Session.

[1.2]   Bache, H. H. (1987). "Compact reinforced composite, basic principles." CBL Report No. 41, Denmark, Aalborg Portlland.

[1.3]   Bertero, V. V., Anderson, J. C., and Krawinkler, H. (1994). "Performance of steel building structures during the Northridge Earthquake." Rep. No. UCB/EERC -94-09, Univ. of California at Berkeley, Earthquake Engrg. Res. Ctr.

[1.4]   Engelhardt, M. D., Winneberger, T., Zekany, A. J., and Potyraj, T. J. (1998). "Experimental investigation of dogbone moment connections." Engineering Journal, AISC, 35(4), 128-139.

[1.5]   Kim, T., Whittaker, A. S., Gilani, A. S. J., Bertero, V. V., and Takhirov, S. M., (2002). "Experimental evaluation of plate-reinforced steel moment-resisting connections." Journal of Structural Engineering, ASCE, 128(4), 483-491.

[1.6]   Kirikoshi, K., Kaneko, Y., Mihashi, H., and Abe, T. (2000). "Material properties of steel fiber reinforced high strength high ductility cementitious composite." J. Technol. Des, AIJ, 11, 1-4.

[1.7]   Kunioka, K., Okada, K., and Yamada, S. (2002). "Experimental study on the exposed type column base connected with angle based on semi-rigid concepts," Summaries of Technical Papers of Annual Meeting, AIJ, C-1, pp.771-774.

[1.8]   Kutani, K., and Masuda, K. (2001). "Study on column bases of framed structures with steel footing beams." Summaries of Technical Papers of Annual Meeting, AIJ, C-1, pp. 971-972.

[1.9]   Nakashima, M., Suita, K. Morisako, K., and Maruoka, Y. (1998). "Test of welded beam-column subassemblies. I: Global behavior." Journal of structural Engineering, ASCE, 124(11), 1236-1244.

[1.10]   Recommendations for Design of Connections in Steel Structures. (2001). Architectural Institute of Japan (in Japanese).

[1.11]   Recommended seismic design criteria for new steel moment-frame buildings. (2000). Federal Emergency Management Agency, FEMA350, Washington, D.C.

[1.12]   Reconnaissance Report on Damage to Steel Building Structures Observed from the 1995 Hyogoken-Nanbu Earthquake. (1995). Steel Committee of the Kinki Branch of the Architectural Institute of Japan, Osaka (in Japanese).

[1.13]   Uang, C. M., Yu, Q. S., Noel, S., and Gross, J. (2000). "Cyclic testing of steel moment connections rehabilitated with RBS or welded haunch." Journal Structural Engineering, ASCE, 126(1), 57-68.

LIST OF PUBLICATIONS

Journal papers (full paper reviewed by multiple reviewers and published in recognized journals):

[1] Qian J, **Cui Y**, Fang X, Shear Strength Tests of Concrete Filled Steel Tube Columns, China Civil Engineering Journal, Vol. 40, No. 5, pp. 1-9, May, 2007 (in Chinese).

[2] Yamamoto R, Uemura T, **Cui Y**, Suita K, and Nakashima M, Test on Exterior Column Bases and Strength and Stiffness Evaluation (Hysteretic behavior and strength capacity of shallow-embedded steel column bases Part 3), Journal of Structural and Construction Engineering, AIJ, Vol. 74, No. 635, pp. 129-137, Jan., 2009

[3] **Cui Y**, Tai T, Hitaka T, and Nakashima M, Use of SFRCC in Shallowly Embedded Steel Column Bases, Journal of structural engineering, AIJ, Vol. 55B. , March, 2009

[4] **Cui Y**, Nagae T, Nakashima M, Hysteretic Behavior and Strength Capacity of Shallowly Embedded Steel Column Bases, Journal of structural engineering, ASCE, accepted for publication, 2009

Conference paper (abstract reviewed by multiple reviewers and presented in international conferences):

[1] **Cui Y**, Nakashima M, Hitaka T. Using Steel Fiber Reinforced Cementitious Composites (SFRCC) in Shallow Embedded Column Base. *Composite Construction in Steel and Concrete VI*, Colorado, USA, July, 2008.

[2] **Cui Y**, Yamamoto R, Uemura T, Nagae T, Nakashima M. Hysteretic Behavior and Strength Capacity of Shallow Embedded Steel Column Bases. The 14th World Conference on Earthquake Engineering, Beijing, China, October, 2008.

Technical papers presented at domestic conferences:

[1] Uemura T, Yamamoto R, **Cui Y,** Nagae T, Suita K, and Nakashima M, Hysteretic Behavior and Seismic Capacity of Shallow Embedded Steel Column Bases: Part 1 Cyclic loading tests of exterior shallow embedded steel column bases, *Summaries of Technical Papers of Annual Meeting Kinki Branch AIJ*, No. 47, pp. 149-152, June, 2007

[2] Yamamoto R, Uemura T, **Cui Y,** Nagae T, Suita K, and Nakashima M, Hysteretic Behavior and Seismic Capacity of Shallow Embedded Steel Column Bases: Part 2 Evaluation of stiffness, strength and energy dissipation, *Summaries of Technical Papers of Annual Meeting Kinki Branch AIJ*, No. 47, pp. 153-156, June, 2007

[3] Uemura T, Yamamoto R, Nagae T, **Cui Y,** Suita K, and Nakashima M, Hysteretic Behavior and Seismic Capacity of Shallow Embedded Steel Column Bases: Part 1 Cyclic loading tests of

exterior shallow embedded steel column bases, *Summaries of Technical Papers of Annual Meeting AIJ* (Kyushu), C-1 (III), pp. 697-698, August, 2007

[4] Yamamoto R, Uemura T, Nagae T, **Cui Y**, Suita K, and Nakashima M, Hysteretic Behavior and Seismic Capacity of Shallow Embedded Steel Column Bases: Part 2 Evaluation of the stiffness, *Summaries of Technical Papers of Annual Meeting AIJ* (Kyushu), C-1 (III), pp. 699-700, August, 2007

[5] **Cui Y**, Yamamoto R, Uemura T, Nagae T, Suita K, and Nakashima M, Hysteretic Behavior and Seismic Capacity of Shallow Embedded Steel Column Bases: Part 3 Evaluation of maximum strength, *Summaries of Technical Papers of Annual Meeting AIJ* (Kyushu), C-1 (III), pp. 701-702, August, 2007

[6] Tai T, Uemura T, **Cui Y**, Hitaka T, and Nakashima M, Using SFRCC in Shallowly Embedded Steel Column Bases: Part 1 Outline of test and overall behavior, *Summaries of Technical Papers of Annual Meeting Kinki Branch AIJ*, No. 48, pp. 425-428, June, 2008

[7] **Cui Y**, Tai T, Uemura T, Hitaka T, and Nakashima M, Using SFRCC in Shallowly Embedded Steel Column Bases: Part 2 FEM analysis, *Summaries of Technical Papers of Annual Meeting Kinki Branch AIJ*, No. 48, pp. 429-432, June, 2008

[8] Tai T, Uemura T, **Cui Y**, Hitaka T, and Nakashima M, Test on Seismic Performance of Shallow Embedded Steel Column Bases Using SFRCC: Part 1 Outline of test and test results, *Summaries of Technical Papers of Annual Meeting AIJ* (Chugoku), C-1 (III), pp. 1099-1100, Sep., 2008

[9] **Cui Y**, Uemura T, Tai T, Hitaka T, and Nakashima M, Test on Seismic Performance of Shallow Embedded Steel Column Bases Using SFRCC: Part2 FEM analysis, *Summaries of Technical Papers of Annual Meeting AIJ* (Chugoku), C-1 (III), pp. 1101-1102, Sep., 2008

[10]Tai T, Song SH, **Cui Y**, Hitaka T, and Nakashima M. Full Scale Test on Beam-Column Connections Using SFRCC: Part 1 Design of specimens and test setup, *Summaries of Technical Papers of Annual Meeting Kinki Branch AIJ*, 2009 (in press).

[11]Song SH, Tai T, **Cui Y**, Hitaka T, and Nakashima M. Full Scale Test on Beam-Column Connections Using SFRCC: Part 2 Test results and FEM simulation, *Summaries of Technical Papers of Annual Meeting Kinki Branch AIJ*, 2009 (in press).

[12]Hitaka T, **Cui Y**, Tai T, Song SH, and Nakashima M. Push-out Test on Shear Stud Connectors in Solid SFRCC Slab: Part 1 Experiment and results, *Summaries of Technical Papers of Annual Meeting Kinki Branch AIJ*, 2009 (in press).

[13]**Cui Y**, Hitaka T, Tai T, Song SH, and Nakashima M. Push-out Test on Shear Stud Connectors in Solid SFRCC Slab: Part 2 Numerical analysis, *Summaries of Technical Papers of Annual Meeting Kinki Branch AIJ*, 2009 (in press).

CHAPTER 2

Test on Shallowly Embedded Column Base with

Conventional Concrete Slab

2.1 Introduction

2.1.1 Background

Steel moment resisting frames are commonly used in seismic regions. The column base has significant effects on the behavior and performance of these frames. The column base is commonly classified into two types: 1) the exposed column base that consists of a steel base plate welded to the end of the column and anchor bolts that connect the base plate to a reinforced concrete (RC) foundation beam, and 2) the embedded column base where the column is embedded in a reinforced concrete foundation. Although the embedded column base is greater in fixity against rotation than is the exposed column base, the exposed column base has been popularly used for low- to medium-rise structures because of better constructability and low cost.

Extensive research was conducted on the seismic behavior of exposed column bases, for example, studies on the effect of the base plate thickness on the column base behavior (DeWolf, 1982; Astaneh et al, 1992) and the effect of the base plate size on ductility (Burda and Itani, 1992). In the U.S., publications such as DeWolf (1982), Thambiratnam and Paramasivam (1986), and the AISC Design Guide No. 1 (Fisher and Koliber, 2006) are commonly used as guidelines for the design of exposed column bases. Design provisions have been offered, for instance, AISC Manual of Steel Construction (AISC, 2005), and AISC Seismic Provisions (AISC Seismic, 2005) in the U.S, the ENV1993 Eurocode 3 (ENV, or EuroNorm Vornorm, represents a European pre-standard) (CEN 1992) in Europe, and Recommendation for Design of Connections in Steel Structures (AIJ 2006) in Japan.

Under the cyclic loading conditions that must be considered in seismic design, the exposed column base exhibits pinching due to the elongation of anchor bolts, which lowers the energy dissipation. This pinching and the associated reduction in energy dissipation relative to when the embedded column base is used and column yielding and plastification dominates instead of the column base failure are regarded as the normal fate of the exposed column base. The consequences of these shortcomings inherent have been recorded in reconnaissance after the 1995

Hyogoken-Nanbu earthquakes (AIJ 1995; Nakashima et al. 1998). However, in many cases of actual practice a floor slab is present that covers the exposed column base. The contribution of such a slab to the resistance of the column base is ignored in current design provisions, with the assumption that the contribution is minimal.

A preliminary study (Nakashima and Igarashi 1986; Morino et al. 2003), however, indicated that contribution of such a slab to the stiffness, strength, and energy dissipation is more than minimal, and that particularly if the column base is properly reinforced in the slab a dramatic increase is likely in these properties. This leads us to a possibility of making the column base as strong as the fully embedded column base so that the column yielding and failure precedes the column base failure. Here, we call such a column base the "shallowly embedded column base".

2.1.2   Organization

The chapter consists of three parts. The first part presents a series of tests of shallowly embedded column bases under cyclic loading conditions, and examines the important design parameters, i.e., the elastic stiffness, maximum strength, and energy dissipation of the column base. The effects of the slab thickness, slab shape, and reinforcement on these properties are investigated, and the possibility of making the shallowly embedded column base as strong as the embedded column base is explored. In the second part, a simple but workable procedure to estimate the maximum strength of the shallowly embedded column base is proposed based on the plastic theory. The third part presents the proposed evaluation of the elastic stiffness based on the elastic theory following the individual components adopted for the strength evaluation.

2.2 Test Program

2.2.1   Test specimens

The test specimens were designed to simulate interior column base connections that commonly exist in steel structures in Japan. Eight specimens were fabricated in an approximately 2/3 scale, with all specimens having the global dimensions shown in Fig.2.1. The dimensions were based on typical configurations found in low- to medium- rise steel buildings constructed in Japan. A relatively strong column was used to ensure that the base plate connection and/or the covering slab would initiate the development of damage during cyclic loading before significant deformation or damage was developed in the column. All eight specimens comprised a cold-formed, square-tube cross section column (200 mm in the width, with a thickness of 9 or 12 mm), a shop-welded, hot-rolled, square base plate (300 mm and 25 mm in the width and thickness), twelve machined anchor bolts, and a reinforced concrete (RC) foundation beam. Here, the base plate level is the same for all specimens. A RC floor slab (floor slab hereinafter) is placed on top of the foundation beam to form a shallowly embedded column base. Table 2.1 summarizes the test variables of the eight specimens. The test variables and other important features of the test specimens are discussed as follows.

To investigate the floor slab effect on the column base connection, Specimen 'Standard', an exposed column base designed following the associated provisions of Recommendation for Design of Connections in Steel Structures (AIJ, 2006), was fabricated as a baseline specimen. All other seven specimens were arranged with different types of slab configuration. To ensure the anchor bolt yielding, the foundation beam was designed strong enough so that a cone-like failure of concrete would not occur. Normal strength concrete was used for the foundation beam, and high-strength non-shrinkage mortar was adopted to fill in the gap between the base plate and foundation beam.

Two groups of shallowly embedded column base specimens were designed. In the first group, a floor slab reinforced only by mesh bars was adopted to investigate the effect of the floor slab shape. In the second group, a floor slab strengthened further by eight bent horizontal rebars was adopted to investigate the contribution of rebars. In the discussion to follow, the strengthened slab refers to the slab adopted for the specimens in the second group.
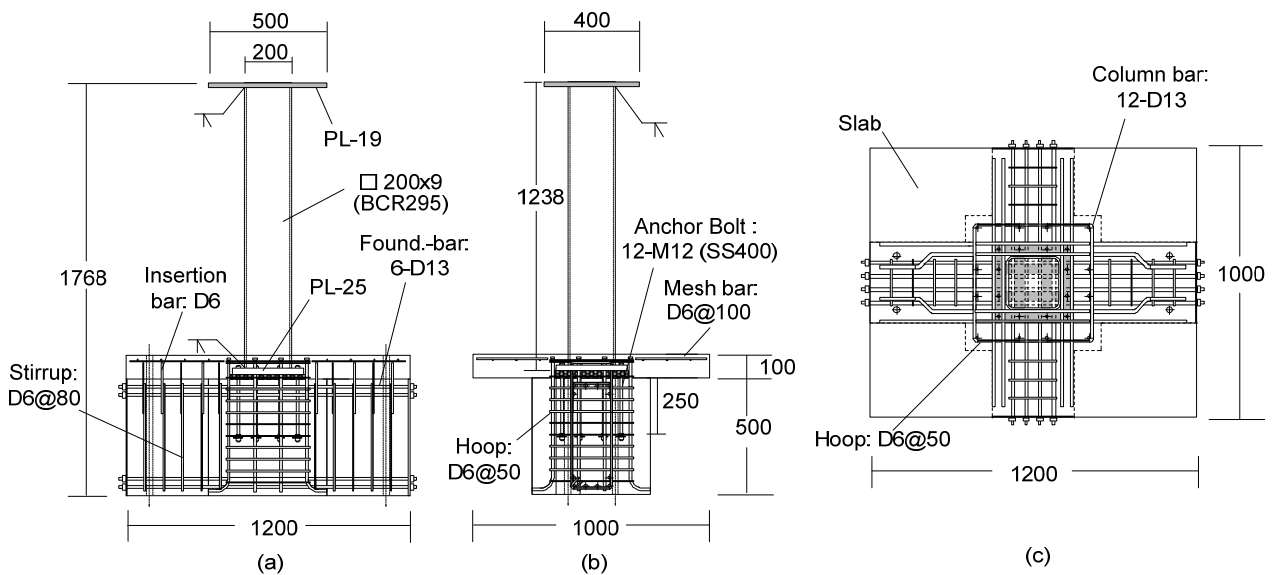
Fig. 2.1 Test specimen (SL-100-st):
(a) front elevation; (b) side elevation; and (c) plane view (unit: mm)

Four types of slab shape, shown in Fig. 2.2, were adopted. The detail shown in Fig.2.2 (a), (b), designated as 'SL-100' and 'SL-200', respectively, represents a column base with a flat floor slab. The thickness of the flat floor slab was set at 100mm and 200mm, in which the 100 mm thick slab corresponds to the commonly used slab. The detail shown in Fig. 2.2 (c), designated as 'Foot-100', has a 100mm thick flat floor slab, but the thickness around the column base is partially increased to 200mm, for an area of 500mm × 500mm. The detail in Fig.2.2 (d), designated as 'Found.-100', represents a column base with an elevated foundation beam. The specimen consists of three parts: a standard exposed column base, a 100mm thick elevated foundation beam that covers the column base, and a 100mm thick flat floor slab on top of the beam.

Specimens 'SL-100-st', 'Found.-100-st-t9', and 'Found.-100-st-t12' are the specimens with the strengthened floor slab. Deformed reinforcing bars (horizontal rebars) are placed to restrict both the

rotation of the base plate and the separation of the floor slab. To this end, the bent part of the rebars is set approximately perpendicular to the failure surface in the floor slab (Fig. 2.3). All horizontal rebars are set around the column and upon the base plate, two pieces at each column side and in each direction. The two specimens: 'Found.-100-st-t9' and 'Found.-100-st-t12' were identical except for the column thickness. Specimen 'Found.-100-st-t9' had a smaller thickness and eventually a smaller column strength, while the column base detail remained the same between the two specimens.

The material properties of the steel and concrete used for the specimens were obtained from the associated material tests and are summarized in Table 2.1.
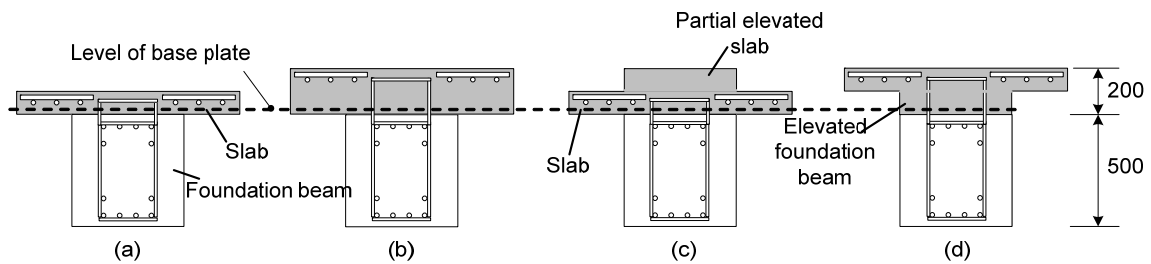
Fig. 2. 2 Shape of concrete slab: (a) Flat slab type 'SL-100'; (b) Flat slab type 'SL-200'; (c) Partial elevated slab type 'Foot-100'; and (d) Elevated foundation type 'Found.-100' (Unit: mm)
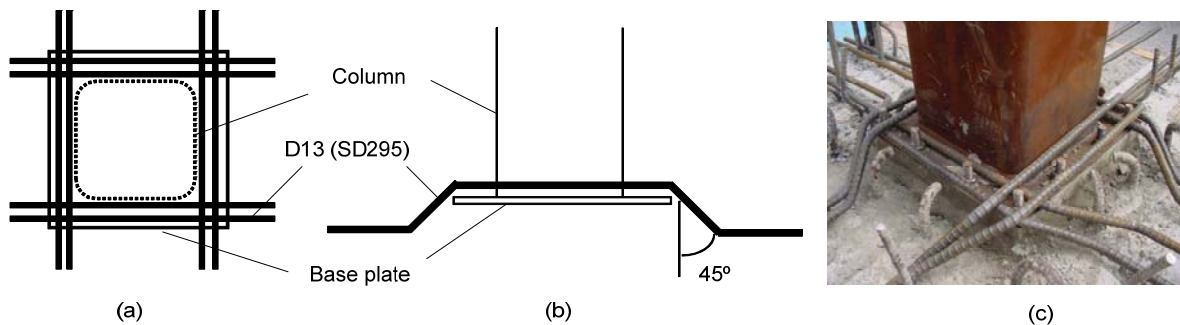
Fig. 2. 3 Arrangement of reinforcing bars:
(a) plan view; (b) elevation; and (c) arrangement of reinforcing bars

Table 2.1 Material properties (concrete and steel)

Sampled plates	Steel	Yield strength σ_y (N/mm^2)	Tensile strength σ_u (N/mm^2)
Column	□-200×9, BCR295	387	460
	□-200×12, BCR295	373	412
Column Base	Anchor bolt	306	439
	Base plate	409	546
Slab	Steel bar D13	374	515
	Concrete	30.5	

2.2.2   Test setup and loading program

The test specimen was placed in the loading frame shown in Fig. 2.4. The foundation beam was clamped to the reaction floor. The column top was clamped to two hydraulic jacks, one in the horizontal direction and the other in the vertical direction. The specimen was subjected to a constant vertical force of 511 kN, corresponding to 0.2 times the yield axial load of the column (9 mm thick). A displacement-controlled cyclic load was applied quasi-statically in the horizontal direction. The displacement was expressed in terms of the drift angle, defined as the horizontal displacement at the loading point relative to the height of the column (1238mm). The height was defined as the distance between the loading point and bottom face of the base plate. Drift angles of 0.005, 0.015, 0.0225, 0.03, 0.04, 0.06, 0.08, and 0.1 rad were adopted, and two cycles were performed at each drift angle. The test was terminated when the drift angle reached 0.1 rad or ten of the twelve anchor bolts fractured, which was regarded as a complete failure.
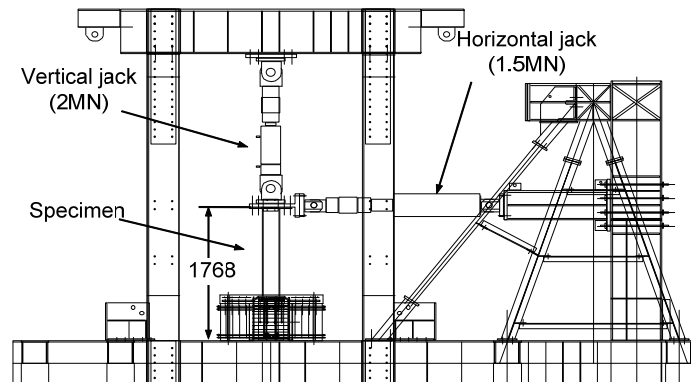
Fig. 2. 4 Elevation of the loading system (unit: mm)

2.3 Test Results

2.3.1   Moment-rotation relationships

Figure 2.5 shows the force-deformation relationships for all eight specimens in terms of the end-moment (M) applied at the bottom of the base plate versus drift angle (θ). Here, the end moment includes the moment induced by the P-Δ effect. In view of the moment-rotation relationships, the following observations are notable. Specimen 'Standard' has the smallest maximum strength among all specimens, and the hysteretic loop is severely pinched primarily due to the plastic elongation of the anchor bolts. Other Specimens 'SL-200', 'Foot-100', 'Found.-100', 'Found.-100-st-t9', and 'Found.-100-st-t12', show larger maximum strengths and hysteresis loops. The hysteresis loops of specimens with the strengthened slab, i.e., Specimen 'SL-100-st', 'Found.-100-st-t9', and 'Found.-100-st-t12', are fatter than those of the corresponding specimens. The specimens exhibited slip behavior similar to that observed in Specimen 'Standard', except for Specimen 'Found.-100-st-t9', the one having the largest hysteresis loops. That specimen exhibited a different mode of failure whose detail will be discussed in the next section.   All specimens arrived at the maximum strength at around 0.03 rad. The strength of the specimens with the floor slab decreased

sharply after the maximum strength. The deterioration is due primarily to the punching shear failure of the floor slab, and eventually the strength was lowered to the level of Specimen 'Standard'. On the other hand, specimens with the strengthened slab ('SL-100-st' and 'Found.-100-st-t12') sustain 90% of their maximum strength till the rotation of 0.06 rad. The strength deterioration of these specimens was delayed significantly due to the presence of the horizontal rebars.
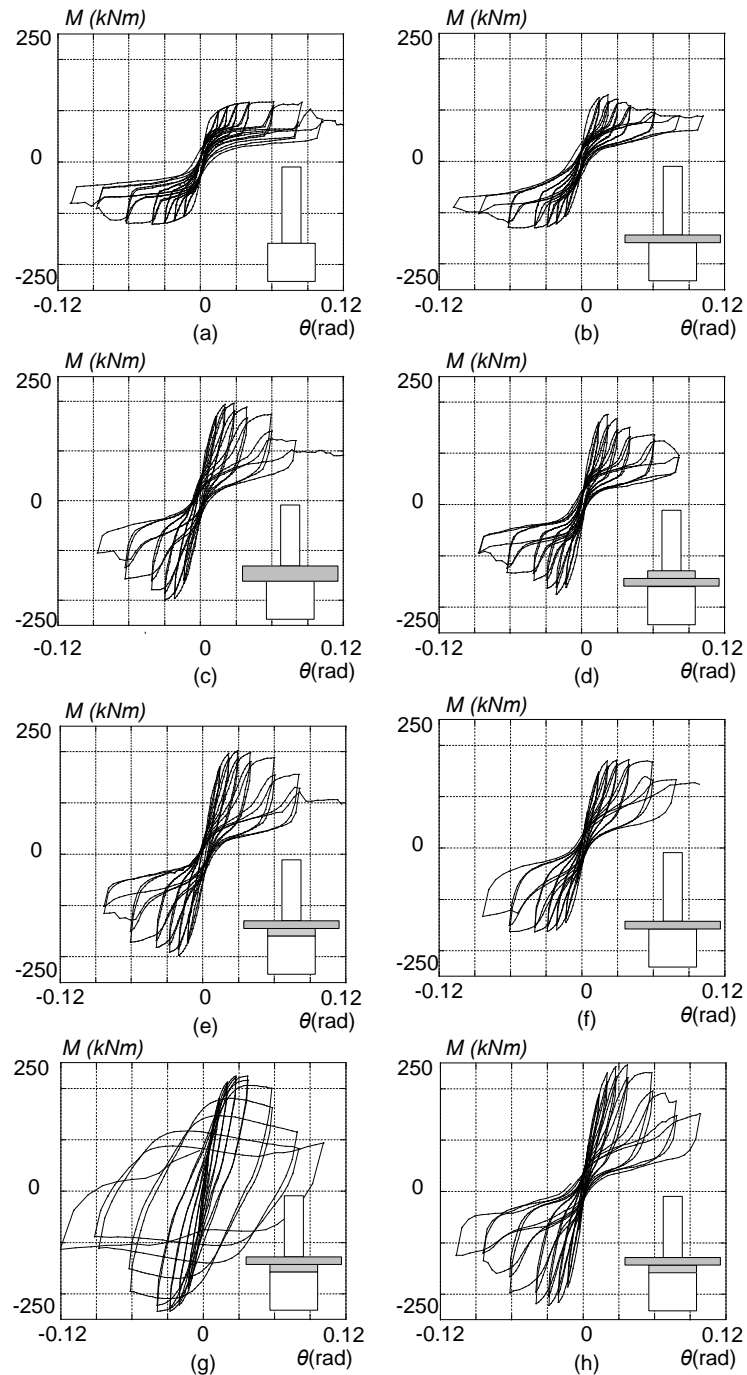

Fig. 2. 5 Moment versus rotation relationships: (a) Standard; (b)) SL-100; (c) SL-200; (d) Foot-100; (e) Found.-100; (f) SL-100-st; (g) Found.-100-st-t9; and (h) Found.-100-st-t12

Table 2.2 summarizes the results, including the elastic stiffness (K_0), the maximum strength (M_{max}), the failure mode, and the dissipated energy (E_p). The elastic stiffness of the specimen is

defined as the secant stiffness between the origin and the point at 0.005 rad. The value was adopted in light of the Japanese seismic design regulation such that the story drift angle be limited to 0.005 rad in the elastic design aiming at serviceability checking (AIJ 2005). The dissipated energy (E_p) was estimated from the total area of the hysteretic loops. For all specimens, the calculation was made from the start of loading to the completion of 0.03 rad drift angle amplitude. As shown in Table 2.2, the elastic stiffness, maximum strength, and dissipated energy varies with the slab configuration (thickness and shape) and the reinforcement (with/without the horizontal rebars).

Table 2.2 Test results

Sepc.	K_0 (kN·m)	M_{max} (kN·m)	Failure mode	E_p (kN·m·rad)
Standard	14128	123.5	Fracture of anchor bolts	7.6
SL-100	15134	134.8	Punching shear	8.3
SL-200	19757	205.8	Punching shear	16.1
Foot-100	18559	182.3	Punching shear	11.5
Found.-100	18307	207.2	Punching shear	15.2
SL-100-st	16350	166.9	Punching shear	11.6
Found.-100-st-t9	20085	234.0	Local buckling	20.3
Found.-100-st-t12	20483	253.4	Punching shear	13.3

Compared with that of the baseline Specimen 'Standard', the elastic stiffness increased 10% and 47% for the specimens with 100mm and 200mm thick slab, respectively. A negligible difference (a difference of 9%) is notable among the specimens with the same slab thickness but different slab shapes ('SL-200', 'Foot-100', 'Found.-100', 'Found.-100-st-t9', and 'Found.-100-st-t12'), it is speculated to be because the bearing height for the column is the same. The difference between the specimens with and without the horizontal rebars is also very small (a difference of 9%). Since the entire column base system remained nearly elastic without visible cracks during the cycle of 0.005 rad, contribution of the horizontal rebars to the elastic stiffness was minimal. In summary, the elastic stiffness is primarily a function of the slab thickness. More accurate prediction of the elastic stiffness in the shallowly embedded column base will be introduced in the following sections.

Improvement in the maximum strength and dissipated energy varied from 10% to 95% and 10% to 170%, respectively. Specimen 'SL-100' (the one with a thinner floor slab) shows the smallest improvement on both the maximum strength and dissipated energy, and the one with a thicker and strengthened floor slab ('Found.-100-st-t12') shows the largest improvement on the maximum strength. While Specimen 'Found.-100-st-t9', which failed in a different mode relative to other specimens, shows the most significant improvement on the dissipated energy, with the improvement by 170%. This occurred because contribution of the strengthened floor slab is large enough to alter the failure mode of the specimen from the column base failure to the buckling of the column's lower portion. For the specimens failed in punching-shear of floor slab, either reinforcement around the base plate portion or increase of the slab thickness is effective in energy

dissipation improvement. The improvement is 53%, when the horizontal rebars were arranged ('SL-100-st'), and 110%, when the slab thickness was increased to 200 mm ('SL-200').

2.3.2 Failure mechanisms

Two types of failure mode occurred in the shallowly embedded column base specimens. They are: a punching shear failure observed in all specimens except for Specimen 'Found.-100-st-t9', as shown in Fig. 2.6(a), and a column buckling failure observed in Specimen 'Found.-100-st-t9', as shown in Fig. 2.6(b). The specimen failed in the column buckling mode when the maximum strength of the base plate connection became greater than the full plastic moment of the column; otherwise the specimen failed in the punching shear failure mode.

The failure mode of all specimens that failed in the punching shear ('SL-100', 'SL-100-st', 'SL-200', 'Foot-100', 'Found.-100', and 'Found.-100-st-t12') was very similar regardless of slab shape and reinforcement. The floor slab was uplifted by the rotation of the base plate, and the punching shear failure occurred on the uplifted side. All cracks were connected and formed a cone-like crack during the cycles of 0.03 rad, when the specimen reached the maximum strength. As the column rotation increased, part of the floor slab around the base plate was forced to be separated. This separation caused the strength deterioration. At the end of loading, a cone with failure surface radiating from the top of the base plate to the surface of the floor slab in a slope angle of about 45° was observed in these specimens.

(a)   (b)
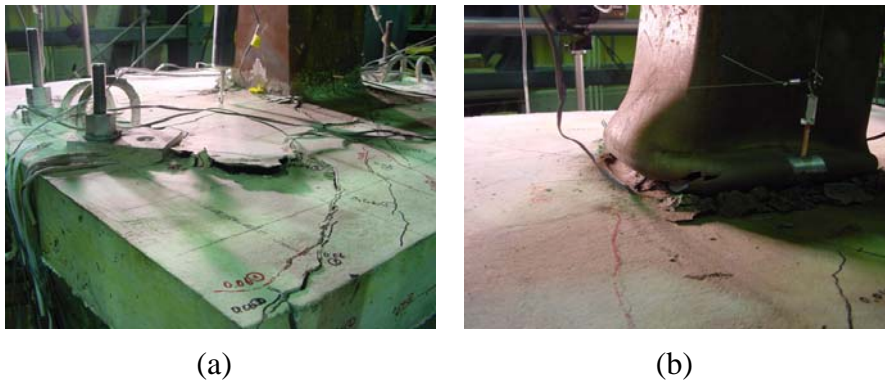
Fig. 2. 6 Failure of reinforced specimens: (a) SL-100-st; (b) Found.-100-st-t9

2.3.3 Effects of floor slab

The effects of the floor slab shapes can be examined from the results of the four shallowly embedded column base specimens without the horizontal rebars ('SL-100', 'SL-200', 'Foot-100', and 'Found.-100'). The largest slab thickness of Specimens 'SL-200', 'Foot-100', and 'Found.-100' was 200 mm, while a 100 mm thick slab was used for Specimen 'SL-100'. The elastic stiffness, maximum strength, and dissipated energy of the specimen with a thicker floor slab ('SL-200') were 1.4, 1.5, and 1.9 times larger than those of the specimen with a thinner floor slab ('SL-100'). As discussed earlier, the elastic stiffness was constant for the specimens with the same slab thickness. The maximum strength and dissipated energy was influenced by the slab shape. As compared with

Specimen 'SL-200', Specimen 'Foot-100' shows 0.9 and 0.7 times smaller in the maximum strength and dissipated energy, while Specimen 'Found.-100' shows nearly the same values as those of Specimen 'SL-200'. In Specimens 'SL-200' and 'Found.-100', the failure region expanding from the base plate was the same. Specimen 'Foot-100' showed a smaller failure region, because the partially elevated portion did not contribute to the resistance to punching failure.

2.3.4   Effects of rebars

The effects of horizontal rebars can be examined from the results of the five shallowly embedded column base Specimens 'SL-100', 'SL-100-st', 'Found.-100', 'Found.-100-st-t9', and 'Found.-100-st-t12'. As evidenced from Table 2.2, the maximum strength of the strengthened specimen is 24% ('SL-100-st') and 20% ('Found.-100-st-t12') greater than that of the corresponding specimens without the horizontal rebars. As described earlier, the specimen reached the maximum strength when the punching shear cracks were connected in the floor slab. Since the presence of the horizontal rebars restricted the separation of the floor slab, the fracture process naturally became slow. The strength deterioration was thereby mitigated, as shown in Fig. 2.5. To Specimen 'Found.-100-st-t9', the failure mode even switched from the slab punching failure to the column buckling because of the strengthening of the column base by the horizontal rebars.

2.4 Evaluation of Maximum Resisting Moment

An analytical model to evaluate the strength of shallowly embedded column bases is described. The level to evaluate the maximum resisting moment is taken at the bottom of the base plate as shown in Fig. 2.7 (a). In consideration of the punching shear failure, the model consists of three parts, as shown in Figs. 2.7, 2.8, 2.9 and 2.10, i.e., 1) the exposed column base component (Fig.2.7), 2) the covering concrete slab component (Figs. 2.8 and 2.9), and 3) the reinforcing bars component (Fig. 2.10). According to the experimental observations, the anchor bolts and rebars arranged for strengthening started yielding before attaining the maximum strength, which occurred just prior to the punching shear failure of the floor slab. Therefore, the theory of plasticity was adopted, and the strengths of the multiple components were added to estimate the maximum strength of the shallowly embedded column base.

2.4.1   Contribution of exposed column base

The moment capacity of the exposed column base component is estimated by a moment couple that consists of the tension force in the anchor bolts and the equivalent compressive force applied at the centroid of the bearing area under the base plate. The assumed stress distribution is shown in Fig.2. 7 (b). Following the procedure adopted in standard design specifications (AISC Design Guide No.1 2006; AIJ 2006), the maximum strength, M_e, is estimated as:

a) When the anchor bolts on the tension side take smaller forces than the yield strength ($N_u \geq N > N_u - T_u$, Fig. 2.7 (b-i))

$$M_e = (N_u - N)d_t \tag{2.1a}$$

b) When the anchor bolts on the compression side take tensile forces ($-T_u \geq N > -2T_u$, Fig. 2.7 (b-iii))

$$M_e = (N + 2T_u)d_t \tag{2.1b}$$

c) Otherwise ($N_u - T_u \geq N > -T_u$, Fig. 2.7 (b-ii))

$$M_e = T_u d_t + \frac{(N + T_u)D_{bp}}{2}\left(1 - \frac{N + T_u}{N_u}\right) \tag{2.1c}$$

Where N is the axial force transferred by the column base; N_u is the maximum compressive strength of the concrete under the base plate, estimated as $0.85BD_{bp}f_c'$; T_u is the maximum tensile strength of the anchor bolts acting in the tension region; f_c' is the compressive strength of concrete in the foundation. Other geometric notations are defined in Fig. 2.7 (b).
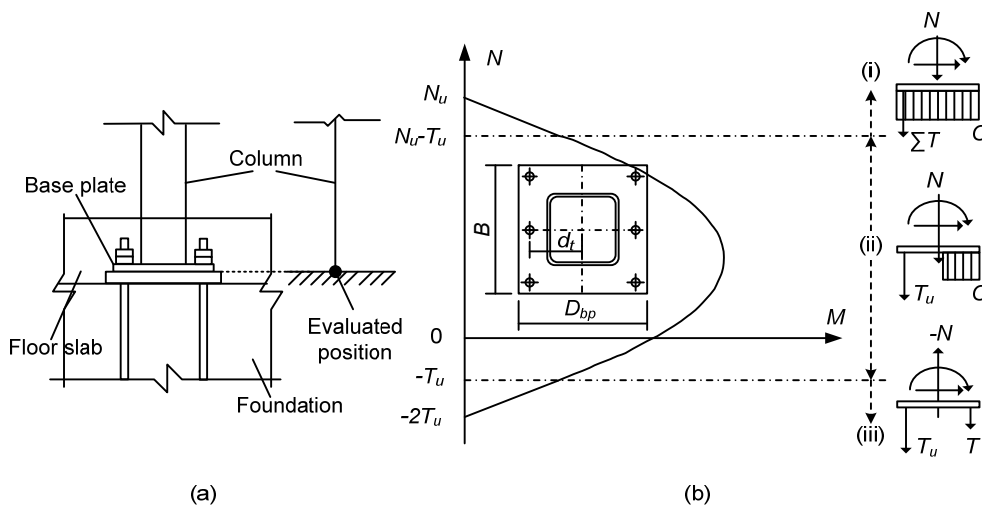

Fig. 2. 7 Model of evaluation of the maximum moment resisted by exposed column base: (a) evaluated level; (b) stress distribution

2.4.2 Contribution of concrete slab

The moment resistance of the covering concrete is assumed to be provided by the following two mechanisms: 1) direct bearing of the slab adjacent to the column in compression (Fig. 2.8); and 2) the punching resistance in the slab uplifted by the rotation of the base plate (Fig. 2.9). The relationship between the compressive stress and strain of the concrete is considered to be rigid perfectly-plastic (Chen 1982). To employ the assumption of rigid-plasticity, the compressive strength of concrete f_c' is adjusted using two independent effectiveness factors, v_c and v_t, for the bearing and punching shear resistance, respectively.

The bearing force is assumed to be applied at the centroid of the bearing area in the column front surface. This is analogous to the internal forces to resist bending in a compressive section of concrete. It is assumed that concrete yields uniformly in the bearing area. In accordance with the stress block recommended in ACI-318 (2002) and AIJ (1990), an effectiveness factor v_c of 0.85 and an effective depth of $0.8d$ are adopted. Then, the moment resistance M_{cc} supplied by the concrete in

compression is obtained by Eq. (2.2), with the associated notation defined in Fig. 2.8.

$$M_{cc} = \upsilon_c \cdot f_c{'} \cdot D \cdot 0.8d \cdot (0.6d + t_{bp})$$ (2.2)
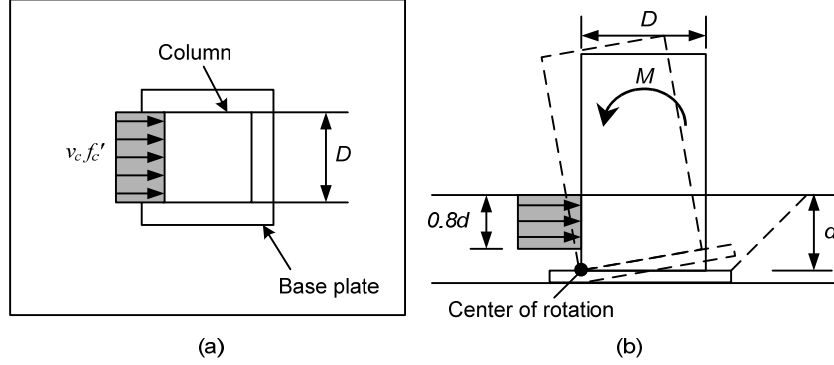
Where, t_{bp} is the thickness of the base plate.

Fig. 2. 8 Model of compressive mechanism in concrete slab: (a) plan view; (b) elevation view

In reference to the test results, the projected area shown in Fig. 2.9 (a) is assumed to contribute to the punching resistance. The slope angle of the punching-shear failure surface (Fig. 2.9 (b)) is assumed as 45°. The upper-bound theorem of the limit analysis is adopted. The punching-failure mechanism is taken to be the separation of the punched-out concrete with an upward velocity V, while the surrounding slab remains rigid. As shown in Fig. 2.9 (c) and (d), the direction of the velocity of the punched-out concrete varies with the rebar detail. For the floor slab, it is simply vertical upward. For the strengthened floor slab, since the horizontal rebars were set to prevent the separation caused by the punching failure, the direction of the velocity is taken to be normal to the punching-shear surface. The work equation for the assumed failure mechanism is:

For floor slab:

$$Q \cdot V = \frac{1 - \sin 45°}{2} \cdot A \cdot \upsilon_t f_c{'} \cdot V$$ (2.3a)

For strengthened floor slab:

$$Q \cdot V \cdot \cos 45° = \frac{1 - \sin 45°}{2} \cdot A \cdot \upsilon_t f_c{'} \cdot V$$ (2.3b)

Where Q is the ultimate punching load caused by the base plate, as shown in Fig. 2.9 (c) and (d). A is the area of the punching-shear surface as shown in Fig. 2.9 (b), and calculated as

$$A = B \cdot \frac{d}{\cos 45°} + \frac{\pi}{2} \cdot (\frac{d}{\cos 45°})^2 + (B - D) \cdot \frac{d}{\cos 45°}$$ (2.4)

The effective coefficient υ_t for the punching shear is calculated as:

$$\upsilon_t = 0.7 - \frac{f_c{'}}{200}$$ (2.5)

Eq. (2.5) was proposed by Nielsen (1984). Assuming that the punching load caused by the base plate be distributed uniformly, the moment resistance provided by the punching-shear mechanism is evaluated as:

$$M_{ct} = Q \cdot D_t \tag{2.6}$$

Where D_t is the distance (125 mm) between the centroid of the column section and the centroid of the punching load, as shown in Fig. 2.9.
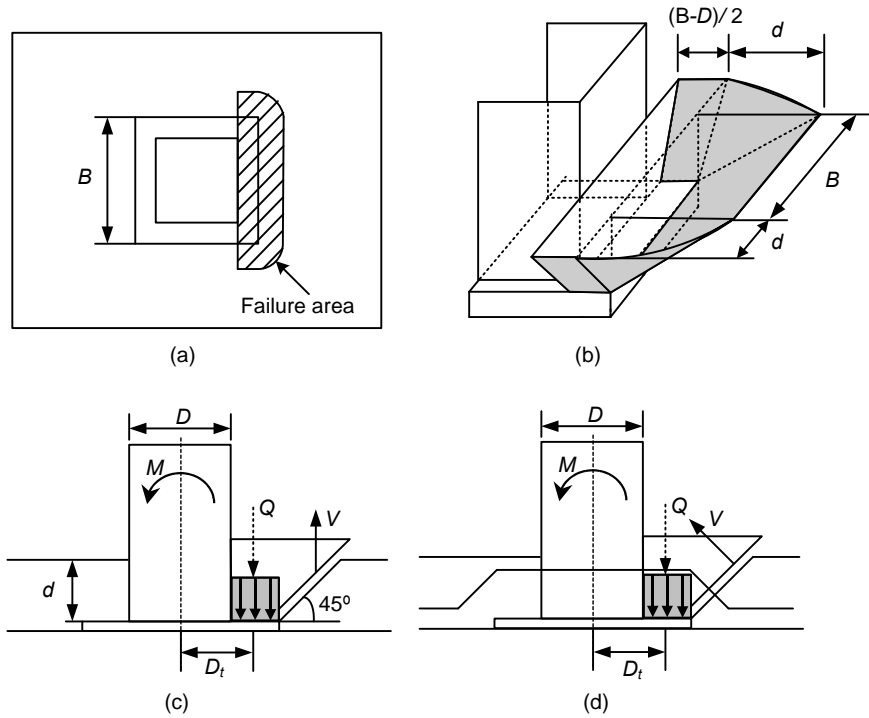

Fig. 2. 9 Model of punching shear mechanism in concrete slab: (a) plan view; (b) punching-shear surface; (c) evaluation model for floor slab; and (d) evaluation model for strengthened floor slab

2.4.3   Contribution of rebars

In the strengthened specimens, the horizontal rebars were bent by 45°, which is almost perpendicular to the punching failure surface in the slab. According to the strain gauge data obtained from the test, the bent parts yielded when the maximum moment of specimens was achieved. A total of eight bent parts of the six rebars located in the punching shear part provided resistance to the rotation of the column base, as shown in Fig.2.10. The vertical component of the axial force in the rebars corresponds to the force that constrains the base plate. Thus, the contribution provided by the rebars M_{st} is evaluated as:

$$M_{st} = T_y \cdot \cos 45° \cdot l \cdot 8 = A_r \sigma_y \cdot \cos 45° \cdot l \cdot 8 \tag{2.7}$$

Where l is the horizontal distance (150 mm) from the centroid of the column section to reinforcing bars; A_r is the cross sectional area of reinforcing bars (127 mm^2); and σ_y is the yield strength of rebars (373 N/mm^2).
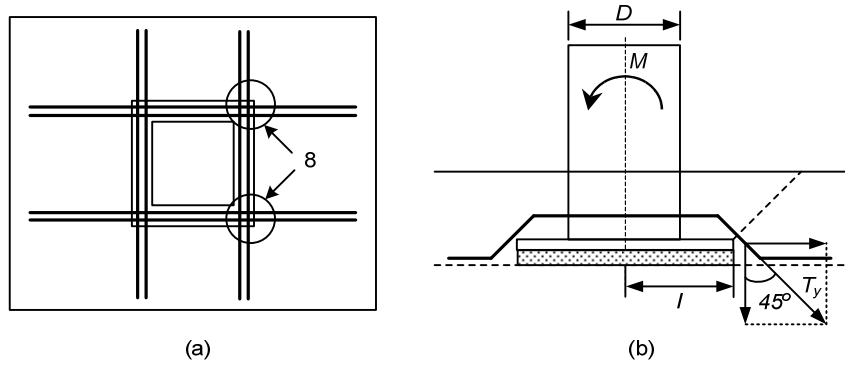
Fig. 2. 10 Model of contribution of rebars: (a) plan view; (b) elevation view

2.4.4   Verification

The maximum strength of the shallowly embedded column base, M_u, is taken to be the summation of Eqs. (2.1), (2.2), (2.6), and (2.7). These calculated maximum strengths are compared with the corresponding experimental results (shown as black bars) in Fig. 2.11. For each specimen, the contributions of respective mechanisms are shown separately. The proposed equations provide reasonable estimates of the moment capacity, with the predicted values ranging 82% to 92% of the corresponding experimental strengths. The relationship between the predicted strength and the full-plastic moment of the column, M_p, agrees with the failure mode of the specimen. Specimen 'Found.-100-st-t12' failed in floor slab punching shear, in which the predicted strength is smaller than M_p, while Specimen 'Found-100-st-t9' failed in column buckling, in which the predicted strength is larger than M_p. The ratio of M_{cc} (contribution of the bearing resistance of the floor slab) to M_{ct} (contribution of the punching resistance of the floor slab) changes according to the thickness and shape of the slab. For specimens with the flat floor slab ('SL-100' and 'SL-200'), the ratio of M_{cc} to M_{ct} increases with the increase of the slab thickness since the slab thickness contributes to the bearing resistance more than the punching resistance. This is because the bearing and punching resistances are proportional to the square and linear of the slab thickness, respectively. For specimens with partially elevated slabs ('Foot-100'), M_{ct} is relatively small because the failure surface area generated by the punching shear does not increase by the partially elevated portion. For specimens embedded in the foundation beam whose height was increased by an additional 100 mm floor slab ('Found.-100'), the estimated strength is the same as that of the specimen with a floor slab of 200 mm ('SL-200'), because the failure surface area is the same.
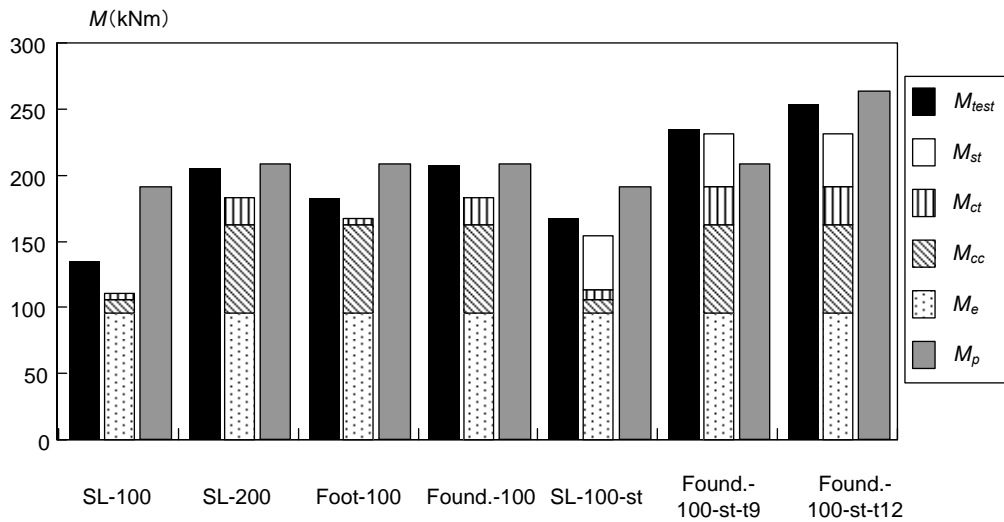
Note: Specimen 'Found.-100-st-t9' failed in column-buckling instead of slab punching-shear

Fig. 2. 11 Maximum strength of specimen

2.5 Evaluation of Elastic Stiffness

In this section, an analytical model to evaluate the elastic stiffness of shallowly embedded column bases is described. The evaluation procedure of elastic stiffness is developed following the individual components, i.e. the exposed column base component, the covering concrete slab component and the reinforcing bars components, adopted for the strength evaluation introduced in Section 2.4. According to the test results, the presence of rebars has minimal effects on the elastic stiffness. Therefore, the contribution of rebars to the elastic stiffness is not considered in the evaluation procedure. As introduced in Section 2.3.1, the elastic stiffness of the specimen is defined as the secant stiffness between the origin and the point at 0.005 rad. Since the entire column base system remained nearly elastic without visible cracks during the cycle of 0.005 rad, the elastic theory was adopted for the elastic stiffness evaluation instead of the plastic theory which was adopted for the strength evaluation.

As shown in Fig. 2.12, the deformation of the column base is composed of the rotation of the column and the rotation of the base plate, which is resisted by the anchor bolts and the covering slab, as shown from Fig.2.13 to Fig.2.16. The elastic stiffness of the column and base plate connection act in series. The elastic stiffness provided the anchor bolts and that of the covering slab act in parallel. The evaluation of elastic stiffness of each component is introduced as follows.
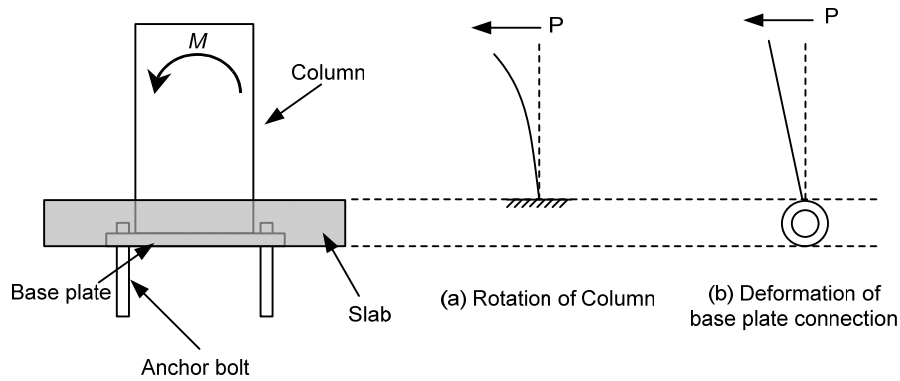
Fig. 2. 12 Mechanism model for stiffness evaluation

2.5.1 Resistance of anchor bolts

The stiffness from the anchor bolts, K_{AB}, can be calculated following the AIJ guidebook (AIJ 2006). The elongation of the anchor bolts only in the tension part is considered.

$$K_{AB} = \frac{E \cdot n_t \cdot A \cdot (d_c + d_t)^2}{2l_b} \tag{2.8}$$

Where E is Young's Modulus of anchor bolts (205,000 N/mm^2); n_t is the number of anchor bolts in the tension side (6); A is the section area of anchor bolts (113.1mm^2); d_c is the horizontal distance (100 mm) from the centroid of the column section to the edge of column section on the compression side; d_t is the horizontal distance (103.3 mm) from the centroid of the column section to the centroid of the group of anchor bolts on the tension side; and l_b is the length of the anchor bolts (250 mm), as shown in Fig. 2.13.
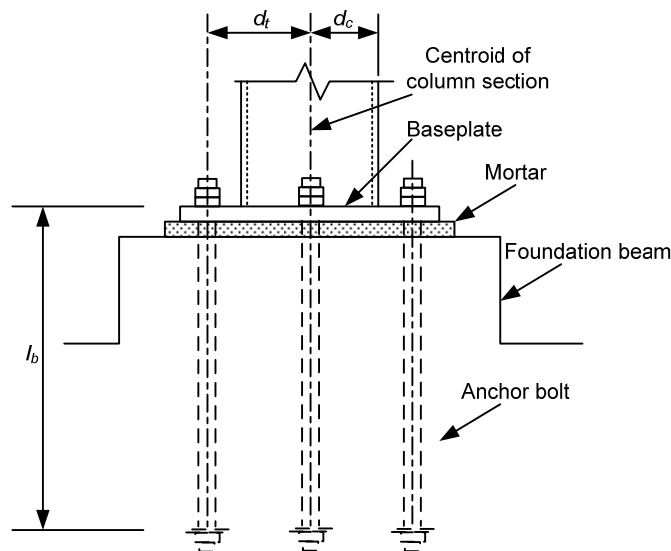

Fig. 2. 13 Dimension of exposed column base (AIJ 2006)

2.5.2 Resistance of the covering slab

The stiffness contributed by the covering slab is considered to consist of two components, the bearing resistance in the compression region (Fig. 2.15) and the punching resistance in the tension region (Fig.

2 - 15

2.16). To simplify the calculation, the stiffness contributed from each component is evaluated separately.

According to the test results, Specimens 'SL-200', 'Foot-100', and 'Found.-100', which shared the same embedded depth of the column, showed nearly the same elastic stiffness. As illustrated in Fig. 2. 14, the covering slabs of these three specimens also share the same area 500mm × 500mm around the column. Therefore, the 500mm × 500mm area of slab (shown in gray of Fig. 2.14) is considered as the region effective to evaluate the resistance of the covering slab.
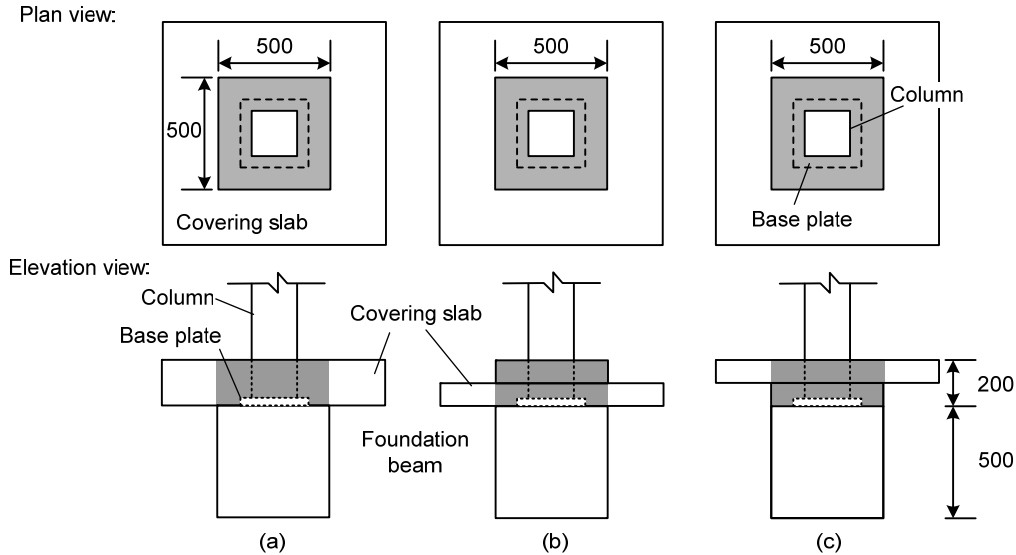

Fig. 2. 14 Effective region in slab for the elastic stiffness evaluation:
(a) SL-200; (b) Foot- 100; and (c) Found.-100 (Unit: mm)

Resistance in compression region

The stiffness contributed by the bearing resistance in the slab compressive region, K_{CC}, is evaluated as follows. As shown in Fig. 2.15, the portion in the slab which is considered as the effective part to resist the compressive force is a slab with the thickness of d, width of D, and length of $100 + (B-D)/2$. Here, d is measured from the top surface of the base plate to the surface of the covering slab, C is the width of the column section, and B is the length of the base plate. It is assumed that the pressure from the column distributed in a triangle shape, and the maximum compressive deformation at the top surface of the slab is δ_{CC}. Therefore, the moment resisted by the slab is:

$$M_{CC} = E_c \cdot \frac{\delta_{CC}}{100 + (B-D)/2} \cdot d \cdot \frac{1}{2} \cdot D \cdot \frac{2}{3} d \qquad (2.9)$$

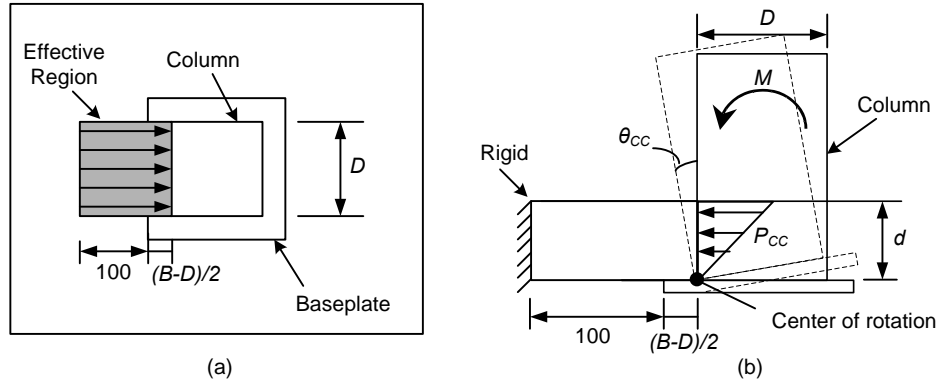Where E_c is Young's Modulus of concrete (23,103 N/mm^2).

Fig. 2. 15 Model of compressive resistance in concrete slab:
(a) plan view; (b) elevation view (Unit: mm)

And the rotation of the direct bearing section of the slab is:

$$\theta_{CC} = \frac{\delta_{CC}}{d} \tag{2.10}$$

The stiffness contributed by the bearing resistance in the covering slab in the compression region is:

$$K_{CC} = \frac{M_{CC}}{\theta_{CC}} = \frac{E_c \cdot D \cdot d^3}{3[100 + (B-D)/2]} \tag{2.11}$$

Resistance in punching region

The rotation of the base plate is assumed as θ_{CT}. The punching force from the base plate is represented by a concentrated force P_{CT} at the point where the slab is touched by the end of the base plate. Therefore, the deflection at the contacted point δ_{CT} is:

$$\delta_{CT} = \frac{Pl^3}{3E_c I} = \frac{P \cdot 100^3}{3E_c I} \tag{2.12}$$

Following the deformation conditions,

$$\delta_{CT} = \theta_{CT} \cdot \left(D + \frac{B-D}{2} \right) \tag{2.13a}$$

$$\theta_{CT} \cdot \left(D + \frac{B-D}{2} \right) = \frac{P_{CT} \cdot 100^3}{3E_c I} \tag{2.13b}$$

We obtain:

$$K_{CT} = \frac{M_{CT}}{\theta_{CT}} = \frac{P_{CT}\left(D + \dfrac{B-D}{2}\right)}{\theta} = \frac{\left(D + \dfrac{B-D}{2}\right)^2 \cdot 3E_c I}{100^3} = \frac{\left(D + \dfrac{B-D}{2}\right)^2 \cdot 3E_c}{100^3} \frac{D \cdot d^3}{12} \tag{2.14}$$

The effective region for the punching resistance of the slab is shown as the gray region of Fig.2.16. The region acts as a cantilever beam, with D as the width, $(B-D)/2+100$ as the length, and d as the depth.
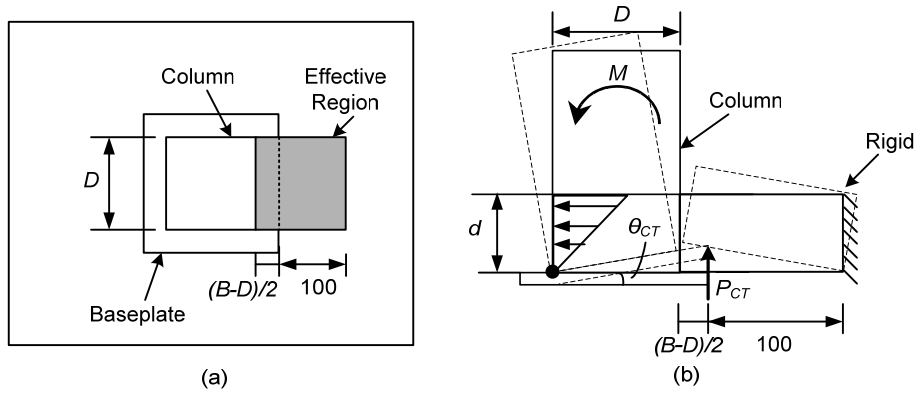
Fig. 2. 16 Model of punching resistance in concrete slab:
(a) plan view; (b) elevation view (Unit: mm)

As described above, the resistance of the anchor bolts, that of the slab in the compression region, and that of the slab in punching region act in parallel. The stiffness contributed by the base plate connection portion is the summation of these three components.

$$_{sta}K_{is} = K_{AB} + K_{CC} + K_{CT} \tag{2.15}$$

The rotated stiffness of the column is:

$$K_c = \frac{3E_s I_c}{L_{fix}} \tag{2.16}$$

Where L_{fix} is the distance from the top of the column to the top surface of floor slab, I_c is the moment of inertia of the column section, and E_s is Young's Modulus of steel (205,000 N/mm^2).

The initial stiffness of the shallowly embedded column without axial force, K_0, is calculated by considering the stiffness of the base plate connection, with the three components acting in parallel, and the rotated stiffness of the column acted in series.

$$K_0 = \frac{1}{\dfrac{1}{_{sta}K_{is}} + \dfrac{1}{K_c}} \left(= \frac{1}{\dfrac{1}{K_{AB} + K_{CC} + K_{CT}} + \dfrac{1}{K_c}} \right) \tag{2.17}$$

2.5.3　Initial stiffness with axial force

As observed in the test, when the axial force was applied, the base plate was detached before 0.005 rad, the drift angle adopted as the elastic limitation for the quantification of initial stiffness. Here, the stiffness of the specimen is different before and after the detachment.

It is assumed the base plate will not rotate until the detachment occurs and only the column will deform. The stiffness before the detachment, thereby, is evaluated by Equation (2.18).

The detached rotation is calculated as follows.

$$\theta = \frac{P L_c^2}{3E_s I_c} = \frac{M L_c}{3E_s I_c} = \frac{N w L_c}{3E_s I_c} \tag{2.18}$$

As shown in Fig.2.17, N is the applied axial force (511 kN), P is the corresponding detached lateral load, L_c is the column height (1228.5 mm), and w is the distance from the center of rotation to

the centroid of the column (100 mm). The stiffness after detachment is the elastic stiffness without the axial force, K_0, as introduced before. The relationship between the stiffness before and after detachment is shown in Fig. 2.18.
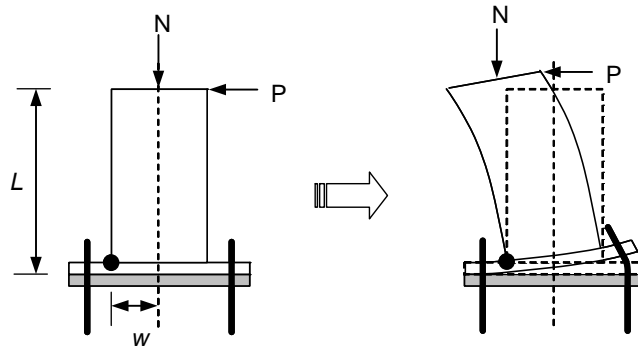
Fig. 2. 17 Deformation of the column before and after detachment
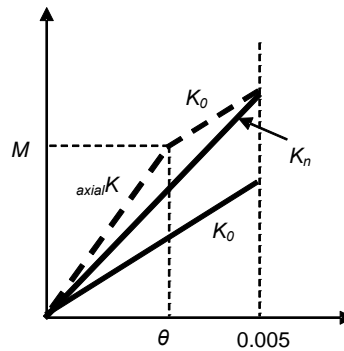
Fig. 2. 18 Definition of the initial stiffness with axial force

The rotated stiffness of the column is

$$_{axial}K = \frac{3E_s I_c}{L_c} \tag{2.19}$$

Therefore, the stiffness considering the contribution of axial force (K_n) is evaluated as follows.

a) When the detachment occurs ($K_0 < {}_{axial}K$)

$$K_n = \frac{{}_{axial}K \cdot \theta + K_0 \cdot (0.005 - \theta)}{0.005} \tag{2.20a}$$

b) When the detachment does not occur ($K_0 \geq {}_{axial}K$)

$$K_n = K_0 \tag{2.20b}$$

2.5.4   Verification

The calculated elastic stiffnesses are compared with the corresponding experimental results (shown as black bars) in Fig. 2.19. The proposed equations provide reasonable estimates of the elastic stiffness, with the differences between the two not greater than 15%. The difference is minimal (1%) for the specimen with 100 mm thick slab ('SL-100') is minimal (1%). The difference tends to

increase as the slab thickness increases. The difference for specimens being the slab in the same thickness also varies with respect to the shape. It is speculated that the assumed effective area for the stiffness evaluation varies as the thickness and shape of slab change. The difference is around 8% for the specimens with the strengthened slabs ('SL-100-st' and 'Found-100-st'). It is partially because the contribution of rebars to the elastic stiffness is ignored in the evaluation.
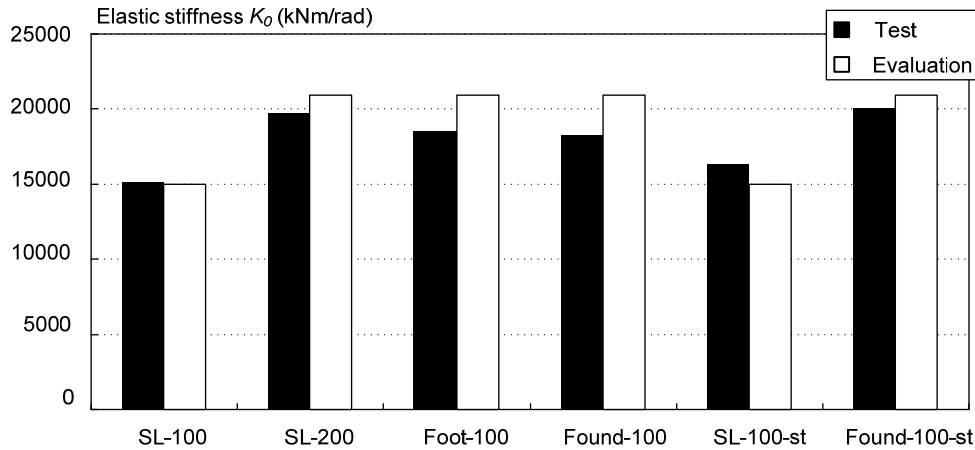
Fig.2.19 Initial stiffnesses of specimens

The differences of elastic stiffness between the shallowly embedded column base and corresponding embedded column base, in which the level of slab surface is assumed to be the same, is shown in Fig. 2.21. The elastic stiffness of the embedded column base, $_{emb}K$, is calculated following the specification of AIJ (2006).

$$_{emb}K = \frac{3E_s I_c}{L_{emb}}$$
(2.21)

Where L_{emb} is the distance from the inflection point of the column to the level that is below the surface by a distance of 1.5 times the column width, I_c is the moment of inertia of the column cross section, and E_s is Young's Modulus of steel (205,000 N/mm^2).

Fig. 2. 20 Comparison between embedded column base and shallowly embedded column base

Using the proposed evaluation, the elastic stiffness is plotted with respect to the thickness in Fig.2.21. The abscissa is the ratio of thickness of the floor slab to the column section, t/D, and the ord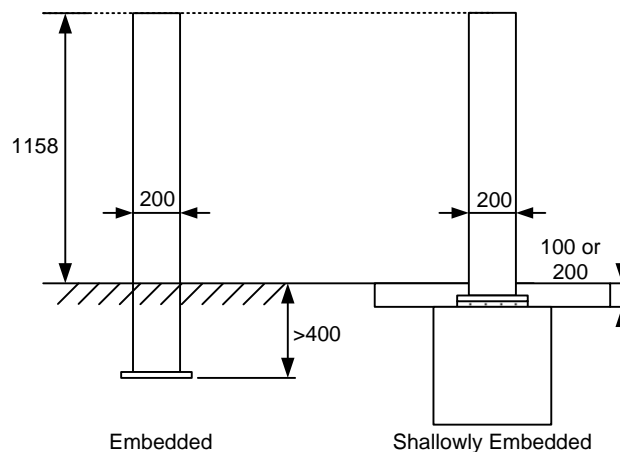inate is the ratio of elastic stiffness between the shallowly embedded column base and corresponding embedded column base, $K_n/_{emb}K$. The proposed evaluation generally provides an upper bound of the test results. It is notable that the elastic stiffness of the shallowly embedded column base becomes larger than that of the corresponding embedded column base when the ratio of the floor slab thickness to the column section (t/D) is larger than 0.65. It is primarily because the fixity of the base plate connection is enhanced by the presence of anchor bolts for thicker slabs. Contribution of the anchor bolts was not counted in the evaluation of elastic stiffness for embedded column bases. For the sake of conservatism, the ratio ($K_n/_{emb}K$) is suggested not greater than 1.0.
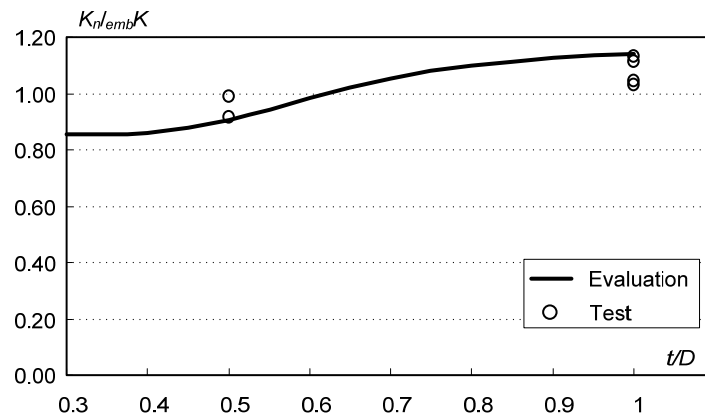
Fig. 2. 21 The ratio of elastic stiffness between shallowly embedded and embedded column base

Considering the workability of design practice, it would be easier that the elastic stiffness of the shallowly embedded column base is evaluated based on that of the corresponding embedded column base, like:

$$K_n = \alpha \cdot {}_{emb}K \tag{2.22}$$

Where α is a factor to estimate the elastic stiffness as a fraction of the embedded column base. In light of Fig. 2.21, the suggested value α is given as follows.

When $t/D<0.7$,

$$\alpha = 0.9 , \tag{2.23a}$$

When $t/D \geq 0.7$,

$$\alpha = 1.0 , \tag{2.23b}$$

2.6 Conclusions

A series of quasi-static cyclic loading tests of steel column bases were conducted to investigate how the floor slab would contribute to the seismic performance of column bases. Major test variables were the thickness, the shape of the floor slab, and the horizontal rebars. Major observations obtained from this study are as follows.

(1) The elastic stiffness, maximum strength, and dissipated energy were improved by the

presence of the floor slab. The elastic stiffness of the shallowly embedded column base specimens was about 1.1 times and 1.5 times for the 100 mm and 200 mm thick floor slabs, respectively. For the same thickness slab, neither the slab shape nor the horizontal rebars contributed to the improvement of elastic stiffness.

(2)   Configuration (thickness and shape) of the floor slab influenced the maximum strength significantly. The presence of horizontal rebars further increased the maximum strength. Compared with the baseline exposed column base specimen, the maximum increase was around 2.0 times for the specimen featured with both the thickest slab and horizontal rebars.

(3)   The deformation capacity was improved by the installation of horizontal rebars. Strength deterioration due to punching shear failure of the floor slab started at around a drift angle of 0.03 rad. Because of the presence of horizontal rebars, the strengthened specimens sustained 90% of the maximum strength until the drift angle reached 0.06 rad.

(4)   The punching shear failure in the floor slab was the main failure mode of the shallowly embedded column base. However, the failure mode was converted to the column local buckling mode when the strength of the column base became larger than the full-plastic moment of the column.

(5)   Considering the performance and the volume of concrete, the shallowly embedded column base having elevated foundation shape is recommended in practice. The elastic stiffness, maximum strength and dissipated energy increased 1.5, 2.0, and 2.7 times as compared with that of the corresponding exposed column base.

(6)   Using the plasticity theory applied to the punching shear failure on the uplifted side of the floor slab and the compressive failure on the compressive side of the floor slab, the maximum strength of the slab can be estimated with reasonable accuracy regardless of the thickness and geometrical condition of the floor slab. The evaluated results show no more than 20% errors compared with the corresponding test results.

(7)   Using the elasticity theory applied to the same model adopted for the strength evaluation, the elastic stiffness can be estimated with reasonable accuracy regardless of the geometric condition of the floor slab and presence of rebars. The evaluated results show no more than 15% errors compared with the corresponding test results. A simplified equation is proposed to assess the elastic stiffness as a fraction of the corresponding elastic stiffness of fully embedded column bases.

REFERENCES

[2.1]   American Institute of Steel Construction (AISC). (2005). Steel construction manual, Chicago.

[2.2]   American Institute of Steel Construction (AISC). (2005). Seismic provisions for structural steel buildings, Chicago.

[2.3]   American Concrete Institute (ACI). (2002). Building code requirements for structural concrete and commentary, Farmington Hill, Michigan.

[2.4]   Architectural Institute of Japan (AIJ). (1990). Design guidelines for earthquake resistant reinforced concrete buildings based on ultimate strength concept, Tokyo (in Japanese).

[2.5]   Architectural Institute of Japan (AIJ). (2005). Design standard for steel structures- based on allowable stress concept, Tokyo (in Japanese).

[2.6]   Architectural Institute of Japan (AIJ). (2006). Recommendations for design of connections in steel structures, Tokyo (in Japanese).

[2.7]   Astaneh, A., Bergsma, G., and Shen J. H. (1992). "Behavior and design of base plates for gravity, wind and seismic loads." Proceedings of the National Steel Construction Conference, Las Vegas, Nevada, AISC, Chicago, Illinois.

[2.8]   Burda, J. J. and Itani, A. M. (1999). "Studies of seismic behavior of steel base plates." Report No. CCEER 99-7, Center for Civil Engineering Earthquake Research. Dept. of Civil Engineering, Univ. of Nevada, Reno, Nevada.

[2.9]   Chen, W.F. (1982). "Plasticity in reinforced concrete." McGraw-Hill, Inc.

[2.10]   DeWolf, J.T. (1982). "Column base plates." Structural Engineering Practice, 1(1), 39-51.

[2.11]   European Committee for Standardization (CEN). (1992). ENV 1993 Eurocode 3; Design of steel structures, Brussels, Belgium.

[2.12]   Fisher, J. M. and Kloiber, L. A. (2006). "Base plate and anchor rod design (Second edition)." Steel Design Guide Series No. 1, AISC, Chicago.

[2.13]   Morino, S., Kawaguchi, J., Tsuji, A., and Kadoya, H. (2003). "Strength and stiffness of CFT semi-embedded type column base." Proceedings of ASSCCA 2003 Conference, Sydney, Australia, A. A. Balkema, Sydney, Australia.

[2.14]   Nakashima, M., Inoue, K., and Tada, M. (1998). "Classification of damage to steel buildings observed in the 1995 Hyogoken-Nanbu Earthquake." Engineering Structures, 20(4-6), 271-281.

[2.15]   Nakashima, S. and Igarashi, S. (1986). "Behavior of steel square tubular column bases for interior columns embedded in concrete footing under bending moment and shearing Force, Part 1 Test program and load-displacement relationships." J. Struct. Constr. Eng., Transaction of AIJ, 366, 106-118. (in Japanese).

[2.16]   Nielsen, M.P. (1984). "Limit analysis and concrete plasticity." Prentice-Hall, Inc., Englewood Cliffs, New Jersey 07632.

[2.17]   Steel Committee of the Kinki Branch of the Architectural Institute of Japan (AIJ). (1995). Reconnaissance report on damage to steel building structures observed from the 1995 Hyogoken-Nanbu earthquake, Osaka.

[2.18]   Thambiratnam, D. P. and Paramasivam, P. (1986). "Base plate under axial loads and moments." J. Struct. Eng., 112(5), 1166-1181.

CHAPTER 3

Numerical Analysis of Shallowly Embedded Column Base with Conventional Concrete Slab

3.1 Introduction

3.1.1   Background

To enhance the understanding of the test results shown in Chapter 2, extensive numerical analysis was carried out in this chapter. A general-purpose finite element program ABAQUS version 6.7 was used to analytically study the behavior of the test specimens and furthermore generalize the behavior of shallowly embedded column bases.

As introduced in Chapter 2, the concrete slab is one of the controlling components of the shallowly embedded column base. Some typical mechanical properties of concrete under uniaxial, biaxial, and triaxial states of stress are summarized in this chapter. These data form the basis to choose an appropriate concrete model to simulate the floor slab in the shallowly embedded column base.

3.1.2   Characteristics of concrete

Concrete is a brittle material. Its deformation characteristics are related to the development of micro-crackings in the material body, quite different from that of dislocations of crystals in metal. The propagation of these microcracks during loading contributes to the nonlinear behavior of concrete at low stress level and causes volume expansion near failure. This microcrack is the primary reason for the low tension strength of concrete material. A brief summary of the key facets of the experimental behavior of plain concrete is given here.

Uniaxial behavior of concrete
Uniaxial-compression behavior
A typical stress-strain relationship for concrete subjected to uniaxial compression is shown in Fig. 3.1. The stress-strain curve has a nearly linear-elastic behavior up to about $0.3\,f_c'$. For stress above this point, the curve shows a gradual increase in curvature up to about $0.75\,f_c'$ to $0.90\,f_c'$, whereupon it bends more sharply and approaches the peak point at f_c'. Beyond this peak, the stress-strain curve has

a descending part until crushing failure occurs at some ultimate strain ε_μ (around 0.003). The shape of the stress-strain curve is similar for concrete of low, normal, and high strength. A high-strength concrete behaves in a linear fashion to a relatively higher stress level than the low-strength concrete, but all peak points are located close to the strain value of 0.002. On the descending portion of the stress-strain curve, higher-strength concretes tend to behave in a more brittle manner, the stress dropping off more sharply than it does for concrete with lower strength.
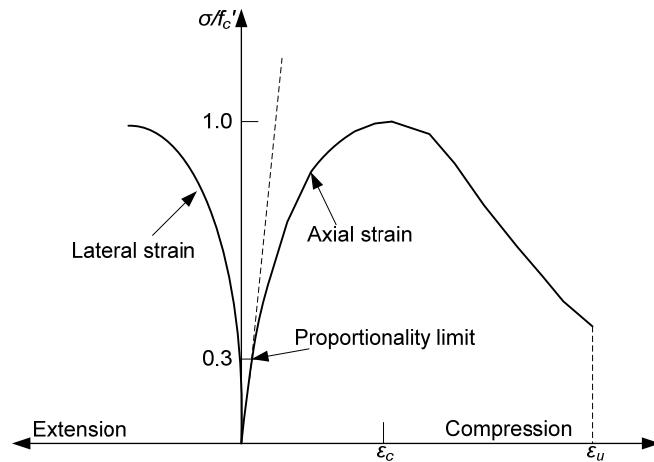

Fig. 3. 1 Typical stress-strain curves for concrete in uniaxial compression test (Chen, 1982)
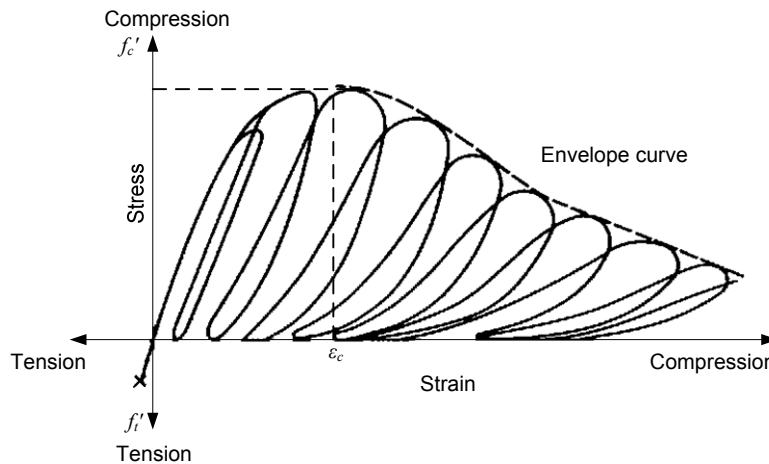
Fig. 3. 2 Cyclic uniaxial compressive stress-strain curve (Karsan and Jirsa, 1969)

The behavior of plain concrete subjected to cyclic compressive loading is shown in Fig.3.2. The envelope curve observed for cyclic loading is close to the uniaxial stress-strain curve for monotonic loading. The large residual strains that remain after unloading can be observed. It suggests that the inelastic response is due to damage to the internal structure of the concrete.

Uniaxial-tension behavior

The shape of the stress-strain curves for concrete in uniaxial tension shows many similarities to the uniaxial-compression curves (Fig.3.3). However, compared to the corresponding compressive strength f_c', these curves have a markedly lower tensile strength f_t'. For stress less than about $0.6 f_t'$, the

curves show a nearly linear-elastic behavior. Thus, this stress level will correspond to a limit of elasticity. The ratio between uniaxial tensile and compressive strength usually ranges from 0.05 to 0.1.
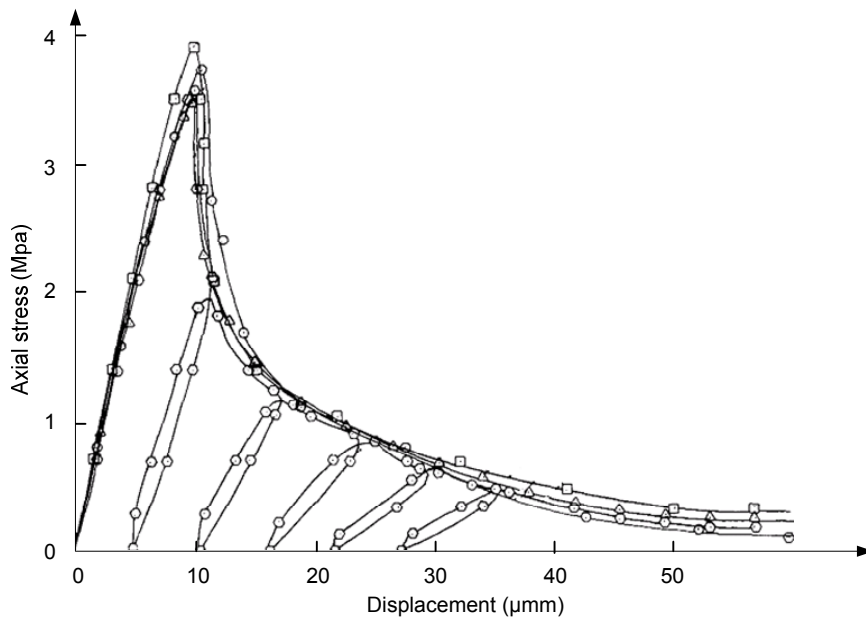

Fig. 3. 3 Cyclic uniaxial tensile stress-strain curve (Gopalaratnam and Shah, 1985)

Biaxial behavior of concrete

Failure modes of biaxial loading concrete are shown in Fig.3.4. The main characteristics of concrete behavior under biaxial stress state are summarized as follows:

(1)   The maximum compressive strength increases for the biaxial-compression state. A maximum strength increase of 22%~27% is achieved at a stress ratio of $\sigma_2/\sigma_1=0.5$ and is reduced to about 16% at an equal biaxial-compression state ($\sigma_2/\sigma_1=1$).

(2)   Under biaxial compression-tension, the compressive strength decreases almost linearly as the applied tensile stress is increased.

(3)   Under biaxial tension, the strength is almost the same as that of uniaxial tensile strength.

(4)   Concrete ductility under biaxial stresses has different values depending on whether the stress states are compressive or tensile. For uniaxial and biaxial compression the average maximum tensile strain varies from approximately 2000 $\mu\varepsilon$ to 4000 $\mu\varepsilon$; and the average maximum compressive strain is about 3000 $\mu\varepsilon$. In uniaxial and biaxial tension the average value of the maximum principal tensile strain is about 80 $\mu\varepsilon$.

(5)   As the failure point is approached, an increase in volume occurs as the compressive stress continues to increase, which is called dilatancy. It is usually attributed to progressive growth of major microcracks in concrete.

(6)   The maximum-strength envelope is largely independent of load path for normal concrete. But there is some indication that nonproportional loading produces a lower strength than proportional loading for lightweight concrete.
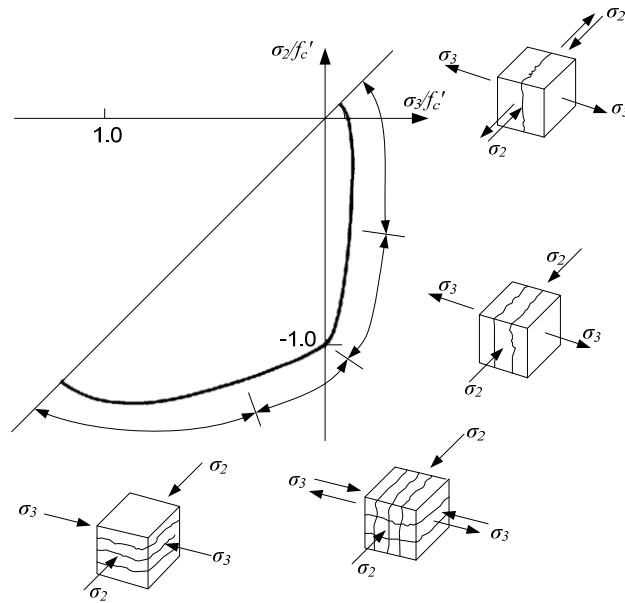
Fig. 3. 4 Failure modes of biaxially loaded concrete (Nelissen, 1972)

Triaxial behavior of concrete

For triaxial stress states, depending on the confining stress, concrete can act as a quasi-brittle, plastic-softening, or plastic-hardening material. Confined concrete specimens exhibit a certain degree of ductility before failure. But for confining stresses beyond a certain value, the increasing lateral pressure will decrease the ductility.
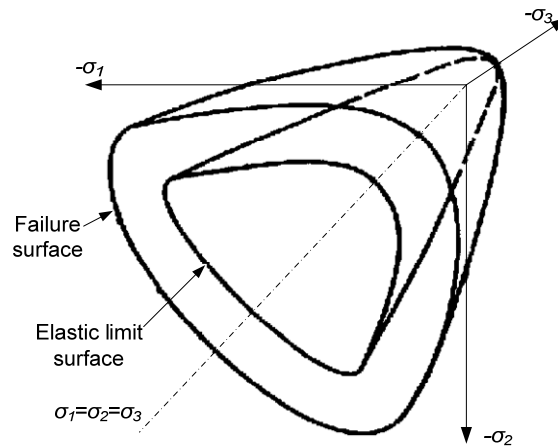
Fig. 3. 5 Schematic representation of elastic limit and failure surfaces of concrete in three-dimensional stress space (Chen, 1982)

Under triaxial loading, experiments indicate that concrete has a fairly consistent failure surface that is a function of the three principal stresses. If isotropy is assumed, the elastic limit, the onset of unstable crack propagation, and the failure limit all can be represented as surfaces in three-dimensional principal-stress space. Fig. 3.5 shows schematically the elastic-limit surface and failure surface. The characteristics of these failure surfaces are summarized as follows:

(1)   The failure surface is curved, smooth and convex in both deviatoric plane and meridian

plane.

(2)   The failure curves in meridian plane are nonlinear. The failure curves in deviatoric plane is nearly triangular for tensile for small hydrostatic compressions, and becomes increasingly bulged (more circular) for increasing hydrostatic compressions.

3.1.3   Plastic-damage model of concrete

There are some typical macroscopic behaviors of materials. Figure 3.6 (a) shows a typical behavior of an elastic-plastic solid. The stiffness of elastic unloading-reloading does not change with plastic deformation. Material nonlinearity is due to the existence of plastic strains. This type of material behavior can generally be described by the theory of plasticity. On the other extreme, Fig 3.6 (b) shows a typical behavior which is perfectly elastic. Upon unloading, the material returns to its stress and strain-free state without any plastic deformation occurred. However, the slope of the unloading-reloading line decreases with increasing straining. Material nonlinearity is induced by the stiffness degradation. This type of behavior is due to microcracks of the material. Fig 3.6 (c) is a combination of these two behaviors. Concretes exhibited the same behavior as sketched in Fig.3.6 (c), particularly in its softening range.
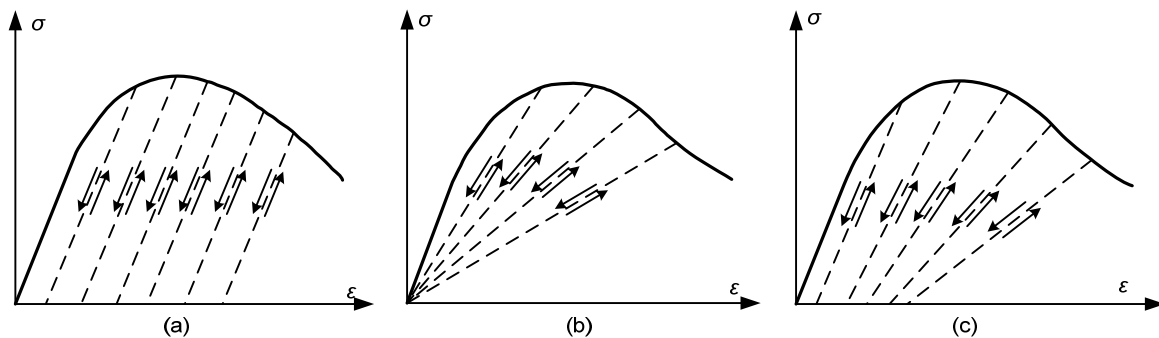

Fig. 3. 6 Typical material behaviors:
(a) elastoplastic solid; (b) progressively fracturing solid; and (c) plastic-fracturing solid

The modeling of crack initiation and propagation is one of the most important aspects in the failure analysis of concrete structures. The cracking process in concrete is a continuous forming and connecting of microcracks (Mehta and Monteiro 1993). The formation of microcracks is represented macroscopically as softening behavior of the material, which causes the localization and redistribution of strain in a structure. On the other hand, the microcracking process also causes stiffness degradation, which can be observed in concrete subjected to cyclic loading (Karsan and Jirda 1969; Gopalaratnam and Shah 1985). Therefore, the nonlinear material behavior of concrete can be attributed to two distinct material mechanical processes: plasticity and damage (microcracks and microvoids).

The strain-softening behavior of concrete at the macroscopic level can be modeled by plasticity theories (Willam and Warnke 1975, Bazant 1978, Pramono and Willam 1989, and Chen 1994). The main characteristic of these models is a plasticity yield surface that includes pressure sensitivity, path

sensitivity, non-associative flow rule, and work or strain hardening. However, these works failed to address the degradation of the material stiffness due to the damage of concrete. On the other hand, others have used the continuum damage theory alone to model the material nonlinear behavior such that the mechanical effect of the progressive microcracks and strain softening are represented by defining the relationship between stresses and effective stresses. Comprehensive reviews on continuum damage mechanics are given by Kachanov (1986) and Lemaitre and Chaboche (1990). Several models for concrete based on continuum damage mechanics have been developed (Mazars 1986; Mazars and Pijaudier-Cabot 1989; Cervera et al. 1995). However, without inelastic (or plastic) strains the continuum damage mechanics theory cannot provide an appropriate dilatancy control, which is very important for simulating plain and reinforced concrete structures under multiaxial loading. Since both microcracks and irreversible deformations are contributing to the nonlinear response of concrete, a constitutive model that accounts for both plasticity and damage is necessary. In this study, the plastic-damage model proposed by Lee and Fenves (1998) is adopted to simulate the cyclic behavior of concrete.

3.1.4   Organization

This chapter consists of three parts. The first part describes the details of the analysis model, including the material properties, interaction among various components, i.e. the shell-to-coupling interaction between the column and base plate and the contact interaction between the nuts of anchor bolts and base plate, and boundary conditions. The second part presents the analytical results applied to the specimens described in Chapter 2 in terms of the elastic stiffness, maximum strength, and the failure region. In the third part, the model is simplified to monotonic loading. After the calibration with cyclic analysis results, the simplified model is applied for a series of parametric analyses of shallowly embedded column bases primarily for the examination of the maximum strength and initial stiffness. Finally, the design procedure to estimate the elastic stiffness and maximum strength proposed in Chapter 2 is calibrated against the analysis results.

3.2 Numerical Analysis

3.2.1   Analysis model

Half of the specimen was modeled by taking advantage of symmetry in the model. As shown in Fig. 3.7, the following Cartesian coordinate system was chosen: the axis along the short edge of the slab was denoted as Ox, the axis along the long edge of the slab was denoted as Oy, the axis Oz ran from the top to bottom along the column. The geometry and boundary conditions of the model conformed to the experimental conditions. The models of shallow embedded column base are subdivided into a column, a baseplate, and a flat slab that surrounds the base plate, as shown in Fig. 3.7.
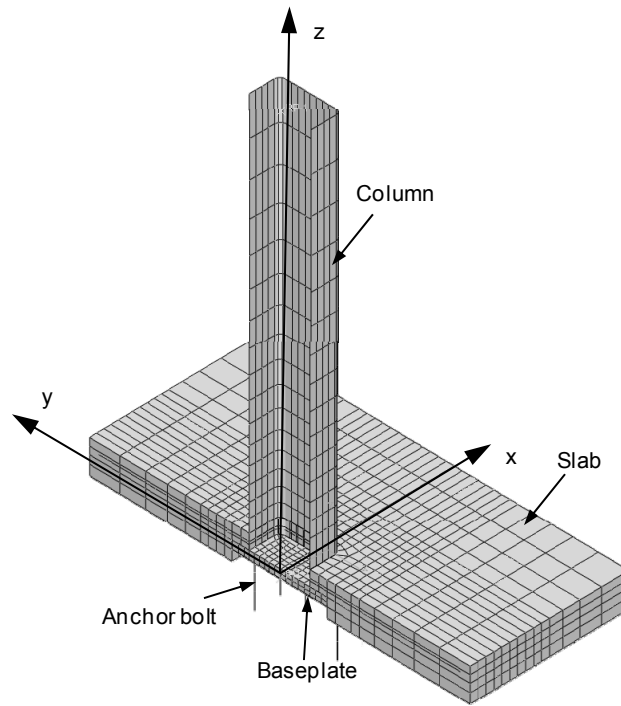
Fig. 3. 7 Analysis model

Modeling column and base plate

A four-node linear reduced integration with hourglass control shell element (S4R) was used for the column. Two layers of eight-node hexahedral incompatible mode elements (C3D8I) were adopted to model the base plate to accurately trace the bending behavior. Care should be taken since there are joints between different element types, shell and 3D solid elements. The problem is the mismatch of the types of DOFs between the shell and 3D solid elements. The rotational DOF cannot be transmitted onto the node on a shell element node, simply because it does not have rotational DOF. Modeling techniques are therefore required to fix this problem. The shell-to-solid coupling was used to create a connection between the two types of element. In Abaqus/Standard the shell-to-solid coupling (Fig. 3.8) is enforced by the automatic creation of an internal set of distributing coupling constraints between nodes on the shell edge and nodes on the solid surface. Compatibility between the difference in DOFs at a node in shell and 3D solid elements is fully enforced. The foundation beam and mortar were considered as a rigid plate underneath the base plate, since the behavior of these two parts was rigid and remained elastic in the test. Interaction between the bottom of the base plate and top surface of mortar was modeled to allow for a contact behavior with friction.
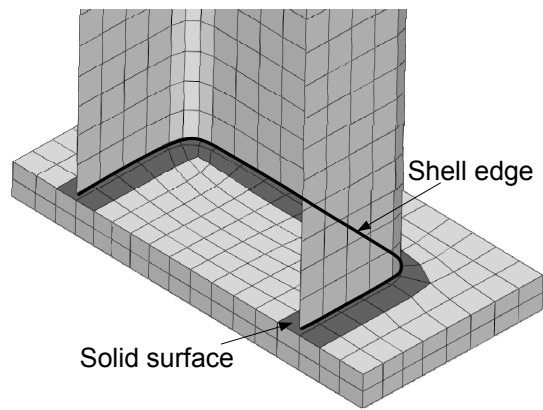
Fig. 3. 8 Shell-to-solid coupling between the column and baseplate

Modeling anchor bolts

As shown in Fig. 3.9, the bolts were modeled as four circular truss elements, having a diameter equal to the nominal bolt diameter of 12 mm, arranged end-to-end, and restrained at the lower node. The freedoms of the top end node were coupled with the relative nodes in the base plate to represent the constraint from the bolt holes to anchor bolts. To model the entire anchor bolt, the upper end of the rod was connected to the appropriate node at the head of bolts simulated by shell elements. The head of the bolts were modeled as shell disks, S4R, having a constant thickness equal to the average thickness of the actual bolt head. The sections were modeled to be rigid by giving them a linear elastic material response.
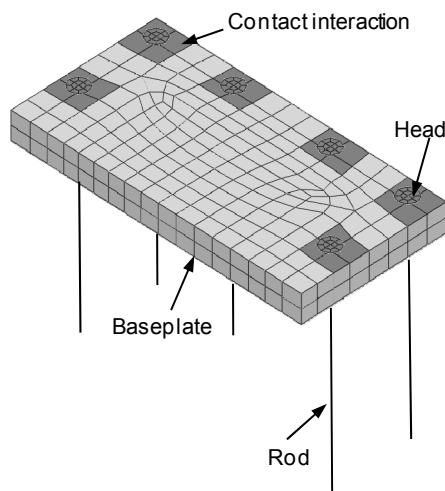
Fig. 3. 9 Modeling of anchor bolts

Modeling Slab

The flat slab was meshed by an 8-node hexahedral element with reduced integration (C3D8R) element instead of higher-order solid elements with a larger number of integration points. This was chosen to reduce the computational effort without losing the accuracy. Mesh bars were modeled by a 'rebar layer' option available in the ABAQUS package. ABAQUS treats each rebar layer as a smeared layer with a constant thickness equal to the area of each rebar divided by the rebar spacing.

3 - 8

The mesh of different configuration slab is illustrated in Fig. 3.10.

Fig. 3. 10 Modeling of slabs: (a) SL-100/SL-100-st; (b) Foot-100;
(c) Found.-100/ Found.-100-st; and (d) SL-200

3.2.2   Material Properties

Steel

In this analysis, the multilinear kinematic hardening option was selected to simulate the metal behavior, with the parameter value pro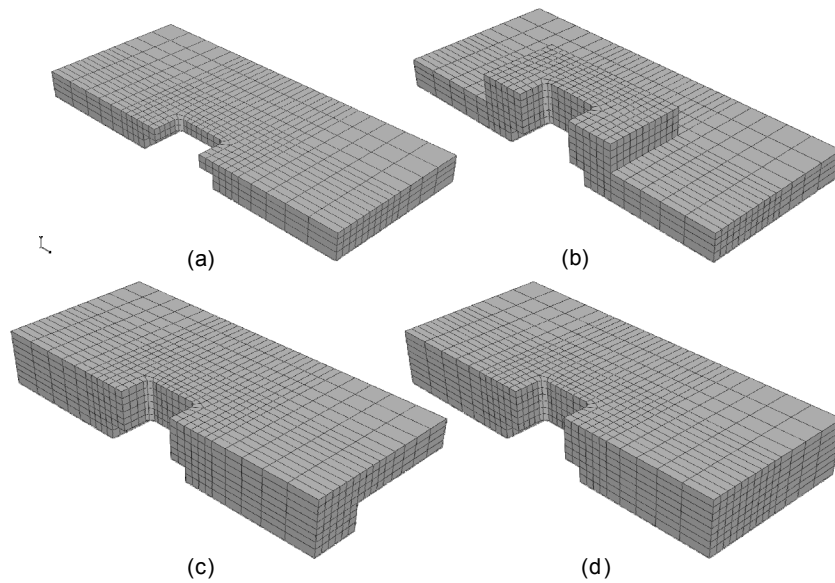vided by the associated material tests. The Mises yield surface was used in combined stress states. The uniaxial stress-strain relations for base plate and anchor bolt are shown in Fig. 3.11. To make sure the failure occurred in the slab, elastic column was defined in the analysis. For the base plate and reinforcing bars, the stress-strain curve was assumed to be bilinear with a strain hardening ratio of $E_s/100$, where E_s is the Young's modulus of steel. For the reinforced concrete, the main steel reinforcement was treated as an equivalent uniaxial material embedded in the concrete slab solid elements, and the bond-slip effect between the concrete and steel was not considered. For the anchor bolts, multilinear curve-fitting was adopted to describe the behavior. A smaller fracture strain at 0.2, compared with the material test, was defined to reflect the effect of the bond stress from the foundation beam.

Concrete

The plastic-damage model, which provides a general capability for the analysis of concrete structures under cyclic loading in ABAQUS, was adopted to model the behavior of concrete. Different from the concrete smeared cracking model, this model considers the failure mechanism of tensile cracking and compressive crushing, separately. Default values were adopted to describe the flow potential and yield surface for concrete, as recommended by ABAQUS Manual. Typical yield surfaces are shown in Fig. 3.12 on the deviatoric plane and in Fig. 3.13 for the plane stress

condition.
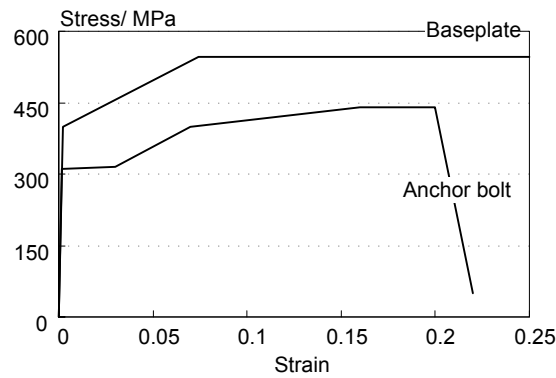
Fig. 3. 11 Material Property for base plates, columns and anchor bolts
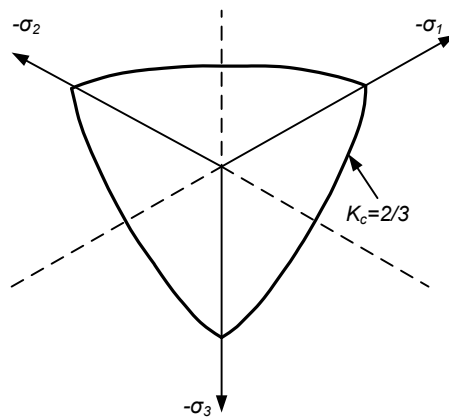

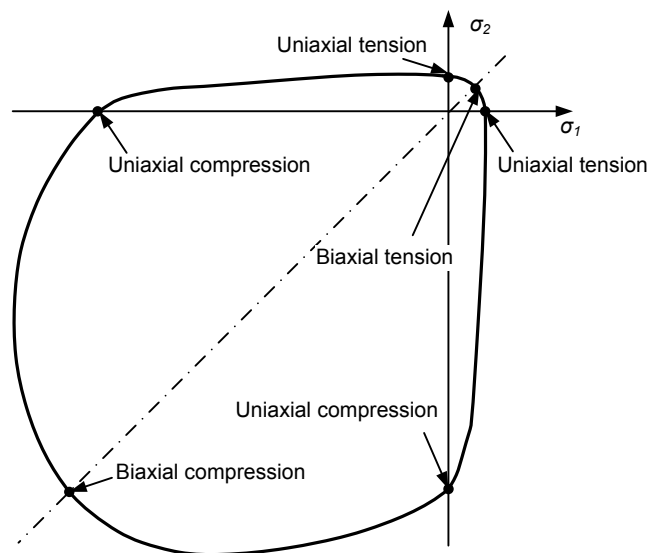Fig. 3. 12 Yield surfaces in the deviatoric plane

Fig. 3. 13 Yield surface in plane stress

The rate-independent, plastic-damage constitutive model proposed by Lee and Fenves (1998) was adopted to describe the uniaxial stress-strain behavior of concrete. The model is developed for cyclic loading using the concept of fracture-energy-based damage. It provides a simple and effective

approach for the analysis of cyclically loaded concrete structures. In this model, two damage variables, one for tensile damage and the other for compressive damage, to account for several damage states. The concept of the fracture-energy-based multiple-hardening variables is used to represent tensile and compressive damage independently. The uniaxial strength functions are factorized into two parts to represent the effective stress and degradation of elastic stiffness (degradation damage). The constitutive system for the elastoplastic responses is described completely by the effective-stress and damage variable, which can lead to a decoupled algorithm for the effective-stress computation and degradation evaluation. A thermodynamically consistent scalar model is used to simulate the stiffness degradation and recovery (cracking opening and closing).

The relation between the uniaxial stress, denoted by σ_κ, and the corresponding scalar plastic strain, denoted by ε_p, is assumed as

$$\sigma_\kappa = f_{\kappa 0}\left[\left(1+a_\kappa\right)e^{-b_x\varepsilon^p} - a_\kappa e^{-2b_\kappa\varepsilon^p}\right] \tag{3.1}$$

where $f_{\kappa 0}$= initial yield stress, defined as the maximum stress without damage; and a_κ and b_κ= constants. The state is uniaxial tensile for $\kappa = t$ and uniaxial compressive for $\kappa = c$. The degradation also takes an exponential form

$$D_\kappa = 1 - e^{-d_\kappa\varepsilon^p} \tag{3.2}$$

where d_κ= a constant.

Uniaxial version of the damage variable, denoted by $0 \le \kappa_\kappa \le 1$, is defined as

$$\kappa_\kappa = \frac{1}{g_\kappa}\int_0^{\varepsilon^p} \sigma_\kappa(\varepsilon^p)d\varepsilon^p \tag{3.3}$$

where

$$g_\kappa = \int_0^\infty \sigma_\kappa\left(\varepsilon^p\right)d\varepsilon^p \tag{3.4}$$

The quantity g_κ= dissipated energy density during the entire process of microcracking. Therefore,

$$g_\kappa = \frac{G_\kappa}{l_\kappa} \tag{3.5}$$

where G_κ= fracture energy in uniaxial stress state and l_κ= the characteristic length to maintain objective results at the structural level.

Cyclic loading examples

Several applications of the numerical model for cyclically loaded concrete tests are presented in this section using two single four-node plane stress quadrilateral isoparameteric elements. The loads are applied by displacement control, and for all cases Poisson's ratio is 0.2.

To compare the rate-independent model with the existing experimental results(Gopalaratnam and Shah 1985, Karsan and Jirsa 1969), the following material properties are used: (1) for cyclic tensile case, E_0=31000 MPa, f_t'=3.48 MPa, $G_t = 40$N/m, l_t= 82.6 mm, and $\widetilde{D}_t = 0.5$; and (2) for cyclic compressive case, E_0=31000 MPa, f_c'=27.6 MPa, $G_c = 5690$ N/m, l_c= 82.6 mm, $\widetilde{D}_c = 0.4$. Figure 3.14 shows the simulated tensile and compressive stress-strain behaviors, respectively. The

numerical simulations represent the experimental reasonably. For both cases the degradation of stiffness is simulated at each unloading/reloading cycle as well as the softening behavior. The hysteresis on reloading cannot be simulated by the model because of the rate-independent elastic loading/unloading assumption.
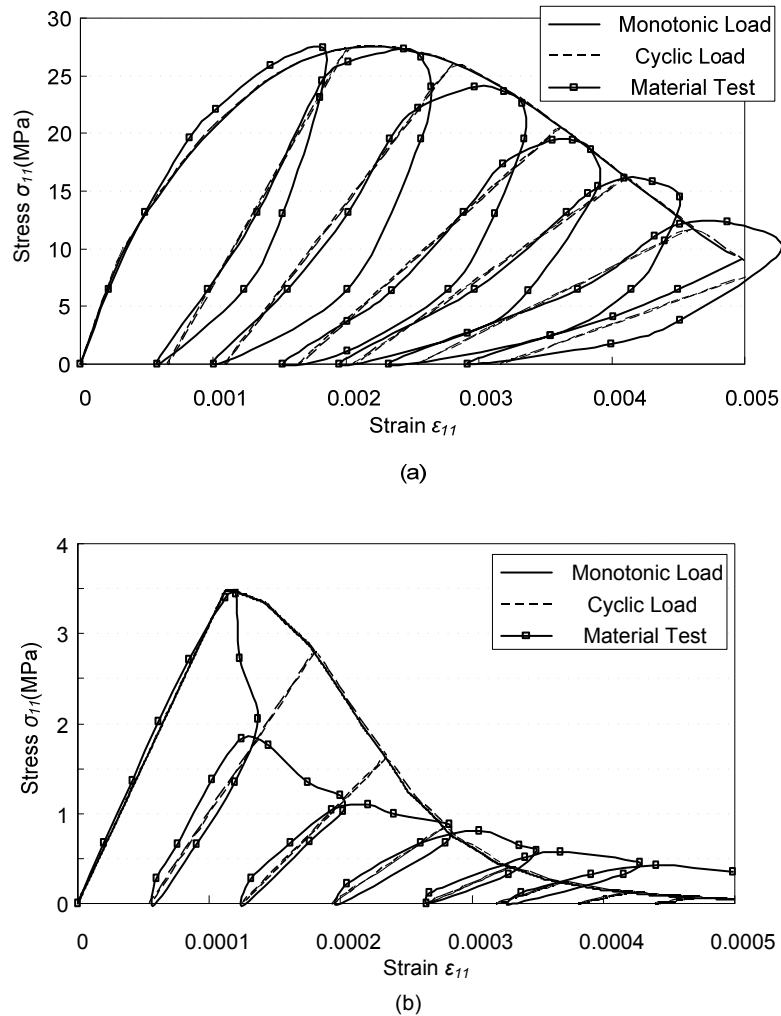

(a)

(b)

Fig. 3. 14 Numerical solutions of cyclic uniaxial loading compared with experimental results: (a) compressive case (Karsan and Jirsa 1969); (b) tensile case (Gopalaratnam and Shah 1985)

As another example, cyclic loading under large tension and compression strains is imposed on two elements patch with the material properties: E_0=31000 MPa, f_t'=3.48 MPa, f_c'=27.6 MPa, G_t = 40N/m, G_c = 5690 N/m, l_t= 82.6 mm, l_c= 82.6 mm, $\widetilde{D}_t$ = 0.5, and $\widetilde{D}_c$ = 0.4. The result is illustrated in Fig. 3.15 with the loading path A-B-C-D-E-F. During the tensile unloading-compressive loading path (path A-B and C-D), the stiffness is recovered. The compressive strength after tensile loading is not degraded (path A-B), which means that the compressive damage is not affected by the tensile damage. On the other hand, the tensile strength depends on the compressive load path because the stiffness degradation from compressive damage is not recovered during tensile unloading (path B-C). This is physically reasonable, because the compressive failure is mainly caused by dilatancy, which affects the subsequent compressive and tensile strengths.
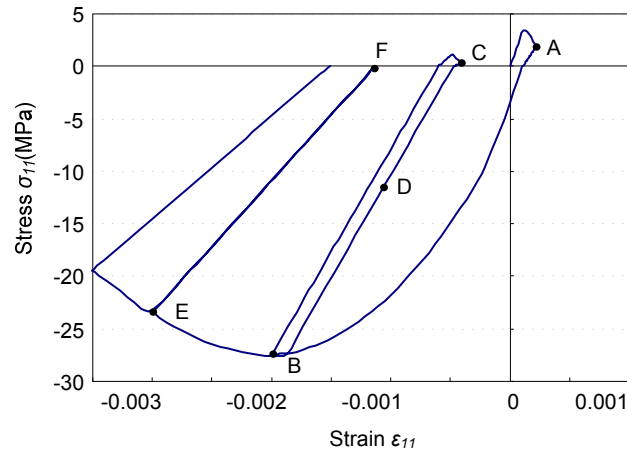
Fig. 3. 15 Numerical solution for full cyclic loading (path: O-A-B-C-D-E-F)

3.2.3 Boundary Condition and Loading

The chosen boundary conditions reflected the symmetric nature of the model. The standard symmetric boundary conditions were introduced at plane $x=0$ as follows. The nodes located on plane $x=0$ were restricted not to move in the direction of the Ox axis. The rotations around the Oy and Oz axes were assumed to be zero. The nodes at the bottom surface of the slab and base plate and the nodes were fixed to the rigid surface of the model. Fig. 3.16 shows the boundary condition of the models adopted in this analysis.

The models were loaded in two steps. The first step was to apply a constant axial load, whose magnitude was the same as that adopted in the tests, i.e., 251 kN (0.2 of ratio of axial force). The imposed load was applied to the reference node of the column end-plate in the negative direction of the Oz axis. The second step was to apply cyclic load to the top of the column. The load was applied by imposing displacements to the reference node of the column end-plate along the Oy axis, i.e., 6 mm, 18mm, 27mm, and 40 mm, which represents drift angle of 0.5%, 1.5%, 2.25%, and 3%, respectively. Two cycles were applied for each drift angle.
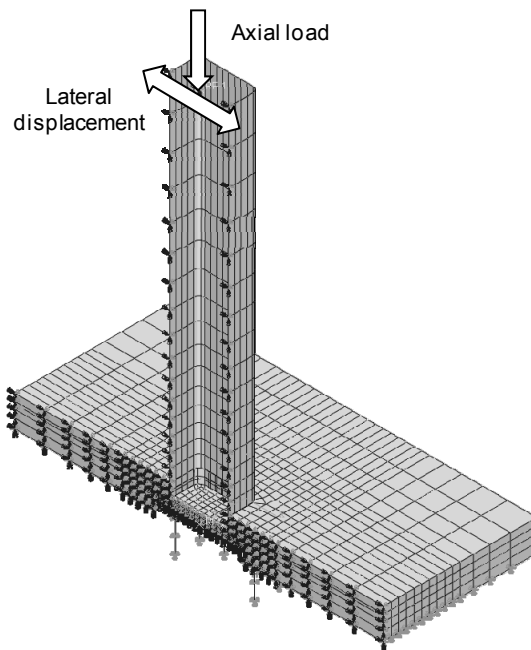
Fig. 3. 16 Application of load and boundary conditions

3.3 Analysis Results

3.3.1 Moment-rotation curves

Figure 3.17 shows the relationship between the column base bending moment and rotation angle. It is notable that the slip caused by the separation between the nut of anchor bolts and base plate was successfully reproduced by the numerical model. In addition, the unload stiffness of the numerical model agreed well with the test results for all specimens.

The experimental and analytical elastic stiffnesses are compared in Fig. 3.18. The elastic stiffness was defined as the secant stiffness between the origin and the point at 0.005 rad story drift angle, following the definition adopted for the experimental results. The difference of the experimental and analytical values ranges between 4% and 16%. The analytical elastic stiffness of Specimen 'Standard' is 16% smaller than the experimental results, since the truss elements assigned for the anchor bolts cannot take the transverse load. When the floor slab is applied to the specimen, the difference is reduced to 2%. It is speculated that the contribution of anchor bolts to the elastic stiffness is less in shallowly embedded column base compared with the exposed column base. As the slab thickness increases, the difference of experimental and analytical results increases. Generally, the analysis provides conservative estimate.
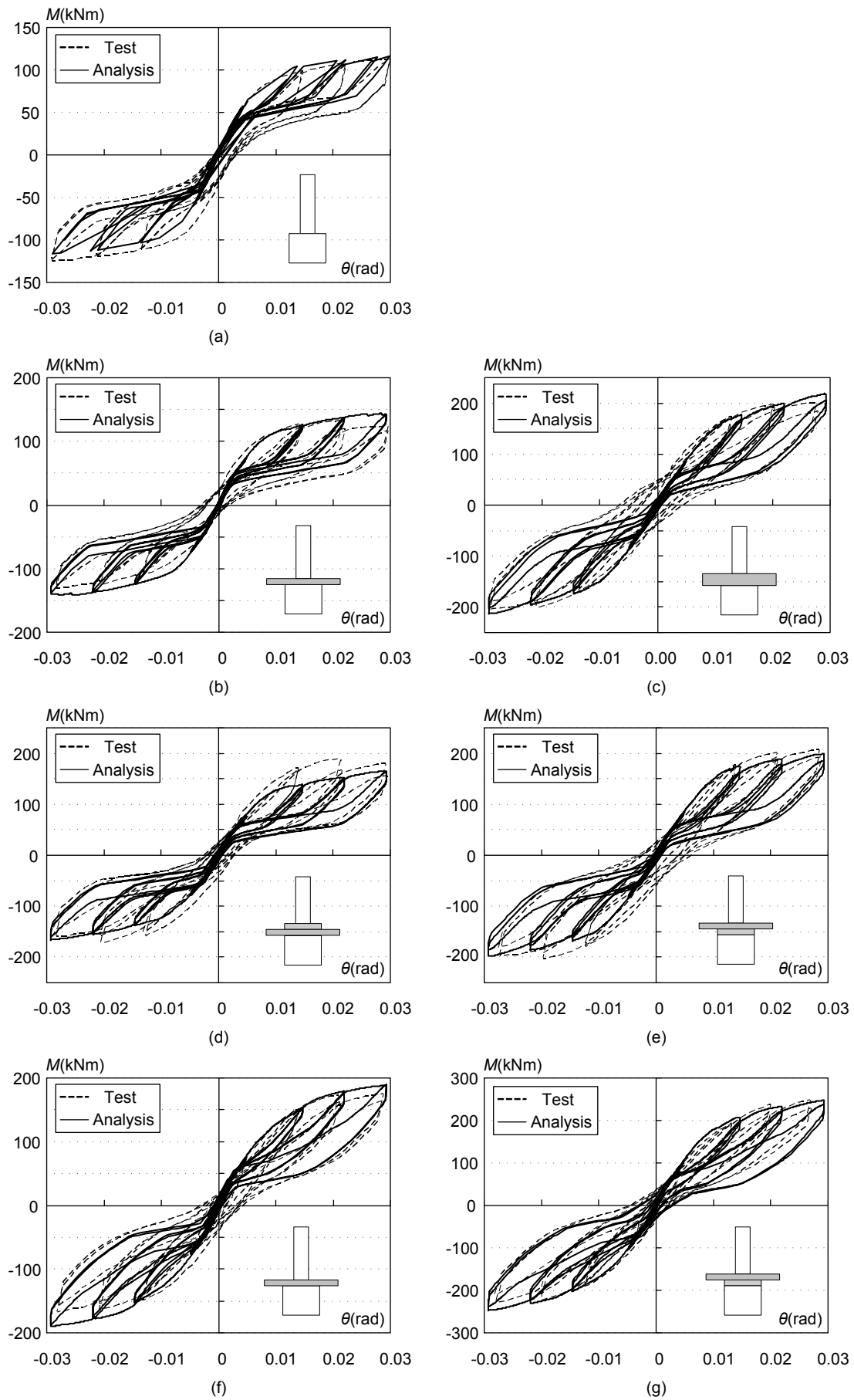
Fig. 3. 17 Comparison of moment-rotation curves: (a) Standard; (b) SL-100; (c) SL-200; (d) Foot-100; (e)Found.-100; (f) SL-100-st; and (g) Found.-100-st-t12
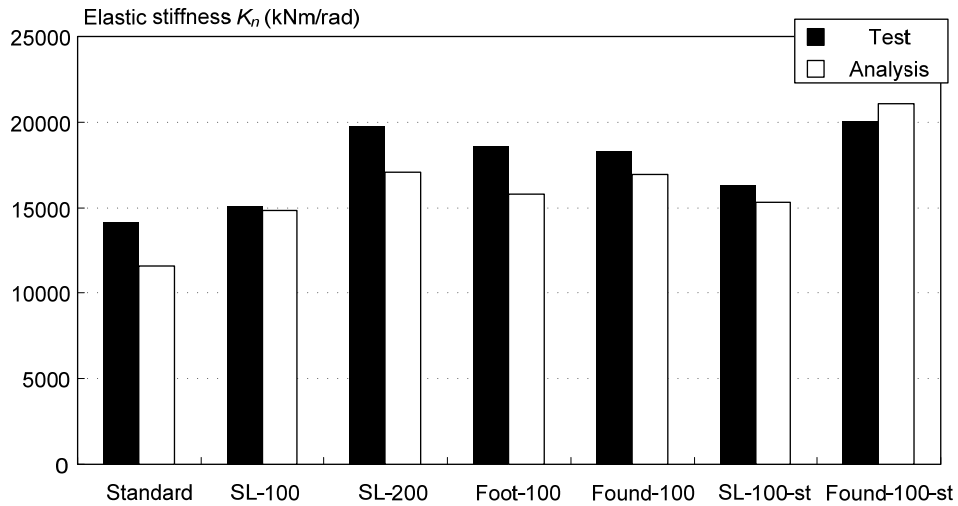
Fig. 3. 18 Comparison of elastic stiffness between test and analysis

The experimental and analytical maximum strengthes are compared in Fig. 3.19. The difference in the maximum strength ranges between 3% and 14%. Except Specimen 'Standard', the analytical results are larger than the experimental counterpart. The difference between the test and analysis is larger when the rebars are present. It is because that the bond behavior between rebars and slab was not considered in the analysis. In the analysis, the rebars are completely embedded in the slab, therefore the contribution of rebars to the strength is larger than that in the test.
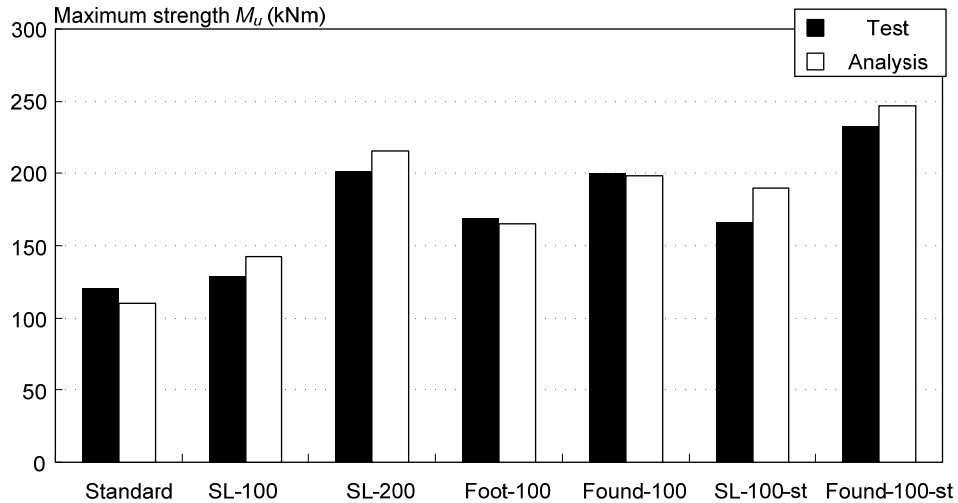
Fig. 3. 19 Comparison of maximum strength between test and analysis

3.3.2   Failure region

In the physical test, cone-like cracks caused by the punching shear formed around the column in the slab. The same observation was also duplicated by the analysis. Figure 3.20 shows the slab deformation of each specimen in the last cycle of 3% drift angle, depicting the contours of the maximum principal plastic strain (PE) distribution. The failure regions are marked in white, where the compressive strain is larger than 0.3%, at which strain level the concrete is supposed to lose the

resisting capacity completely. It is notable that the shape of the analytical failure region of the slab is cone-shaped. The slope angle of the cone-shaped failure region is around 45°, which is also similar as that observed in the tests. The slabs of 'SL-200', 'Foot-100', and 'Found.-100' are in the same thickness but with different slab shapes (details presented in Chapter 2). As observed in the tests, the analysis results also express the difference, i.e., the failure region of 'Foot-100' (Fig. 3.20 (d)) concentrated at the partially elevated slab, which is smaller than the failure region of both 'SL-200' and 'Found.-100' (Fig. 3.20 (c) and (e)).
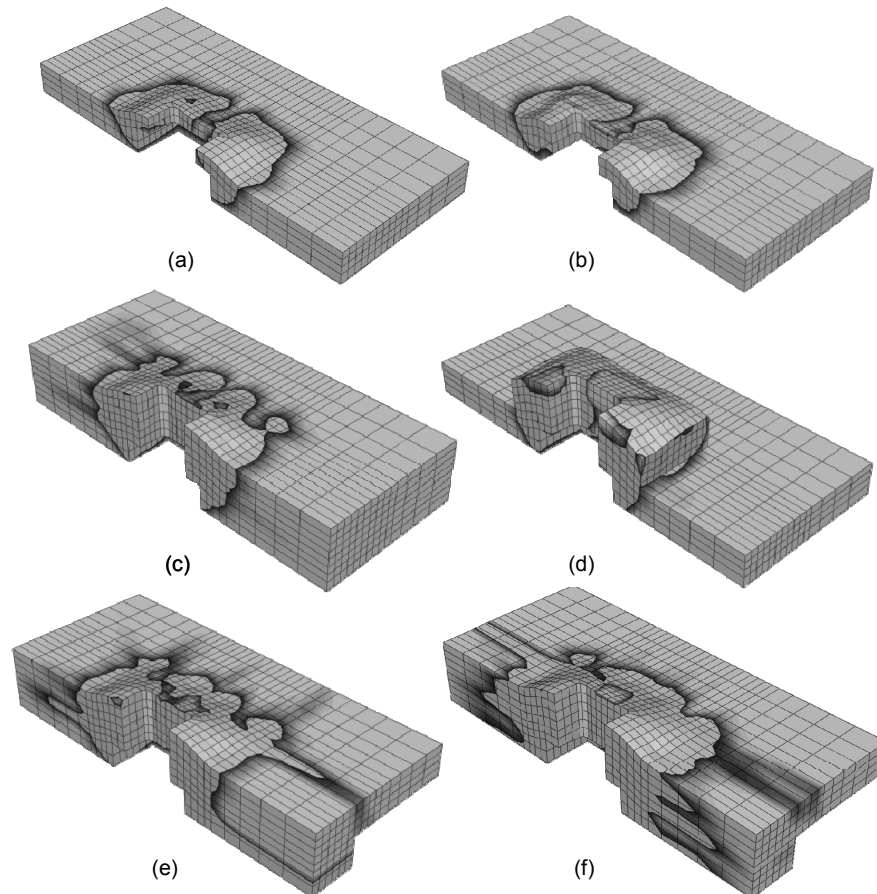
Fig. 3. 20 Failure region obtained from analysis: (a) SL-100; (b) SL-100-st; (c) SL-200; (d) Foot-100; (e) Found.-100; and (f) Found.-100-st-t12

3.3.3 Simplified model

Ability of cyclic numerical analysis was demonstrated in the previous section. However, because of the combination of nonlinear behavior of concrete and interaction between different components, the calculation was extremely consuming in both time and data. Here, simplified analysis was sought. Considering that the elastic stiffness and maximum strength are the most critical in the design practice, the analysis model should be able to accurately predict these two values. Figure 3.21 shows two analyses for the same specimen, one in the monotonic loading condition, and the other in the cyclic loading condition. The difference between the two analyses was small in the elastic stiffness and maximum strength. Therefore, the monotonic loading was adopted for further analysis.

Fig. 3. 21 Comparison between monotonic and cyclic loading analysis: (a) SL-100; (b) SL-100-st

In addition, since the loading direction did not change in the monotonic loading, interactions between different components, for example, the interaction between the nuts of anchor bolt and base plate, was unchanged, which made the modeling simple. In the simplified model, three-dimensional 2-node connector elements, CONN3D2, were adopted to simulate the anchor bolts. The behavior of the AXIAL elements was defined for the relative motion between two nodes, o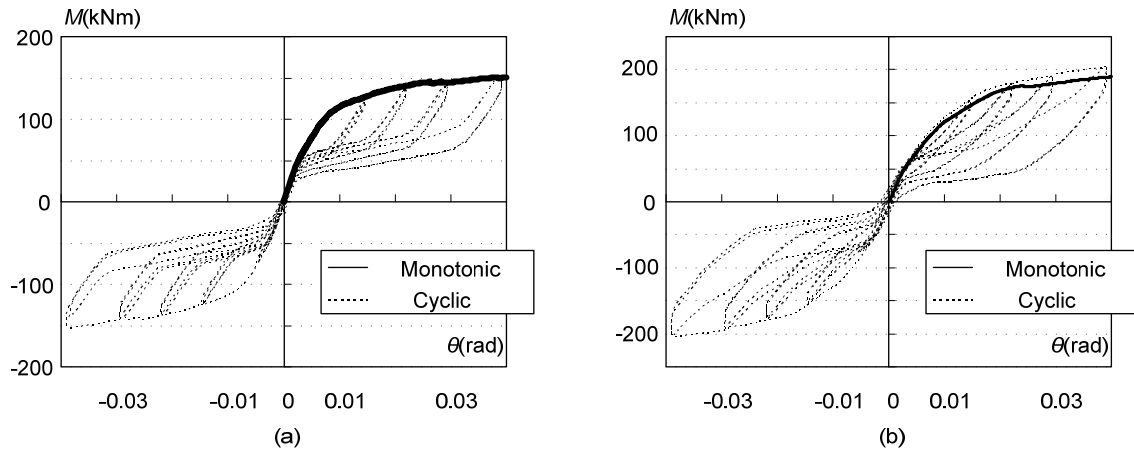ne on top of the base plate where the anchor bolts were located, and the other located on the ground. The relative motion between these two nodes was defined based on the results from coupon tests of anchor bolts. Furthermore, the fracture displacement was defined as 10 mm, in which the rotation of specimen was around 6%, when the first anchor bolt fracture observed in the tests. The difference between the analysis results of the different models of anchor bolts is shown in Fig. 3.22. In Fig. 3.22, 'Truss_AB' indicates the anchor bolts were modeled by the truss elements while 'Con._AB' indicates the anchor bolts were modeled by connector elements, in which the simulation of anchor bolts was simplified. Although there is slightly difference (around 10%) in the maximum strength, the global behavior of moment-rotation curves remains the same. Balancing the time and accuracy, the simplified model was adopted to perform the parametric analysis for monotonic loading.
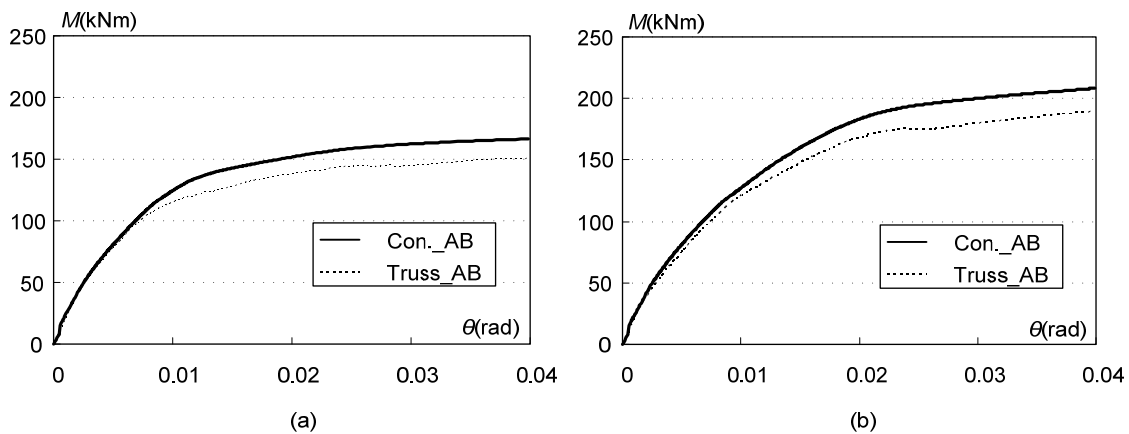
Fig. 3. 22 Comparisons between different models of anchor bolts: (a) SL-100; (b) SL-100-st

3.4 Parametric Analysis

The parametric study in this chapter is to generalize the behavior of shallowly embedded column bases. Considering the relative importance, the influence of anchor bolts, axial force, and slab are mainly investigated. Other factors such as rebars and material properties are out of the scope here.

3.4.1   Effect of anchor bolts

The number and arrangement of anchor bolts are varied to investigate the effect of anchor bolts. As shown in Fig. 3.23, the number of anchor bolts is varied among 4, 8, and 12. The nomenclature used to identify the layout of anchor bolts is based on the number and arrangement of anchor bolts. For example, the label of "4AB" means four anchor bolts are adopted in the base plate connection. The number in the round bracket indicates the layout of anchor bolts as shown in the second row of Fig. 3.23. The exposed column bases are included as the baseline and named as 'Standard'. The shallowly embedded column bases with 100 mm unreinforced slabs are named as 'SL-100', while the ones with 100 mm reinforced slab were named as 'SL-100-st'. The axial force ratio of 0.2 is assigned for the analysed specimens.

Fig. 3. 23 Layout of anchor bolts

Fig. 3. 24 Influence of anchor bolts: (a) elastic stiffness; (b) maximum moment

The elastic stiffness and maximum strength of the analyzed specimens are shown in Fig. 3.24. The number of anchor bolts affects both the elastic stiffness and maximum strength. The same tendency is observed for both the exposed column b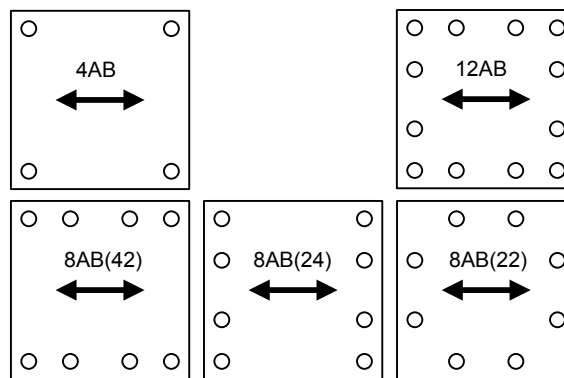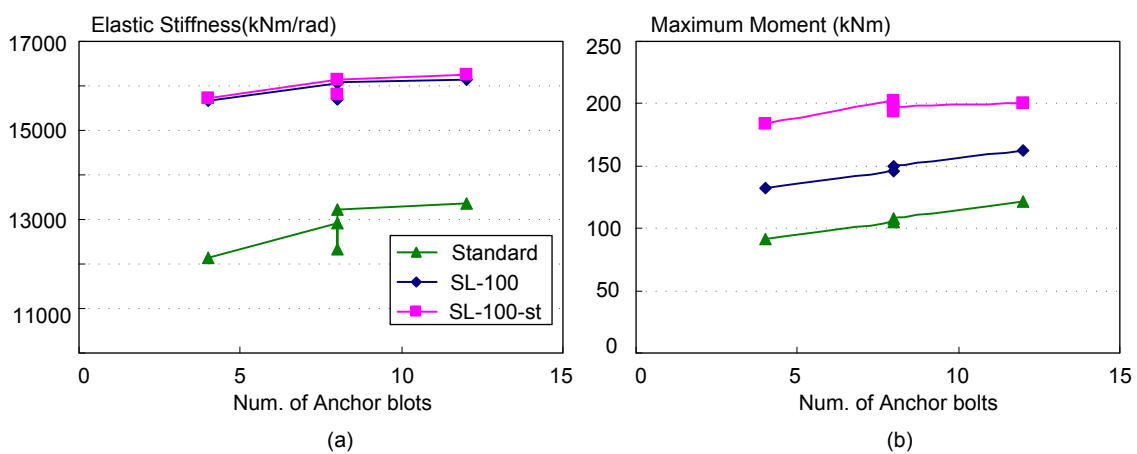ases and shallowly embedded column bases. However, the degree of improvement for the shallowly embedded column bases with reinforced slab decreases when the number of anchor bolts increase from eight to twelve, as shown in 'SL-100-st' of Fig. 3.24 (b).

As shown in Fig. 3.24, the layout of anchor bolts clearly affects the elastic stiffness of the exposed column bases ('Standard'), while it shows a slight effect on the elastic stiffness of the shallowly embedded column bases ('SL-100' and 'SL-100-st'). The layout of anchor bolts affects the maximum strength for both the exposed and shallowly embedded column bases slightly. It is because that the distance from the center of anchor bolt group to the rotation center of the column bases changes rather little for different layouts of anchor bolts. The distance is changed from 90 mm to 130 mm when the layout of '8AB(42)' is changed to '8AB(22)' in Fig. 2.23.

For the shallowly embedded column bases ('SL-100' and 'SL-100-st'), changes of the elastic stiffness and maximum strength by the number and layout of anchor bolts are not significant, i.e., the elastic stiffness and maximum strength of the column bases with 100 mm unreinforced slab increase only by 3% and 20%, respectively, when the number of anchor bolts increased by three times (from four to twelve). The contribution of the floor slab to the elastic stiffness and maximum strength is obviously larger than that of the anchor bolts.

3.4.2   Effect of axial force

Four levels of axial force ratio (0.05, 0.1, 0.2, and 0.3) are chosen to investigate the influence of axial force. Same as the investigation mentioned before, the exposed column bases labeled as 'Standard' are included as the baseline. For the shallowly embedded column bases, the 100 mm unreinforced and reinforced slab are adopted to investigate the influence of axial force, while the number of anchor bolts is fixed as twelve.
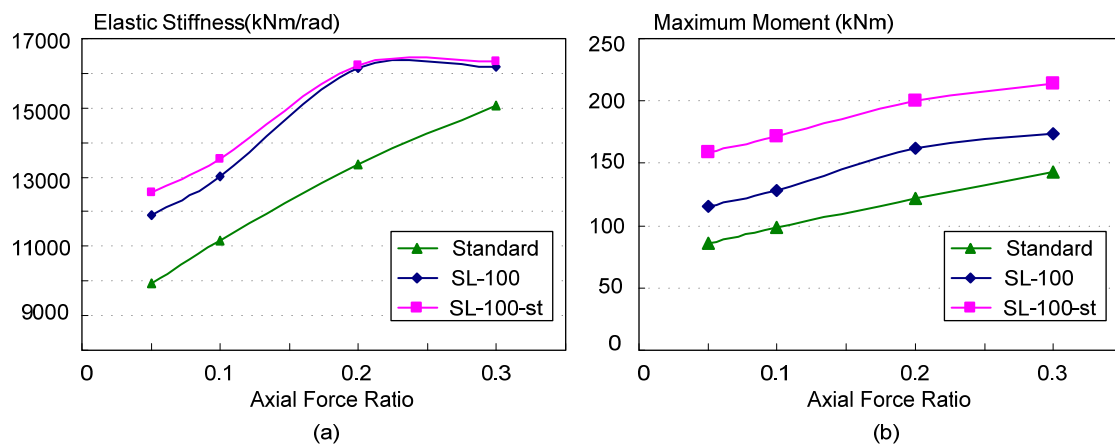

Fig. 3. 25 Influence of axial force ratio: (a) elastic stiffness; (b) maximum moment

The elastic stiffness and maximum strength of the exposed column bases increase with the increase in the axial force ratio as shown in Fig. 3.25. For the shallowly embedded column bases, the maximum strength shows the same tendency. However, the elastic stiffness of the shallowly embedded column bases stops increasing when the axial force ratio increases from 0.2 to 0.3.

When the axial force ratio is smaller than 0.2, the amount of increase of the elastic stiffness is almost the same between the exposed column bases and the shallowly embedded column bases. For the maximum strength, the same improvement is also observed. It is primarily because that the axial force affects both the stiffness and strength of the base plate connection (anchor bolts) directly. According to the analysis results, the axial force affects the behavior of shallowly embedded column bases by the base plate connection (anchor bolts) rather than by the floor slab. Therefore, it is suggested that the contribution of axial force for the estimation of the elastic stiffness and maximum strength of the exposed column base portion should be considered in the design of the shallowly embedded column bases.

3.4.3   Effect of slab thickness

According to the AIJ connection guideline (2006), the fully embedded column base behavior would be guaranteed when the embedded depth of column is not smaller than two times of the column width. As a counterpart of the fully embedded column bases, the embedded depth or the slab thickness is designed smaller than two times of the column width for the shallowly embedded column bases. In this section, slabs with the thickness of 0.5, 0.75, 1.0 and 1.5 times the column width are chosen to investigate the effect of slab thickness, as shown in Fig. 3.26. Both the unreinforced and reinforced concrete slab are examined in this analysis. Twelve anchor bolts and axial force ratio of 0.2 are assigned for the analysed column base connections.
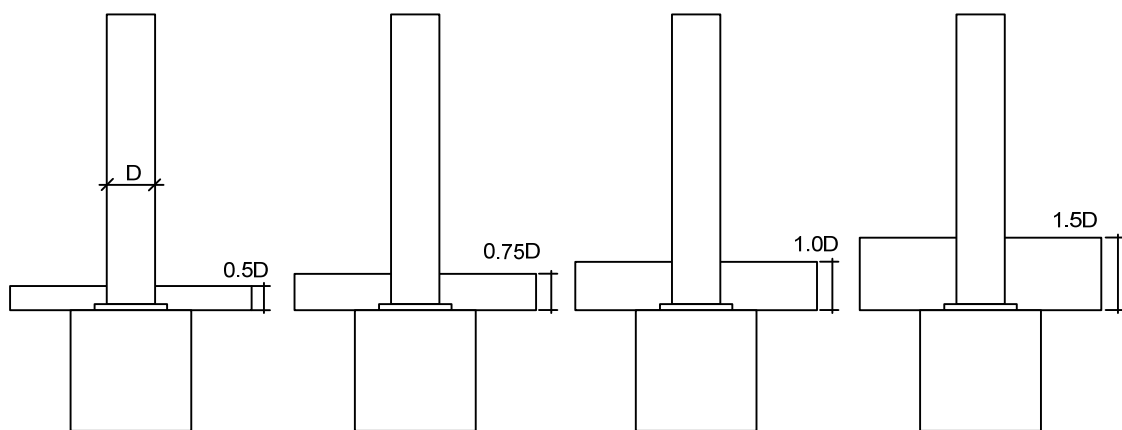
Fig. 3. 26 Shallowly embedded column base with different thickness of slab

As shown in Fig. 3.27, the elastic stiffness and maximum moment increase almost linearly with increase of the slab thickness. Both the elastic stiffness and maximum strength increase by 50% and 90%, respectively, when the slab thickness increases from 0.5D to 1.5D. The rebars contributed to the maximum strength rather than the elastic stiffness. As shown in Fig. 3.27 (a), there is almost no difference of the elastic stiffness between the column bases with unreinforced and reinforced slabs.

As shown in Fig. 3.27 (b), the maximum strength of the column bases increases by around 40 kNm by the presence of rebars. Compared with the anchor bolt and axial force, the slab thickness is much more influential to the behavior of shallowly embedded column bases.
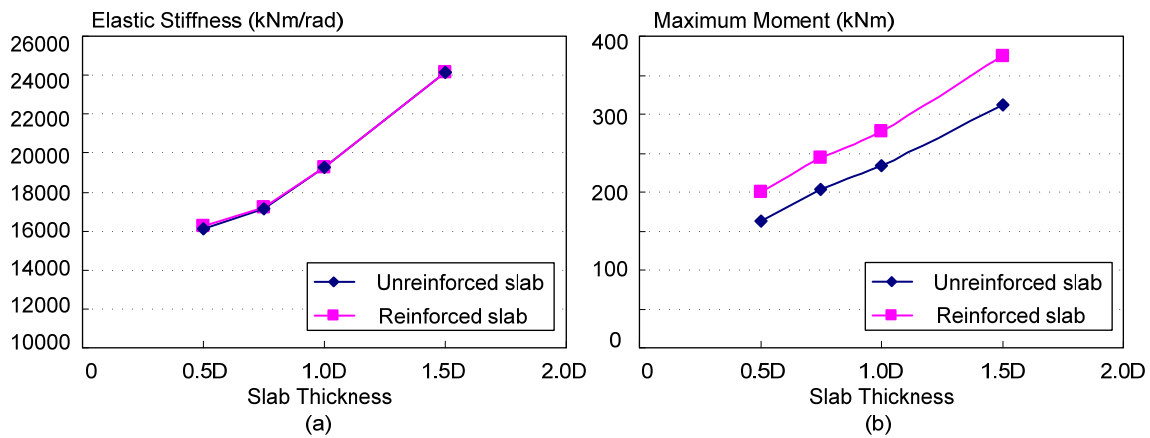
Fig. 3. 27 Influence of axial force ratio: (a) elastic stiffness; (b) maximum moment

3.5 Calibration of Evaluation of Elastic Stiffness

A procedure to evaluate the elastic stiffness is proposed in Chapter 2. In this section, the evaluation procedure is calibrated with the numerical analysis results. The feasibility of the evaluation procedure of the elastic stiffness will be verified with respect to the layout of anchor bolts, axial force, and slab thickness. Finally, a simplified evaluation procedure is proposed.

3.5.1   Effect of anchor bolts

The evaluated elastic stiffnesses for different numbers of anchor bolts are compared in Fig. 3.28. Label "Evaluation" indicates the evaluated elastic stiffness using the proposed evaluation procedure, and label "Analysis" indicates the values obtained from the numerical analyses. The abscissa of Fig. 3.28 shows the name of the specimens with different numbers and layouts of anchor bolts referred to from Fig. 3.23. It is notable that the results obtained from both prediction procedures agree very well, with the difference of around 10% for shallowly embedded column bases.

In Fig. 3. 29, the column base with twelve anchor bolts is chosen as the baseline. The contribution of anchor bolts to the elastic stiffness obtained from the proposed evaluation and numerical analysis is compared. Both prediction procedures exhibited similar tendency for the changes of the elastic stiffness caused by anchor bolts. In comparison with the analysis results, however, the proposed evaluation overestimates the contribution of anchor bolts to the elastic stiffness.

Fig. 3. 28 Comparisons of predicted elastic stiffness with respect to number of anchor bolts
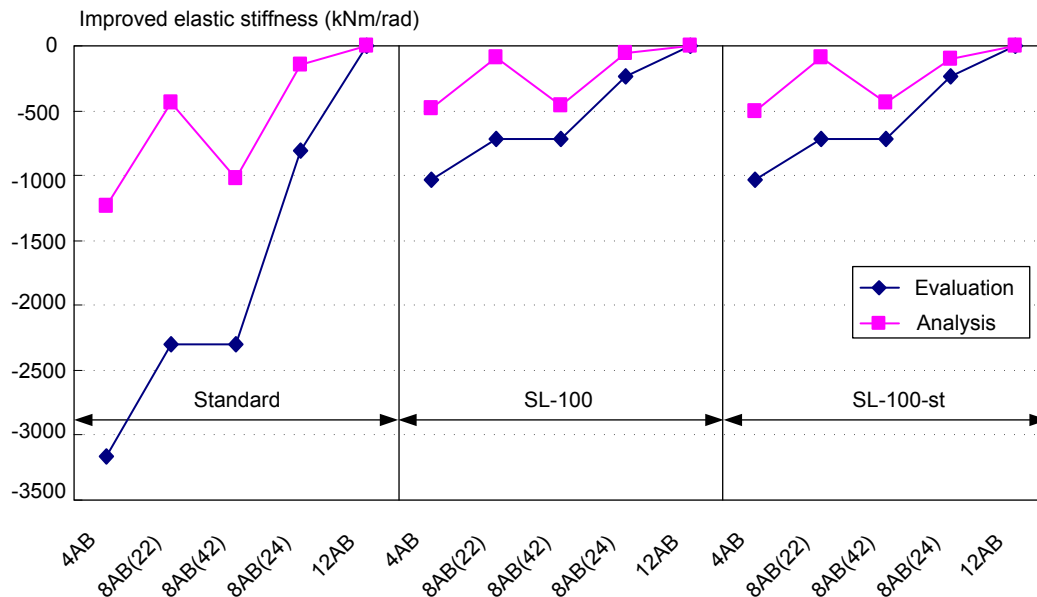
Fig. 3. 29 Comparisons of increased elastic stiffness with respect to number of anchor bolts

3.5.2 Effect of axial force

The evaluated elastic stiffnesses based on the proposed evaluation procedure and numerical analyses are compared in Fig. 3.30 for various axial force ratios. Improvements of the evaluated elastic stiffnesses by the two prediction procedures are compared in Fig. 3.31 by setting the column base with the axial force ratio of 0.2 as the baseline. The abscissa of Fig. 3.30 and Fig. 3.31 shows the axial force ratio. The difference between the two prediction procedures is around 10% for the shallowly embedded column bases. In comparison with the analysis results, the proposed evaluation underestimates the elastic stiffness with the difference not greater than 8% when the axial force ratio is not greater than 0.2, while the elastic stiffness is overestimated by 8% when the axial force ratio is

0.3. Also, as indicated in Fig. 3.31, it is noted that the evaluated contributions of axial force to the elastic stiffness by the proposed evaluation procedure and numerical analyses agree well when the axial force ratio is not greater than 0.2. According to the numerical analysis, the axial force has a minimal effect on the elastic stiffness when the axial force ratio is 0.3. However, the proposed evaluation did not consider such phenomena. Therefore, the proposed procedure to evaluate the elastic stiffness is available when the axial force ratio is not greater than 0.2.
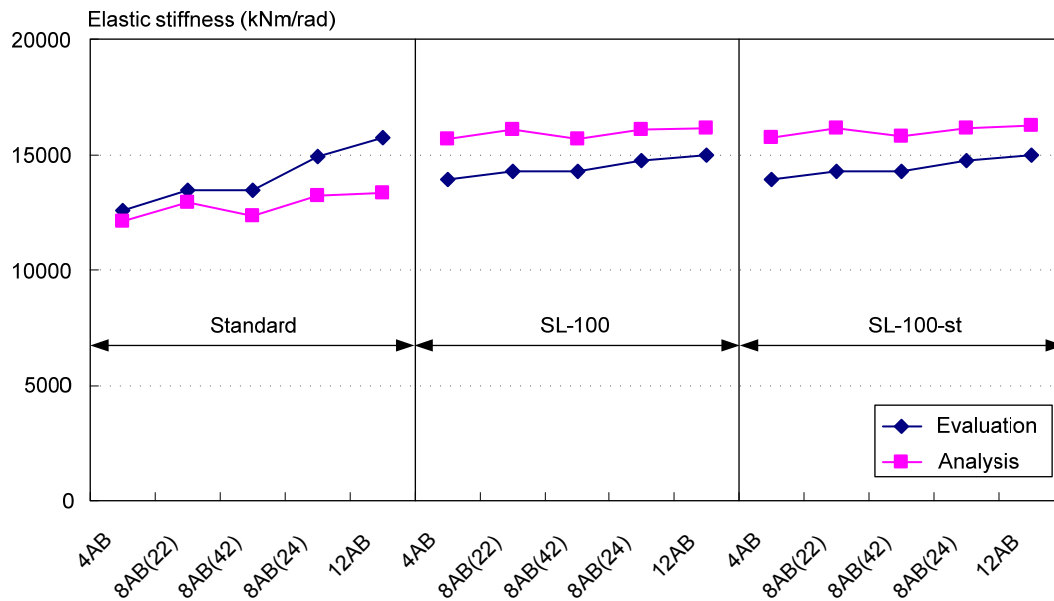

Fig. 3. 30 Comparisons of predicted elastic stiffness with respect to axial force ratio
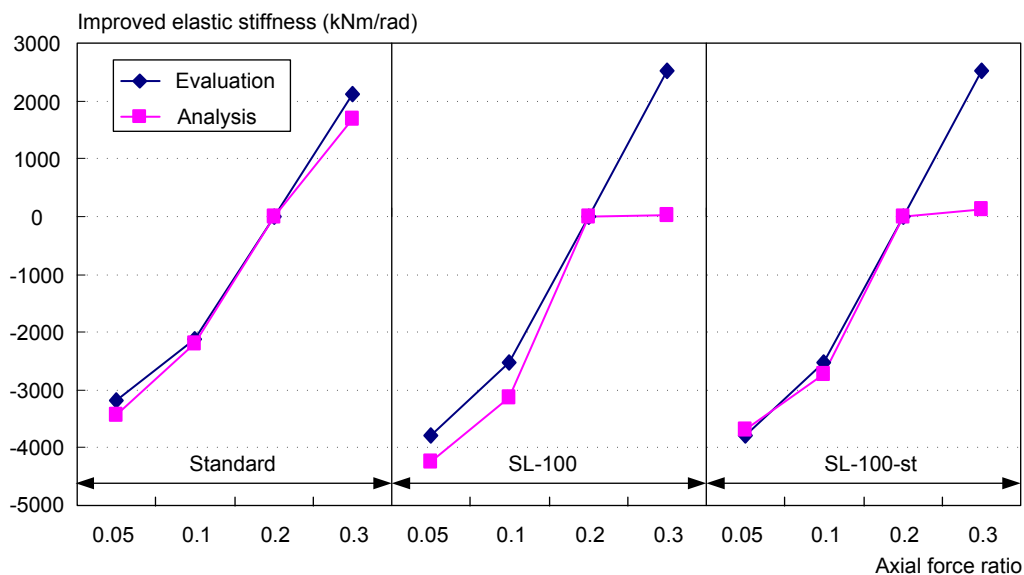
Fig. 3. 31 Comparisons of increased elastic stiffness with respect to axial force ratio

3.5.3 Effect of slab thickness

The evaluated elastic stiffnesses for various different slab thicknesses are compared in Fig. 3.32. The values are obtained from the proposed evaluation procedure (label as "Evaluation") and numerical

analysis (label as "Analysis"). By choosing the column base with the 100 mm thick slab as the baseline, improvements of the evaluated elastic stiffness by the two prediction procedures are compared in Fig. 3.33. The abscissa of Fig. 3.32 and Fig. 3.33 is the name of the specimens with different slab thickness, i.e., Specimen '0.75D' is the specimen with the covering slab thickness of 0.75 times the column section, and '-re' means the specimen with reinforced slab. The difference between the two prediction procedures is around 8%. In comparison with the analysis results, the proposed evaluation underestimates the elastic stiffness when the slab thickness is 100 mm (0.5D), while the elastic stiffness overestimates when the slab thickness is larger than 100 mm. As shown in Fig. 3.33, it is noted that the evaluated contribution of the concrete slab to the elastic stiffness is overestimated by the proposed evaluation. This overestimate for the contribution of the concrete slab is believed to be the reason for the overestimate of the elastic stiffness when the slab thickness is larger than 100 mm. However, the proposed evaluation traces the tendency observed in the numerical analysis.
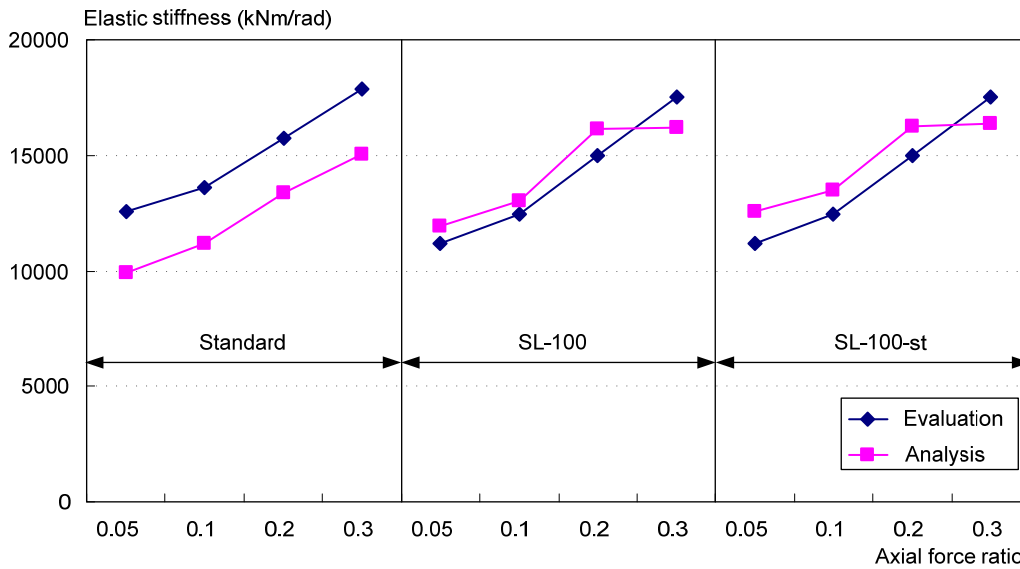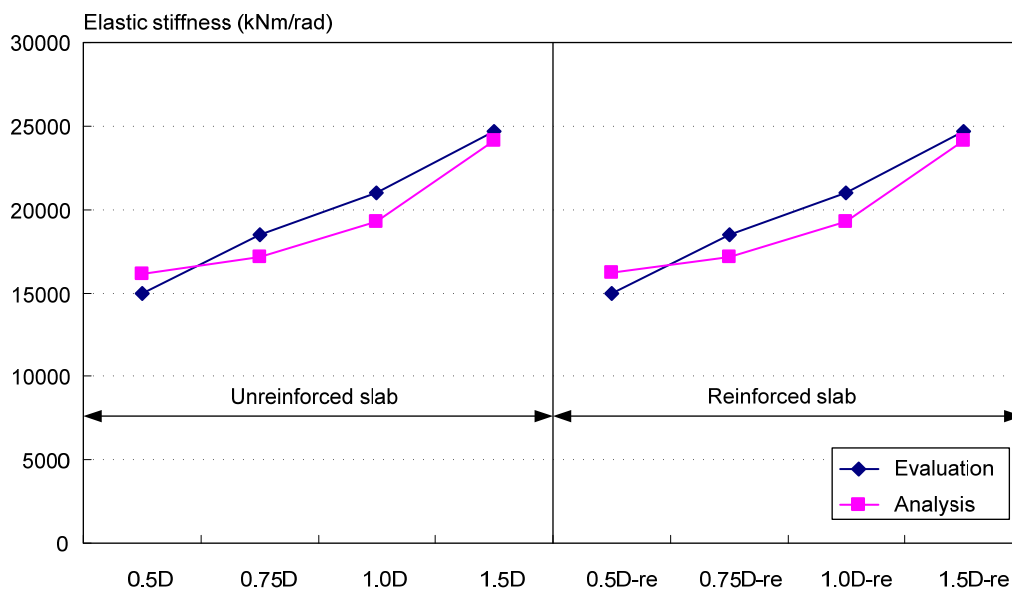

Fig. 3. 32 Comparisons of predicted elastic stiffness with respect to slab thickness
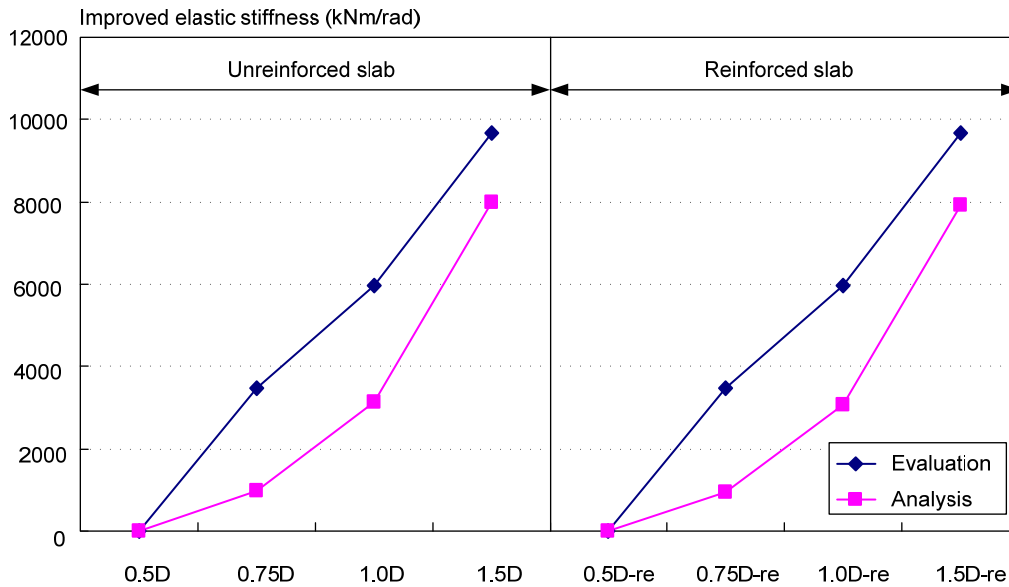
Fig. 3. 33 Comparisons of increased elastic stiffness with respect to slab thickness

3.5.4 Simplified evaluation method

As discussed previously, the evaluated elastic stiffness using the proposed formula agrees reasonably with that obtained from the numerical analysis. However, the calculation of the proposed evaluation is rather complicated. Attempted here is a simple prediction method using an analogy for the prediction of the elastic stiffness of embedded column bases (Fig. 3.34). As shown in Fig. 3.34, the top surface of the slab is located at the level same as for the embedded and shallowly embedded column bases. The elastic stiffness of the corresponding embedded column base is calculated following the specification of AIJ (2006). The ratio of elastic stiffness between the shallowly embedded column base and the corresponding embedded column base is shown in Fig.3.35. The left part of Fig. 3.35 shows how the ratio varies with respect to the number of anchor bolts (see Fig. 3.23) for shallowly embedded column bases with 100 mm thick slab. The right part of Fig. 3.35 shows the relation between the ratio and the slab thickness of shallowly embedded column bases. It is notable that the ratio is around 1.0 for the 100 mm thick slab. The ratio increases when the slab thickness increased.

According to the numerical analysis, the ratio of the elastic stiffness relative to that of the corresponding embedded column base is 0.95, 1.0, 1.1, and 1.3 for the shallowly embedded column bases with the slab thickness of 0.5D, 0.75D, 1.0D, and 1.5D, respectively. It coincides with the values obtained by the proposed simplified evaluation presented in Chapter 2. To summarize, the proposed simplified evaluations in Chapter 2 (Eq. 2.22 and 2.23) are suggested for the design practice.
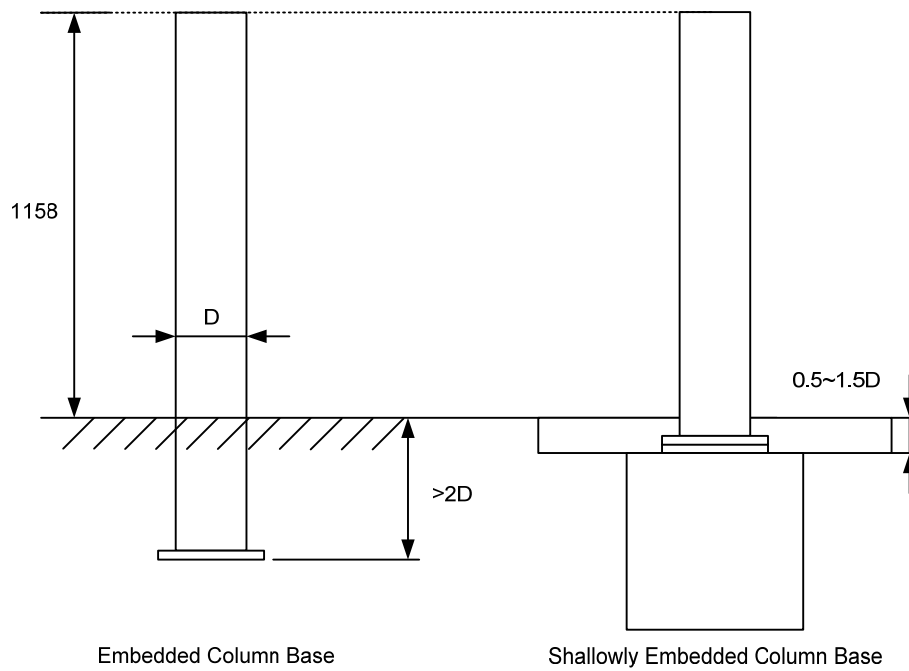
Fig. 3. 34 The corresponding embedded column base
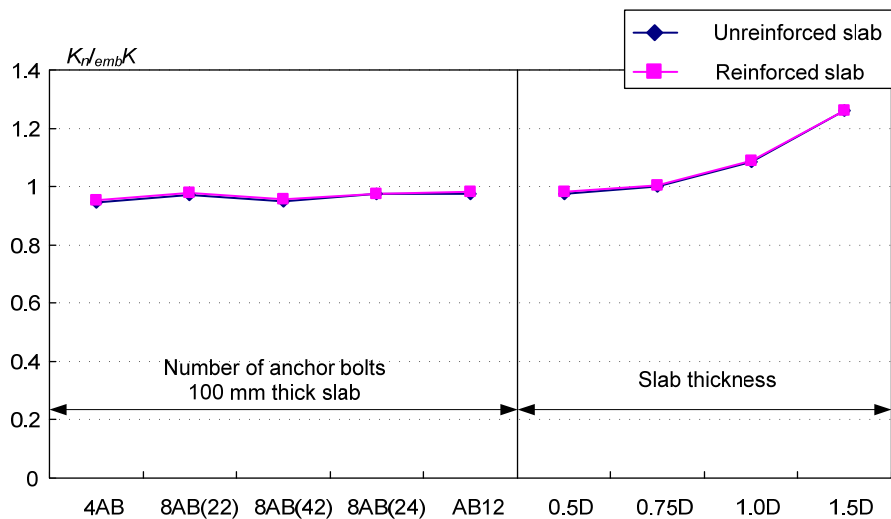
Fig. 3. 35 The ratio of the elastic stiffness based on the corresponding embedded column base

3.6 Calibration of Evaluation of Maximum Moment

A procedure for the evaluation of the maximum moment is also proposed in Chapter 2. The predicted maximum moments using the proposed formula are compared with the values obtained from the numerical analysis in Fig. 3.36 to Fig. 3.41. The feasibility of the evaluation procedure of the elastic stiffness will be verified with respect to the layout of anchor bolts, axial force, and slab thickness.

3.6.1   Effect of anchor bolts

The evaluated maximum strengths for various layouts of anchor bolts obtained from the proposed evaluation procedure and numerical analysis are compared in Fig. 3.36. The abscissa of Fig. 3.36 is the name of the analysed specimens with various layouts of anchor bolts referred from Fig. 3.23. As

shown in Fig. 3.36, the proposed evaluation procedure traced reasonably the tendency of the analysis results. The proposed evaluation underestimates the maximum strengths with the difference of around 30% compared with the analysis results. There are two reasons for the discrepancy. The first is the different stress level of anchor bolts is considered. Strain-hardening of anchor bolts is defined in the numerical analysis, while the yield stress is adopted in the proposed evaluation procedure. The difference stress level of anchor bolts at the maximum strength caused some difference on the evaluated maximum strength. On the other hand, numerical analysis overestimates the specimen behavior as compared with test results. Taking into account with such overestimate, the difference would be reduced. As presented in Chapter 2, the evaluation procedure underestimates the test results within the differences of 18%. Therefore, the difference of 30% between the proposed evaluation procedure and numerical analysis is set as the tolerance for the evaluation in the following discussion.

Fig. 3. 36 Comparisons of predicted maximum moment with respect to number of anchor bolts
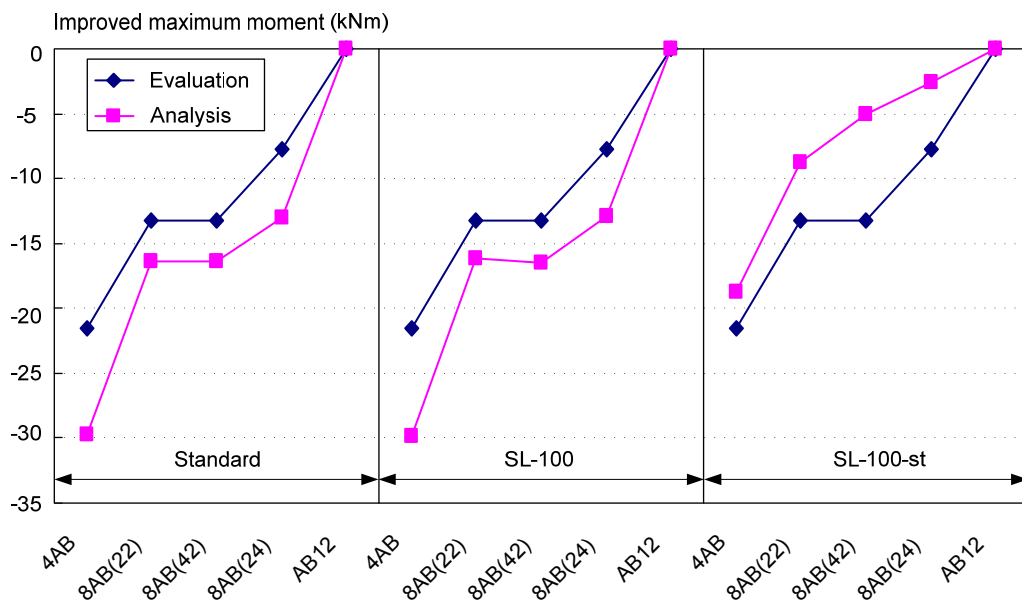
Fig. 3. 37 Comparisons of increased maximum moment with respect to number of anchor bolts

In Fig.3.37, the column base with twelve anchor bolts is chosen as the baseline, whose evaluated strengths by the proposed evaluation procedure and numerical analysis have been verified with respective to the corresponding test results, and the differences of the maximum strengths affected by the anchor bolts are shown. The contribution of anchor bolts increases as the number of anchor bolts increases in both prediction procedures. However, the amount of maximum strength affected by the anchor bolts is overestimated by the proposed evaluation procedure relative to the numerical analysis when the slab is reinforced. According to the values obtained from the numerical analysis, the maximum strength affected by anchor bolts is less significant for the specimens with reinforced slab ("SL-100-st") compared with other two types specimens, the exposed column base specimens ("Standard") and the specimen with unreinforced slab ("SL-100"). It is primarily because that the sustained strain of the anchor bolts is smaller for shallowly embedded column base with reinforced slab than for the exposed column base and shallowly embedded column bases with unreinforced concrete slab when the maximum strength is achieved. Since the strain-hardening is included in the numerical analysis, a smaller stress of the anchor bolts is achieved at the maximum strength. Reduction of contribution of anchor bolts to the maximum strength caused by the rebars is not taken into considered in the proposed evaluation procedure. Different contributions of anchor bolts to the unreinforced and reinforced slab is a subject of future study.

3.6.2   Effect of axial force

The evaluated maximum strengths for various axial force ratios are shown in Fig. 3.38. The evaluated values based on the proposed evaluation procedure and numerical analyses are compared. The abscissa of Fig. 3.38 shows the axial force ratio. The values obtained from the proposed evaluation procedure are underestimated by not greater than 30% with respect to the values obtained from the numerical analyses. The proposed evaluation procedure reasonably traces the tendency of the analysis results.
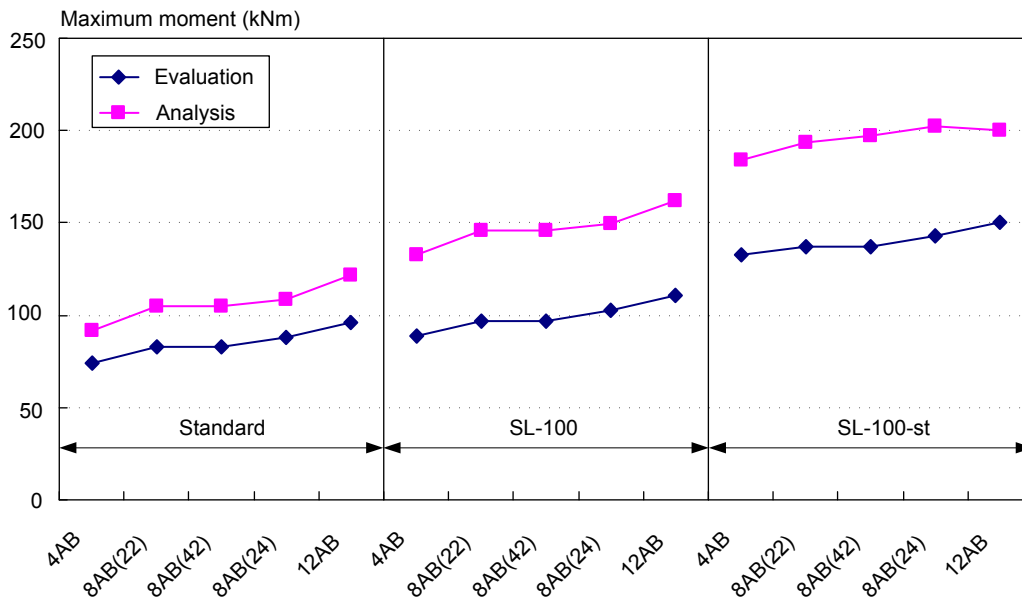

Fig. 3. 38 Comparisons of predicted maximum moment with respect to axial force ratio
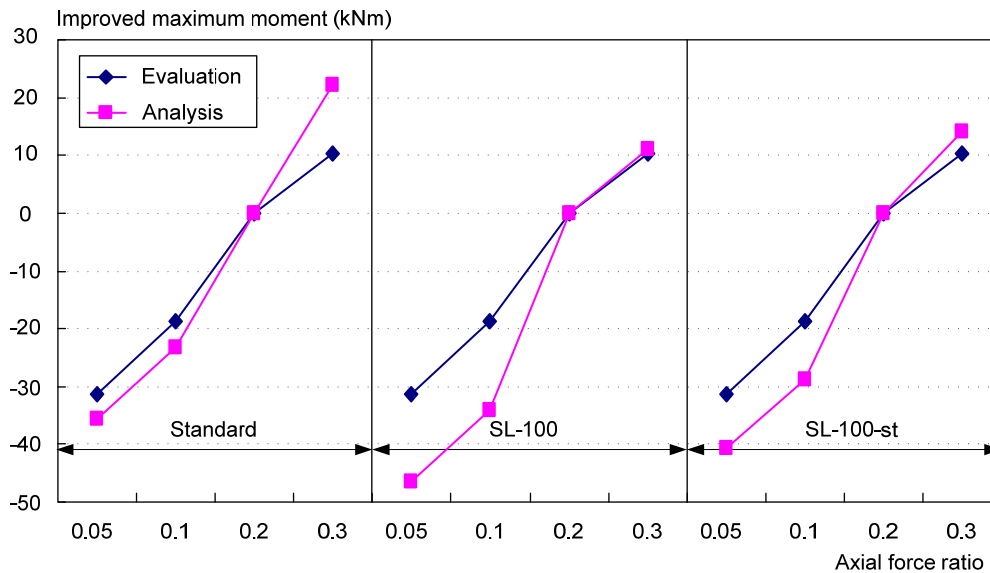
Fig. 3. 39 Comparisons of increased maximum moment with respect to axial force ratio

Choosing the column base with the axial force ratio of 0.2, whose experimental results is available, the contributions of the axial force ratio predicted by the proposed evaluation procedure and numerical analysis are compared in Fig. 3.39. The contribution of the axial force ratio increases as the axial force ratio increases based on both two prediction procedures. The proposed evaluation procedure compared with the numerical analysis provide conservative estimate for the contribution of axial force ratio.

3.6.3   Effect of slab thickness

The evaluated maximum strengths by the proposed evaluation procedure and numerical analysis for various slab thicknesses are compared in Fig. 3.40. The abscissa of Fig. 3.40 is the name of the specimens with various slab thicknesses. The difference between the two ways ranges from 30% to 2%. In comparison with the analysis results, the proposed evaluation procedure underestimates the maximum strength when the slab thickness is not greater than 200 mm (1.0D). When the slab thickness is 300 mm (1.5D), the proposed evaluation is slightly overestimated by 2%. It is primarily because of the overestimation of the contribution of the slab, which is discussed as follows.

Choosing the column base with the 100 mm thick slab as the baseline, the contributions of the slab evaluated by the two prediction procedures are compared in Fig. 3.41. It is noted that the evaluated contribution of the slab to the maximum strength agrees well with the numerical analysis results when the slab thickness is not greater than 200 mm (1.0D). However, the contribution of the slab is overestimated when the slab thickness is 300 mm (1.5D). It is because that according to the analysis results a different failure mode occurs when the slab thickness is 300 mm (1.5D), such as the mixed failure between the punching shear and separation between the floor slab and the foundation. Therefore, contribution of the punching region of the slab is smaller in the numerical analysis than in the proposed evaluation. Further research is required to clarify the reason.
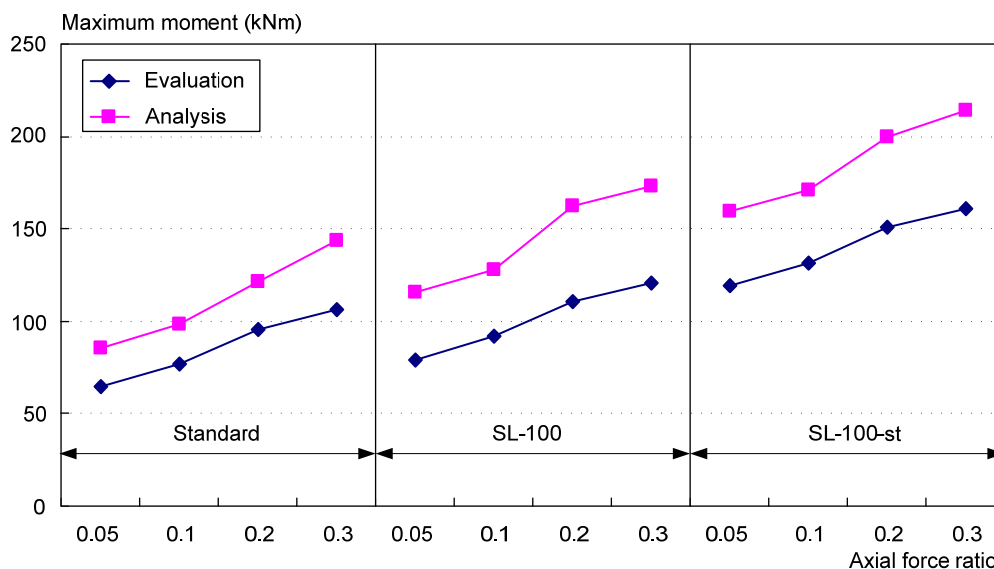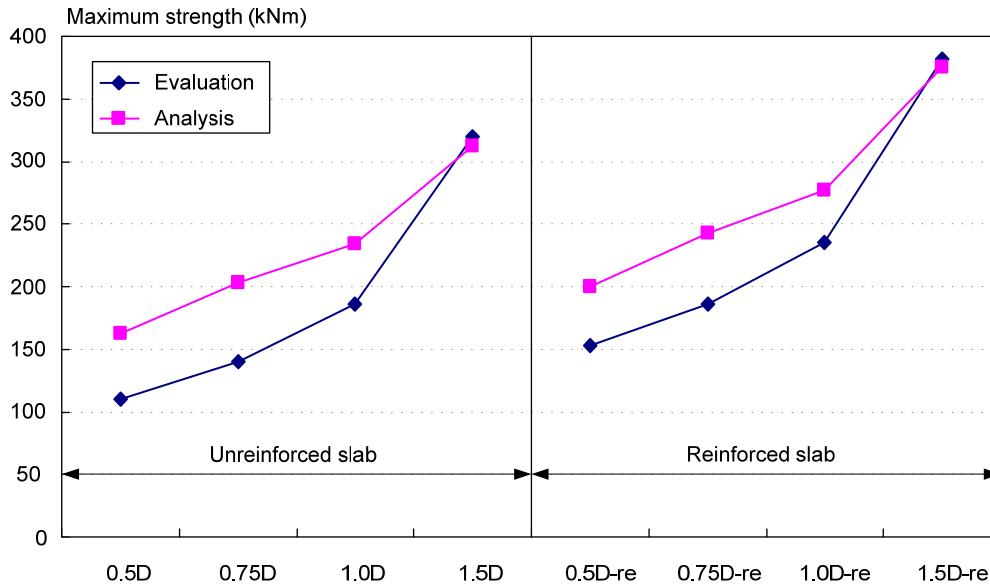
Fig. 3. 40 Comparisons of predicted maximum moment with respect to slab thickness
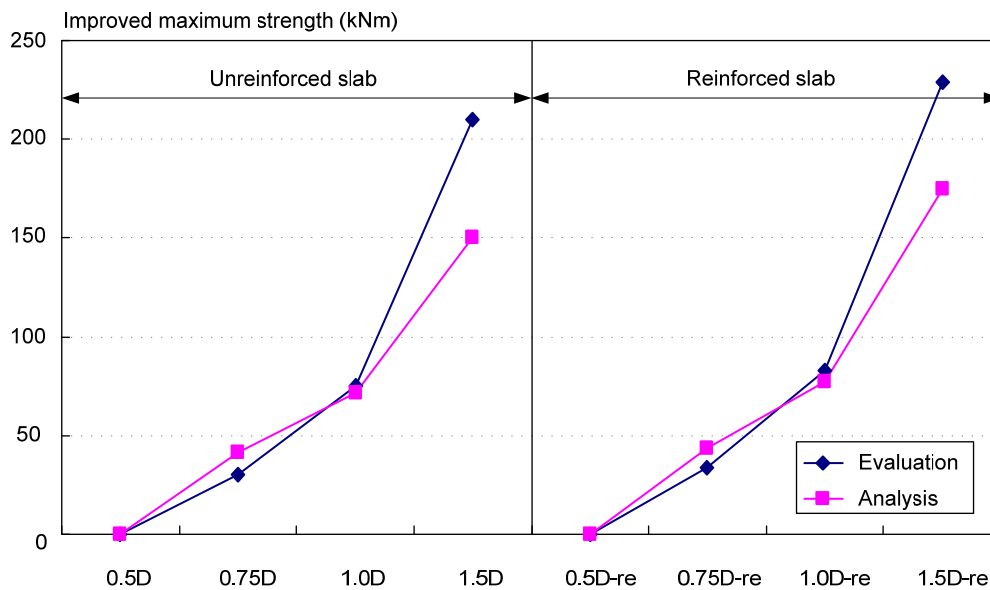
Fig. 3. 41 Comparisons of increased maximum moment with respect to slab thickness

As discussed above, the proposed evaluation reasonably traces the effects of the layout of anchor bolts, axial force, and slab thickness reasonably. The maximum strengths of the specimens are underestimated by the proposed evaluation procedure within the difference of 30% relative to the numerical analysis results, which is conservative for the design practice. Workability of the proposed evaluation of the maximum strength presented in Chapter 2 is proven to be reasonable.

3.7 Conclusions

To enhance the understanding of the test results shown in Chapter 2, extensive numerical analysis

was carried out. The numerical model was developed to simulate the cyclic behavior of specimens by incorporating a contact model between the base plate and anchor bolts and adopting a concrete damage plasticity model.

(1)   The slip of hysteresis curves of the test specimens was successfully reproduced by adopting contact interaction between the head of anchor bolts and base plate. By using the concrete damage plastic model, cyclic behavior of concrete was simulated reasonably.

(2)   The maximum strength and elastic stiffness from the numerical results agreed with the test results with the difference not greater than 15%. Punching failure regions of the slab were successfully estimated from the analysis.

Furthermore, the behavior of shallowly embedded column bases was generalized through a series of parametric analysis. Investigation was given to the effects of three parameters, i.e. the thickness of concrete slab, number of anchor bolts, and axial force ratio. Moreover, a design procedure to estimate the elastic stiffness and strength proposed in Chapter 2 was calibrated against the analytical results. Several conclusions can be drawn from the results.

(1)   The elastic stiffness is mainly affected by the slab thickness and axial force ratio. The number of anchor bolts has a minimal effect on the elastic stiffness with an increase of 10% when the number increases from 4 to 12.

(2)   The maximum strength is influenced by the slab thickness, number of anchor bolts, and axial force ratio. Among these three parameters, the slab thickness shows the most significant effect on the maximum strength.

(3)   The design procedure to estimate the elastic stiffness proposed in Chapter 2 is calibrated against the analysis results. The difference between the prediction and analysis is at most around 10%. To simplify the evaluation of the elastic stiffness, the elastic stiffness is suggested to be a fraction of the elastic stiffness of the corresponding embedded column base.

(4)   The design procedure to estimate the maximum strength proposed in Chapter 2 is calibrated against the analytical results. The proposed evaluation was conservative in comparison with the analytical results. The difference between the prediction and analysis ranges from 10% to 30%.

REFERENCES

[3.1]   ABAQUS/ Standard user's manual , version 6.7, Hibbitt, Karlson and Sorensen, Inc. 2007

[3.2]   Architectural Institute of Japan (AIJ). (2006). Recommendations for design of connections in steel structures, Tokyo (in Japanese).

[3.3]   Bazant, Z. P. (1978). "On endochronic inelasticity and incremental plasticity." *Int. J. Solids Struct.*, 14(9), 691-714.

[3.4]   Cervera, M., Oliver, J., and Faria, R. (1995). "Seismic evaluation of concrete dams via continuum damage models." *Earthquake Engrg. And Struct. Dyanamic*, 24, 1225-1245.

[3.5]   Chen, W. F. (1994). Constitutive equations for engineering materials, Vol. 2, Elsevier, New York, N.Y.

[3.6]   Chen, W. F. (1982). Plasticity in reinforced concrete, McGraw-Hill, New York, N.Y.

[3.7]   Gopalaratnam, V. S., and Shah, S. P. (1985). "Softening response of plain concrete in direct tension." *ACI. J.*, 82(3), 310-323.

[3.8]   Kachanov, L. M. (1986). Introduction to continuum damage mechanics. Martinus Nijhoff Publishers, Dordrecht, The Netherlands.

[3.9]   Karsan, I. D., and Jirsa, J. O. (1969). "Behavior of concrete under compressive loadings." *J. Struct. Div.*, ASCE, 95(12), 2535-2563.

[3.10]   Lee, J., and Fenves, G. L. (1998). "Plastic-damage model for cyclic loading of concrete structures." *Journal of engineering mechanics*, ASCE, 124(8), 892-900.

[3.11]   Lee. J., and Fenves, G. L. (1998). "A plastic-damage concrete model for earthquake analysis of dams." *Earthquake engineering and structural dynamics*, 27(9), 937-956.

[3.12]   Lemaitre, J., and Chaboche, J. L. (1990). Mechanics of solid materials. Cambridge University Press, New York, N.Y.

[3.13]   Mazars, J. (1986). "A model of a unilateral elastic damageable material and its application to concrete." *Fracture toughness and fracture energy of concrete*, F.H. Wittmann, ed., Elsevier Science Publishers, Amsterdam, The Netherlands, 61-71.

[3.14]   Mazars, P. K., and Monteiro, P. J. M. (1993). Concrete: Structure, properties, and materials, 2nd Ed., Prentice-Hall, Inc., Englewood Cliffs, N.J.

[3.15]   Pramono, E., and Willam, K. (1989). "Fracture energy-based plasticity formulation of plain concrete." *J. Engrg. Mech.*, ASCE, 115(6), 1183-1203.

[3.16]   William, K. J, and Warnke, E. P. (1975). "Constitutive model for the triaxial behavior of concrete." *Int. Asso. Bridge Struct. Engrg. Proc.*, 19, 1-30.

CHAPTER 4

Test on Shallowly Embedded Column Base with SFRCC Slab

4.1 Introduction

4.1.1 Background

Degree of fixation and energy dissipation of the exposed column base may be improved if the column base is embedded in the base concrete shallowly. A preceding study introduced in Chapter 2 conducted a series of exposed column bases covered by a floor slab (theses column bases are called "shallowly embedded column base", hereafter), which is present in many buildings. Effects of the covering slab are commonly neglected in seismic design on the assumption that the contribution is minimal. The preceding study, however, showed that such a floor slab can be effective to improve the structural performance of the exposed column base, even to the extent that can be expected for the embedded column base. Punching shear failure in the floor slab around the column is the major mode of failure for this type of column bases, and how to avoid or delay this failure becomes an issue of future exploration.

SFRCC (Steel Fiber Reinforced Cementitious Composites) is a new fiber-reinforced cement-based composites utilizing hydraulic cements containing fine aggregates and large contents of discontinuous discrete steel fibers. The material has a large compressive strength (120 to 160 MPa). SFRCC also has a larger tensile strength and deformation capacity compared with the conventional concrete. Such improvement is achieved by mixing a large content of steel fibers (2 to 12% in volume) in the matrix (Kaneko et al. 2001 and Kirikoshi et al. 2000). In addition, reinforcing bars can work much more effectively with the matrix since the development of large cracks is prevented by the large amount of steel fibers (Bache 1989). Several tests on the application of SFRCC have been implemented by Kaneko. Applications of SFRCC to column-beam connections (Kaneko et al. 2001 and Kaneko et al. 2002) and encased column bases (Kaneko et al. 2006) have been proposed. The column base encased by filling SFRCC is named as the simple column base, as sketched in Fig. 4.1. In the simple column base system, the encased depth of column is reduced to not greater than the column section by using SFRCC from not less than 2.5 times the column section by using normal concrete. According to the test results, the simple column base connection showed a larger stiffness, strength and ductile hysteresis characteristics in comparison to the ordinary encased column base. In this chapter, proposed is an application of SFRCC to the slab of shallowly embedded column bases to

effectively improve the structural performance by using a relative thin floor slab even to the level as expected for the embedded column base.
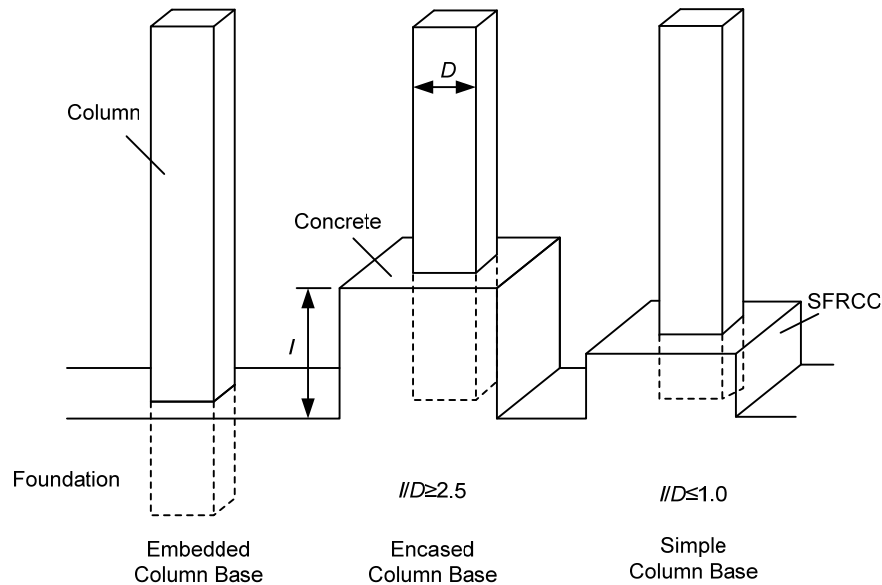
Fig. 4. 1 Simple column base connection (Kaneko et al. 2006)

4.1.2   Organization

The chapter consists of four parts. The first part introduces the basic principles of SFRCC, and the material of SFRCC is compared with normal concrete, high strength concrete (HSC) and fiber reinforced concrete (FRC). Then the second part presents the test results of shallowly embedded column bases with 100 mm thick SFRCC slab. The contribution of SFRCC is characterized by the comparison between the results with concrete slab and those with SFRCC slab.   In the third part, the FE models are developed to reproduce the test results using a general-purpose FEM program, ABAQUS. Finally, the procedure to estimate the elastic stiffness and maximum moment of shallowly embedded column bases with normal concrete (see Chapter 2 for details) is calibrated for the applicability to those with SFRCC.

4.2 Basic Principles of SFRCC

The development of SFRCC is based on a new strategy in which fracture mechanics play a central role. As the fiber reinforced cement based composites, large amount of steel fibers (generally 6% by volume) are placed in the SFRCC matrix. A comparison of mechanical properties obtained so far for different cemtentious material, such as normal concrete, HSC, FRC, and SFRCC, is given in Table 4.1 (Bache 1981 and Li 1998). The SFRCC material has excellent mechanical properties, including improvement in all strength properties, fracture toughness, and exhibit strain-hardening behavior beyond first cracking in tension. Moreover, the tensile strains at which the SFRCC matrix crack are increased exceed 3 mm/m, whereas ordinary reinforced concrete typically cracks at strains of about

0.1-0.2 mm/m. Such properties promised SFRCC matrix is able to follow the tensile deformations of the rebars as a coherent, crack-free, load-bearing body right up to yielding of the rebars. Because of the significant improvement in mechanical properties, SFRCC is recommended to work with the main reinforcements, even over-reinforced, in a given structural member. The bending behavior of SFRCC-beam and conventional concrete beam are compared in Fig.4.2. For the SFRCC beam, the strains correspond to the maximum strains with ideal linear elastic behavior. The load capacity was extremely high, which is about 5-10 times that of normal reinforced concrete. However, the very high load capacities of the SFRCC beam are primarily secured by the densely arranged main reinforcement, which transmits about 70~80% of the load at the start of yielding (Bache 1987).

Table 4.1 Properties of varies cementitious materials

	Compressive strength (MPa)	Tensile strength (MPa)	Tensile strain (mm/m)	E-Modulus (GPa)	Fracture energy (N/m)
Concrete	30	3.0	0.2	29.6	40
HSC	>60	3.0	0.2	29.6	120
FRC	55	4.3	0.35	32.5	4900
SFRCC	128	27.2	3.0	50	8130
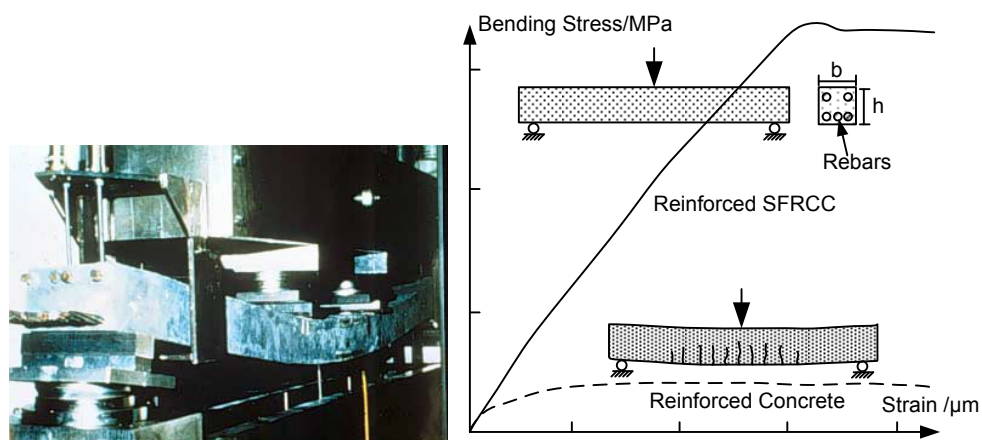
Fig. 4. 2 Behavior of reinforced SFRCC beam and reinforced concrete beam in bending
(Cross section 50x50 mm, span 447 mm, bending stress is $M/(1/6bh^2)$) (Bache 1987)

This section reviews past studies on the application of fracture mechanics to develop SFRCC. This is followed by the introduction of the basic design principle of SFRCC, and the summary of the preparation and mechanical properties of SFRCC.

4.2.1 Application of fracture mechanics

Cementitious materials such as concrete and fiber reinforced concrete (FRC) are quasi brittle materials. The failure of a uniaxial tension specimen of those materials is characterized by a gradual reduction of tensile stress (so called tensile strain softening) rather than drops to zero abruptly as a

brittle material does due to the development of a single macrocrack instead of sudden changes to non-traction cracks.

The strain-softening diagram shown in Fig. 4.3 is defined by the strength limit f_t for which a fracture zone is initiated and the area G_f under the diagram. The area G_f under the curve is called the fracture energy, which is assumed to be a material property. G_f is defined as the amount of energy required to create one unit of area of a continuous crack, and can be expressed as (Hillerborg, 1984):

$$G_f = \int \sigma_n dw \qquad (4.1)$$
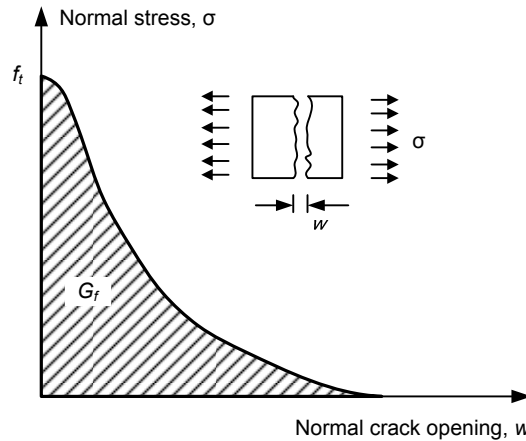
Fig. 4. 3 Tensile stress vs. crack opening displacement diagram (Rots et al., 1985)

The fracture of cementitious materials is governed by the existence of a fracture process zone. Initially, a limited number of such cracks develop in the specimen, but when somewhere in the specimen, the local tensile stress reaches a certain strength limit f_t, additional deformation due to microcracks will localize within a so-called fracture zone (see Fig. 4.4). In such a fracture zone the stress gradually decreases while the strain increases, and strain-softening occurs as shown by the descending branch curve in Fig. 4.3. Near the end of a descending branch, the microcracks coalesce into one continuous macrocrack.

Crack bridging and fracture process zone of fiber cementitious materials are illustrated in Fig. 4.4. The crack length, a, is considered as the region where traction is free. Preceding this is the fracture process zone, which includes fiber bridging, interlock, and coalescing microcracks. The transferred stress in the fracture process zone is so call "Bridging Stress". The bridging stress is mainly composed of aggregated bridging in plain concrete. The structural performances of fiber cementitious materials are strongly influenced by the crack bridging stress, which in turn depends on not only the material property of fibers but also the bond behavior of fiber/matrix interfaces. Because of the bridging of fibers between the crack surfaces, the descending branch rises. With the increasing level of the descending branch the fracture energy and the characteristic length increase, which means the material becomes more ductile.
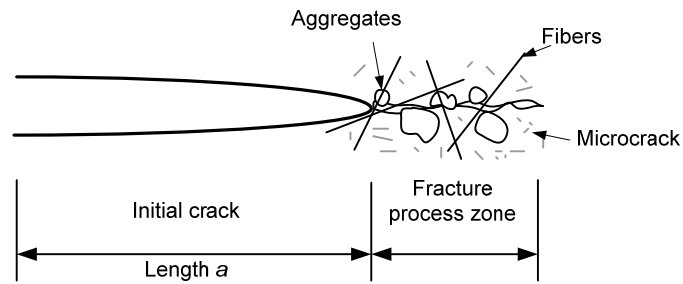
Fig. 4. 4 Fracture process along a crack plane

The behavior of cementitious material structures depends on the material properties of the structure, but also depends on the dimension of the structure. This can be formulated in a brittleness number which gives the relation between the elastic energy stored in the structure versus the energy needed to let a crack propagate through the structure (Elfgren. 1989). The brittleness number, B, is expressed as

$$B = \frac{\text{Elastic energy}}{\text{Fracture energy}} = \frac{L^3 f_t^2 / E}{L^2 G_f} = \frac{L f_t^2}{E G_f} \tag{4.2}$$

Where L is a characteristic size of the structure. Here L^3 denotes a volume and f_t^2/E is the stored elastic energy at failure for a unit volume, while L^2 denotes a crack area and G_f is the fracture energy for a unit area. For small values of the brittleness number, the structure behavior is ductile. The carrying capacity is high because all yield reserves are utilized, and the failure deformations are big and dominated by crack zone deformations. Structure bodies in this range are relatively insensitive to small cracks and local stress concentrations. For large values of the brittleness number, the behavior is brittle and the carrying capacity is low because there are no yield reserves. Structure bodies in this range are very sensitive to cracks and local stress concentrations.

SFRCC is based on the strong binder material, which provided large f_t, given very high ductility by means of fibers, which greatly increase the fracture energy G_f. In addition, cooperating with main reinforcement, the material body is divided in smaller parts. The global ductility of structure is thereby ensured by the smaller brittleness number.

4.2.2   Characteristics of SFRCC

There are three characteristics for SFRCC distinguished with other cement materials.

New ultra-strong cement based materials

The cement paste of SFRCC is the densified cement materials containing homogeneously arranged, ultra-fine particles. The densely packed particles are normally Portland cement, and the ultra-fine particles silica fume. The structure of the fresh paste is shown in Fig.4.5, in which it is compared with that of ordinary cement paste and superplasticized cement paste.

By using distinct gap grading (large diameter ratio), dense particle packing could be achieved. In the conventional cement paste, the dense packing is prevented by surface forces, as shown in Fig. 4.5 (a). But with the advent of effective dispersants that eliminate the locking effect of surface forces, it became possible to pack fine particle systems densely on the basis of purely geometrical principles, as

illustrated in Fig. 4.5 (b). The cement particles (particle size 5-10μm) were very densely packed, secured by an efficient dispersing agent. And the space between them was additionally filled with a high concentration of silica fume (particle size 0.1-0.2μm) (Fig. 4.5 (c)). This resulted in very dense, extremely high-strength concrete.
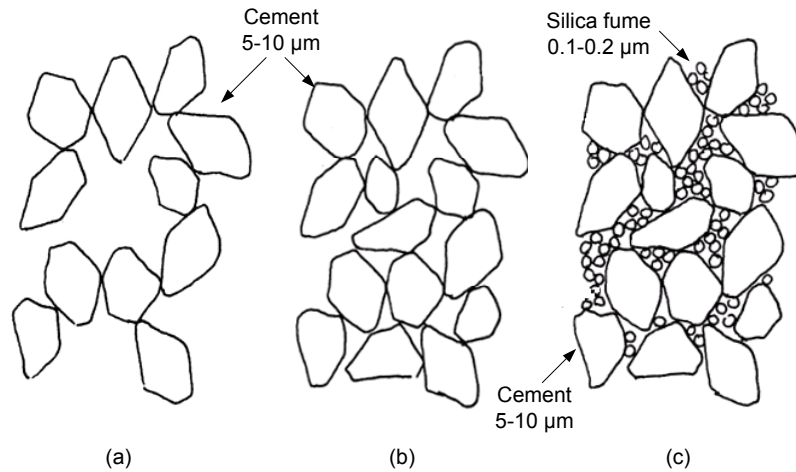
Fig. 4. 5 The structural of the matrix:
(a) normal concrete; (b) high strength concrete; and (c) SFRCC (CBL No.41)

Due to the addition of 10~50% by volume ultra-fine silica fume particles occupied the space between the cement particles in this densely packed matrix, the water requirement is considerably reduced. The amount of water required to achieve an easily castable fluid densely packed matrix is thus considerably lower than that used in ordinary superplasticized concrete mortar (typically between 0.12 and 0.18 by weight in comparison with 0.3 by weight for ordinary concrete mortar).
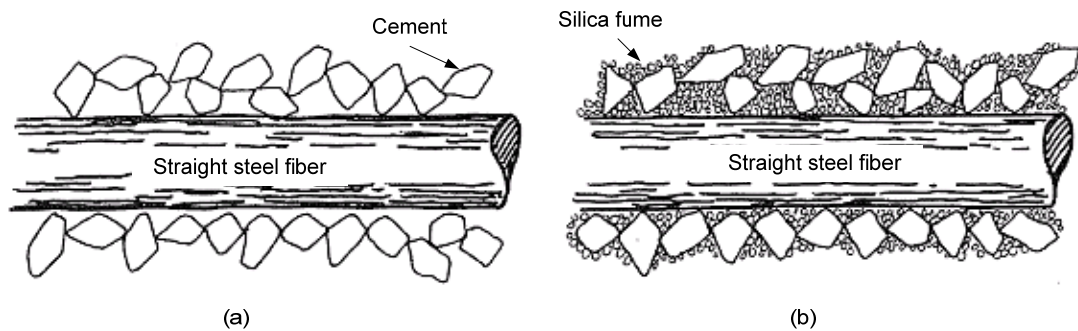
Fig. 4. 6 Straight fibers embedded in different paste:
(a) cement paste; (b) densely packed cement paste (CBL No.40)

Due to the very dense hardened structure, the strength and durability are very much increased compared with ordinary cement-based materials. The densely packed cement matrix also results in improved anchorage of reinforcement. Pull-out tests on very smooth 6 mm steel bars embedded 60 mm in the densely packed cement matrix resulted in a pull-out force of about 9 kN, compared with about 2 kN for ordinary mortar (CBL No.40). The very dense material structure of the cement matrix makes it particularly suitable for mechanical anchorage of straight fibers, which are not normally

fixed firmly in conventional cement matrix, as illustrated in Fig.4.6. The mechanical fixation of the fine fibers is greatly increased by incorporating the silica fume particles in the spaces between the densely packed cement because the dimensions of roughness and wave configuration on the reinforcement that are necessary for "mechanical locking" of the reinforcement in the matrix are thereby strongly reduced.

Application of a high content of steel fibers

The densely packed cement matrix exhibits ultra strong compressive strength. However, the material has proved to be extremely brittle. Steel fibers were therefore adopted to conquer the serious brittleness problems. Fibers work with the matrix utilizing two mechanisms: the spacing mechanism and the crack bridging mechanism. Based on the spacing mechanism, a large number of fibers are required to be well distributed within the concrete matrix to arrest any existing micro-crack that could potentially expand and create a macro-crack. The second mechanism termed crack bridging requires stronger fibers with adequate bond to the cement matrix, in which most fibers are pull out at a load which is close to that required to break the fibers. As aforementioned, in SFRCC a high content of fine, strong and stiff fibers are well fixed to the matrix due to the densely packed material structure. In addition, because of the special rheological properties of the fresh matrix, it is possible to mix far more fibers in the densely packed cement matrix than in conventional concrete.

By using a high content of steel fibers, the brittle matrix is enable to strain harden under tensile loading, in the same way as the metal behavior, as sketched shown in Fig. 4.7. In tensile fracture the brittle material deforms largely elastically up to a state with maximum tension. Thereafter, fracture occurs by the opening of a single crack. Before the crack develops, local deformations occur in a very narrow zone –the crack zone. Conventional fiber reinforcement has little effect on the formation of the first matrix crack, but if the material is very effectively reinforced with extremely fine, strong, stiff fibers, the fibers can immediately take over large loads before a crack zone develops into a real crack. Increasing loads will thus not result in fracture but in the formation of new crack zones distributed over the entire body. The brittle material is thereby given the capacity of strain hardening. The fracture energy is thereby increased.
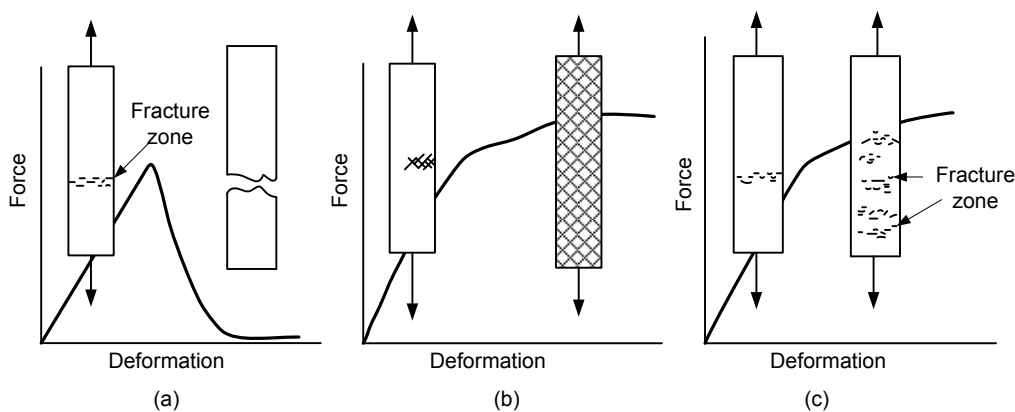

Fig. 4. 7 Tensile behavior of different material: (a) concrete; (b) steel; and (c) SFRCC (Elfgren, 1989)

Dense main rebars

The most important mechanism in SFRCC is a further, marked increase in the tensile strain capacity of the ductile, fiber-reinforced matrix material, achieved by very effective fixation to very dense main reinforcement. In reinforced SFRCC, the main rebars act as the stiff frame that divides the matrix into many small volumes. The crack zone deformations are thereby distributed out over the body when the material is forced, during tensile deformation, to follow closely the elongations of the main reinforcement.
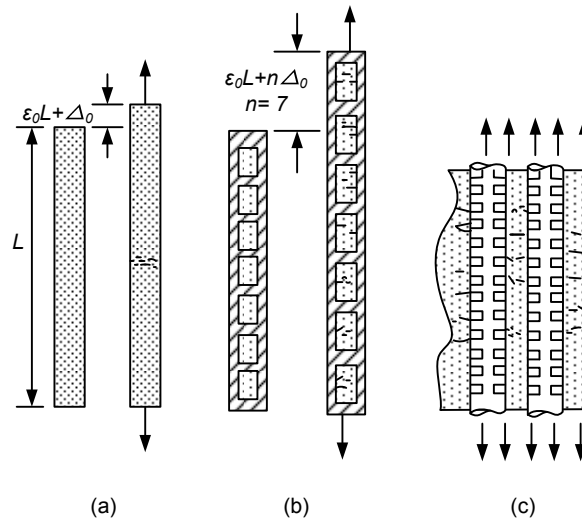
Fig. 4. 8 Tensile deformation of bar of different material:
(a) cement bar; (b) cement fixed by a stiff frame; and (c) SFRCC with densely arranged rebars
(Elfgren, 1989)

The difference between reinforced SFRCC and ordinary reinforced concrete is that SFRCC has been able to ensure really effective utilization of a very high amount of reinforcement while remaining substantially free of cracks (Fig. 4.8). In normal reinforced concrete (with moderate amount of reinforcement), the concrete cracks past the reinforcement, which resists the tensile stresses but retains acceptable inner coherence. If we attempt to use more reinforcement, the concrete cracks and splits, and the inner coherence is lost. With SFRCC we are now able to achieve an extremely large amount of reinforcement without losing inner coherence and without cracking for loads right up to yield limit of the steel.

4.2.3 Preparation of SFRCC

Figure 4.9 shows the mixing components of SFRCC in this study. Compositions for per m^3 SFRCC were summarized in Table 4.2. 6% volume portion of steel straight fiber (diameter of 0.4mm, length of 12.0mm, tensile strength of 1350MPa) was used, in comparison of 2% vol. steel fibers for the conventional FRC. Water binder ratio was 0.2, and in order to ensure the necessary fluidity of the matrix an effective quantity of water-reducing admixture (Flowric SF200S, amino sulfonic acid system compound) was adopted. The mixing of SFRCC was performed in a planetary mixer as follows:

The cement, microsilica, and sand were dry-mixed for three minutes. Water and water-reducing

agent were then added, and mixing continued for a further five minutes. Fibers were then added, and mixing continued for another two minutes.

The mass had a dry appearance for the first few minutes of mixing after water had been added. It then underwent a rather sudden change into a doughy mass which gradually changed into a softer, glossy, viscous mass, indicating complete saturation of the system.

The texture remained the same after the addition of fibers, but there was far greater resistance to shear during the mixing.

The result of a typical slump test is shown in Fig. 4.10.

Table 4.2 Compositions for 1 m^3 SFRCC

High early strength Portland cement	801 kg
Silica fume	164kg
Fine aggregate	1235 kg
Steel fiber	471 kg
Water	190 kg
High-range water-reducing agent	32 kg

Fig. 4. 9 Mixing components of SFRCC

Fig. 4. 10 Slump test of SFRCC (unit: mm)

4.2.4   Mechanical properties of SFRCC

SFRCC with such a large amount of fiber (6% in volume) while maintaining an acceptable

workability is manufactured using a large content of water reducing agent composed of much microsilica and with water/binder ratios, e.g. 0.2 or lower. Compared to conventional concrete, SFRCC has a remarkably large compressive strength and a better tensile behavior in terms of the strength and the ductility, as shown in Fig. 4.11. Because of the large content of steel fibers, the matrix becomes very ductile. It is made possible to utilize reinforcing bars much more effectively, since the development of large cracks is effectively prevented by the bridging of steel fibers. Furthermore, the distance between reinforcing bars and the cover layer to the reinforcement can be as small as 15mm, because relatively small sizes of the fibers and fine aggregate are used. Because of the highly compacted material structures of SFRCC, durability and resistance to corrosion are also to be good, so that such a small cover to reinforcement is still sufficient.
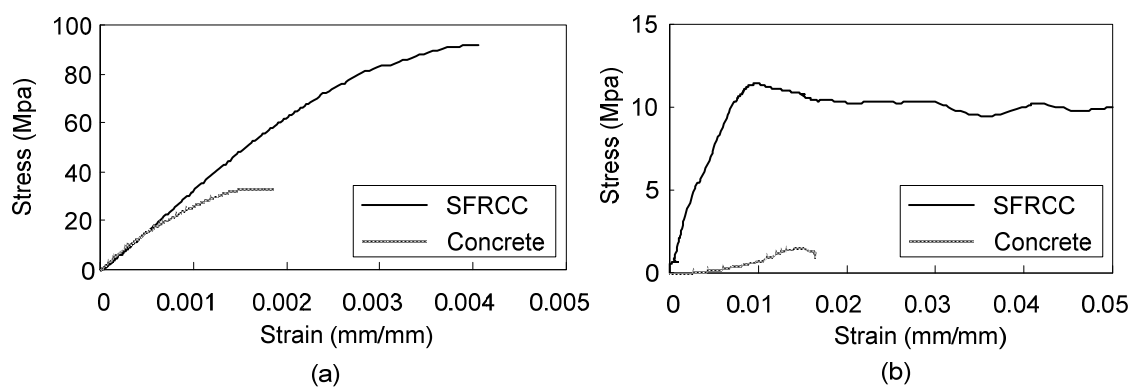
Fig. 4. 11 Stress-strain behavior of concrete and SFRCC: (a) in compression; (b) in tension

4.3 Test Program

4.3.1 Test specimens

Five specimens were tested. The details of the specimens are the same as the specimens with concrete slab described in Chapter 2. The global dimensions are shown in Fig. 4.12. Table 4.3 summarizes the test variables of the five specimens. Two specimens tested in the previous research introduced in Chapter 2, 'SL-100' and 'SL-100-st' are referred to as 'CS' and 'CR13', and included in Table 4.3. These specimens were referred to for the comparison with the specimens featured with SFRCC slab.

Specimen 'SS', an exposed column base covered by a floor slab reinforced only by mesh bars, was the baseline specimen. All other four specimens were strengthened further by eight bent horizontal deformed rebars. These rebars were placed to restrict both the rotation of the base plate and the separation of the floor slab. As shown in Fig. 4.13, the bent part of the rebars is set approximately perpendicular to the failure surface that occurred in the floor slab as described in Chapter 2. All horizontal rebars are set around the column and upon the base plate, two pieces at each column side and in each direction. The rebars parallel to the loading direction are expected to resist the rotation of the base plate directly, hence these rebars are placed closer to the base plate,

beneath the other four rebars.

As the test parameters of reinforced specimens, the size and strength of rebars were selected. Specimens 'SR13' and 'SR19', with SFRCC floor slab were reinforced by D13 and D19 of SD295 deformed rebars, respectively. It is noted that the covering concrete of the rebar is only 17 mm thick, which is smaller than the covering thickness required for normal concrete components (AIJ 1990). Specimens 'SR785' and 'CR785' were the specimens with the SFRCC and concrete floor slab, both strengthened by 13 mm diameter high strength steel bars.

The material properties of the steel and concrete used for the specimens are summarized in Table 4.4.
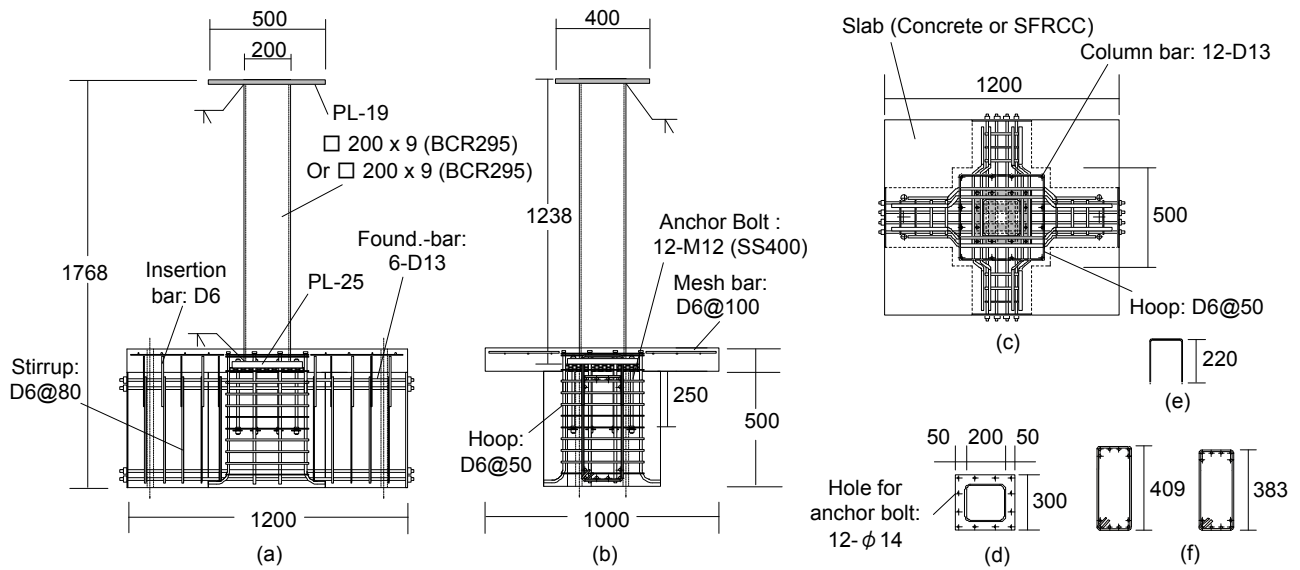

Fig. 4. 12 Test specimen: (a) front elevation; (b) side elevation; (c) plane view;
(d) baseplate; (e) insertion bar; and (f) stirrup (unit: mm)
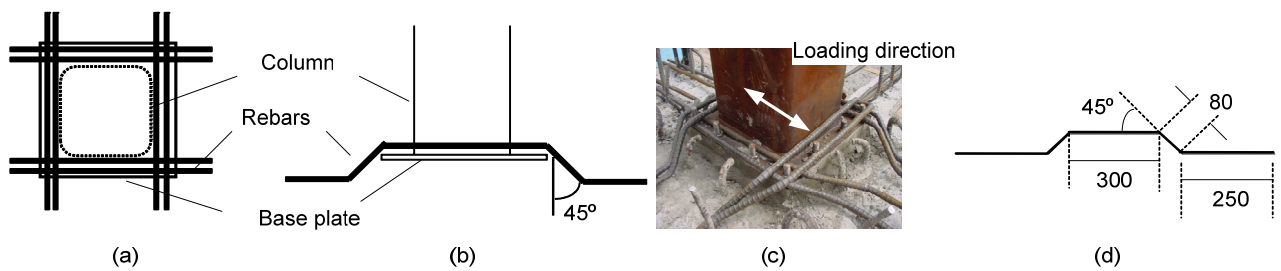
Fig. 4. 13 Configuration of reinforcing bars:
(a) plan view; (b) elevation; (c) arrangement of rebars; and (d) detailing of rebars (unit: mm)

Table 4.3 Summary of test specimens

Specimen	Slab material	Rebar		Column	
		diameter (mm)	material	thickness (mm)	material
CS	Concrete	--	--	9	BCR295
CR13		13	SD295	9	
CR785		13	KW785	12	
SS	SFRCC	--	--	12	SM490A
SR13		13	SD295	12	
SR19		19	SD295	12	
SR785		13	KW785	12	

Table 4.4 Material properties (concrete and steel)

		Yield strength σ_y (N/mm^2)	Tensile strength σ_u (N/mm^2)
Column	□-200×12, SM490A	353	512
Column Base	Anchor bolt,SS400	317	450
	Base plate, SM490A	322	510
Reinforcement	D13,SD295	325	461
	D19,SD295	332	514
	KW785	716	970

		Compressive strength $f_c{}'$ (N/mm^2)	Splite strength $f_{sp}{}'$ (N/mm^2)
Slab	SFRCC	93.2	11.5
	Concrete	34.5	1.6
Foundation Beam	Filled mortar	66.7	--
	Concrete	34.5	--

4.3.2 Test setup and loading program

The test specimen was placed in the loading frame shown in Fig. 4.14. The foundation beam is clamped to the reaction floor. The column top is clamped to two hydraulic jacks, one in the horizontal direction and the other in the vertical direction. The specimen was subjected to a constant vertical force of 511 kN, as was done in the previous research. A displacement-controlled cyclic load was applied quasi-statically in the horizontal direction. The displacement was expressed in terms of the drift angle, defined as the horizontal displacement at the loading point relative to the height of the column (1,238mm). Drift angles of 0.005, 0.015, 0.0225, 0.03, 0.04, 0.06, 0.08, and 0.1 rad were adopted, and two cycles of loading were performed at each drift angle. The test was terminated when the drift angle reached 0.1 rad or ten of the twelve anchor bolts fractured, which

was regarded as a complete failure.
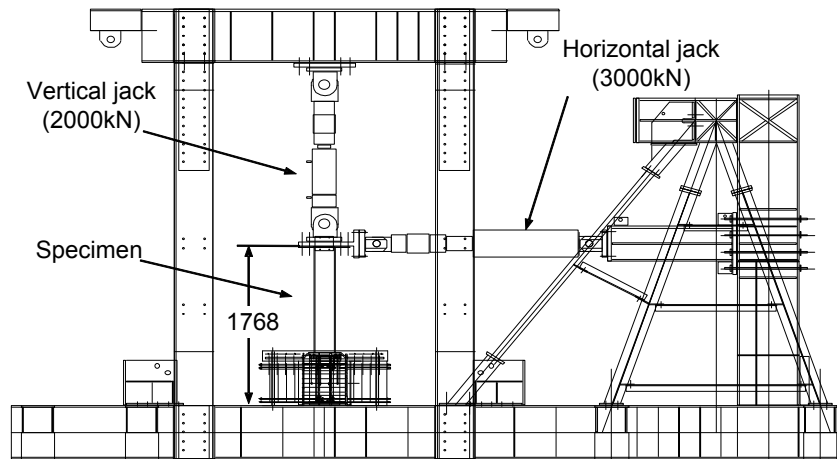

Fig. 4. 14 Elevation of the loading system (unit: mm)

4.4 Test Results

In the following, the relevant material properties of SFRCC as well as the interaction characteristics with reinforcing bars in uniaxial tension are briefly presented and the test results of shallowly embedded column base with SFRCC slab under cyclic loading conditions are presented. In the subsequent sections, the contribution of SFRCC slab are investigated and compared to the corresponding concrete slab. The evaluation of composite performance focuses on elastic stiffness, maximum strength, ductility, and energy dissipation as well as other indices, such as extent of damage, and matrix/reinforcement interaction.

4.4.1 Moment-rotation relationships

Figure 4.15 shows the moment-rotation relationships for all specimens including the two specimens with concrete slab ('CS' and 'CR13') in terms of the end-moment (M) applied at the bottom of base plate versus drift angle (θ). Here, the end moment includes the moment induced by the P-Δ effect. All SFRCC specimens were larger in both the initial stiffness and maximum strength than the concrete specimens. Specimen 'SS' has the smallest maximum strength of all the SFRCC specimens and shows significant decrease in resistance after reaching the maximum strength with the progress of the punching shear failure of the floor slab. When the specimen was reinforced by horizontal rebars, strength deterioration was mitigated. For concrete specimens, Specimen 'CR785' exhibited almost the same moment-rotation relationship as Specimen 'CR13', although the high strength rebars was applied instead of the normal strength rebars. On the contrary, Specimen 'SR785' exhibited slightly better ductility than Specimen 'SR13'. Among all the specimens, Specimen 'SR19' exhibited the largest strength and ductility. Moreover, the SFRCC specimens had fatter hysteresis loops than the corresponding concrete specimens in which slip behavior was significant. This fatter hysteresis was attributed to the material properties of SFRCC, which prevented rapid degradation of both the strength and stiffness.
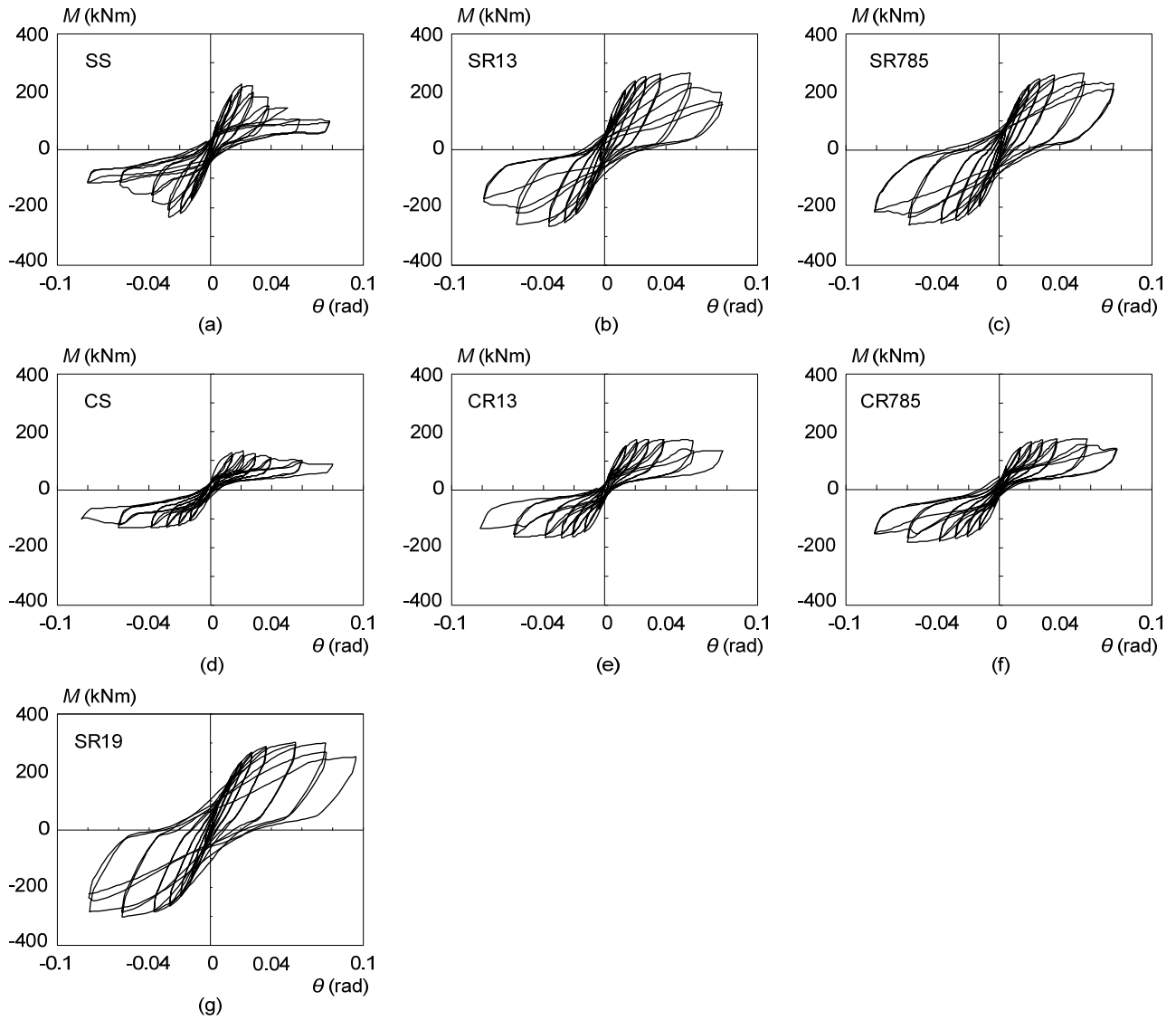
Fig. 4. 15 Moment versus rotation relationships: (a) SS; (b) SR13;
(c) SR785; (d) CS; (e) CR13; (f) CR785; and (g) SR19

Table 4.5 Test results

Sepc.	K_0 (kN·m)	M_{max} (kN·m)	E_p (kN·m·rad)
SS	20607	230	38.0
SR13	20492	265	64.6
SR19	20750	301	72.0
SR785	20581	262	66.5
CR785	17426	179	32.5
CS	15134	135	22.7
CR13	16350	167	33.0

Table 4.5 shows the elastic stiffness (K_0), maximum strength (M_{max}), and dissipated energy (E_p) of

each specimen. The elastic stiffness (K_0) was defined as the secant stiffness between the origin and the point at 0.005 rad, because the story drift angle is limited to 0.005 rad in the current Japanese elastic design (AIJ 2005). The dissipated energy (E_p) was calculated as the total area of the hysteretic loops. For all specimens, the calculation was made from the start of loading to the completion of 0.06 rad drift angle amplitude. As shown in Table 4.5, concrete specimens showed smaller values, because of the relatively weak properties of concrete. A difference of only 5% is noticed in the initial stiffness among the specimens with SFRCC slab ('SS', 'SR13', 'SR19', and 'SR785'). Since the entire column base system remained nearly elastic without visible cracks up to 0.005 rad rotation, contribution of the horizontal rebars to the elastic stiffness became minimal. Improvement of the maximum strength due to the presence of horizontal rebars varied from 14% to 30% in the SFRCC specimens. Specimen 'SR13' (reinforced by D13 normal strength rebars) and 'SR785' (reinforced by D13 high strength bars) shows smaller improvement of 14% and 15%, respectively, and the one with the large size normal strength rebars ('SR19') shows the largest improvement of 30%. Because of the presence of the horizontal rebars, the dissipated energy increased to about two times that of the corresponding specimen without rebars ('SS').

4.4.2 Experimental observation

All specimens failed by punching shear in the slab. Failure pattern of all specimens with floor slab was similar, regardless of the differences in slab material or reinforcement detailing. Crack patterns of the specimens are shown in Fig. 4.16. The dash lines roughly circled the punching region of each specimen. It is notable that the punching region is larger for concrete specimens compared with SFRCC specimens. The damage development of the specimens is characterized as follows.

In Specimen 'SS' (plain SFRCC) prior to 2.25% drift, few cracks formed around the column with the average width of 0.03mm. At 3% drift, cone-like crack formation around the column caused by punching shear in the slab was initiated. Beyond this stage, the number of cracks remained constant; however, the formed cone-like cracks (Fig. 4.16 (a)) increased in width to accommodate the induced displacements at the top of the column. The punching cracks connected through the thickness of the slab simultaneously. The maximum strength was obtained at 2.25% drift with the moment of the column base of 230.12 kNm. Speration of punching region from the slab became apparent beyond 3% drift and coincide with a decrease in applied lateral load at subsequent displacement stages. However, due to the presence of steel fiber, the punching failure part did not totally separated from the whole slab till the end of loading.

Specimen 'SR13' (reinforced SFRCC, ribbed normal strength rebar with 13 mm diameter) and SR785 (reinforced SFRCC, high strength rebar with 13 mm diameter) showed several cracks around the column with the maximum width of 0.20 mm before 4% drift. Beyond this deformation stage, the cone-like cracks caused by punching shear in slab was connected around the column, while other cracks stablized in number and maximum crack width (Fig. 4.16 (b),(c)). The maximum strength was reached at 4% drift with the moment of the column base of 265.30 kNm and 262.46 kNm, respectively. Till the end of loading, the rupture of the steel reinforcement was observed (Fig. 4.17 (a)). Throughout the test, bond splitting, spalling, and buckling of reinforcement were not observed.

The behavior of Specimen 'SR19' (reinforced SFRCC, with ribbed normal strenght rebar with 13 mm diameter) was similar to the Specimens 'SR13' and 'SR785'. Nevertheless the damage developed late in SR19. Prior to 4% drift, less cracks compared to other specimens formed in the slab. The cone-like cracks caused by punching shear in slab was connected at 8% drift (Fig. 4.16 (g)). The maximum strength was reached at 6% drift with the moment of the column base of 301.33 kNm. Till the end of loading, the rupture of the steel reinforcement was not observed. It should be noted that the failure region for the Specimen 'SR19' was not even formed completely.

On the contrary of Specimen 'SR785', Specimen 'CR785' (reinforced concrete, high strength rebar with 13 mm diameter) showed more serious damage. Both the punching shear cracks and the cracks radiated from the column formed at 2.5% drift. Beyond this stage, the cracks keep progating, the number of cracks also increased. The maximum strength was reached at 4% drift at the moment at the column base of 179.32 kNm. Till the end of loading, the buckling of the steel reinforcement was observed (Fig. 4.17 (b)). Additonally, the punching failed part was totally separated from the concrete slab. A large punching shear circle was formed compared with SFRCC specimens, as shown in Fig. 4.16(e).
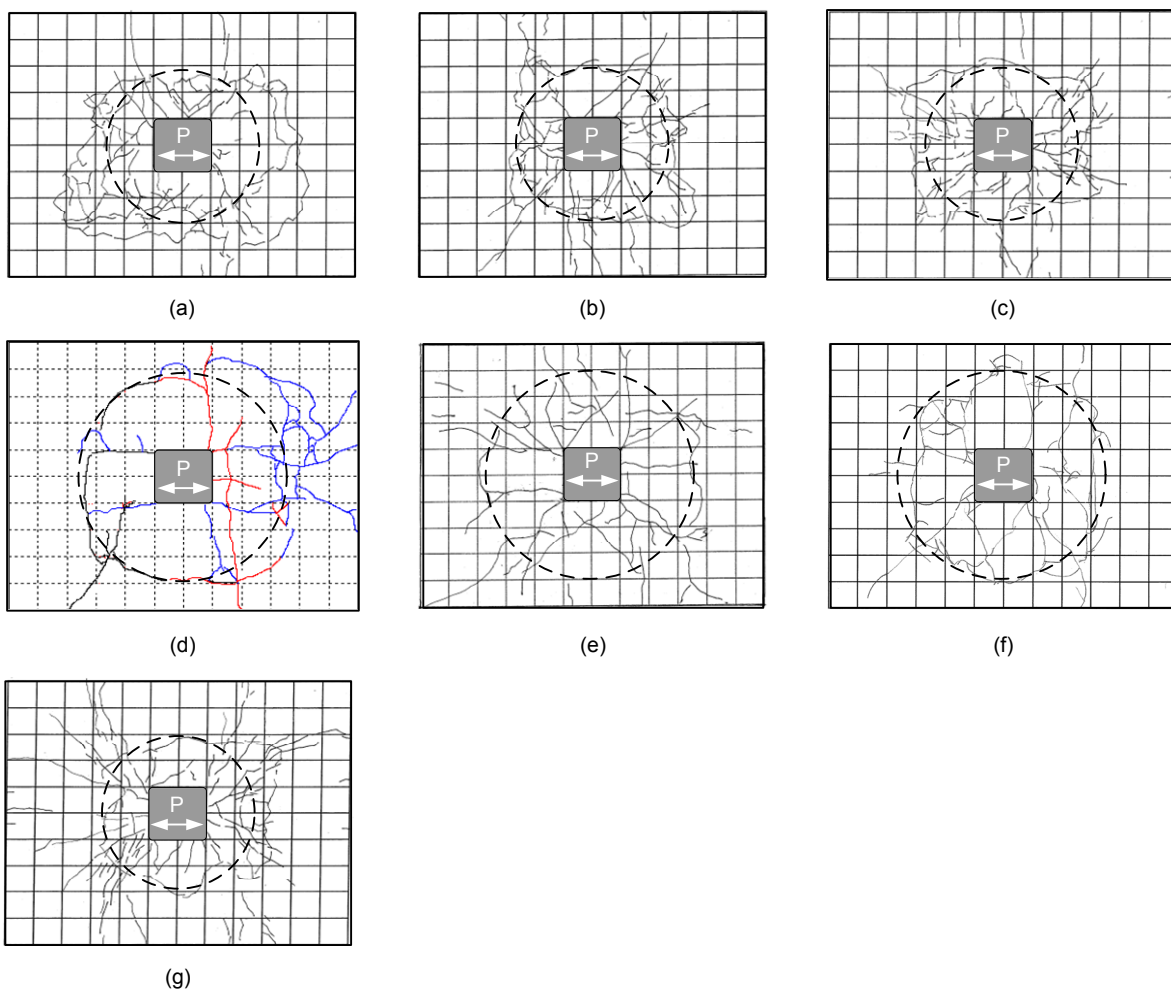

Fig. 4. 16 Cracking patterns of slab:
(a) SS; (b) SR13; (c) SR785; (d) CS; (e) CR13; (f) CR785 and (g) SR19

The overall behavior of anchor-bolts was similar among all specimens, with the first fracture of the bolts occuring in the bolts located close to the corners during the loading cycle of 6% drift. Similar behavior was observed for the specimen without slab ('Standard'), which was presented in Chapter 2. Fracture of anchor bolts was slightly retarded when SFRCC or reinforcement was adopted. However, the effect of the slab on the behavior of the bolts remained small.

In reference to the results of a previous specimen in which the column failed instead of the column base, the horizontal capacity of the steel tube used for the specimens described in this study was 234kN. As shown in Table 4.5, the maximum strength of the SFRCC specimens are larger than this value, except Specimen 'SS' whose maximum strength is slightly smaller. This indicates that the shallowly embedded column base with a 100 mm SFRCC floor slab has a large potential to realize the column failure mechanism.
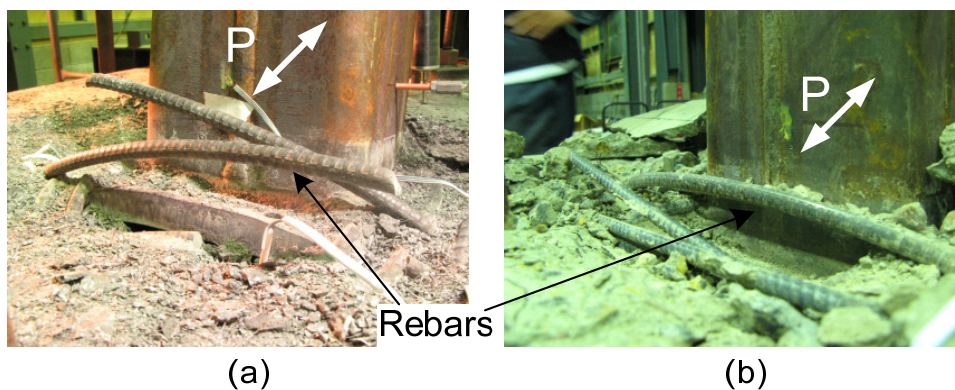

(a)   (b)

Fig. 4. 17 Deformation of reinforcement: (a) rupture; (b) buckling

4.4.3   Effects of floor slab

The effect of floor slab can be examined from the results of the two shallowly embedded column base specimens, both having the same thickness and not reinforced by horizontal rebars (Specimen 'SS', 'CS'). As evidenced from Table 4.5, the elastic stiffness, maximum strength, and dissipated energy of the specimen with SFRCC floor slab (Specimen 'SS') were 1.4, 1.7, and 1.7 times larger than those of the specimen with concrete floor slab (Specimen 'CS'). Improvement of the stiffness and strength was attributed to the higher Young's modulus and compressive strength of SFRCC as introduced in Section 2. Since the presence of steel fibers restricted the propagation of cracks, the fracture process naturally became slow for Specimen 'SS', which contributed to the increase of dissipated energy. In view of the moment-rotation relationships of these two specimens, Specimen 'SS' exhibited fatter hysteretic loops till 0.03 rad, although the slip behavior was present in the last few cycles. Moreover, when the floor slab was reinforced by the horizontal rebars, the maximum strength and dissipated energy were further improved in relation to the corresponding Specimen 'SS'. The improvement by using reinforced SFRCC slab was in a range of 15% to 30% for the maximum strength and 70% to 90% for the dissipated energy.

4.4.4 Effects of rebars

As evidenced in Table 4.5, a slight difference is present in maximum strength between Specimens 'SR13' and 'SR785' for SFRCC Specimens and Specimens 'CR13' and 'CR785' for concrete specimens. The diameter of rebars for these specimens was 13 mm, and for Specimens 'SR785' and 'CR785' high strength rebars were used. From the data collected by the strain gauges glued on the rebars, it was observed that all the conventional rebars yield immediately after the maximum strength. On the other hand, the high strength bars remained elastic, and contributed by nearly the same strength as the yield strength of the converntional rebars. However, the presence of high strength rebars retarded the strength deterioration. As evidenced from Fig. 4.18, the cumulative dissipated energy of each loading cycles was increased by 10 kN·m·rad by high strength rebars for both the SFRCC and concrete specimens, primarily due to the larger reserved strength possessed by high strength rebars. This suggests that the benefit of high strength rebars is primarily to retard the strength detereration rather than to increase the maximum strength.

In this study, a larger size rebars with a 19 mm diameter were adopted only for one SFRCC Specimen 'SR19', since the concrete covering (17 mm) was smaller than that required for concrete specimens. As shown in Table 4.5, Specimen 'SR19' showed the largest maximum strength and dissipated energy.
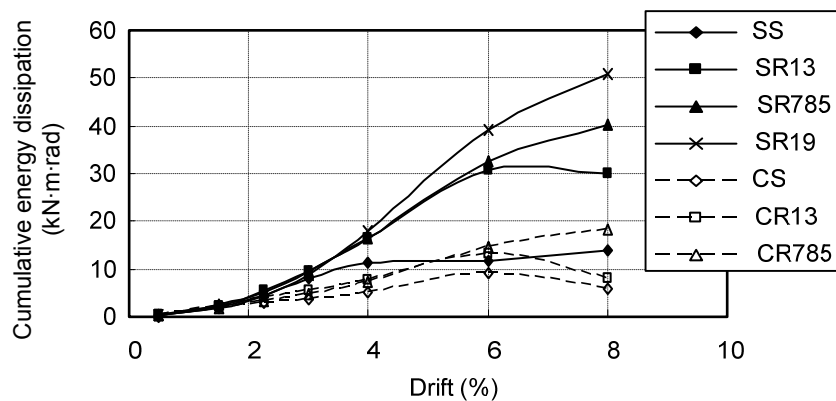
Fig. 4. 18 Cumulative energy dissipation of each loading cycle

4.4.5 Fixation of rebars

Since concrete is weak and brittle, rebars should be arranged with decent spacing and covers. As mentioned before, because the large content of steel fibers makes the matrix of SFRCC very ductile, the limitations of rebars spacing and covers can be relaxed. As evidenced in Specimen 'SR19', it exhibited the best seismic behavior in this study, although the covering depth was only 17 mm.

As shown in Table 4.5, SFRCC specimens with horizontal rebars showed two times as large energy dissipation capacity as the corresponding concrete specimens. Such significant improvement was a result of the combined effect of the steel fibers and the plastic deformation of horizontal bars. As shown in Fig. 4.17, rebars perpendicular to the loading direction ruptured at a very large rotation (0.1 rad) in the SFRCC specimen, while rebars were only bent in the concrete specimens. This

suggests that slips occurred in rebars embedded in the concrete slab, but such slips remained minimal and therefore the rebars ruptured in the SFRCC slab. The difference in bonding capacity was very notable between concrete and SFRCC.

4.5 Numerical Analysis

4.5.1 Analysis model

To supplement the experimental data, a numerical study is conducted for shallowly embedded column bases with SFRCC slabs. The general-purpose finite element program ABAQUS version 6.7 was used to analyze a 3D model, which is the same as the numerical model introduced in Chapter 3.

Half of the specimen was modeled by taking advantage of symmetry in the model. The models of shallow embedded column base are subdivided into an exposed column base, a flat slab that surrounds the base plate, and the lower part of column, as shown in Fig. 4.19. The chosen boundary conditions reflected the symmetric properties of the model. The details, including the element type and mesh size, of the numerical model of shallowly embedded column base with SFRCC slab exactly to follow those of the model used for shallowly embedded column base with concrete slab.
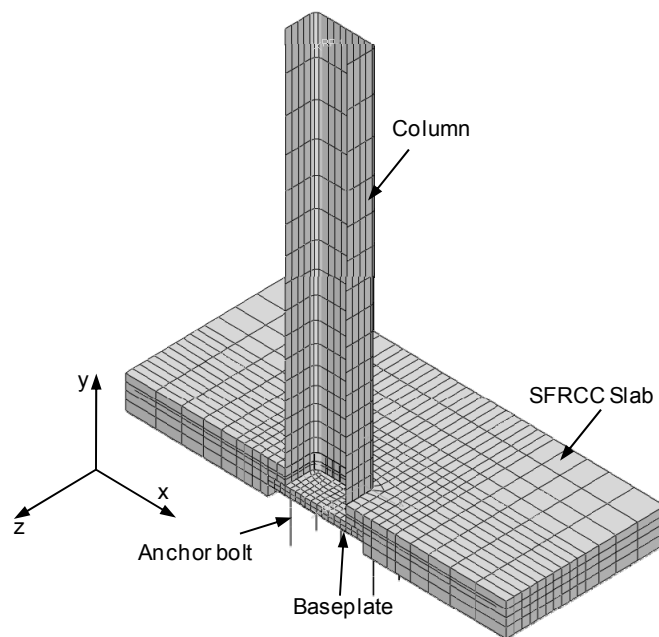
Fig. 4. 19 Analysis model

4.5.2 Constitutive model for SFRCC

As introduced in Section 4.2, SFRCC exhibited material behavior significantly different from that of normal concrete. Therefore, a different uniaxial strain-stress (σ-ε) relation model is needed for SFRCC. The damage plasticity model, a material model commonly used for the analysis using ABAQUS was continuously adopted to represent the material characteristics of SFRCC. This model,

not the concrete smeared cracking model, was adopted, because this model considers the failure mechanism of tensile cracking and compressive crushing, independently.

Since SFRCC is a relatively new material, research on its constitutive model is very limited, especially on the tensile behavior, which is more difficult to measure than compressive behavior. Nielsen (1995) did a series of basic material research on SFRCC. According to the test results, the uniaxial tensile and compressive strengths increase with the fiber parameters. A satisfactory linear relationship is found, depending on the fiber reinforcement index $V_f(L_f/d_f)$, where V_f is the fiber content by volume, L_f is the length of fiber, and d_f is the diameter of fiber, as follows.

Tensile strength:

$$f_t = \left(6 \cdot V_f \frac{L_f}{d_f} \right) \text{MPa} \tag{4.1a}$$

Fracture energy:

$$G_f = \left(100 + V_f \frac{L_f}{d_f} L_f \right) \text{N/m} \tag{4.1b}$$

Compressive strength:

$$f_c = \left(145 + 25 \cdot V_f \frac{L_f}{d_f} \right) \text{MPa} \tag{4.1c}$$

Compressive strain:

$$\varepsilon_c = \left(0.24 + 0.18 \cdot V_f \frac{L_f}{d_f} \right) \% \tag{4.1d}$$

In this study, the SFRCC of W/B =0.20 and V_f =6% was adopted, and the fiber was 12.0 mm in length and 0.4 mm in diameter. Based on the Equation (4.1), the basic material properties of SFRCC adopted in this analysis are shown in Table 4.6.

Table 4.6 Basic material properties of SFRCC in analysis

Tensile strength f_t (MPa)	Fracture energy G_f (N/m)	Compressive strength f_c (MPa)	Compressive strain ε_c
10.8	121.6	190	0.00564

In uniaxial compression SFRCC exhibits a rather ductile failure. According to the research of Nielsen (1995), the compressive stress-strain relationship of the model is defined by the following equation,

$$\frac{\sigma}{f_c} = \frac{4 \dfrac{\varepsilon}{\varepsilon_c}}{1.5 + \left(\dfrac{\varepsilon}{\varepsilon_c} \right)^{2.5}} \tag{4.2}$$

where ε_c and f_c are the compressive strain and stress at the peak point; the σ-ε relation is graphically shown in Fig. 4.20 (a).
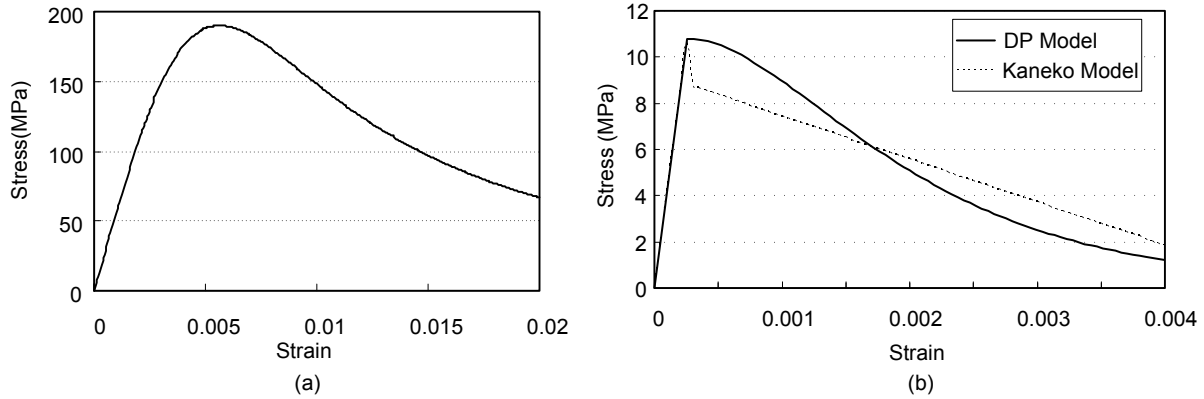

Fig. 4. 20 Material Property: (a) compression; (b) tension

However, the tensile constitutive model of SFRCC was not described in the report of Nielsen (1995). Here, the tensile constitutive model of SFRCC proposed by Kaneko (2000) is adopted for the basic tensile behavior of SFRCC. Then, the equations (introduced in Chapter 3, Eq. (3.1) ~ (3.5)) associated with the tensile behavior proposed by Lee and Fenves (1998) is adopted to describe the tensile behavior of SFRCC in the damaged plasticity model.

The tensile constitutive model of SFRCC proposed by Kaneko (2000) is introduced as follows.

The behavior of SFRCC in tension is described by the linear stress-strain relation (σ_t-ε_t) before cracking, and thereafter by the bilinear stress-strain relation as shown in Eq. (4.3).

Before Cracking:

$$\sigma_t = E_0 \varepsilon_t , \quad \varepsilon_t \leq \varepsilon_{cr} \tag{4.3a}$$

After Cracking:

$$\sigma_t = \alpha f_t \left(\frac{\varepsilon_{tu} - \varepsilon_t}{\varepsilon_{tu} - \varepsilon_{cr}} \right) , \varepsilon_{cr} \leq \varepsilon_{tu} \tag{4.3b}$$

$$\alpha = \frac{2G_f}{1.5 f_t w_t^{cr1}} \tag{4.3c}$$

$$w_{tcr2} = 2 w_{tcr1} = 2.0 mm \tag{4.3d}$$

Where E_0 is an initial elastic modulus, f_t is a tensile strength, w_t is a crack opening displacement, w_{tcr1} is the critical crack opening displacement, w_{tcr2} is the crack opening displacement at the complete release of stress, G_f is the fracture energy, and α and β are the strength reduction coefficient. In this model, β=0.5α and w_{tcr1}=1.0 mm are adopted.

4.5.3 Analysis results
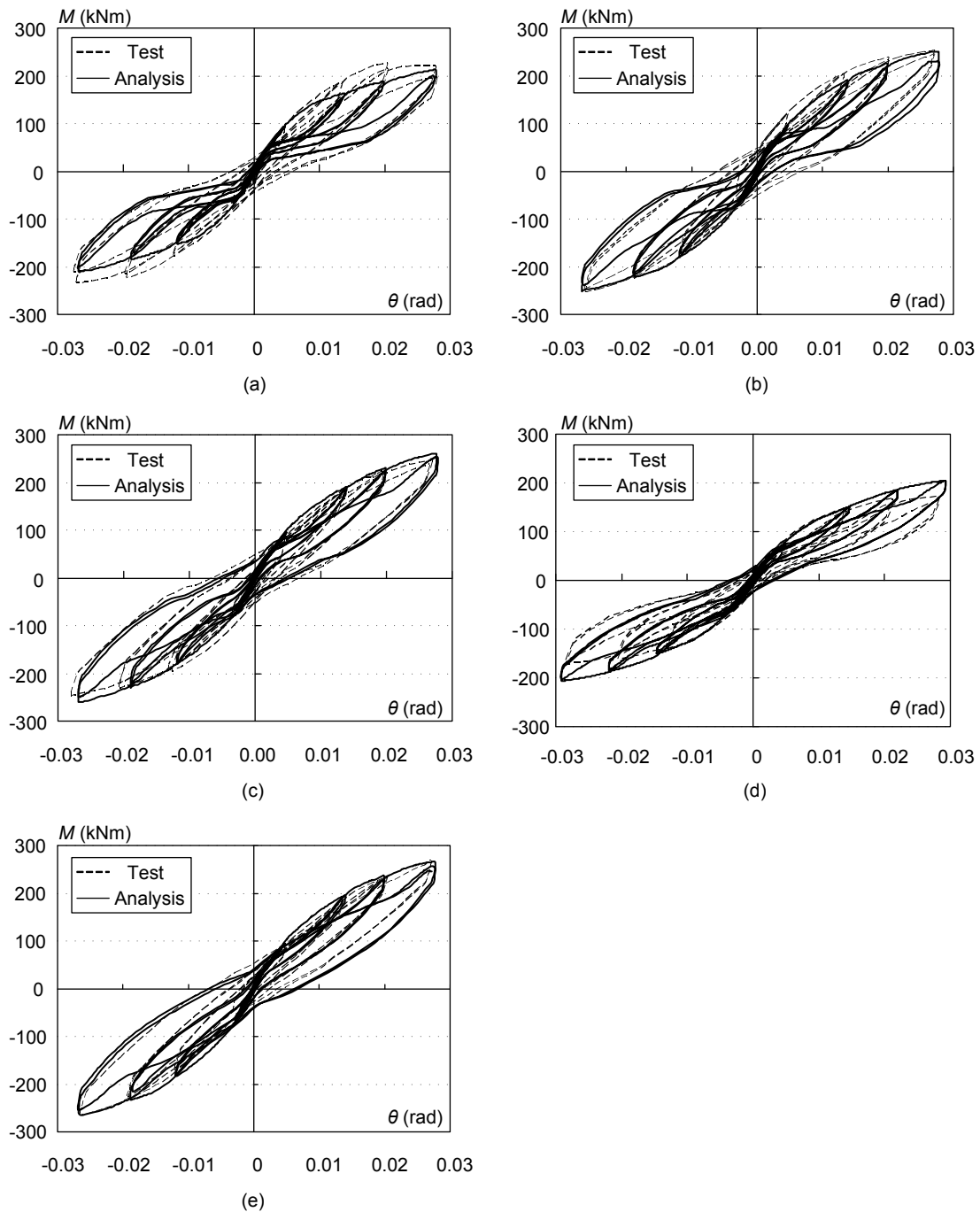
Fig. 4. 21 Comparison of moment-rotation curves:
(a) SS; (B) SR13; (c) SR785; (d) CR785 and (e) SR19

Figure 4.21 shows the relationships between the column base bending moment and rotation angle for all specimens, plotting the curves from the amplitudes of 0.005 to 0.03 for cyclic loading. In these analyses, slip behavior is traced very reasonably. The slip caused by the separation between the nut of anchor bolts and base plate was successfully reproduced. It is notable that the pinching of hysteresis curves is reduced by the presence of rebars. In addition, the degree of pinching reduced varied with respect to the amount of the rebars.

The experimental and analytical elastic stiffness and maximum strength are compared in Fig. 4.22 and Fig. 4.23, respectively. The difference in the elastic stiffness is about 3% for SFRCC specimens and 10% for Specimen 'CR785'. The analytical results proved that the elastic stiffness depends on the slab thickness, and the rebars has little contribution. The difference in the maximum strength is around 2% for SFRCC specimens expect for Specimen 'CR785'. The specimens with high strength bars, i.e. Specimens 'SR785' and 'CR785', exhibited about 15% difference between the experimental and analytical results. It is speculated that the interaction between slab and high strength rebars was not considered in the analysis model.
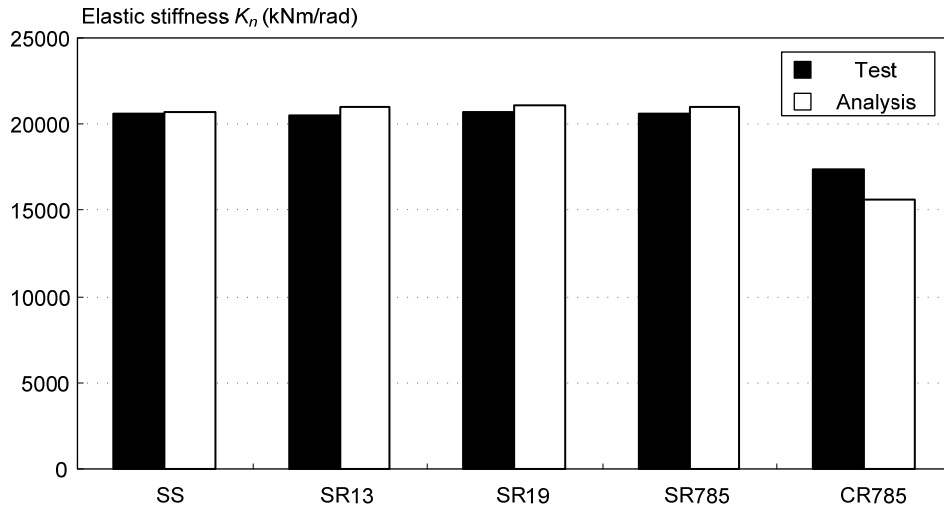
Fig. 4. 22 Comparison of elastic stiffness
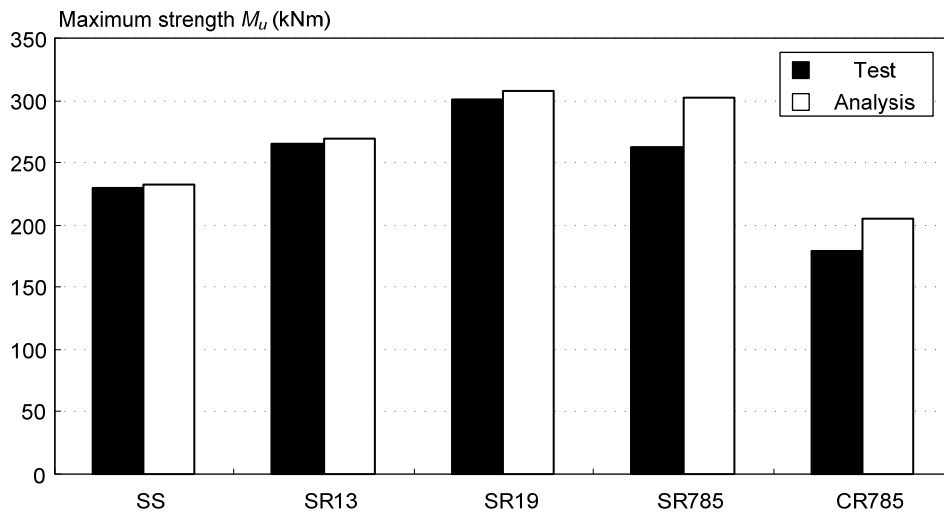
Fig. 4. 23 Comparison of maximum strength

As observed in the tests, the SFRCC specimens showed smaller failure region compared with the concrete specimens, as shown in the pictures of Fig.4.24. The same observation was also duplicated in the numerical analysis. Fig. 4.24 shows Specimens 'SR785' and 'CR785' in the deformation after the 0.03rad drift angle loading, with the contours of the maximum principal plastic strain (PE) distribution. The failure regions are marked in white, where the tensile strain is

larger than 0.03% and 0.3% for concrete and SFRCC, respectively. It should be noted that the failure region for the SFRCC specimen is obviously smaller than the corresponding concrete specimen. It is mainly because that the tensile strain of SFRCC is 10 times larger of concrete tensile strain. Therefore, the concrete slab failed earlier and its failure region propagated more significantly in comparison with SFRCC slab.

(a)   (b)
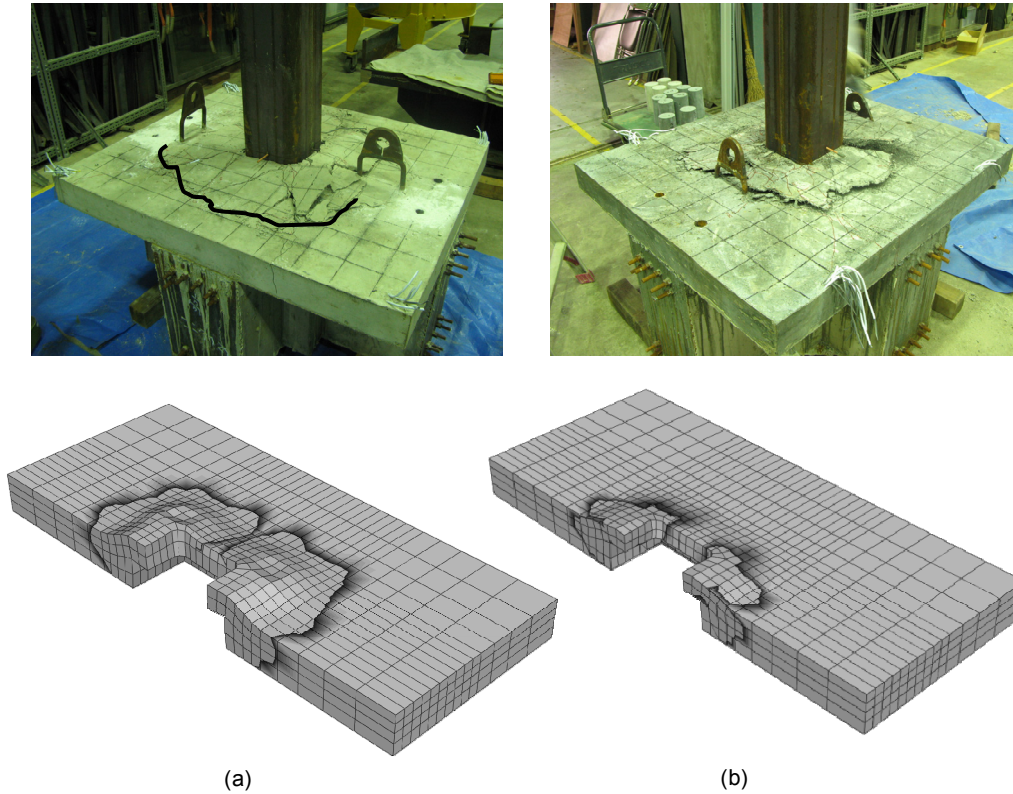
Fig. 4. 24 Failure region obtained from experiment and analysis: (a) CR785; (b) SR785

4.6 Evaluation of Elastic Stiffness

An evaluation procedure for the elastic stiffness of shallowly embedded column bases with concrete slab was proposed in Chapter 2. The mechanism model for this evaluation is shown in Fig. 4.25. Here workability of this evaluation procedure is calibrated for shallowly embedded column bases with SFRCC slab based on the test results and the numerical parametric analysis results.

4.6.1   Evaluation method

The stiffness from the anchor bolts, K_{AB}, is calculated following the AIJ guidebook (AIJ 2006).

$$K_{AB} = \frac{E \cdot n_t \cdot A \cdot (d_c + d_t)^2}{2l_b} \qquad (4.4)$$

Where E is Young's Modulus of anchor bolts (205,000 N/mm^2); n_t is the number of anchor bolts in the tension side (6); A is the section area of anchor bolts (113.1mm^2); d_c is the horizontal distance (100 mm) from the centroid of the column section to the edge of column section in compression side;

d_t is the horizontal distance (103.3 mm) from the centroid of column section to the centroid of the group of anchor bolts in tension side; l_b is the length of anchor bolts (250 mm).

Fig. 4. 25 Mechanism model for elastic stiffness evaluation

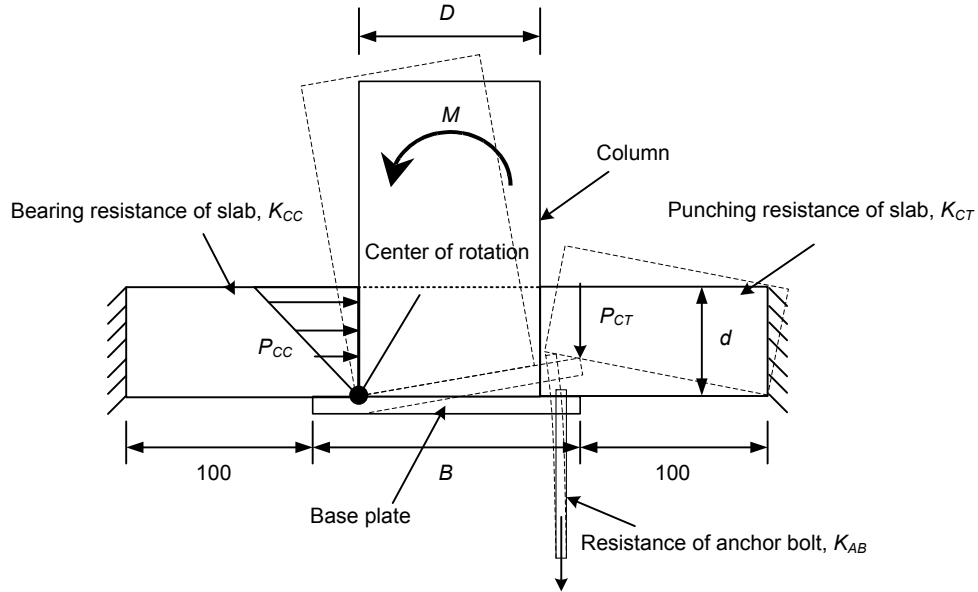The stiffness contributed from the bearing resistance in the slab compressive region, K_{CC}, is

$$K_{CC} = \frac{E_c \cdot D \cdot d^3}{3[100 + (B - D)/2]} \tag{4.5}$$

Where E_c is Young's Modulus of concrete (23,103 N/mm^2), D is the width of the column section (200 mm), d is measured from the top surface of the base plate to the surface of the covering slab (45 mm), and B is the length of the base plate (300 mm).

The stiffness contributed from the punching resistance in the slab punching region, K_{CT}, is

$$K_{CT} = \frac{\left(D + \frac{B - D}{2}\right)^2 \cdot 3E_c}{100^3} \frac{D \cdot d^3}{12} \tag{4.6}$$

The three part of resistance act in parallel, the fixity against rotation of the base plate connection is

$$_{sta}K_{is} = K_{AB} + K_{CC} + K_{CT} \tag{4.7}$$

The rotated stiffness of the column which portion is above the floor slab is

$$K_c = \frac{3E_s I_c}{L_{fix}} \tag{4.8}$$

Where L_{fix} is the distance from the top of the column to the top surface of floor slab, I_c is the moment of inertia of column section, and E_s is Young's Modulus of steel (205,000 N/mm^2).

The initial stiffness without the axial force, K_0, is calculated by considering the stiffness of the base plate connection, in which the three components, i.e. anchor bolts, bearing portion of slab, and punching portion of slab, acted in parallel, and the rotated stiffness of the column acted in series.

$$K_0 = \cfrac{1}{\cfrac{1}{{}_{sta}K_{is}} + \cfrac{1}{K_c}} \left(= \cfrac{1}{\cfrac{1}{K_{AB} + K_{CC} + K_{CT}} + \cfrac{1}{K_c}} \right) \qquad (4.9)$$

When the axial force is applied, the detachment of column base would occur for some shallowly embedded column base. By considering the detachment phenomena, the contribution of axial force was included.

The detached rotation is calculated as follows.

$$\theta = \frac{NwL_c}{3E_s I_c} \qquad (4.10)$$

where N is the applied axial force (511 kN), L_c is the height of column (1228.5 mm), w is the distance from the center of rotation to the centroid of the column (100 mm), I_c is the moment of inertia of the column section (49,800,000 mm^4), and E_s is Young's Modulus of steel (205,000 N/mm^2).

The rotated stiffness of the column is

$$_{axial}K = \frac{3E_s I_c}{L_c} \qquad (4.11)$$

The elastic stiffness of shallowly embedded column bases in consideration of the contribution of axial force, K_n, is estimated as:

a) When the detachment occurred ($K_0 < {}_{axial}K$)

$$K_n = \frac{{}_{axial}K \cdot \theta + K_0 \cdot (0.005 - \theta)}{0.005} \qquad (4.12a)$$

b) When the detachment did not occurr ($K_0 \geq {}_{axial}K$)

$$K_n = K_0 \qquad (4.12b)$$

4.6.2   Verification

The estimated elastic stiffnesses are compared with the corresponding experimental results (shown as black bars) in Fig. 4.26. The proposed equations provide reasonable estimate of the elastic stiffness. The difference between the corresponding experimental elastic stiffness is around 10%. As discussed previously, the elastic stiffness varies only with the thickness of the floor slab, and the rebars do not contribute the elastic stiffness. The same tendency has also been observed by the numerical parametric analysis.

The influence of floor slab thickness is presented in Fig. 4.27. The abscissa is the ratio between the floor slab thickness and the column section, t/D. The ordinate is the ratio of the elastic stiffness of the shallowly embedded column base to that of the corresponding embedded column base (see Fig.3.34), $K_n/{}_{emb}K$. The effect of concrete and SFRCC slab are shown as well. The effect of the floor slab thickness exhibits the same tendency between the evaluation and analysis. However, the evaluation does not clearly reflect the effect of the different material of slab (concrete and SFRCC). The simplified evaluation procedure of elastic stiffness proposed in Chapter 2 is adopted here.

$$K_n = \alpha \cdot {}_{emb}K \qquad (4.13)$$

According to the analysis results, the coefficient α for the SFRCC floor slab is given in Table 4.7. For the design application, the coefficient α is suggested not greater than 1.0, in which the elastic stiffness of the shallowly embedded column base is considered the same as that of the corresponding embedded column base (see Fig.3.34). Therefore, for shallowly embedded column bases with SFRCC slab, the elastic stiffness is recommended as the same elastic stiffness of the corresponding embedded column base when the slab thickness is greater than 0.5 times the column section.

Fig.4.26 Elastic stiffness of specimen
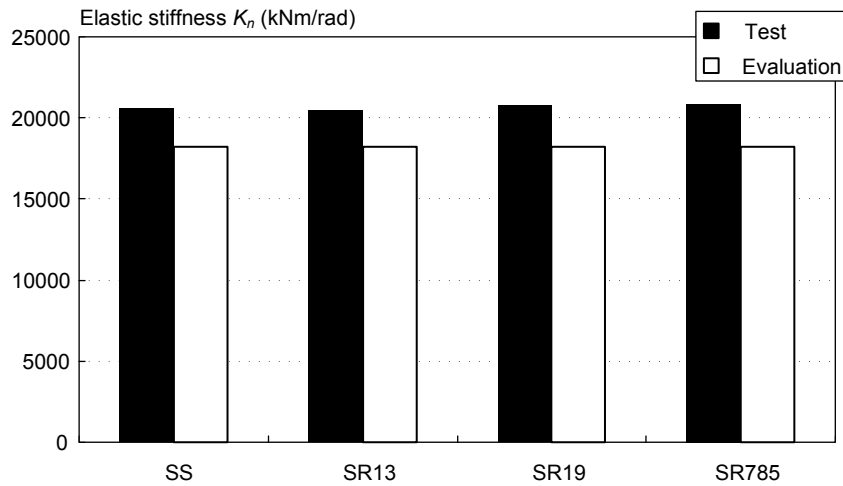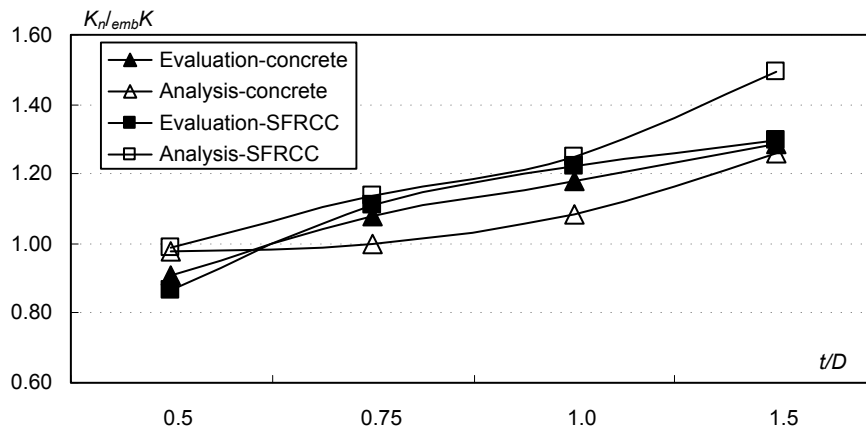
Fig.4.27 Comparisons of predicted elastic stiffness with respect to slab thickness

Table 4.7 The coefficient α ($K_n/_{emb}K$)

t/D	0.5	0.75	1.0	1.5
α	0.99	1.14	1.25	1.49

4.7 Evaluation of Maximum Resisting Moment

An evaluation procedure for the maximum resisting moment of shallowly embedded column bases

with concrete slab has been proposed in Chapter 2. Here workability of the evaluation is calibrated for shallowly embedded column bases with SFRCC slab.

4.7.1 Evaluation method

In consideration of the punching shear failure, the model consists of three parts (Fig. 4.28), i.e., 1) the exposed column base component, M_e, 2) the covering concrete slab component, M_{cc} (contribution of the bearing resistance of the floor slab) and M_{ct} (contribution of the punching resistance of the floor slab), and 3) the reinforcing bars component, M_{st}. The theory of plasticity was adopted, and the strengths of the multiple components were added to estimate the maximum strength of the shallowly embedded column base.
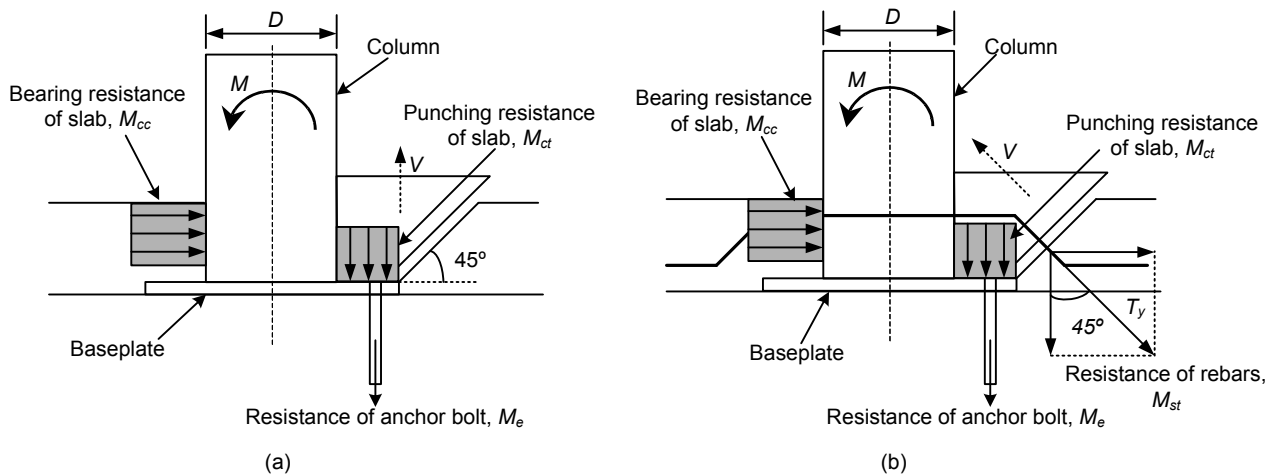
Fig. 4. 28 Mechanism model for maximum resisting moment evaluation:
(a) unreinforced slab; (b) reinforced slab

Following the procedure adopted in standard design specifications (AISC Design Guide No.1 2006; AIJ 2006), the maximum strength, M_e, is estimated as:

a) When the anchor bolts on the tension side take smaller forces than the yield strength ($N_u \geq N > N_u - T_u$)

$$M_e = (N_u - N)d_t \tag{4.14a}$$

b) When the anchor bolts on the compression side take tensile forces ($-T_u \geq N > -2T_u$)

$$M_e = (N + 2T_u)d_t \tag{4.14b}$$

c) Otherwise ($N_u - T_u \geq N > -T_u$)

$$M_e = T_u d_t + \frac{(N + T_u)B}{2}\left(1 - \frac{N + T_u}{N_u}\right) \tag{4.14c}$$

Where N is the axial force transferred by the column base; N_u is the maximum compressive strength of the concrete under the base plate, estimated as $0.85B^2 f_c'$; T_u is the maximum tensile strength of the anchor bolts acting in the tension region; f_c' is the compressive strength of concrete in the foundation. The moment resistance M_{cc} supplied by the concrete in compression is obtained by Eq. (4.11).

$$M_{cc} = \upsilon_c \cdot f_c' \cdot D \cdot 0.8d \cdot (0.6d + t_{bp}) \tag{4.15}$$

Where, t_{bp} is the thickness of the base plate (25 mm), f_c' is the compressive strength of SFRCC in the floor slab (109.6 N/mm²), and υ_c is an effectiveness factor for compressive strength of SFRCC (0.85). Here, considering SFRCC is a cementious material, which is the same as concrete, the value of υ_c was taken to be the same as that for concrete.

The moment resistance provided by the punching-shear mechanism M_{ct} is evaluated as follows.

For floor slab:

$$M_{ct} = \frac{1 - \sin 45°}{2} \cdot A \cdot \upsilon_{t\,S} f_c' \cdot D_t \tag{4.16a}$$

For strengthened floor slab:

$$M_{ct} = \frac{1 - \sin 45°}{2\cos 45°} \cdot A \cdot \upsilon_{t\,S} f_c' \cdot D_t \tag{4.16b}$$

Where D_t is the distance (125 mm) between the centroid of the column section and the centroid of the punching load.

A is the area of the punching-shear surface and calculated as

$$A = B \cdot \frac{d}{\cos 45°} + \frac{\pi}{2} \cdot \left(\frac{d}{\cos 45°}\right)^2 + (B - D) \cdot \frac{d}{\cos 45°} \tag{4.17}$$

The effective coefficient υ_t for the punching shear of concrete slab is about 0.6. As mentioned before, both SFRCC and concrete are cementious materials. Therefore, the same effective coefficient υ_t was adopted for SFRCC slab.

The contribution provided by the reinforcing bars M_{st} is evaluated as:

$$M_{st} = A_r \sigma_y \cdot \cos 45° \cdot l \cdot 8 \tag{4.18}$$

Where l is the horizontal distance (150 mm) from the centroid of the column section to reinforcing bars; A_r is the cross sectional area of reinforcing bars (127 mm² for D13 and KW785 rebars and 287 mm² for D19 rebars); and σ_y is the yield strength of reinforcing bars (373 N/mm² for D13 rebars, 373 N/mm² for KW785 rebars, and 332 N/mm² for D19 rebars).

4.7.2   Verification

The calculated maximum strengths are compared with the corresponding experimental results (shown as black bars) in Fig. 4.29. The proposed equations underestimate the maximum strength by about 30%. The influences of the floor slab thickness and rebars on the strength are compared in Fig. 4.30. The abscissa is the ratio between the floor slab thickness and the column section, t/D. As shown in Fig. 4.30, the evaluation underestimates the maximum strength and the difference ranging from 40% to 10%. The difference is reduced as the slab thickness increases. The contribution of floor slab is likely underestimated for the SFRCC slabs. To improve the estimate, a modified procedure is presented in the next section.
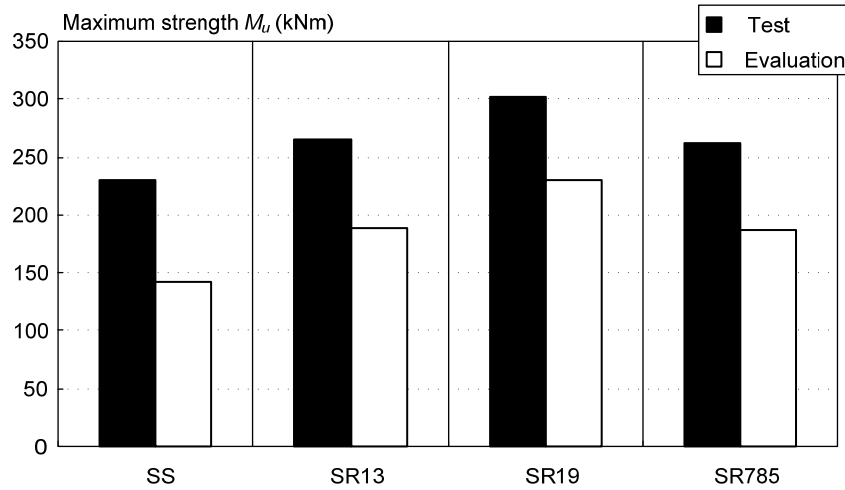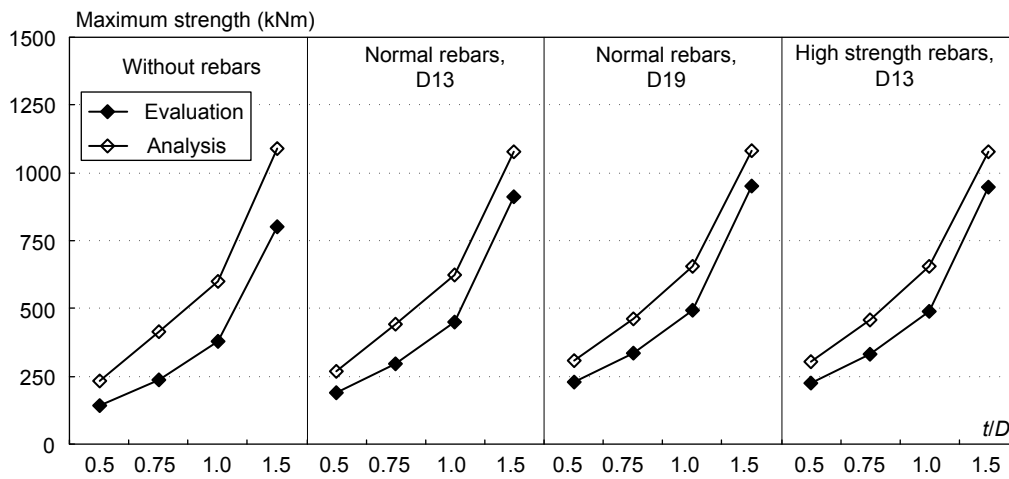
Fig.4.29 Maximum strength of specimen

Fig.4.30 Comparisons of predicted maximum strength with respect to slab thickness

4.7.3   Revised evaluation for SFRCC slab

As discussed in the beginning of this chapter, SFRCC shows better tensile behavior than conventional concrete. The tensile strength of concrete is commonly neglected in the design practice. Considering the high tensile strength and tensile strain at the peak tensile stress of SFRCC, the contribution of tensile behavior was included in the revised evaluation for SFRCC slab. On the other hand, since large amount of steel fibers was adopted in this test, the contribution of steel fibers should also be counted. In the revised evaluation, contribution of steel fibers is considered to be the same as that of the rebars. In the revised evaluation, contribution of the punching resistance of the floor slab, M_{ct}, is modified as follows.

Because of the presence of steel fibers and rebars, the direction of velocity of punching region is taken to be perpendicular upward to the punching-shear surface (see Fig. 2.9 (d) for details). The work equation for the assumed failure mechanism is:

$$Q \cdot V \cdot \cos 45° = (\frac{1-\sin 45°}{2} \cdot f_c' + \frac{\sin 45° - \sin \phi}{1-\sin \phi} \cdot f_t) \cdot \upsilon_t \cdot A \cdot V \qquad (4.19a)$$

4 - 30

Where φ is the angle of friction of SFRCC (37˚), and f_t is the tensile strength of SFRCC in the floor slab (11.5 N/mm²)

Assuming that the punching load caused by the base plate be distributed uniformly, the moment resistance provided by the punching-shear mechanism is evaluated as:

$$M_{ct} = (\frac{1-\sin 45°}{2} f_c' + \frac{\sin 45° - \sin \phi}{1-\sin \phi} f_t') \cdot \upsilon_t \cdot A \cdot D_t \qquad (4.19b)$$

The revised evaluated maximum strengths are compared with the corresponding experimental results (shown as black bars) in Fig. 4.31. The difference between the corresponding experimental maximum strength is reduced to not greater than 20%.
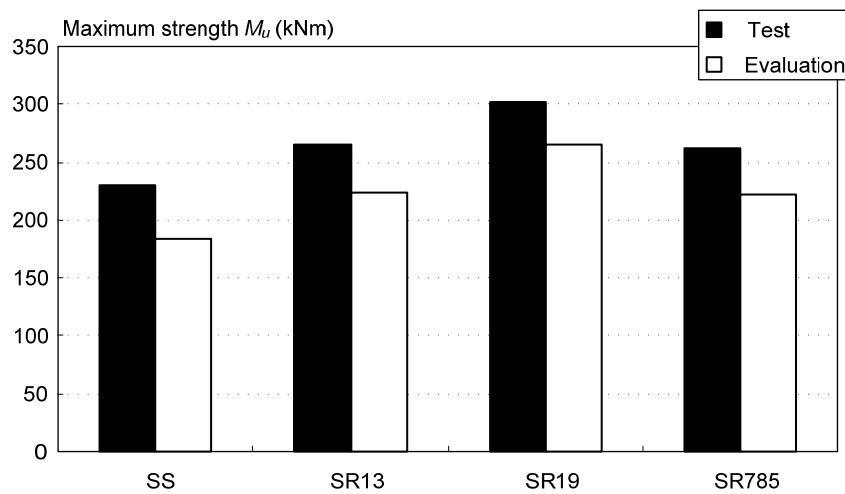
Fig.4.31 Maximum strength of specimen

The revised evaluated results are compared with analysis results in Fig. 4.31. The abscissa is the ratio between the floor slab thickness and the column section, t/D. The evaluation agrees with the numerical results very reasonably for all the cases. Although the revised evaluation provides larger maximum strength than the analysis results when the slab thickness is 1.5D, the difference is still less than 20%.
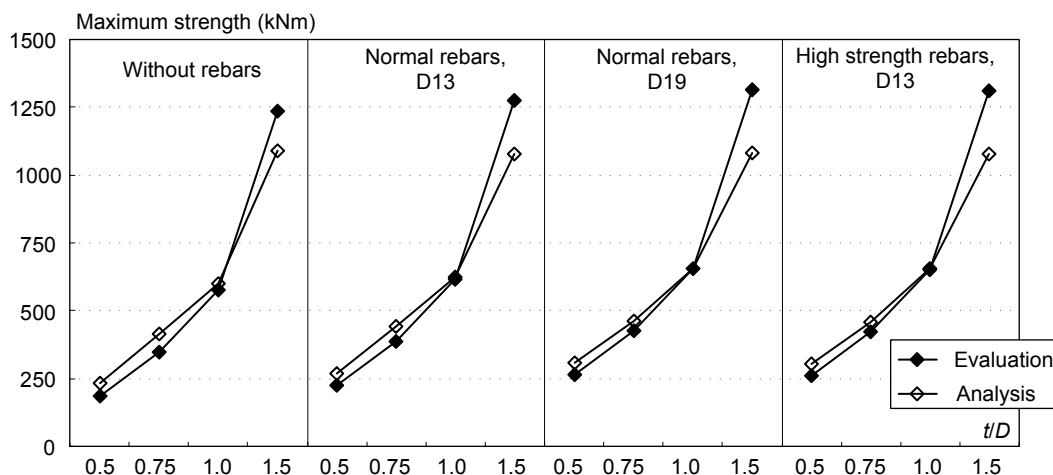
Fig.4.32 Comparisons of revised predicted maximum strength with respect to slab thickness

4 - 31

4.8 Conclusions

A series of tests were conducted for shallowly embedded steel column bases with SFRCC floor slab. Major findings obtained from the tests are summarized as follows:

(1) The elastic stiffness, maximum strength and energy dissipation of shallowly embedded column bases were improved by 40%, 70%, and 70%, respectively, by using SFRCC instead of conventional concrete in the presence of the floor slab but without horizontal rebars.

(2) With horizontal rebars, the maximum strength was further improved by 15% to 30%, and the strength deteriorated more gradually. As a result, energy dissipation of reinforced SFRCC specimens increased to about two times. The improvement was achieved even when the rebars were closely arranged and covered with SFRCC of a small thickness.

(3) Contribution of high strength rebars to the performance was primarily toward the improvement of ductility, because the rebars yielded after large deformation. On the contrary, application of large size normal rebars was more effective to improve both the maximum strength and energy dissipation.

The experimental study provided fundamental information on the behavior of shallowly embedded column bases featured with SFRCC floor slab. A separate numerical study using FEM was conducted to reproduce the test results and quantify the effects of various parameters such as the slab thickness and rebars on the elastic stiffness and maximum strength.

(1) By the application of the damaged plasticity model, the cyclic behavior of SFRCC is simulated reasonably.

(2) The maximum strength and stiffness obtained from the analyses agree with the test results within a 20% difference. The failure region is also estimated successfully from the analysis.

(3) The elastic stiffness of shallowly embedded column bases is essentially controlled by the slab thickness. A simplified equation is proposed to assess the elastic stiffness as a fraction of the corresponding elastic stiffness of fully embedded column bases.

(4) Considering the material characteristics of SFRCC, the proposed equation to evaluate the maximum strength is revised for SFRCC slabs. The contribution in the tensile behavior is included in the revised evaluation of the punching resistance portion. The revised equation provides values within 20% errors with respect to the analytical results.

REFERENCES

[4.1]   Architectural Institute of Japan (AIJ). (2006). Recommendations for design of connections in steel structures, Tokyo (in Japanese).

[4.2]   Architectural Institute of Japan (AIJ). (2006). Recommendations for Design of Connections in Steel Structures, Tokyo.

[4.3]   Architectural Institute of Japan (AIJ). (1990). "Design guidelines for earthquake resistant reinforced concrete buildings based on ultimate strength concept." Tokyo.

[4.4] Architectural Institute of Japan (AIJ). (2005). "Design standard for steel structures- based on allowable stress concept." Tokyo.

[4.5] Bache, H. H. (1981). "Densified Cement/Ultrafine Particle-Based Materials." Presented at Second International Conference on Superplasticizers in Concrete, Ottawa, Canada.

[4.6] Bache, H. H. (1981). "Densified Cement Ultra-fine Particle-based Materials." CBL Report No.40, Aalborg Portland.

[4.7] Bache, H. H. (1987). "High-strength Concrete Development through 25 Years." CBL Report No.17, Aalborg Portland.

[4.8] Bache, H. H. (1987). "Compact Reinforced Composite, Basic Principles." CBL Report No.41, Aalborg Portland.

[4.9] Elfgren. L. (1989). Fracture Mechanics of Concrete Structures - From theory to application. Chapman and Hall, London.

[4.10] Fisher, J. M. and Kloiber, L. A. (2006). "Base plate and anchor rod design (Second edition)." Steel Design Guide Series No. 1, AISC, Chicago.

[4.11] Gert, Heshe. (1998). "Experimental Research on Compact Reinforced Composite (CRC) Beams." CBL Report No. 19, Aalborg Portland.

[4.12] Hillerbog, A., Modeer, M., and Peterson, P.E., (1976). "Analysis of Crack Formation and Crack Growth in Concrete by Means of Fracture Mechanics and Finite Elements." Cement and Concrete Research, Vol. 6, 773-782.

[4.13] Kaneko Y., Mihashi H., and Kirikoshi K. (2001). "Mechanical Properties and Application of Steel Fiber Reinforced Cementitious Composite." Cement Science and Concrete Technology, Vol. 54, 723-730.

[4.14] Kaneko Y., Mihashi H., Kirikoshi K., and Abe T. (2001). "New Application Field of Steel Fiber Reinforced Cementitious Composites – Experiment on column-beam joint in steel structures." Journal of architecture and building science, Vol. 116, No.1481, 119-122.

[4.15] Kaneko Y., Mihashi H., Kirikoshi K., and Abe T. (2002). "Simple Column-Beam Joint of Steel Structures Employing Steel Fiber Reinforced Cementitious Composite: Experimental verification on structural performance of joint." Journal of structural and construction engineering (Transactions of AIJ), No.558, 219-225.

[4.16] Kaneko Y., Mihashi H., Kirikoshi K., and Suwanai Y. (2006). "Simple Column Base System of Steel Strucutres Employing Steel Fiber Reinforced Cementitious Composite: Experiment on structural performance of basic model and applied model." Journal of structural and construction engineering (Transactions of AIJ), No.600, 179-186. (in Japanese).

[4.17] Kaneko Y., Mihashi H., and Osaku R. (2006). "Column Base System of Steel Structures employing Steel Fiber Reinforced Cementitious Composite and Deformation characteristics: Evaluation of joint-deformation based on mechanical model for shear failure." Journal of structural and construction engineering (Transactions of AIJ), No.609, 181-188. (in Japanese).

[4.18] Karihaloo, B. L. (1995). "Fracture Mechanics & Structural Concrete." Concrete Design & Construction Series, Longman Scientific & Technical.

[4.19] Kirikoshi K., Kaneko Y., Mihashi H., and Abe T. (2000). "Material Properties of Steel

Fiber Reinforced High Strength High Ductility Cementitious Composite." Journal of architecture and building science, Vol. 115, No. 1464, 1-4.

[4.20] Lee, J., and Fenves, G. L. (1998). "Plastic-damage model for cyclic loading of concrete structures." *Journal of engineering mechanics*, ASCE, 124(8), 892-900.

[4.21] Li. V.C. (1998). "Engineered Cementitious Composites – Tailored Composites Through Micromechanical Modeling." *Fiber Reinforced Concrete: Present and the Future*, Canadian Society for Civil Engineering, Montreal, pp.64-97.

[4.22] Nielsen, Claus Vestergaard. (1995). "Ultra High-Strength Steel Fibre Reinforced Concrete – Part 1: Basic Strength Properties of Compresit Matrix", Ph.D. thesis from the Technical University of Denmark, 1995.

[4.23] Rots, J. G., Nauta, P., Kusters, G.M.A, and Blaauwendraad, J., "Smeared Crack Approach and Fracture Localization in Concrete." Heron, Vol. 30, No. 1, 1985.

[4.24] Shah, S. P., Swartz, E. S., and Ouyang, C. (1995). "Fracture Mechanics of Concrete." John Willey & Sons, Inc.

[4.25] Uemura T., Yamamoto R., Nagae T., Terada T., Suita K., and Nakashima M. (2008). "Test on Reinforced Column Bases and Plastic Deformation Capacity: Hysteretic behavior and strength capacity of shallow-embedded steel column bases Part 2." Journal of structural and construction engineering (Transactions of AIJ). Vol. 73, No.623, 111-117. (in Japanese).

[4.26] Yamamoto R., Kurata M., Nagae T., Terada T., Suita K., and Nakashima M. (2007). "Cyclic Loading Test and Strength Evaluation: Hysteretic behavior and strength capacity of shallow-embedded steel column bases Part 1." Journal of structural and construction engineering (Transactions of AIJ), No.613, 147-153. (in Japanese).

CHAPTER 5

Push-out Test on Headed Stud Connectors in Solid SFRCC Slab

5.1 Introduction

5.1.1　Background

"Composite bridges", the Rock Rapids Bridge in Rock Rapids, Iowa, made use of curved steel I-beams embedded in concrete , and "composite buildings", the Methodist Building in Pittsburgh had concrete-encased floor beams, appeared in the U.S. in the same year, 1894 (Moore 1988 and Viest 1992). Since then, the popularity of composite construction has been increasing. The steel-concrete composite construction exhibited the enormous potential in overall performance improvement of structures, such as the high stiffness and strength, inherent ductility and high constructability.
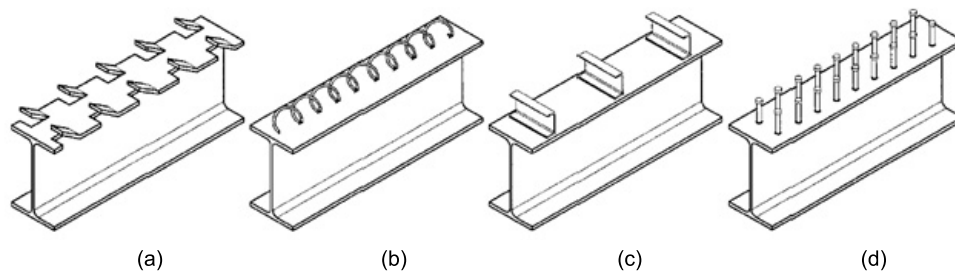

(a)　　　　　　(b)　　　　　　(c)　　　　　　(d)

Fig. 5. 1 Historical development of shear connectors:
(a) shearing tabs system, (b) spiral connectors, (c) channels, and (d) welded studs

Mechanical connectors are used to develop the composite action between steel beams and concrete. This connection is provided mainly to resist lateral shear, and is referred to as the "shear connection". Fig. 5.1 shows several types of shear connectors. The use of welded headed studs (in 1956) has gained popularity in both building and bridge structures due to the contributions of Viest (1956) on the headed stud connectors. On the other hand, it can be welded semi-automatically to the upper flange either directly in the shop or on site (Fig. 5.2). Such economic manufacturing strengthens the popularity of headed stud connectors (studs hereinafter).

The behavior and resistance of studs are commonly examined by means of the push-out tests. Two failure modes are possible, i.e., the stud failure and failure of the concrete surrounding the headed stud. The test provides a load-slip curve such as the one shown in Fig. 5.3 for the stud

failure. The behavior is characterized by a large initial stiffness and large deformations capacity to failure. Such ductile behavior makes possible the shear force redistribution at the steel beam-concrete slab interface. When the slab fractures, the concrete fractures on one side due to the stress concentration near the studs head and on the other side, the concrete is crushed due to high bearing stress of the shank of the stud. Commonly the slab fracture is avoided in design.
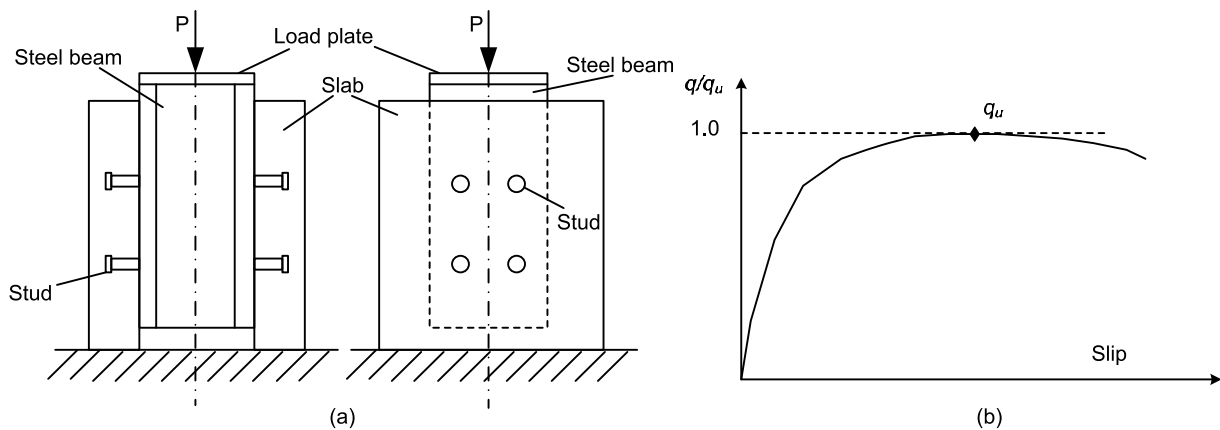

Fig. 5. 2 Welding of headed studs

Fig. 5. 3 Test on shear connectors:

(a) Push-out specimen and (b) non dimensional load-slip relationship

The design standards for shear studs in solid concrete slabs are available in AISC (2005) and other design specifications, such as AIJ (1985) and Eurocode 4 (1994), et al. These specifications associate the resistance of a stud with the failure of either the concrete, which crushes in the zone at the lower part of the stud shank, or the stud shank, which fractures directly above the weld collar under shear, flexure, and tension. Interaction between these two modes of failure is not explicitly accounted for in order to maintain design simplicity. The format of the design rules is the same among the three design specifications, although the design values of the resistances are quite different, due partly to the different philosophies on which the three codes are based and partly to the different sets of data on which the adopted strength model was calibrated. The shear resistance q_u of an individual stud is the lesser of

$$q_{u,c} = k_c A_{sc} \sqrt{f_c' E_c}$$ (5.1a)

$$q_{u,s} = k_s A_{sc} F_u$$ (5.1b)

where A_{sc}: the cross-sectional area of the stud; f_c': the concrete compressive strength; E_c: the modulus of elasticity of concrete; and F_u: the ultimate tensile strength of the stud. The AISC and AIJ specifications assume $k_c=0.5$ and $k_s=1.0$, while in Eurocode 4 $k_c=0.29$ and $k_s=0.8$.

Experimental results had proven that the height-to-diameter ratio for the stud (H_{sc}/d_{sc}) affects the resistance $q_{u,c}$: the full resistance is developed only when $H_{sc}/d_{sc} \geq 4$. All studs in the study by Ollgaard et al. (1971), on which AISC and AIJ rules are based, satisfy this requirement. The AISC and AIJ specifications apply only to studs with $H_{sc}/d_{sc} \geq 4$, even if this requirement is not explicitly stated. The European code aims at permitting use of a wider range of studs (studs with lower height may be conveniently used in shallow floor systems). Therefore, it specifies a reduction coefficient of the resistance $q_{u,c}$ expressed as $\alpha=0.2[(H_{sc}/d_{sc})+1] \leq 1$. In any case, studs with $H_{sc}/d_{sc}<3$ cannot be used. With regards to this design equation, it should be noted that these specifications also stipulate lower bounds of the applicable pitch and gage length for using the stud connectors as shown in Table 5.1.

Table 5.1 Specified minimum spacing

	Longitudinal spacing (pitch) (mm)	Transverse spacing (gage) (mm)
AISC	$6d_{sc}$ (132)	$4d_{sc}$ (88)
AIJ	$7.5d_{sc}$ (165)	$5d_{sc}$ (110)
Eurocode 4	$5d_{sc}$ (110)	$2.5d_{sc}$ (55)
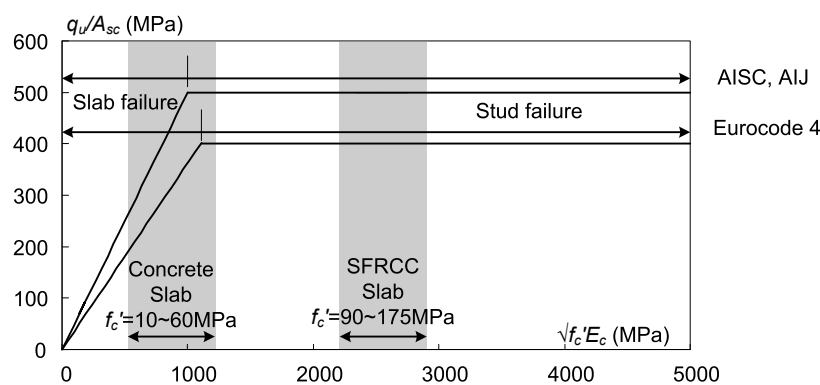
Fig. 5. 4 Nominal shear strength of one stud embedded in solid slab

According to AIJ, AISC, and Eurocode 4 formula, shown in Fig. 5.4, the studs can possess the shear capacity when the compressive strength of concrete is fairly large, more than 60 MPa, and the slab have to be reinforced sufficiently to prevent the unexpected cracks. As introduced in Chapter 4, SFRCC has larger strength in both compression and tension compared with concrete. With a

compressive strength of around 130MPa (approximately four times larger of that of normal concrete, which typically is 30 MPa) and modulus of elasticity E_c of 50GPa (approximately two times larger of that of normal concrete, which typically is 21GPa) in SFRCC, the use of this material is expected to switch the failure mode from brittle concrete slab failure to ductile steel stud shank failure in the stud connection, as shown in Fig. 5.4. Moreover, because of the large amount of steel fibers (6% in volume) in the matrix, the development of large cracks is prevented. The ductility of SFRCC was greatly improved with a tensile strain capacity of approximately 0.15% and fracture energy of 13kN/m (approximately ten times larger of magnitude value of normal concrete, which typically has corresponding value of 0.01% and 30N/m, respectively). The requirement for spacing of studs is expected to be relaxed by using SFRCC instead of concrete for the slab.

The objective of this study is to investigate the influence of material properties of SFRCC on the behavior of studs and the influence of studs spacing to the behavior of studs. Feasiblity of utilizing SFRCC to replace concrete to avoid brittle fracture failure is also examined. The results presented and discussed herein serve as a prelude of the new beam-column connection test detailed in Chapter 6.

5.1.2   Organization

The chapter consists of two parts. The push-out tests presented in the first part provide a basis to understand the overall behavior of the headed stud connectors in the solid SFRCC slabs, e.g. the load-slip curve, shear capacity, and failure mode. The effect of the number and layout of studs is discussed. The second part presents the numerical analysis conducted by ABAQUS. The numerical model is calibrated against the test results, and then a series of parametric analysis are conducted based on the numerical model. Based on the analytical simulation, the effect of stud arrangement and transverse rebars to the behavior of the studs are discussed.

5.2 Solid SFRCC Slab Push-out Tests

5.2.1   Test specimens

Four specimens were tested with the global dimensions as shown in Fig. 5.5. Each specimen consists of two concrete slabs, each of which is connected to a 500 mm long structural tee in which headed shear studs are welded. Slabs are 300 mm by 500 mm, and with 130 mm thickness. Each slab is casted horizontally, locating the shear studs in a vertical position. After the SFRCC was placed in the forms, it was vibrated with a mechanical vibrator. SFRCC test cylinders were cast along with the specimens and cured in the same condition. The push-out specimen halves were then bolted through the webs to form a solid slab push-out specimen, which is shown in Fig. 5.5(a). The specimens were tested around 28 days after being cast. The average properties of the cylinders that correspond to the push-out specimen are listed in Table 5.2. This includes the SFRCC compressive strength, $f_c{}'$, the split tensile strength, $f_{sp}{}'$. It is notable that the slabs were cast without any rebars.
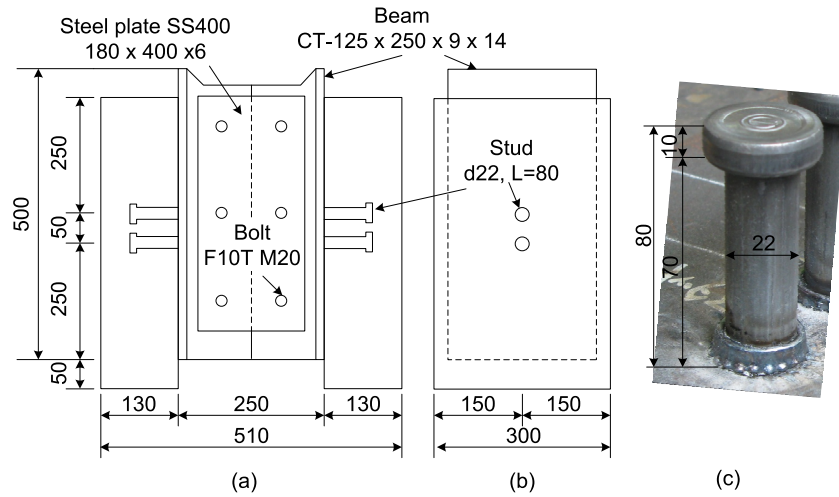
Fig. 5. 5 Details of specimen:
(a) Front view; (b) Elevation view; and (c) stud (unit: mm)

All studs were welded to the steel beam on the same level, and located symmetrically with respect to both vertical axes of beam symmetry. An equal number of studs were embedded in each slab. Headed stud connectors of 22 mm diameter and 80 mm height, as shown in Fig. 5.5 (a), were used for all specimens. The stud with 22 mm diameter is currently the largest studs available for composite slab in Japan. It is expected to transfer the most shear force in SFRCC slab among various sizes of stud. As mentioned previously, the push-out test is a prelude to the following new beam-column connection test. In the new beam-column connection, the studs are welded closely on the beam flange. Therefore, the spacing, the center-to-center distance of the studs, was set as 50 mm, which is the minimum spacing to allow the stud welding without trouble. It is notable that the spacing was smaller than the requirements for concrete slab in the Specifications, as suggested in Table 5.1. In comparison with the requirement of AIJ (1985), the spacing of the studs in this test is 70% and 55% smaller than the required longitudinal and transverse spacing, respectively.
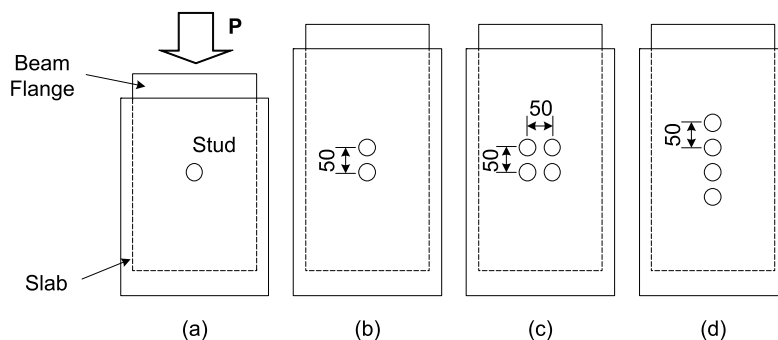

Fig. 5. 6 Layout of studs:
(a) 1S; (b) 2P50; (c) 4PG50; and (d) 4P50 (unit: mm)

The number (one to four) and layout of studs were designed as the test parameters, as illustrated in Fig. 5.6. Specimen '1S', one stud for each side beam flange, was designed as the baseline

5 - 5

specimen to investigate the basic behavior of the stud in SFRCC slab. The other specimens were designed to investigate the group effect, i.e., the longitudinal spacing, transverse spacing and the number of studs. Two and four studs were longitudinally welded on each beam flange for Specimens '2P50' and '4P50', respectively, to investigate the effect of the longitudinal spacing and the number of the studs. In Specimen '4PG50', four studs were welded on each beam flange with an array of two by two to investigate the transverse spacing effect.

Table 5.2 Material properties of SFRCC

Spec.	Compressive strength f_c' (MPa)	Split strength f_{sp}' (MPa)
1S	118.53	18.40
2P50	132.40	20.05
4P50	126.32	17.85
4PG50	129.04	17.27

5.2.2　Test setup

Test was conducted on a 2MN capacity universal machine, as shown in Fig. 5.7. The load was applied by the head of the machine first to a 40mm thick steel plate, placed on the upper end on the beams. The web at the top end (where contacted the load plate) of each half of the beams was cut as shown in Fig. 5.5(a), so that forces would be transferred only to the flange of steel members. The specimen was placed on a layer of mortar, and thin steel strips were inserted into the gap between the steel plate and the flanges in order to achieve a uniform load distribution both in the slab and steel. Four linear variable displacement transducers (LVDTs) were used to measure the slip between the beam and the slabs, as indicated in Fig. 5.7. These devices were fixed on the steel flange at the elevation corresponding to the middle of the stud group, while the head of the LVDT was attached to an acrylic resin plate glued onto the surface of the slab at the same elevation. An average value taken from the four values measured by LVDTs was defined as the slip between the slab and steel flange.
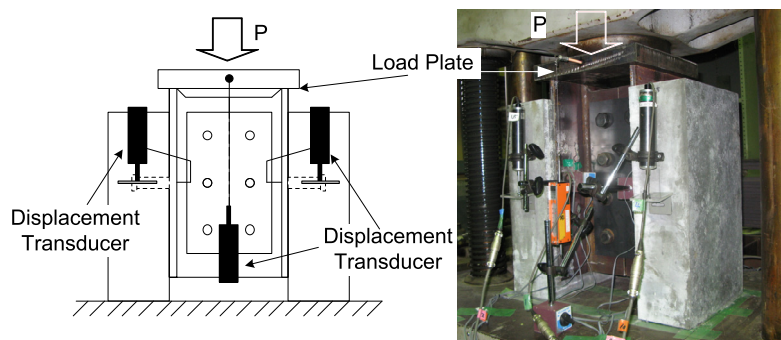

Fig. 5. 7 Setup of push-out tests

5.2.3 Test results

Load-slip curves of all specimens are compared in Fig. 5.8 and a summary of the tests are presented in Table 5.3. The slip reported was the average of four transducers attached to each specimen. The reported loads are the total loads applied to the push-out specimen divided by the corresponding number of studs. As shown in Fig. 5.9, the slip stiffness K_{sc} is defined as the secant modulus at 65% of the ultimate load q_u, and yield strength q_y is defined as the load with respect to the slip determined by the intersection between the ultimate load q_u and the slip stiffness K_{sc}.

Table 5.3 Test Results

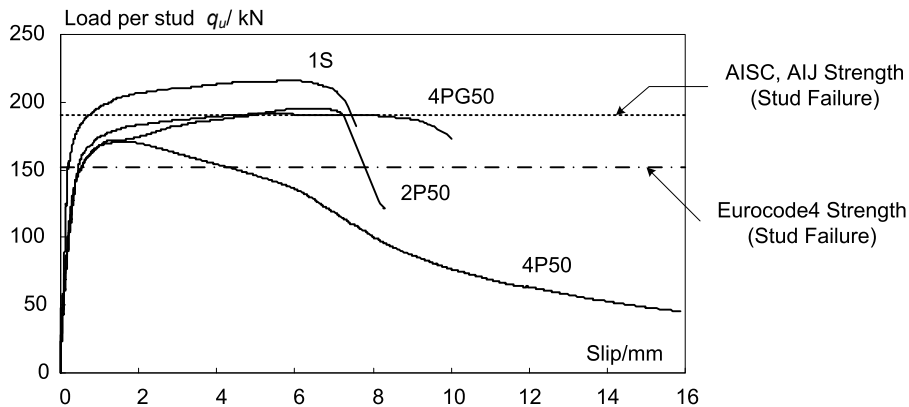| Spec.	Slip stiffness K_{sc} (kN/mm)	Yield load per stud q_y (kN)	Ultimate load per stud q_u (kN)	Slip of fracture (mm)	Failure Mode
1S	1084	156.0	216.7	7.56	Stud fracture
2P50	479	149.4	195.5	7.24	Stud fracture
4PG50	468	154.7	191.9	10.01	Stud fracture
4P50	463	140.8	170.9	1.64	Slab split

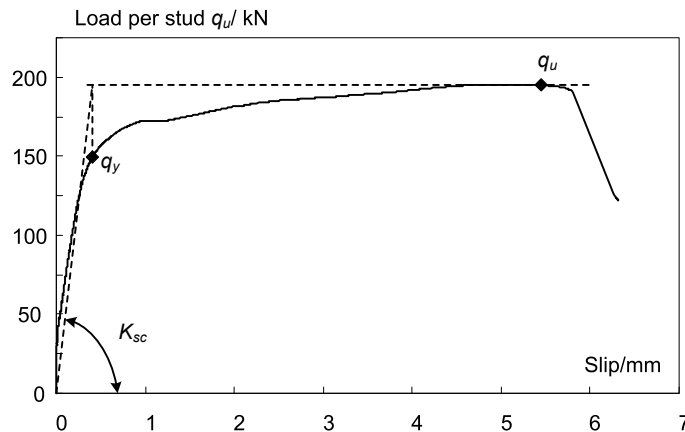Fig. 5. 8 Load-slip curves

Fig. 5. 9 Definition of slip stiffness, yield load and ultimate load

As indicated in Fig. 5.8 and Table 5.3, Specimen '1S' showed the largest slip stiffness. The slip stiffness of the other three specimens (Specimens '2P50', '4PG50', and '4P50') are almost the same with differences of about 1%. The yield strength per stud of the four specimens was similar with about 5% difference. The ultimate loads per stud varied as the number and layout of studs changed. Specimen '4P50' showed the smallest ultimate strength, which is 80% that of Specimen '1S', since the governing failure was slab failure rather than stud failure. For Specimen '1S', in which the longitudinal and transverse spacing was infinite, the AIJ, AISC, and Eurocode 4 formulas correctly predicted that the governing failure is stud failure. From Fig. 5.8, the AIJ and AISC formula for the stud shear capacity when the stud failure governs better fits the experimental results compared with the Eurocode 4 formula, for which the assessment provided the value close to the measured yield strength. However, since the influence of longitudinal and transverse spacing was not counted in, these formulas could not provide correct prediction for Specimen '4P50', in which the failure occurred in the slab opposite to the predicted stud failure.

Failure Mode

As indicated in Table 5.3, two failure modes were observed. Specimen '4P50' failed by the slab split (Fig. 5.10), while the other specimens failed by shear fracture of studs (Fig. 5.11).

The slab failure of Specimen '4P50' is presented in Fig. 5.10. The arrows with load *P* in Fig. 5.10 represent the direction of the force transferred from the flange. The slab was split, and the studs remained connected to the steel beams, although the studs were bent seriously. Cracks were initially observed at the location at the lower end of the slab right underneath the studs, which eventually developed to completely split the SFRCC slab along the studs. Bending deformation of the studs was larger than any that occurred in the other specimens. The stud transmitted different loads at the same slip level since the deformation of each stud was different and the deformation of the front stud was the largest among all the studs. On the initial loading of the specimen, the studs followed typical load-slip paths of the other specimens failed in studs, as shown in Fig. 5.8. Splitting of the slab caused a very rapid reduction in load in the specimen. The failures occurred at an absolute slip of 1.64 mm, where the load started dropping, and the split cracks started propagating.

Fig. 5.11 shows that the two studs embedded in one slab sheared off. The other slab was still connected to the steel beam. The failure surface was located in the stud shank directly adjacent to the weld flush. There are no visible cracks in the slab. The slab bearing surface in front of the stud was locally crushed, with a "powdery" appearance. A void pocket behind the stud was created; this void represented the original location of the stud when the slab was cast. After testing, the specimens that failed by fracture of studs were sawed along in the center line, and the cut surfaces are shown in Fig. 5.11(c). It is observed that both studs remained upright against the flange. The photo also indicates that the studs did not shear off at the same slip levels since the gaps between the studs and the slab are not the same (Fig. 5.11 (a)) and the local deformation (Fig. 5.11 (c)) of the rear stud is more significant than the front stud. At an average slip of approximately 1.5 mm, there began a plateau in load resistance as the studs yielded and underwent plastic deformations, as shown in Fig.5.8. At an average slip of 7 mm, the first stud fracture occurred, where the load suddenly

dropped. The plateau of the load-slip curves evidenced the stud failed in a ductile failure. However, Specimen '4PG50' showed larger slip of 10 mm when the first stud fracture occurred. The reason will be discussed later.
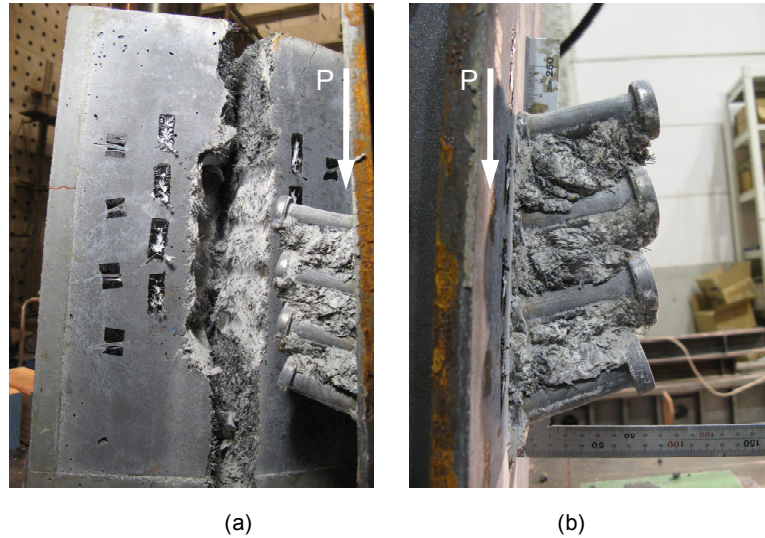

(a)   (b)

Fig. 5. 10 Detail of specimen failed in the slab: (a) slab side; (b) beam side
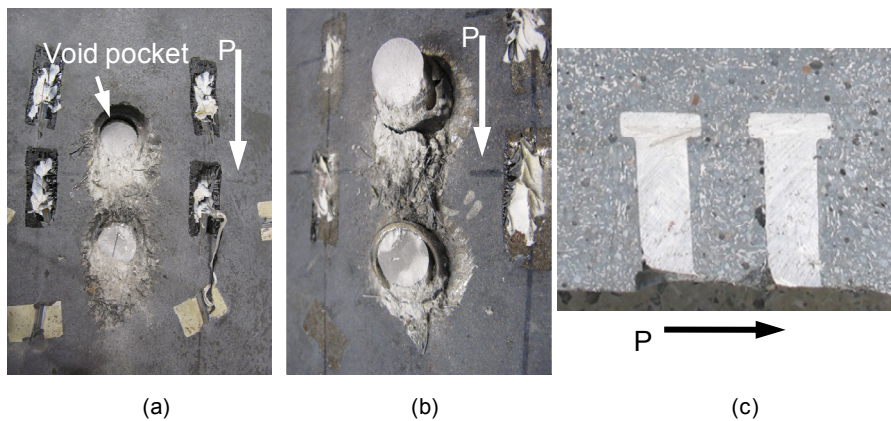

(a)   (b)   (c)

Fig. 5. 11 Detail of specimen failed in the stud:
(a) slab side; (b) beam side; and (c) sawed section

5.2.4   Analysis of results

Effect of stud number (1S, 2P50, 4P50)

Three specimens, Specimens '1S', '2P50', and '4P50', were designed to investigate the effect of the stud number. The studs are welded along the loading direction on the beam flange with the spacing of 50 mm. The number of studs was one, two and four for each specimen. According to the test results, the ultimate load per stud was reduced by 90% and 80% as the number of studs increased to two and four, respectively. The failure mode varied from stud fracture to slab split when the number of studs for each slab was four. The failure region in the SFRCC slab is shown in Fig. 5.12 for the three specimens. It is notable that the crushing portion in front of the stud is connected for Specimen '2P50', and the slab of Specimen '4P50' is split. For Specimen '2P50', since the

5 - 9

resistance of slab in front of the rear stud was weakened by the front one, as shown in Fig. 5.12 (b), the fixity of the rear stud appear to have loosened. Therefore, the ability of the stud to transfer longitudinal load was reduced. When the number of studs increased to four, since the split resistance of the SFRCC slab was not greater than the transferred longitudinal load from the stud, the slab failure occurred prior to the stud failure, as shown in Fig. 5.12(c).
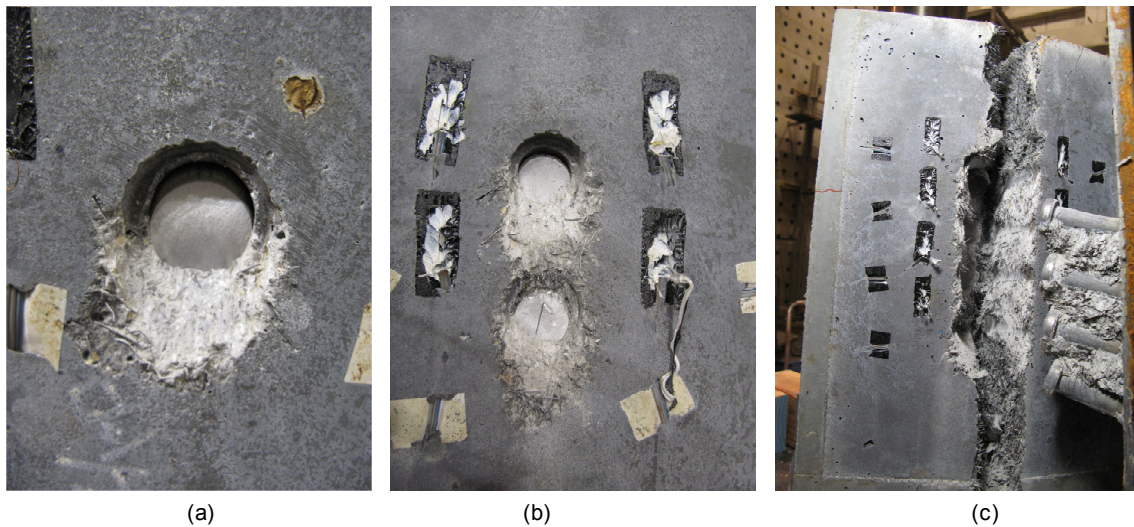

<div align="center">(a)   (b)   (c)</div>

Fig. 5. 12 Failure region in the SFRCC slab: (a) 1S; (b) 2P50; and (c) 4P50

Effect of stud spacing (2P50, 4PG50)

Specimens '2P50' and '4PG50' failed in stud fracture. As observed in the test, no crack on the slab was formed for Specimen '2P50', while a transverse crack was formed behind the rear two studs in the slab of Specimen '4PG50', as shown in Fig. 5.13. Therefore, the slip at the ultimate strength of Specimen '4PG50' is larger than Specimen '2P50'. As shown in Fig. 5.8 and Table 5.3, the ultimate load per stud of Specimen '4PG50' is nearly identical with that of Specimen '2P50'. Note that the ultimate strength per stud was 10% smaller in Specimens '2P50' and '4PG50' than in Specimen '1S'. The same reason of the reduction as Specimen '2P50' can be evidenced in Fig. 5.13. It can be concluded that the longitudinal spacing has significant effect on the shear capacity of stud, while the transverse spacing affects little the shear strength of stud. However, the slip of stud was increased because of the deformation of the slab at the transverse cracks.
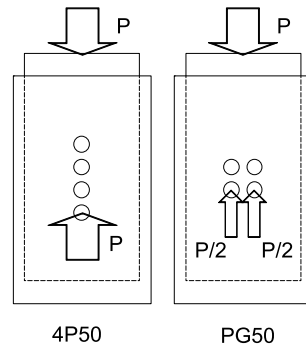

Fig. 5. 13 Transverse crack in Specimen '4PG50'

Fig. 5. 14 Different resisting mechanism in front of studs

Effect of stud arrangement (4PG50, 4P50)

Both Specimens '4PG50' and '4P50' had four studs for each slab, but the arrangement of studs was different, as shown in Fig. 5.6. These two specimens exhibited different stud behavior. For Specimen '4PG50', the maximum strength reached when the studs were sheared off. In contrast, the slab of Specimen '4P50' was split into two separated part, as shown in Fig. 5.10. As evidenced in Table 5.3 and Fig. 5.8, the arrangement of studs has no significant effect on the initial shear properties of stud in terms of the slip stiffness and yield strength. As shown in Fig. 5.14, although the studs in both specimens could transfer the same amount of load, Specimen '4PG50' resisted the load through two lines of stud while Specimen '4P50' through a single line, which is more critical for the slab bearing capacity. Therefore, the slab of Specimen '4P50' was split before the ultimate load reached due to the stud fractured.

5.2.5 Comparison with earlier studies

The shear capacity of headed studs embedded in the solid concrete slab was investigated extensively. The mechanism (Johnson and Oehlers 1981) by which the dowel action transfers the longitudinal shear forces is illustrated in Fig. 5.15. Shear forces and flexural forces are induced in the shank of the stud. These forces are in equilibrium with an eccentric normal force across the stud - slab interface acting at a distance b_f from the flange - slab interface. The shank of the stud is, therefore, subjected to shear and flexural stresses, and the zone immediately in front of the stud is subjected to high compressive stresses. The magnitude of these stresses depends not only on the shear force but on the position b_f of the resultant normal force, which is a function of the stiffness of the slab material relative to that of the steel. For example, if the stiffness of the slab material E_c increases to infinity, then the eccentricity b_f would be reduced to zero, and, similarity, if E_c approaches zero, then b_f would go to half the height of the stud, i.e., the normal stress across the shank-slab interface would be uniformly distributed. The dowel strength of the shear connection, therefore, depends on the strength and stiffness of the stud material and on the compressive strength and stiffness of the slab material in the zone directly in front of the stud. This small region immediately in front of the stud is triaxially restrained and, therefore, exhibited very large stresses. Since the stiffness E_c of SFRCC is two times of that of concrete, the position b_f of the resultant normal force is lower in SFRCC slab than that in concrete slab. If the stud failure precedes the slab

failure, the flexural forces in the stud in SFRCC slab is, hence, larger than that in concrete slab, which will be reflected as that the stud embedded in SFRCC slab transferred more longitudinal load than the one in concrete slab.
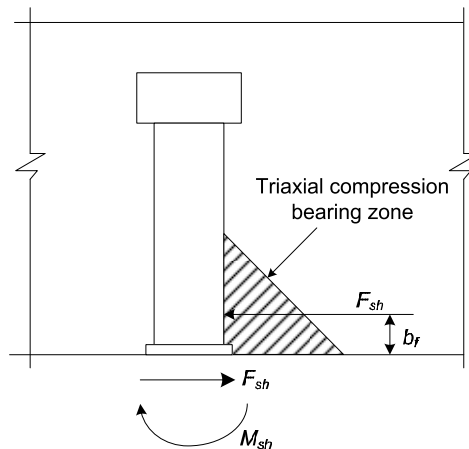

Fig. 5. 15 Dowel action (Johnson and Oehlers 1981)

By comparing with the test results of studs embedded in solid concrete slab, the effect of SFRCC slab can be examined. Only specimens which failed in stud fracture were considered since significant different material behavior present between concrete and SFRCC obviously would cause different shear capacity of studs when the slab fail prior to the stud fracture. As shown in Fig. 5.16, the deformed shape of the stud for the concrete (Ollgaard et al. 1971) is different from that for SFRCC. In the concrete specimen, greater restraint of the stud was apparent from the curvature (Fig. 5.16(a)). The stud was rotated through a large angle at the weld. It is also apparent that the concrete in front of the studs was crushed. In the SFRCC slab, the stud remains nearly straight (Fig. 5.16(b)). The rotation of studs was nearly not apparent. The studs fractured directly adjacent to the weld flush. Comparison of typical load-slip curves of the stud with the same diameter between the concrete (Inoue 1996) and SFRCC slab is shown in Fig. 5.17. It is notable that studs embedded in the SFRCC slab exhibited significantly larger stiffness and strength, which is consistent as the failure mechanism which has been described. According to the test data of Ollgaard (1971), the slip at the ultimate load of studs in concrete slab varied from 5.8 to 10.7 mm. The slip at the ultimate strength varied from 7.2 to 10 mm for the SFRCC slab. The amount of slip at the ultimate load was similar for the concrete and SFRCC slab, since the fracture of stud was determined by the material properties of stud.
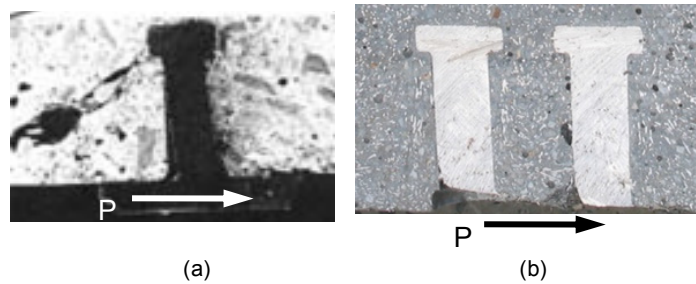
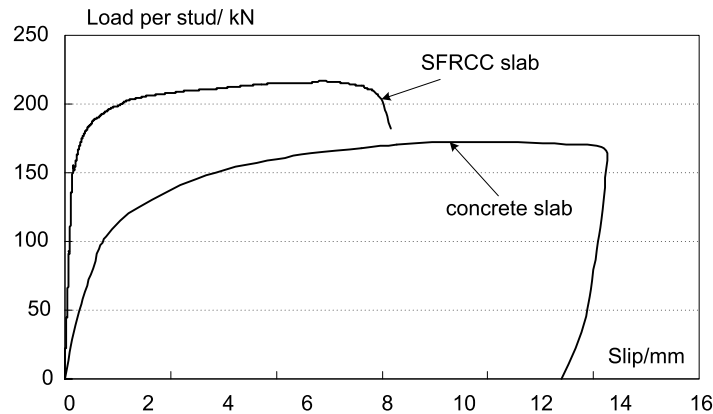Fig. 5. 16 Sawed section: (a) normal concrete slab; (b) SFRCC slab

Fig. 5. 17 Comparison of load-slip curves: concrete vs. SFRCC

The AIJ, AISC and Eurocode formulas are applicable only when the triaxial compression zones, as defined previously, do not overlap. Therefore, this can be promised by placing a limitation to the minimum lateral and longitudinal shear connector spacing, as suggested in Table 5.1. Alternatively, the stud failure strength of closely spaced studs can be reduced to allow for longitudinal and transverse overlaps of the triaxial compression zone. Based on the test results, the longitudinal overlap, with a longitudinal spacing of 50 mm, caused 10% reduction, while there was no reduction from the transverse overlap with the same spacing.

Studs exert concentrated loads to the slab that disperses into the element through shear and transverse tensile stresses. This complex stress state may result in ripping cracks of the slab, longitudinal splitting of the slab (tensile stresses), or formation of inclined (herring bone) cracks, as shown in Fig. 5.18. Such cracks shall reduce the triaxial restraint to the bearing zone and would therefore reduce the dowel strength of the studs. The lateral cracks extending from the sides of the stud occur by the ripping action of the concentrated load on the slab. The extent of the cracks depends on the in-plane compressive forced in the slab (Oehlers 1980). Furthermore, these cracks are considered to have little effect on the dowel strength since they occur away from the high triaxial compression bearing zone. The herringbone formation of shear cracks occurs near the compressive zone and hence may affect the triaxial restraint. However, transverse rebars is usually placed in the slab to prevent shear failure (Mattock and Hawkins 1972). The dispersal of the concentrated load to regions of uniform longitudinal stress induces a region of large lateral tensile stresses in front of the triaxial compression zone, which may cause the slab first split in front of the

stud as in Fig. 5.10 (a) and 5.18. Propagation of this split then induces splitting behind the studs, and also relieves the triaxial restraint to the bearing zone, hence inducing dowel failure through compressive failure of the slab. It has been found that the transverse rebars does not prevent splitting (Oehlers and Johnson 1981), but does limit the propagation of the split (Johnson and Oehlers 1981). Splitting has been found to occur in composite T-beams subjected to monotonic loads (Davies 1969; Chapman 1964), in composite T-beams subjected to longitudinally moving loads (Johnson and Oehlers 1981), and in composite L-beams (Johnson and Oehlers 1982).
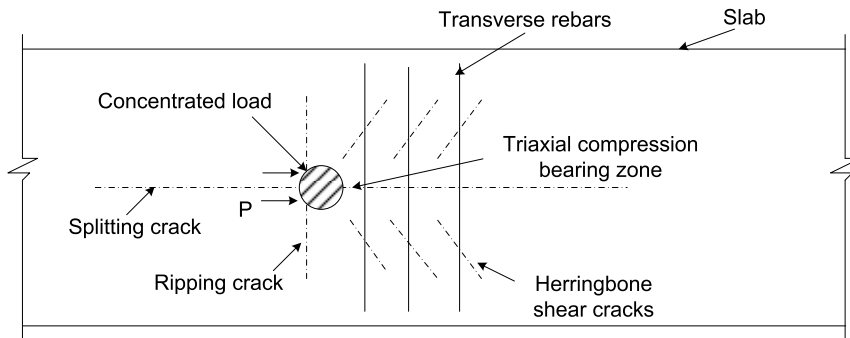

Fig. 5. 18 Tensile cracks induced by concentrated load

Tests of push-out specimens showed that splitting can reduce the strength of the stud to not greater than 20% of its theoretical stud failure strength. As shown in Table 5.3, Specimen '4P50', which failed in slab, exhibited 80% of the ultimate strength per stud for Specimen '1S', which failed in stud and the triaxial compression bearing zone was not affected by cracks or close spacing.

5.3 Numerical analysis

5.3.1 Introduction

The aforementioned push-out tests provided a basis to understand the overall behavior of the headed stud connectors in solid SFRCC slabs, e.g. the load-slip curve, shear capacity, and failure mode. The objective of this numerical analysis is to simulate the behavior of the stud connectors in the SFRCC slab by finite element analysis. The analysis will provide us insight into stress and strain distributions in the studs and slab, which is indeed difficult to directly observe in physical tests.

In this study, three dimensional FE models using ABAQSU (v6.7) were developed to simulate the load-slip behavior of shear stud connectors in solid SFRCC slab. The results from the proposed model were compared with the aforementioned push-out test results to elevate the reliability of the model. Then, a series of parametric analysis were conducted to investigate the effect of longitudinal and transverse spacing of the studs on the behavior of the connection. Furthermore, effects of applying transverse rebars to prevent the split failure of slabs even with densely arranged studs were studied.

5.3.2   Finite element model

Figure 5.19 shows the finite element mesh of the steel beam and the SFRCC slab with two headed studs. This is the model to simulate Specimen '2P50'. Considering the symmetry of the push-out specimen and boundary conditions, only one quarter of the specimen is modeled. Models with varies mesh sizes were tried before settling with the model presented in Fig. 5.19, with which reasonably accurate and stable analyses can be conducted with a relatively short computing time.

Two types of three-dimensional solid elements were used to represent the specimens. These are the three dimensional eight-node element with reduced integration (C3D8R) and the three dimensional twenty-node element (C3D20). In the modeling of the SFRCC slab, the steel stud (shank and head), and the beam flange, C3D20 elements are used. C3D8R are used for the beam web to reduce computing time, because the beam web would remain in elastic for the entire loading, both in the tests and analyses.
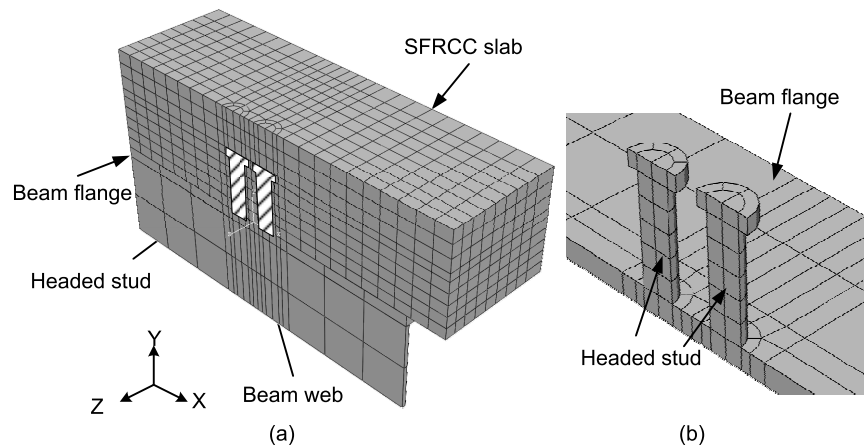

Fig. 5. 19 Model mesh: (a) entire specimen; (b) headed stud connectors

The interfaces between the stud and slab and between the beam flange and slab are treated carefully. Contact interaction without friction behavior is defined along the interface. Contact and detachment between the stud and slab or between the beam flange and slab can be considered automatically.

Material Properties

A classical metal plasticity, which uses Mises yield surface with associated plastic flow, was adopted to define the material properties of the elements that represent the headed stud connectors and steel beam. Based on the coupon tests, an average strength of 500 MPa was taken as the yield stress for the stud. A bilinear stress-strain model with Young's modulus $E_s = 200$GPa was adopted to simulate the headed stud material behavior. For the steel beam, Young's modulus of $E_s = 205$GPa was applied. For the flange, the same bilinear curve with a yield stress of 325 MPa was used.

The damage plasticity model, a material model commonly used for the analysis using ABAQUS to simulate the behavior of concrete structures sustaining cyclic loading, was adopted to represent material characteristics of SFRCC. This model was adopted rather than the concrete smeared

cracking model, because unlike the concrete smeared cracking model, this model can consider a failure mechanism associated with tensile cracking and compressive crushing, independently.

In uniaxial compression SFRCC exhibits a rather ductile failure. According to the research of Nielsen (1995), the compressive stress-strain relationship of SFRCC is defined by the following equation,

$$\frac{\sigma}{f_c{'}} = \frac{4\dfrac{\varepsilon}{\varepsilon_c}}{1.5 + \left(\dfrac{\varepsilon}{\varepsilon_c}\right)^{2.5}} \tag{5.2}$$

where ε_c and $f_c{'}$ are the compressive strain and stress at the peak point; and the σ-ε relation is graphically shown in Fig. 5.20(a). The tensile behavior of the applied material model is defined independently in two strain levels. Up to cracking, the stress-strain relation is linear; and post-cracking behavior is defined by a linear stress-crack opening displacement relationship as shown in Fig.5.20 (b).
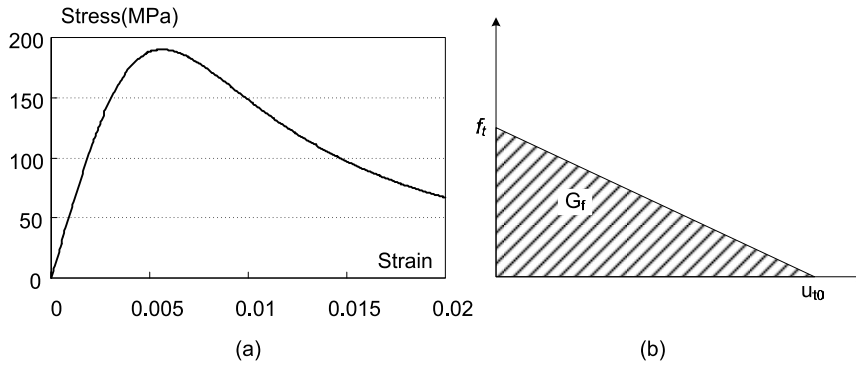

Fig. 5. 20 Material Property: (a) compression; (b) tension

The cracking displacement, at which the tensile strength is reduced to zero, is calculated by Equation (5.3), which is based on the fracture energy. In this test, the water binder ratio (*W*/*B*) and volume fraction of steel fibers (*V_f*) were adopted as 0.20 and 6% for SFRCC. According to the study of Nielsen (1995), the compressive stress at the peak point $f_c{'}$ =190MPa, the tensile stress at the peak point f_t=15MPa, Young's modulus of E_0=50GPa and fracture energy of G_f= 1300N/m were used.

$$\mu_{t0} = 2G_f / f_t \tag{5.3}$$

Boundary Condition and Loading

The boundary and loading conditions were determined to simulate the conditions given in the push-out tests. Load was applied on the nodes on the end surface of the beam flange and web as shown in Fig.5.21. The load was controlled by the displacement in the *X* direction up to 5 mm, which was close to the stud fracture slip (6-7 mm) observed in the test.

The displacement in the *X* axis direction of all nodes of the slab (Surface 1 in Fig.5.21) was

restrained. Considering the symmetry, the displacement in the *Z* axis direction of all nodes along the web end (Surface 2) was restrained; likewise, the displacement in the *Y* axis direction of all nodes for the slab, stud and steel web (Surface 3) were restrained.
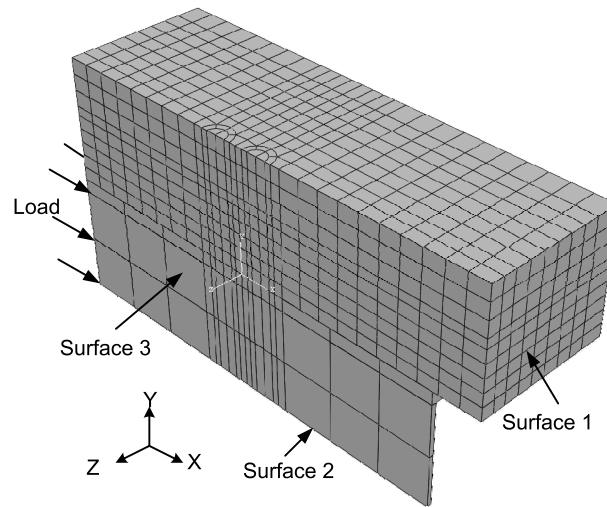

Fig. 5. 21 Application of load and boundary conditions

5.3.3   Analysis results

By means of the ABAQUS post processing, the overall load – slip relations and the stress and strain distribution across in the headed stud and the SFRCC slabs were obtained.

Figure 5.22 shows comparison between the load-slip curves obtained from the tests and analyses. Reasonable agreement between the two results is observed up to 2mm slip. The difference in the initial stiffness obtained from the tests and analyses ranged from 8% to 10%; and the difference the maximum strength ranged from 7% to 20%.
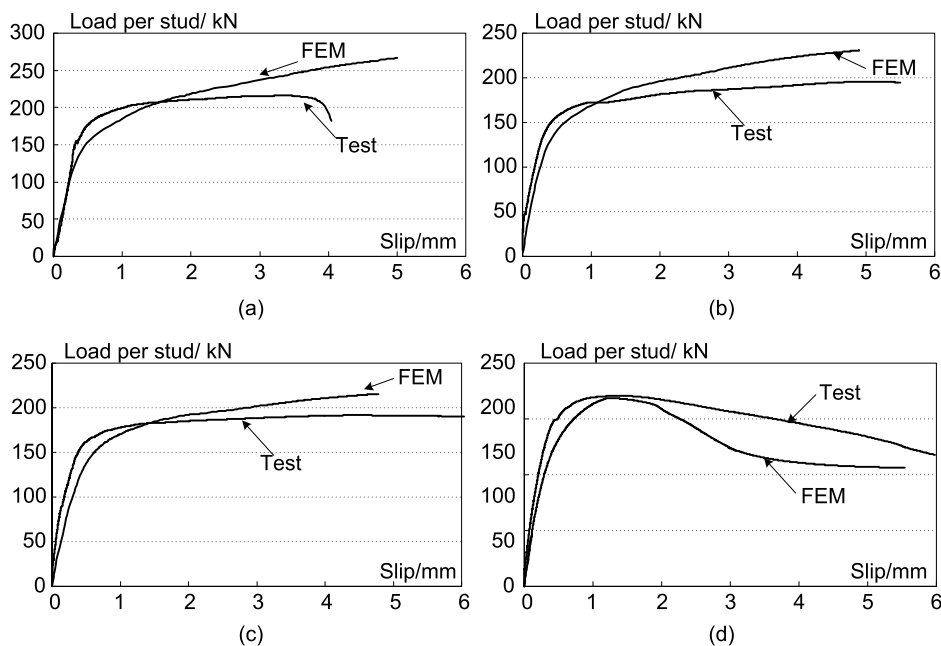

Fig. 5. 22 Load-slip curves of specimens:
(a) 1S; (b) 2P50; (c) 4PG50; and (d) 4P50

At slips larger than 2mm, the analytically obtained shear strength is larger than the corresponding experimental strength. The specimens that failed in shear at the root of the studs in the tests (i.e., Specimens '1S', '2P50', and '4PG50'), the analytical strength kept increasing until failure in both the test and analysis, but strength increase was more significant in the analysis. To large slip levels, very large load deformations occur in the portion close to the stud root, as shown in Fig. 5.23(a). It is speculated that the applied meshing of this portion was too coarse to accurately trace the behavior of the steel in these region. According to the analysis results, the steel underwent extremely large tensile strains greater than 20%. Most importantly the analysis was able to simulate the distinguished between of Specimen '4PG50', which exhibited the fracture of SFRCC. The analytically obtained shear strength - slip curve is presented in Fig. 5.22, in which the deterioration of strength is apparent in both the test and analysis.

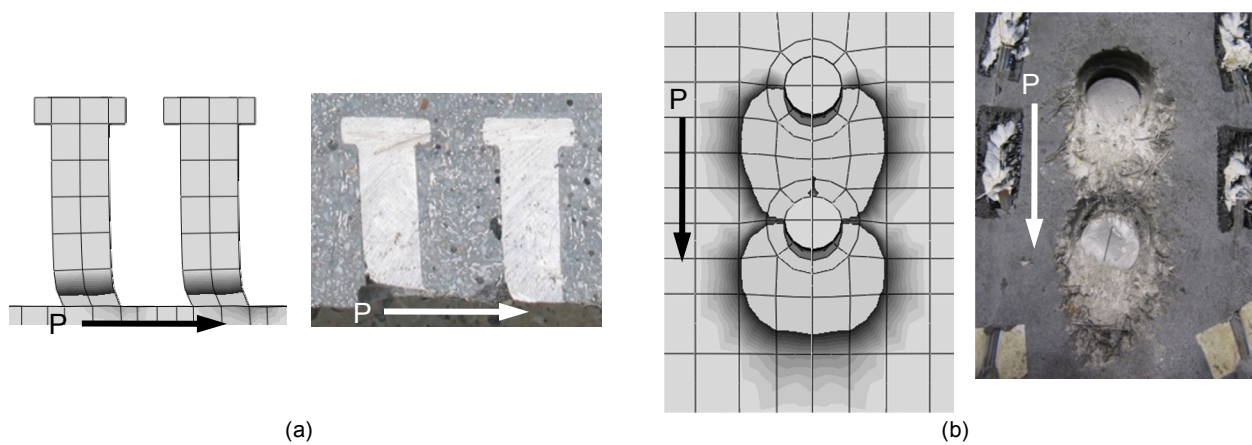(a)   (b)

Fig. 5. 23 Comparison of numerical and experimental behavior of specimen failed in the stud:
(a) deformation of studs; (b) crushed region in the slab

The two failure modes, i.e., the stud fracture and slab split, obtained from the test and analysis are shown in Fig.5.23 and Fig.5.24. The failure regions are marked in white, where the strain reached to the critical levels, i.e., for the studs, the plastic strain is larger than 20%; and for the SFRCC slab, the compressive and tensile equivalent plastic strains are larger than 3% and 0.2%. These are the levels where SFRCC could be crushed or split.

For the specimen failed in the studs (Fig.5.23(a)), the plastic tensile strain is much larger than 20% in the local region close to the lower end of the stud, which indicates fracture of the studs. The other portion of the stud remains mostly elastic and keeps the original geometry. As for the slab, the local region directly in front of each stud was crushed along the loading direction.

For the specimen failed in slab, i.e., Specimen '4P50', the maximum plastic tensile strain (5%) at the root of the studs is substantially smaller than those obtained for the specimens failed in the stud (47%). On the other hand, the tensile strain contour of the slab shows that region failed in tension is along the stud and extended to the end of the slab. These analytically obtained strain distributions indicate that failure of this specimen was caused by splitting cracks formed in the slab. These ultimate state simulated by the analysis are similar to the state observed in the physical test.

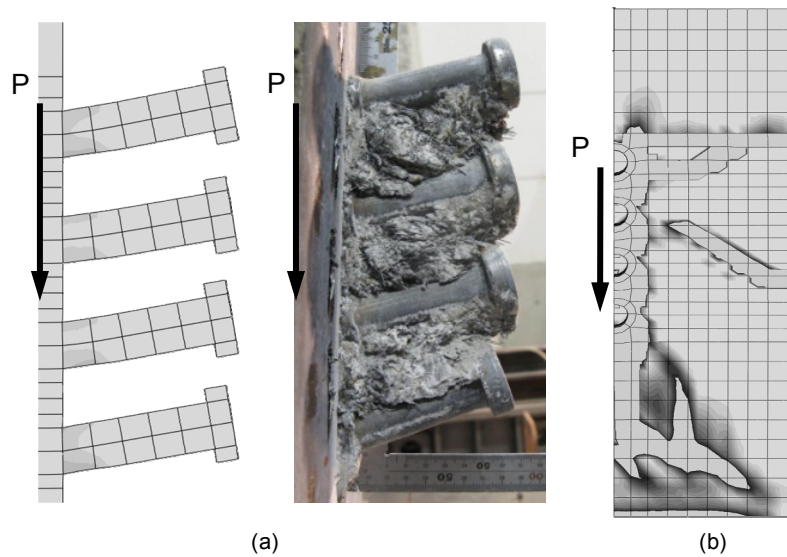The studs are bent in the lower portion and are tilted in the upper portion for Specimen '4P50.'

<center>(a)   (b)</center>

Fig. 5. 24 Comparison of numerical and experimental behavior of specimen failed in the slab:
(a) deformation of studs; (b) splitting of the slab

5.3.4   Parametric analysis

Parametric studies were conducted using the same finite element models. The spacing distance in both the longitudinal and transverse directions, and application of the transverse rebars to prevent the split failure of the slab were chosen as the parameters.

Longitudinal spacing

Figure 5.25 (a) shows the load-slip curves of the two studs arranged in the loading direction. The curves are obtained using different distances between the two studs. The longitudinal spacing ranged from 165 mm, the minimum specified spacing for the concrete slab of AIJ (1985), to 50 mm. It can be seen that the change in the longitudinal spacing has little effect on the initial stiffness of the stud connectors, and that the yield strength (defined as the secant stiffness corresponding to one third of the initial stiffness in this study), only slightly decreases unless the spacing is reduced to not greater than 80mm. When the spacing is reduced to 50mm, the yield strength is dropped by about 10%. Comparing the models of spacing with 80 and 50mm, the crushed regions of the slab in front of the studs merged for 50 mm spacing, while portion of the slab between the two studs remains uncrushed for 80 mm spacing, as shown Fig. 5.25 (b).
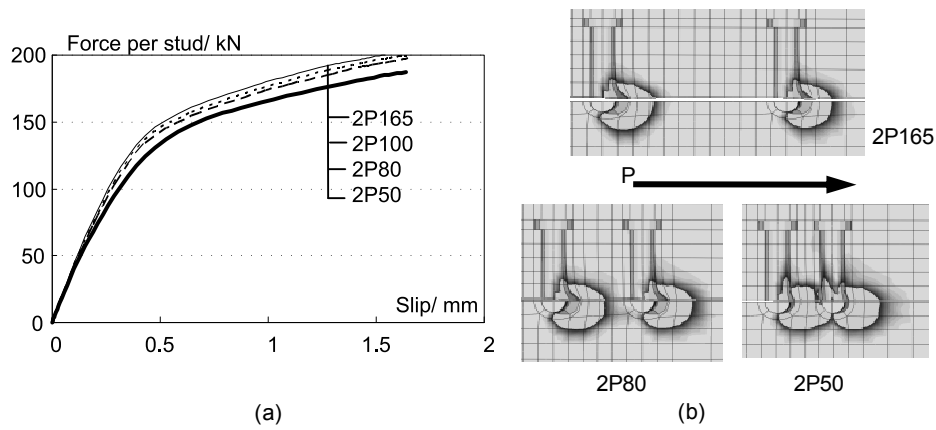
Fig. 5. 25 Effects of the longitudinal spacing:

(a) Load –slip curves; (b) compressive strain contour of the slabs

Transverse spacing

Figure 5.26(a) shows the load-slip curves of the two studs arranged perpendicular to the loading direction. The transverse spacing ranges from 110 mm, the minimum specified spacing for the concrete slab of AIJ (1985), down to 50 mm. It is notable that the change in the transverse spacing affects the load-slip curves very little. Compressive strain distributions are shown in Fig. 5.26 (b), in which the crushed regions of the slab in front of the studs merged in the transverse direction only for the model with the spacing of 50 mm. However, the longitudinally projected length of the crushed region was intact and nearly the same for each model. It is assumed that this is the reason that the effect of the transverse spacing to the shear capacity of studs is small.
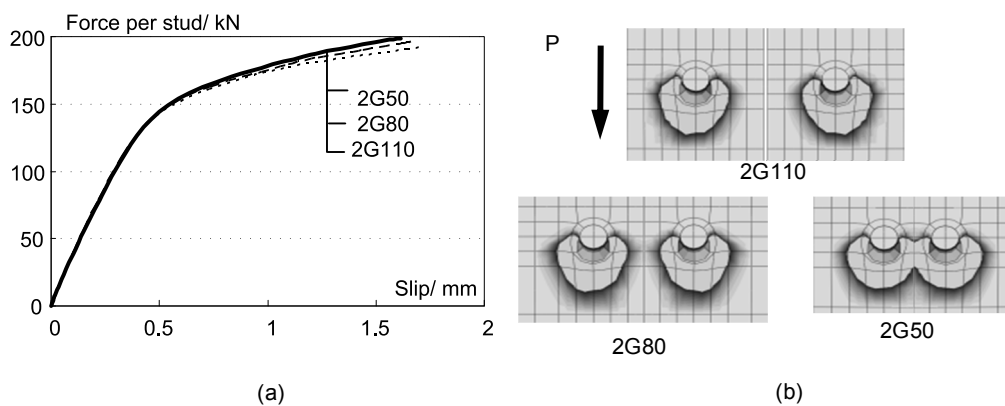

Fig. 5. 26 Effects of the transverse spacing:

(a) Load –slip curves; (b) compressive strain contour of the slabs

Transverse rebars

In construction practice, rebars are arranged in two horizontal directions in the slab. As suggested by Oehlers (1992), fully anchored transverse rebars placed in front of heavily loaded studs neither increase the splitting strength of the slab nor increase the strength after splitting. However, the transverse rebars was found to limit the length of the split and allow a gradual reduction in the shear load after splitting (Oehlers 1992). Also, it has been found that the stiffness of the transverse rebars,

and not its strength, controls the stud failure strength. The reason is that the strength of the slab material in the triaxial compression zone is required to have strength much greater than the uniaxial strength of the slab material. Studs are, therefore, susceptible to failure before the rebars yields which requires a widening of the splitting cracks.

In this section, the effect of transverse rebars on split cracks, the one observed for Specimen '4P50,' is examined. In the counter model, Specimen '4P50-re', four D22 rebars were arranged along the loading direction in front of the front stud (see Fig. 5.27(b)). Fig. 5.27 (a) shows the comparison of load-slip curves of the specimen with and without the transverse rebars. The splitting strength of the slab did not increase, while a gradual reduction in the shear load after splitting was observed. This finding is similar to what was observed previously. In the reinforced model, the failed region of the slab shown in Fig. 5.27(b) and suggested by the tensile equivalent plastic strain does not extend to the end of the slab unlike that of the slab without rebars. Also, for the models with the rebars, the maximum value and distribution of strain, as well as the deformation, of the studs are similar to those of models for specimens shear failed in the studs. This indicates that the failure mode could be switched to the shear failure in the studs from the slab fracture, as shown in Fig. 5.27 (b). It is also noted that according to the analytical results, the force induced in the rebar nearest to the stud is 66% of the summation of the forces induced in the all rebars. It appears that the rebars should be arranged close to the root of studs.
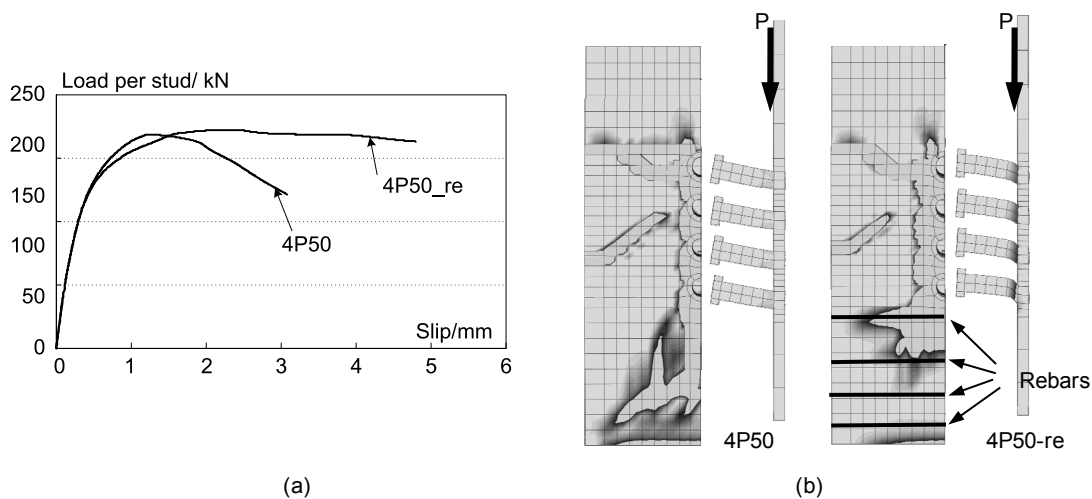

(a)   (b)

Fig. 5. 27 Effects of the transverse rebars:
(a) Load –slip curves; (b) tensile strain contour of the slabs

5.4 Conclusions

A series of push-out tests was conducted on four specimens with SFRCC with multiple studs arranged in small intervals. The results suggested that the application of SFRCC, which has a large tensile strength and ductility, promises larger shear forces transferred through stud connectors allocated in a small area. Major findings obtained from the tests are summarized as follows:

(1)   One headed stud connector embedded in the solid SFRCC slab can transfer the load that 15%

larger than the evaluated strength by AIJ and AISC specification. Compared with the headed stud connectors embedded in the normal concrete slab, the headed stud connectors embedded in SFRCC slab exhibited a larger slip strength and resisting load. It is primarily because of the better material properties of SFRCC, i.e. a larger Young's Modulus.

(2)   The ultimate load per stud was reduced to 90%, when the longitudinal spacing of studs was 50 mm. The reduction occurred because of the overlap of bearing region in front of the studs. The transverse spacing of studs in a interval of 50 mm has no significant effect on the shear capacity of studs.

(3)   The shear capacity of studs was also controlled by the slab bearing capacity. An appropriate amount of rebars is needed to strengthen the slab to guarantee the stud fracture occurred prior to the slab failure.

Finite element models were developed to simulate the behavior of headed stud connectors in solid SFRCC slab. The model took into account the nonlinear material properties. The numerical results agreed reasonably with the results obtained from the experimental results. Furthermore, three series of parametric analyses were conducted, and the following observations were drawn.

(1)   For the model with two studs aligned longitudinally with only 50 mm spacing, the strength is smaller than other models with larger longitudinal spacing. In this model, the two crushed regions of the slab around the studs merge each other.

(2)   The length of uncrushed portion of the slab directly in front of the studs varies only little when two studs are aligned transversely, thus the shear capacity of stud remain the same with the decrease in transverse spacing.

(3)   The transverse rebar is likely to be very effective to improve the shear stud capacity because of the prevention of split cracks in the slab. The rebar closer to the root of the stud are most effective.

This study provided fundamental information on the stud behavior in solid SFRCC slab. For the stud failure, the shear resistance of an individual stud can be evaluated using the AISC formula with a factor of 1.1. For a group of studs, only the longitudinal spacing effect is notable. When the spacing is less than 80 mm, the shear resistance of an individual stud is reduced by 10%. For the failure of slab split, a method to evaluate the shear resistance and to design the transverse rebars is an ongoing research.

REFERENCES

[5.1]   ABAQUS/ Standard user's manual, version 6.7, Hibbitt, Karlson and Sorensen, Inc. 2005.

[5.2]   Architectural Institute of Japan (AIJ). (1985). "Design recommendations for composite constructions." Tokyo (in Japanese).

[5.3]   American Institute of Steel Construction (AISC). (2005). "Seismic provisions for structural steel buildings." Chicago.

[5.4]   Chapman, J. C. (1964). "Composite construction in steel and concrete – the behavior of composite beams." *The Structural Engineer*, 42 (4),115-125.

[5.5]   Davies, C. (1969). "Tests on half-scale steel-concrete composite beams with welded stud

connectors." *The Structural Engineer*, 47(1), 29-40.

[5.6]   Dennis, L., and Ehab, El-L. (2005). "Behavior of Headed Stud Shear Connectors in Composite Beam." *Journal of structural engineering*, 131 (1), 96-107.

[5.7]   Ehab, El-L., and Dennis, L. (2002), "Modeling of headed stud in steel-precast composite beams." *Steel and Composite Structures*, 2 (5), 355-378.

[5.8]   European Committee for Standardization (CEN). (1994). ENV 1994-1-1 Eurocode 4, "Design of Composite Steel and Concrete Structures." Brussels, Belgium.

[5.9]   Johnson, R. P. and Oehlers, D. J (1981). "Analysis and design for longitudinal shear in composite T-beams." *Proceeding of the Institution of Civil Engineers (London). Part 1 - Design & Construction*, 71(pt2), 989-1021.

[5.10]   Johnson, R. P. and Oehlers, D. J (1981). "Design for longitudinal shear in composite L beams." *Proceeding of the Institution of Civil Engineers (London). Part 1 - Design & Construction*, 73(pt2), 147-170.

[5.11]   Inoue, K. (1996). "State of Art and Future of Design and Practice of Connectors Using Headed Studs." *Concrete Journal*, JCI, 34(4), 7-14.

[5.12]   Mattock, A. H., and Hawkins, N. M. (1972). "Shear transfer in reinforced concrete – recent research." *P.C.I.J.*, 17(2), 55-75.

[5.13]   Moore, W. P. Jr. (1988). "An Overview of Composite Construction in the United States." *Composite Construction in Steel and Concrete I*, ASCE, New York, 1-17.

[5.14]   Nielsen, C. V. (1995). "Ultra high-strength steel fiber reinforced concrete, Part I Basic strength properties of compresit matrix." Ph.D. Thesis, Technical University of Denmark.

[5.15]   Oehlers, D. J. (1980). "Stud shear connectors for composite beams." Ph.D Thesis, University of Warwick, Coventry, England.

[5.16]   Oehlers, D. J. and Johnson, R. P. (1981). "The splitting strength of concrete prisms subjected to surface strip or patch loads." *Mag. Concr. Res.,* 33(116), 171-79.

[5.17]   Oehlers, D. J. (1989). "Splitting induced by shear connectors in composite beams." *Journal of structural engineering*, 115(2), 341-362.

[5.18]   Oehlers, D. J. and Park, S. M. (1992). "Shear connectors in composite beams with longitudinally cracked slabs." *Journal of structural engineering*, 118(8), 2004-2022.

[5.19]   Ollgaard, J. G., Slutter, R.G., and Fisher, J.W. (1971). "Shear strength of stud connectors in lightweight and normal-weight concrete." *AISC Engineering Journal*, 8 (2), 55-64.

[5.20]   Viest, I. M. (1956). "Investigation of stud shear connectors for composite concrete and steel T-beams." *ACI Journal*, 52(4), 875-892.

[5.21]   Viest, I. M. (1992). "Composite Construction: Recent Past, Present and Near Future." *Composite Construction in Steel and Concrete II*, ASCE, New York, 1-16.

CHAPTER 6

Beam-Column Connection of Steel Structures Using SFRCC

6.1 Introduction

6.1.1   Background

During the 1994 Northridge earthquake and the 1995 Hyogoken-Nanbu earthquake, a large number of steel building structures sustained severe damage or even collapsed (AIJ 1995, Nakashima et al. 1998). One of the most serious damage appeared to be cracks and brittle fracture at welded beam-to-column connections. Similar to the observation in the 1994 Northridge earthquake (Youssef et al. 1995), the location where premature fractures initiated was typically in the vicinity of the weld between the beam bottom flange and the column.

In order to assure sufficient plastic deformation capacity of welded beam-to-column connections, various attempts were made in the United States and Japan. After extensive investigations, the reduced beam section design (Recommended 2000) has been widely accepted in the United States as an effective and economic solution. On the contrary, based on the observation that cracks often initiated at the toe of the weld access hole, Japanese researchers placed more emphasis on connection details to mitigate stress concentrations at welds and finally recommended the connection without a weld access hole (AIJ 1996). Although these modified connections have shown satisfactory performance in the laboratory, it is realized that the quality of welds get difficult to control in practice as long as the structural fabrication relies on workmanship. The defects as well as insufficient deposition are often of concern regardless of the connection details adopted. As compared to welded connections in the United States, the Japanese practice generally requires larger volume of weld, implying that the Japanese connections are more relevant to the quality assurance problems (Suita et al. 2000).

To overcome the difficulty in the weld quality assurance as well as stringent post-Kobe requirements for welding practice, a "weld-free" beam-column connection using high strength bolts instead of welding has been proposed (Suita et al. 2004a and 2004b, Inoue et al. 2006). Fig. 6.1 shows details of a type of innovative beam-column connection. Wide-flange beams are bolted to the flanges of wide-flange column only at the top flanges. As a result, the beams rotate about the ends of the ends of their top flanges. At the top and bottom of the beam, braces are installed primarily to provide the

structural system with sufficient lateral resistance against design seismic force and, at the same time, dissipate seismic input energy during a strong earthquake.
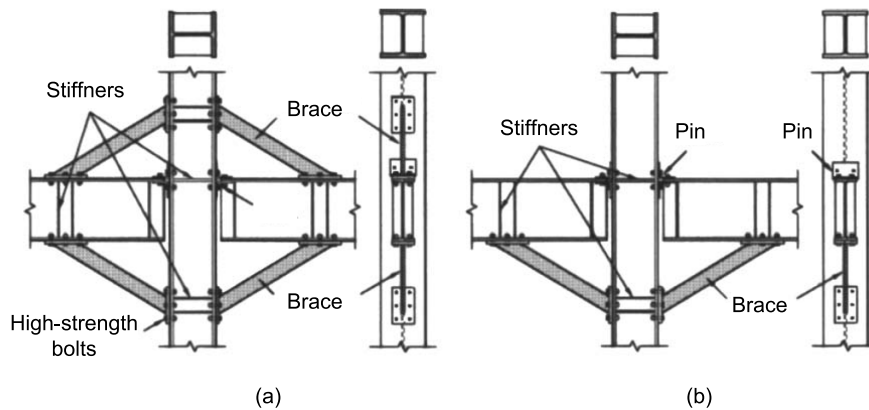

Fig. 6.1 Weld-free beam-column connections: (a) double-side bracing; (b) single-side bracing
(Suita et al. 2004 and Inoue et al. 2006)

Another new beam-column connection with U-shaped bracket where SFRCC was casted has been developed (Kaneko et al. 2001 and Kaneko et al. 2002). Figure 6.2 shows details of the U-shaped bracket beam-column connection. The steel beam is connected to a U-shaped bracket without any welding or high-strength bolts. SFRCC is filled in the gap between the end of steel beam and inside of the U-shaped bracket. The beam load is transferred to the bracket through the compressive strut of the SFRCC. Because of the high strength of SFRCC, the length of U-shaped bracket could be relatively small, for example 0.22 times of the span. The U-shaped bracket beam-column connections with SFRCC give large stiffness and strength without serious damage in comparison to the connections with concrete.
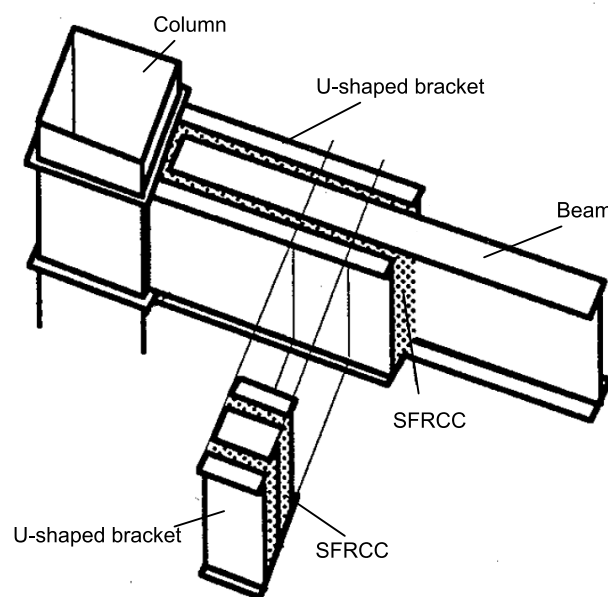

Fig. 6.2 U-shaped bracket beam-column connection (Kaneko et al. 2002)

For a beam-column connection, diaphragms are used to transfer the flange forces to the sides of the column. Common types of diaphragm, through plate diaphragm, internal diaphragm, and external diaphragm, are illustrated in Fig. 6.3.
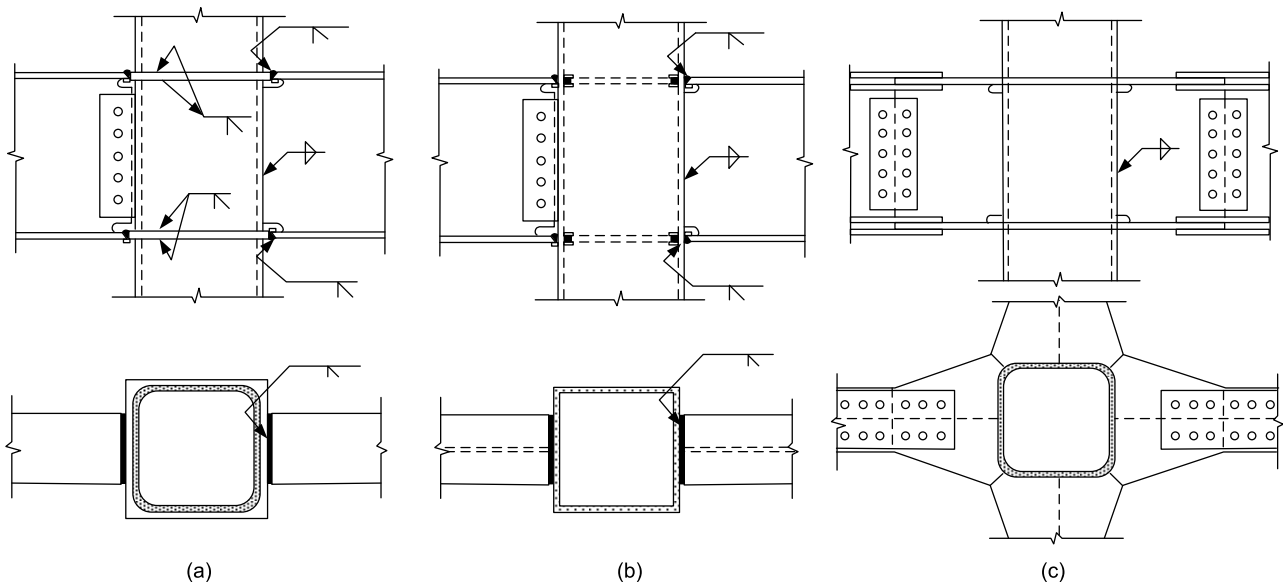

Fig. 6.3 Typical beam-column connections: (a) through plate diaphragm; (b) internal diaphragm; and (c) external diaphragm. (AIJ 2006)

In Japan the through diaphragm is commonly used for the beam-column connection of low- to medium -rise steel frame moment buildings. Usually the column has to be cut off to weld the through-diaphragm plates by which the flange load could be smoothly transferred to the column side. The available flexural strength of the beam is achieved because of the flexibility of the column wall was restricted by the welded diaphragms. However, its fabrication is rather complex since the column has to be cut and large amount of welding is needed.

Different from the other two types of diaphragm, external diaphragm plates are welded around the column to transfer the flange load. Its fabrication is comparatively easy, since the column is continuous and less welding is used. However, the out-of-plane deformation of column wall and the stress concentration at the diaphragm limit the use of external diaphragms.

These diaphragms show relative benefits and shortcomings, in terms of welding quality and constructability, at simultaneity. To overcome the difficulty in the weld quality assurance as well as to enhance the constructability, a new beam-column connection is proposed with the feature of "weld-free".

The proposed beam-column connection is shown in Fig.6.4. The portion of slab around the column is cast by SFRCC and designed to transfer the load from the beam to the column. The SFRCC slab is applied on both the top and bottom beam flange. There is no welding between the column and beam flange. The headed studs are welded on the beam flange to transfer beam load to the SFRCC slab. These studs are closely welded on the beam flange in a limited region of slab near the column to transmit the available load. At the end, the beam hinge is expected to form at the end of the slab edge.

Although the topology of the SFRCC diaphragm is similar as the exterior plate diaphragm, the load transfer mechanism is somewhat different. As illustrated in Fig. 6.4, the tensile load of the beam flange is transferred to the SFRCC diaphragm through the headed studs, and then through the compression of the SFRCC diaphragm the load is further transferred to the opposite side of the column. The compressive load of the beam flange is transferred to the SFRCC diaphragm through the headed studs, and then the compressive load is directly transferred to the column.
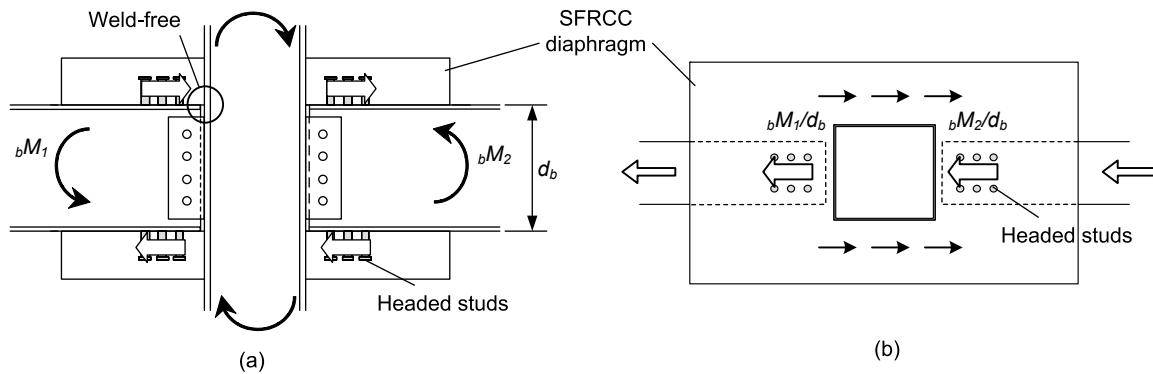

Fig. 6. 4 Proposed beam-column connection: (a) elevation view; (b) plane-view

In the proposed connection a group of studs welded on the beam flange are embedded in the SFRCC slab to directly transfer the flange load to the side of the column instead of conventional welding. In this connection, composite action achieved by headed stud connectors is essential. The shear strength and stiffness of the connection depends not only on the strength of the connector itself, but also on the strength of the material around the stud. As a new cement material, SFRCC exhibits not only the large stiffness and strength but ductile characteristics in comparison to the conventional concrete. These material characteristics are promising to enhance the possibility to embed a large number of studs into a relatively small region to transfer the flange load to the side of the column.

The primary objective of this study was to experimentally prove the feasibility of the proposed connection system. The test program consists of two full-scale cyclic tests on cruciform specimens without floor slabs. Two specimens are designed following two different failure modes. Based on the test results, important design parameters, i.e., the elastic stiffness, maximum strength, and energy dissipation of the connection, are examined. The effect of SFRCC diaphragm and the headed studs are also investigated.

6.1.2 Organization

In this chapter, the development and design of the test program and test specimens is presented first. Information on the construction, test set-up, and instrumentation is also provided. Test results are given as summaries of behavior and test data for respective specimens. These summaries are followed by a discussion of the test results, in which difference in behavior are examined. Seismic behavior of the specimen is compared with that of the conventional bare steel beam-column connections in terms of the strength and energy dissipation. Furthermore, the behavior of studs in the connection specimens is compared with that in the push-out specimens. The effect of rebars is discussed, too.

6.2 Test Program

6.2.1 Test specimens

The test specimens were designed to simulate interior moment-resisting connections of a four-story steel structure with a story height of 3 m and a span length of 6 m. Two specimens 'C-4PG50' and 'C-9PG50' were fabricated in the full-scale as shown in Fig.6.5. The detailing of these two specimens was the same expect the number of the studs. Fig. 6.5 to 6.7 shows the global dimensions of the specimens. A relatively strong column was used to ensure that the beams can initiate the development of yielding during cyclic loading before significant deformation or damage to the column. All specimen comprised a cold-formed, square-tube cross section column (300 mm in the width, with a thickness of 19 mm), two H-shaped steel beams (400 mm in the height and 200 mm in the width, with a thickness of 8 mm and 13 mm for the web and flange, respectively). Two SFRCC slabs were casted on the top and bottom beam flanges, as shown in Fig. 6.5 (a). The size of the SFRCC slab is 1150 mm along the beam (the ratio to the span is 0.1) and 700 mm orthogonal to the beam. The thickness of the SFRCC slab is 150 mm, which is the same as the concrete slab thickness in the steel buildings. In this test, the concrete slab on the beam was not considered. For the real construction practice, there should be some space left between SFRCC and concrete slab to avoid the interaction of the two materials, such as shrinkage, creep and thermal expansion. Considering the construction practice, the new beam-column connection was designed to be fabricated at the plant as the pre-cast column-tree. Therefore, the beam was designed to be spliced at 1 m off the column face. During the construction, the bottom slab was casted first, and then the specimen was flipped over to cast the top slab. On the other hand, since one of the purposes of this test was to investigate the capacity of the SFRCC slab to transfer the flange load as external diaphragms, the beam web was designed to only resist the shear load by using slotted bolt holes of the shear plate, as shown in Fig.6.5 (f).

In specimen 'C-4PG50', four studs were welded on the beam flange to transfer the load. This specimen was designed to investigate the connection behavior when the stud fracture prior to the beam yielding. In addition, since the layout of the studs in specimen 'C-4PG50' was the same as the specimen '4PG50', which was the push-out specimen discussed in Chapter 5. Comparing the stud behavior in these two specimens in terms of the slip stiffness and maximum strength, feasibility of push-out test to evaluate the shear resistance of studs is examined. Specimen 'C-9PG50', in which nine studs were utilized to transmit the load, was designed to investigate the connection behavior when the beams yield prior to the stud fracture. The different seismic behavior between the two specimens (Specimen 'C-4PG50' and Specimen 'C-9PG50') is investigated in terms of the elastic stiffness, strength and energy dissipation. Additionally, the effect of using SFRCC slab instead of the conventional welding was investigated by comparing the behavior with the conventional bare steel beam-column connection in terms of the maximum strength and energy dissipation.

The number of studs was determined based on the test results of the push-out test introduced in Chapter 5. According to the procedure to evaluate the shear resistance of individual studs suggested

in Chapter 5, the shear resistance per stud with the diameter of 22 mm is 190kN when the studs are arranged with 50 mm spacing along the loading direction. Therefore, the bending moment transferred by an individual stud with the diameter of 22 mm is 76kNm. The bending moment governed by the stud fracture was 304 kNm and 684 kNm for Specimen 'C-4PG50' and 'C-9PG50', respectively. It was 0.68 times and 1.54 times of the full-plastic moment M_p of beam (458 kNm).

The SFRCC slab was provided with rebars. To strengthen the slab, both the longitudinal and transverse rebars are needed. The rebar in the longitudinal direction, i.e., along the beam direction, was designed to resist the tensile load in the SFRCC slab, while the rebar in the transverse direction, i.e., perpendicular to the beam direction, was designed to prevent the split cracks induced by the studs. Twelve D22 rebars for each SFRCC slab were arranged to transfer all the flange force when the full-plastic moment of beam was achieved at the column face. For the sake of conservation, six D22 rebars were placed outside of the studs and one D22 rebar was placed between the studs group and the column face to prevent splitting cracks. Rebar rings were adopted for the slab by considering the spacing and cover layer limitation, since the rebars in longitudinal and transverse direction overlapped at the corners of the slab. The rebars were bent by 45° at the corner to directly transfer the force from the transverse direction to the longitudinal direction. As illustrated in Fig.6.6, two layers of three rebars rings are placed around the studs group and column at a 50 mm space both vertically and horizontally. The top layer of rebars is located 60 mm below the top surface of the slab.

The material properties of the steel and SFRCC used for the specimens were obtained from the associated material tests and are summarized in Table 6.1. The mix portion of SFRCC is shown in Table 6.2. According to the certification, the tensile strength of the headed stud is 500N/mm^2. Densit cement was used to mix the SFRCC paste with the water bind ratio of 0.175 (in weight) and the fiber ratio was 6% in volume.
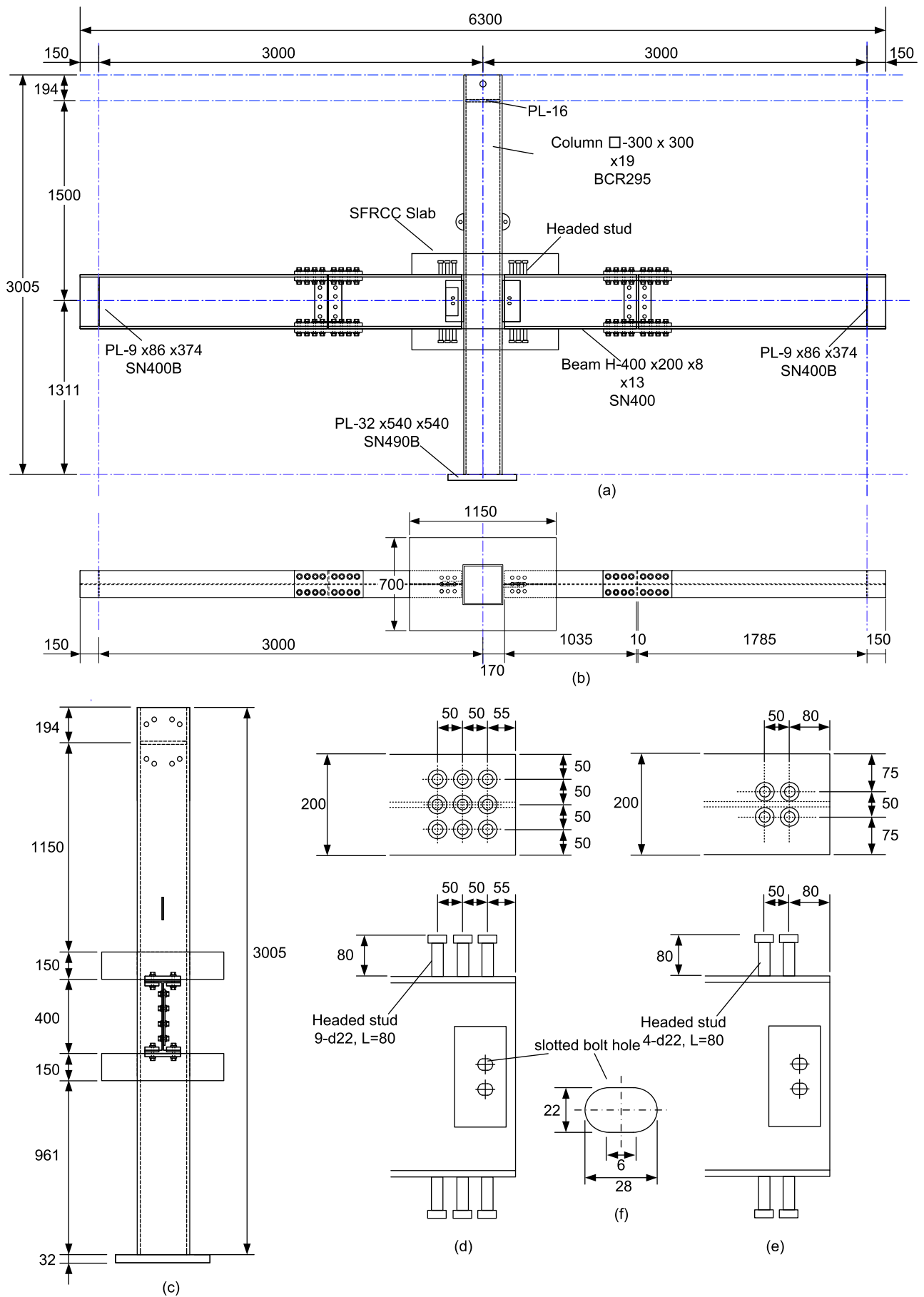
6300

150 3000 3000 150

194

1500

3005

1311

PL-16

Column □-300 x 300 x19 BCR295

SFRCC Slab

Headed stud

PL-9 x86 x374 SN400B

Beam H-400 x200 x8 x13 SN400

PL-9 x86 x374 SN400B

PL-32 x540 x540 SN490B

(a)

1150

700

150 3000 1035 10 1785 150

170

(b)

194

1150

150

400

150

961

32

3005

(c)

50 50 55

200

50
50
50
50

50 80

200

75
50
75

50 50 55

80

Headed stud 9-d22, L=80

50 80

80

Headed stud 4-d22, L=80

slotted bolt hole

22

6

28

(f)

(d)

(e)

Fig. 6. 5   Test specimen: (a) front elevation; (b) plane view; (c) side elevation; (d) studs of Specimen'C-9PG50'; (e) studs of Specimen 'C-4PG50'; and (e) slotted bolt hole (unit: mm)

6 - 7
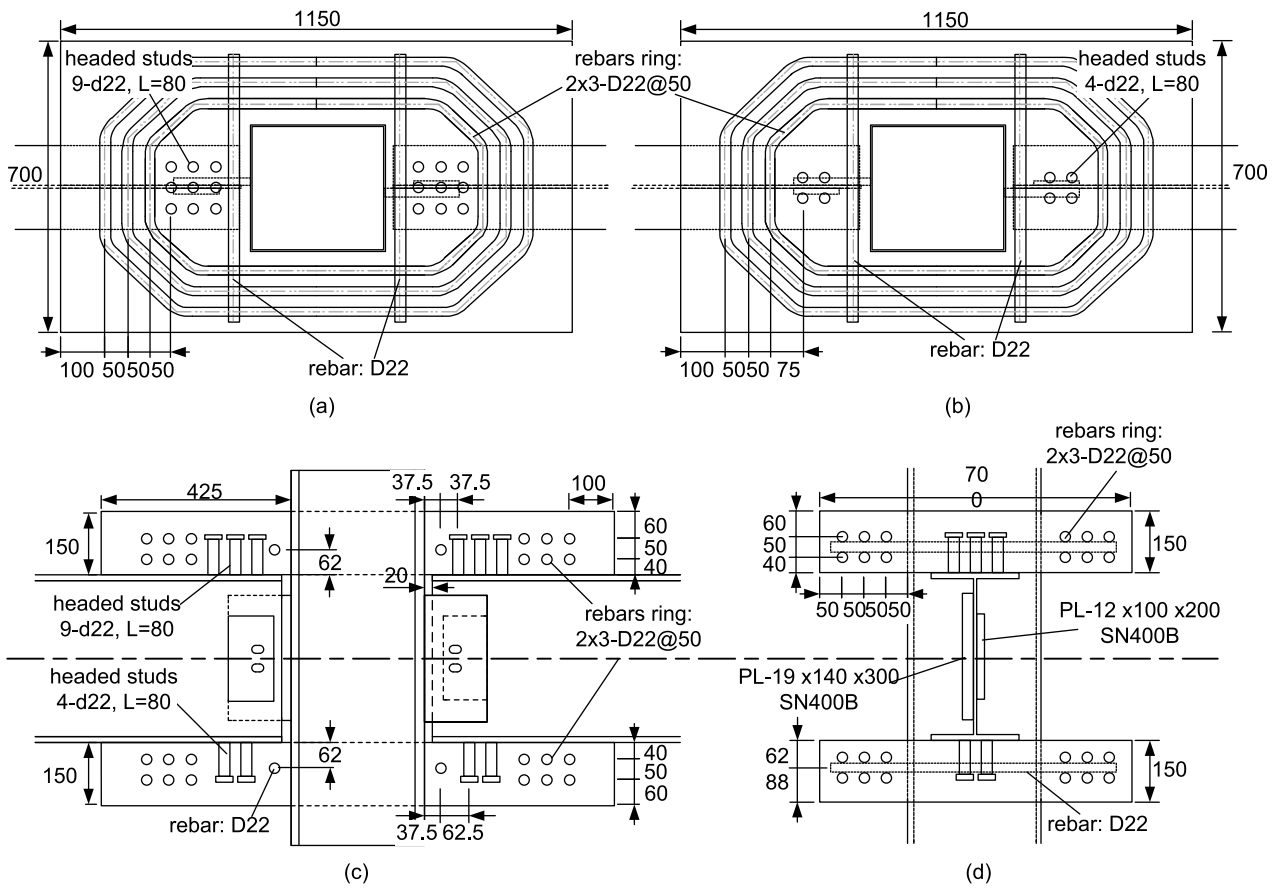
Fig. 6. 6   Details for slab and rebars: (a) plane view of Specimen 'C-9PG50';
(b) plane view of Specimen 'C-4PG50'; (c) front view; and (d) side view (unit: mm)
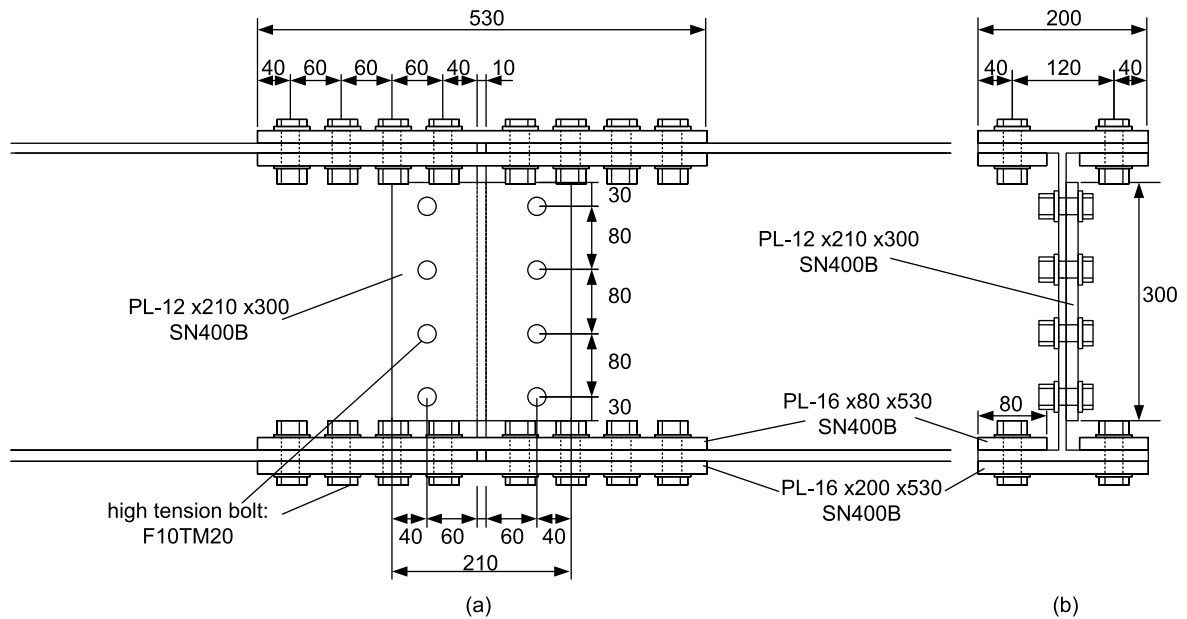

Fig. 6. 7   Details for bolted splice: (a) front view; (b) side view (unit: mm)

Table 6.1 Material properties (steel and SFRCC)

		Yield strength σ_y (N/mm^2)	Tensile strength σ_u (N/mm^2)
Column □-300x300x19 (BCR295)		430	439
Beam H -400x200x8x13 (SN400)	Flange	306	460
	Web	374	484
Rebar (SD295)		396	566

	Compressive strength f_c' (N/mm^2)	Split strength f_{sp}' (N/mm^2)
SFRCC	115	18.1

Table 6.2 Compositions for 1 m^3 SFRCC (unit: kg)

Water	Densit cement	Fine aggregate	Steel fiber
152	868	12000	444

6.2.2   Test setup and loading program

The test specimen was placed in the loading frame shown in Fig. 6.8. The top and bottom of the column and free ends of the beams were pinned supported. The beams were supported vertically by pin-ended struts. The lateral load was applied as a cyclic drift displacement at the top of the column. The drift angle was measured as the displacement at the top of the column divided by the height of the column (3000 mm). Drift angles of 0.005, 0.01, 0.02, 0.03, 0.04, and 0.06 rad were adopted, and two cycles were performed for each drift angle. Loading of specimens was terminated till the specimen lost the resisting capacity completely.
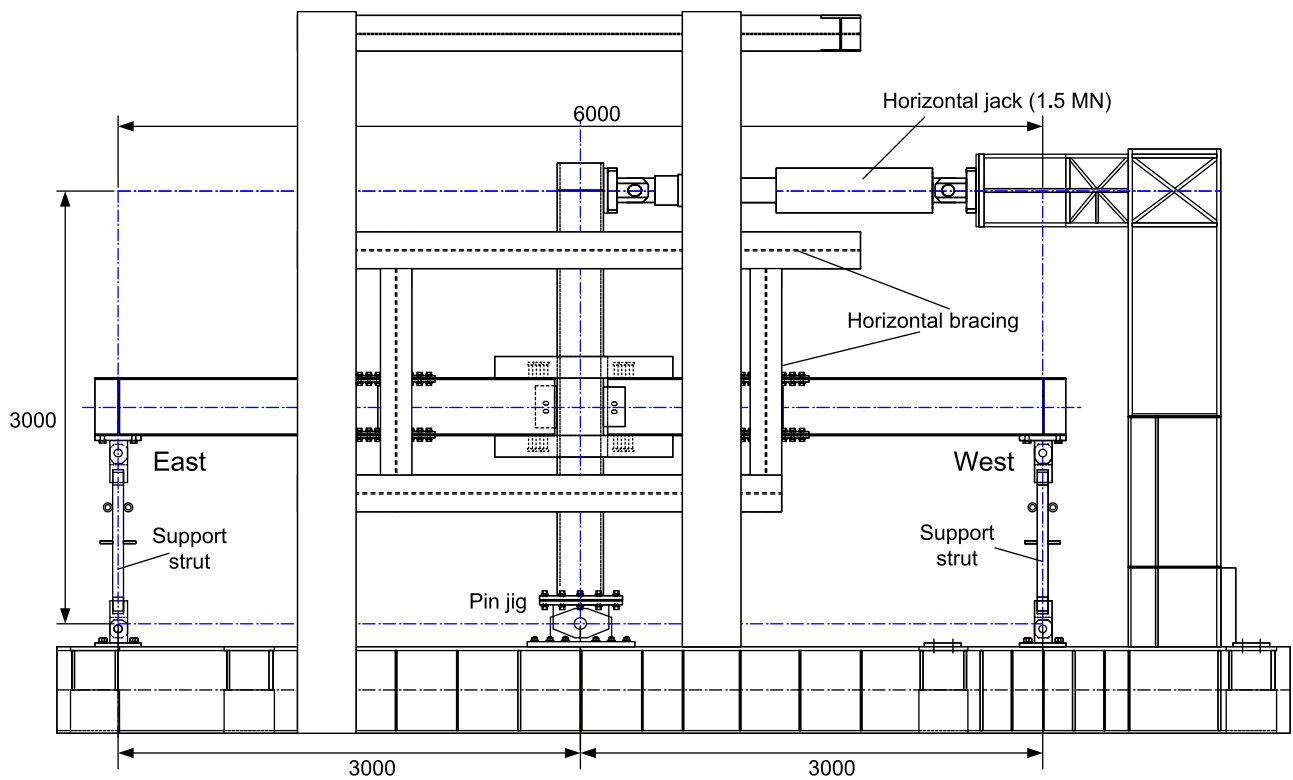
Fig. 6. 8   Test setup (unit: mm)

6.2.3   Instrumentation

Figures 6.9 and 6.10 show the locations of displacement transducers and strain gauges. Twelve linear variable differential transformers (LVDTs) were used to measure displacements at various locations. In-plane (in the East-West direction) displacement LVDT measured the deflection at the top of the column. The relative movement between the SFRCC slab and the beam was measured (Fig. 6.9 (b)). Four LVDTs were fixed on the steel flange at the elevation corresponding to the middle of the stud group, while the head of the LVDT was attached to an acrylic resin plate glued onto the surface of the slab at the same elevation. Measurement of beam rotations was around the connection, tracking the horizontal displacements with respect to the column located above and below the beam (Fig. 6.9(c)). Two LVDTs were oriented to measure changes in displacement relative to the corner of panel zone between the two SFRCC slabs (Fig. 6.9(c)).
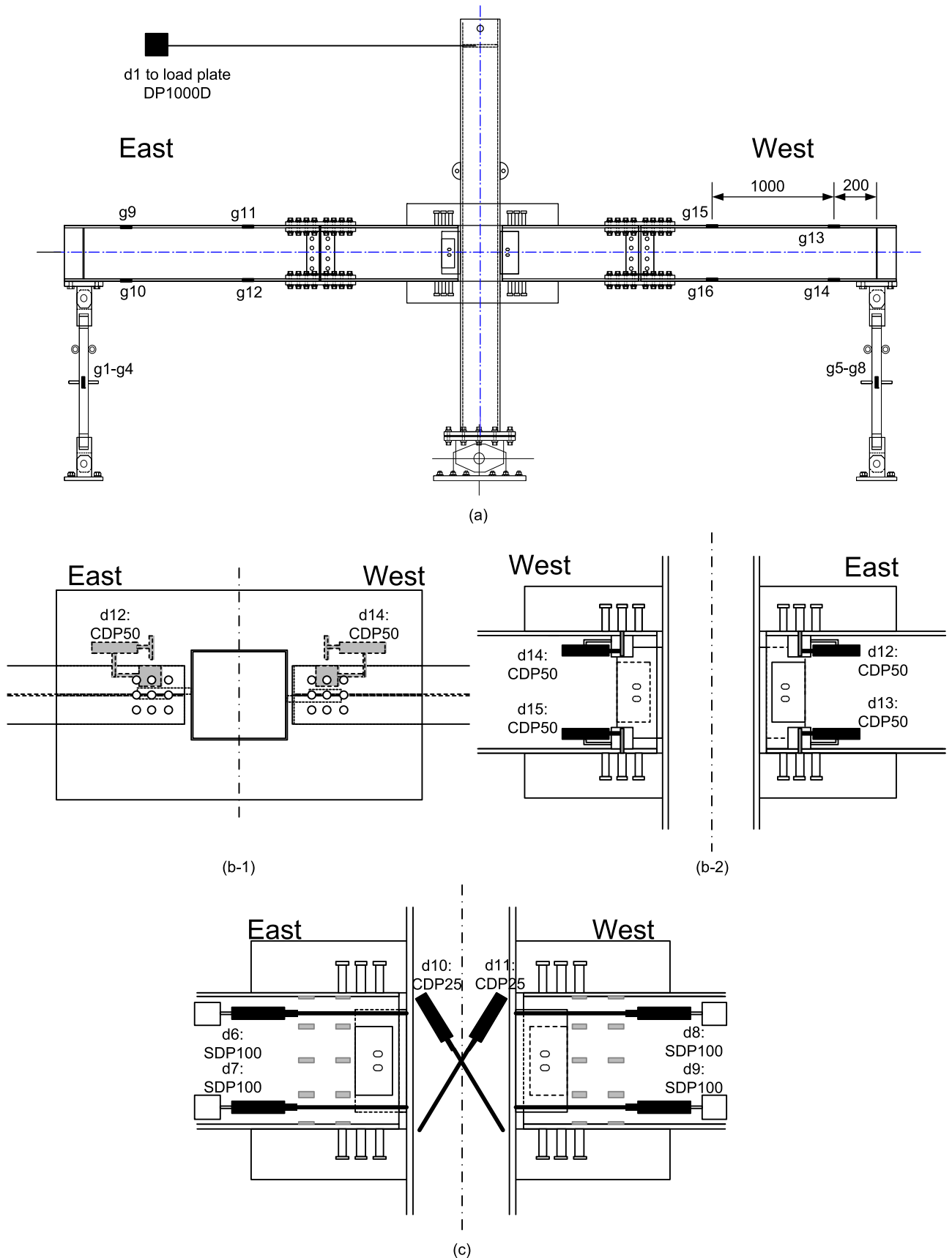
Fig. 6.9 Layout of LVDT: (a) globe view; (b-1) plane view for slip measure;
(b-2) side view for slip measurement; and (c) side view for the rotation of beam and panel zone
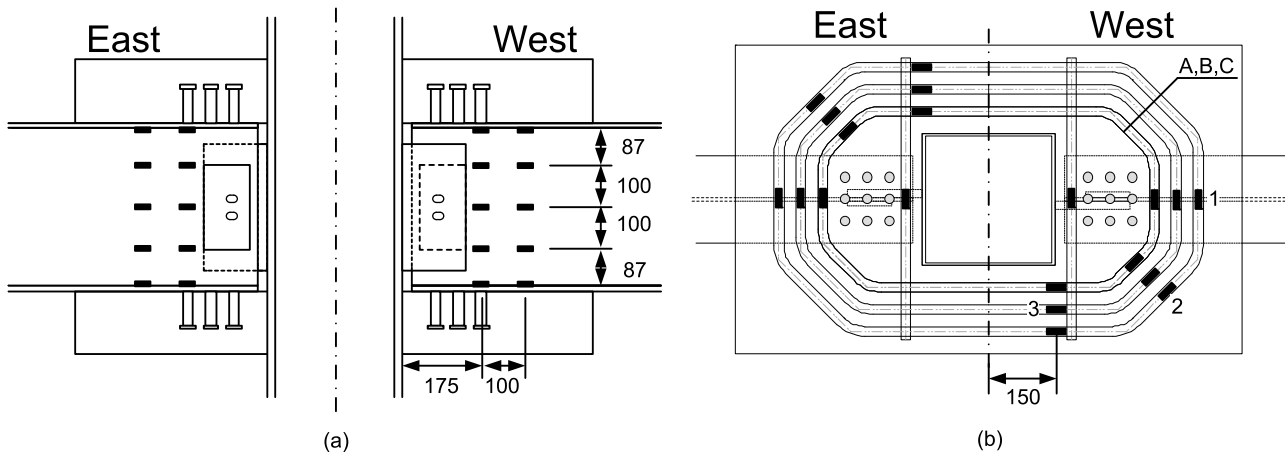(unit:mm)

Fig. 6. 10   Layout of strain gauges: (a) side view of beam; (b) plane view of rebars (unit: mm)

The strut located at the end of each beam was attached with gauges to measure the reaction force. There were some gauges on the beams, near the connection, as well. Four gauges were placed on the column to observe the column yielding. A typical strain gauge layout is shown in Fig. 6.10. The rebars of the bottom SFRCC slab were also instrumented to investigate the contribution of rebars. A grid was drawn on the slab and the cracks were marked at various peak displacements. At each level of the peak displacement, these cracks served as a qualitative measure of the level of damage. Meanwhile, slip between the SFRCC slab and the beam was also measured by way of strips of paper, resembling tape measures at each end of the SFRCC slab.

6.3 Test Results

6.3.1   Moment-rotation relationships

The column tip load versus story drift curves of Specimens 'C-4PG50' and 'C-9PG50' are compared in Fig. 6.11. The story drift equals the lateral displacement at the loading point divided by the column height, 3000 mm. Both specimens showed stable behavior till the story drift of 0.02 rad. For Specimen 'C-4PG50', studs fractured during at the first cycle of 0.03 rad story drift, and the connection lost its strength after the first cycle at 0.03 rad. As illustrated in Fig. 6.11, the connection of Specimen 'C-9G50' exhibits more stable hysteretic behavior up to 0.04 rad of story drift. While the specimen lost its strength during the first cycle of 0.06 rad story drift because of the failure of slab, which will be discussed later. It is also obvious that Specimen 'C-9PG50' showed fatter hysteretic curves than Specimen 'C-4PG50'. However, the stiffness deterioration of Specimen 'C-9PG50' is clear. As mentioned before, the beam load was transferred by the studs to the SFRCC slab and then to the column face by the compression of the SFRCC slab in the new beam-column connection system. During the loading, the stress concentration was significant at the portion of SFRCC around the lower portion of the studs. It is speculated that the local crush of SFRCC caused such stiffness deterioration.
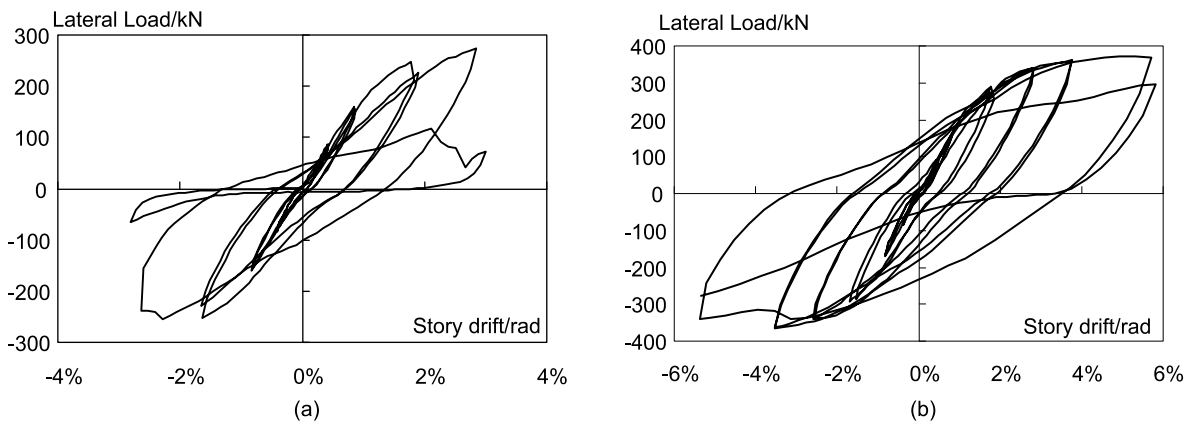
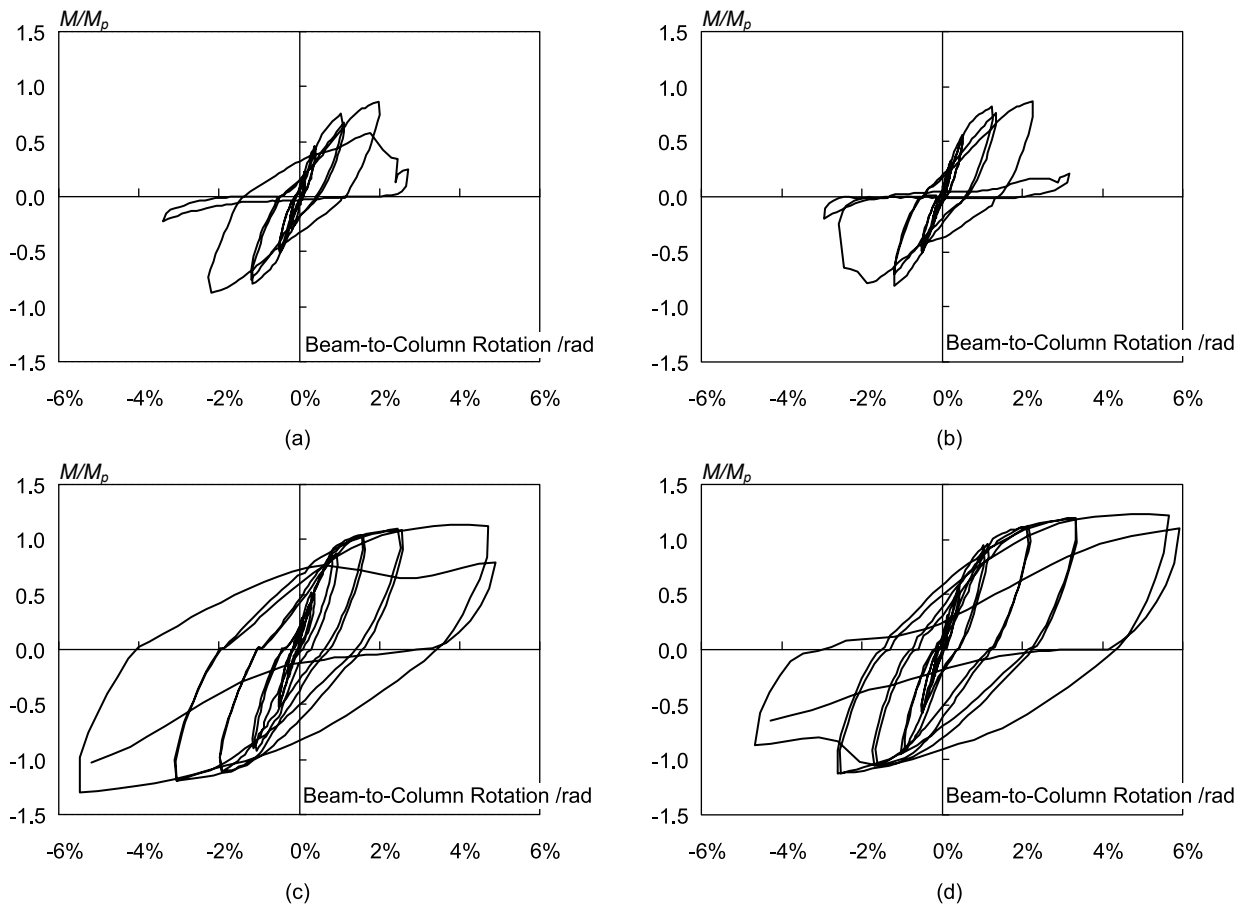Fig. 6. 11 Load versus story drift rotation curves: (a) 'C-4PG50'; (b) 'C-9PG50'

Fig. 6. 12 Beam moment versus beam-to-column rotation curves:
(a) East connection of Specimen 'C-4PG50'; (b) West connection of Specimen 'C-4PG50';
(c) East connection of Specimen 'C-9PG50'; and (d) West connection of Specimen 'C-9PG50'

The performance of each side connection (East and West) is studied in Fig. 6.12 in terms of the normalized beam end moment versus beam-to-column rotation. Here, the beam moment is estimated at the face of the column, and the moment is normalized by the full plastic moment of the beam M_p. For each beam, the applied load was calculated based on the strain measurements of the two support struts attached with strain gauges. The rotation of the beam relative to the column was measured using two LVDTs that were placed near the top flange and bottom flange (see Fig. 6.9

6 - 13

(c)). The definition of loading direction is illustrated in Fig. 6.13. It is notable that East and West beam exhibited almost the same behavior during the loading. The fracture sequence can be examined in reference to Fig. 6.12. The west connection of both specimens failed first during the negative loading of the first cycle at 0.03 rad and 0.06 rad story drift for Specimen 'C-4PG50' and Specimen 'C-9PG50', respectively. The east connection failed at the second loading cycle while the loading direction was positive, when the top beam flange was in compression.

Table 6.3 summarizes the results, including the elastic stiffness (K_0), the maximum moment of each beam (M_{max}), the dissipated energy of each beam (E_p), and the failure mode. It should be noticed that the elastic stiffness (K_0) is defined based on the lateral load (P) - story drift (Δ) relationships, while the maximum strength and dissipated energy are defined based on the beam moment – beam-to-column rotation relationships. The elastic stiffness of the specimen is defined as the secant stiffness between the points at ±0.5% rad of the load (P) versus story drift (Δ) curves. The maximum moment of the East and West beam (M_{max}) are calculated at the column face for both specimens. And the maximum moments in the positive and negative direction were averaged. The dissipated energy (E_p) was estimated from the total area of the hysteretic loops. For both specimens, the calculation was made from the start of loading to the completion of loading with the 3% rad drift angle amplitude.
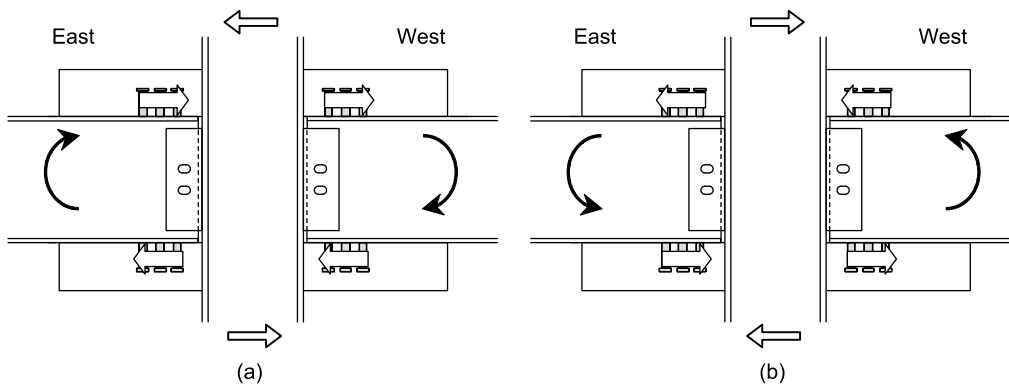

Fig. 6. 13   Definition of loading direction: (a) positive loading; (b) negative loading

Table 6.3 Test results

Sepc.	K_0 (kN/m)	M_{max} (kN·m)		E_p (kN·m·rad)		Failure mode
		East beam	West beam	East beam	West beam	
'C-4PG50'	6804	389.9	375.6	25.69	24.93	Fracture of studs
'C-9PG50'	7143	547.8	527.4	29.00	34.87	Beam yielded following by slab fracture

As shown in Table 6.3, the two specimens showed almost the same elastic stiffness with the difference of 5%. The number of studs had a minimal influence of the initial stiffness. It is speculated to be because the studs of Specimens 'C-4PG50' and 'C-9PG50' were able to transfer the same amount of flange force during initial loading. In addition, the theoretical elastic stiffness (Eq. (6-1))

6 - 14

based on the unit virtual load method using the rigid connected beam-column connection frame mode, shown in Fig. 6.14 is 7391 kN/m. The difference between the test and theoretical elastic stiffness is 8% and 3% for Specimens 'C-4PG50' and 'C-9PG50', respectively. However, the contribution of the SFRCC slab is not counted in the frame model (Fig. 6.14). The beam and column are in part rigidly connected using the studs in the new connection system. The slip between beam flange and SFRCC slab reduced the stiffness, but the SFRCC slab still exhibited a large stiffness. The contribution of the SFRCC slab is speculated to cancel the reduction of the stiffness caused by possible slips. Therefore, it is assumed that the new beam-column connection has similar stiffness properties as the rigid connected beam-column connection.

$$K = \frac{1}{2(\dfrac{H^2 L}{3EI_b} + \dfrac{H^3}{3EI_c})}$$ (6.1)

where

E : Young's Modulus of steel (205,000 N/mm^2)

I_b : moment of inertia of beam section (23,500×10^4 mm2)

I_c : moment of inertia of column section (26,200×10^4 mm2)

H : length of column measured from load point to pin connection (1,500 mm)

L : length of beam measured from point of support strut to center of column section (3,000 mm)
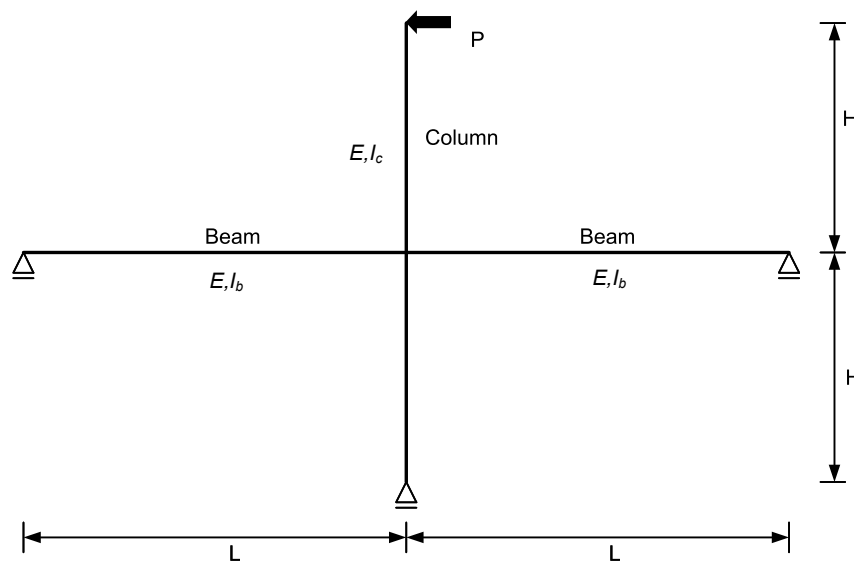

Fig. 6. 14 Cruciform frame model

The maximum beam moment of Specimen 'C-9PG50', in which the beam yielded before the slab fracture, was 30% larger than the moment of Specimen 'C-4PG50', which failed by stud fracture. A conventional bare steel beam-column connection with through diaphragm details (Suita et al. 2009) was chosen to compare with the new beam-column connection specimens. As shown in Fig. 6.15, the beam moments are normalized by the full plastic moment of the corresponding beam, M_p. Since Specimen 'C-4PG50' failed by stud fracture, the maximum moment of the East and West beam are

about 0.8M_p. While the maximum beam moment of Specimen 'C-9PG50' were about 1.2M_p, which is similar to the moment resistance of the bear steel beam-column connection. It is experimentally proved that the new beam-column connection can sustain similar moment resistance as the bare steel beam-column connection.
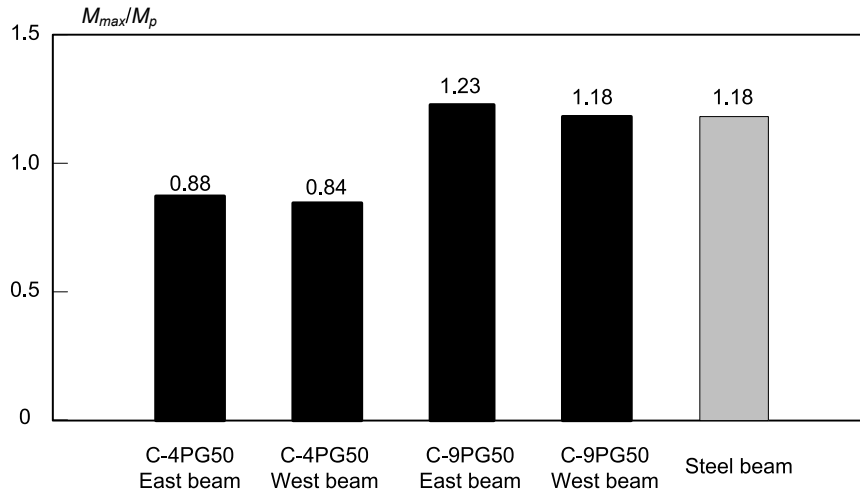

Fig. 6. 15 Normalized maximum moment

Up to 3% rad story drift, the energy dissipation of Specimen 'C-9PG50' is about 1.3 time that of Specimen 'C-4PG50'. The equivalent viscous damping coefficients of both specimens are compared with that of the aforementioned bare steel beam-column connection specimen (Suita et al. 2009) in Fig. 6.16. The equivalent viscous damping coefficient of Specimen 'C-4PG50' is reduced at 3% rad story drift, because of the stud fracture. The coefficient of Specimen 'C-9PG50' is reduced at 6% rad story drift, because of the slab fracture. In comparison with the bare steel beam-column connection specimen (Suita et al. 2009), the new beam-column connection specimens shows similar energy dissipation up to 1% rad story drift. After that, the new beam-column connection specimens dissipated less energy. It is speculated that the SFRCC around the studs are locally crushed, which promoted the pinching of the hysteretic curves.
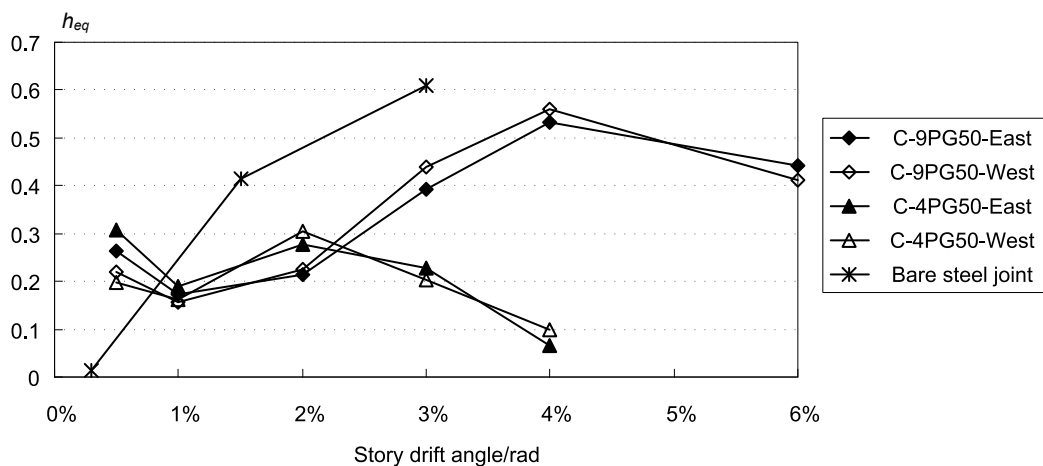

Fig. 6. 16 Equivalent viscous damping coefficient

6.3.2   Failure mechanism

Two failure modes occurred in the specimens as shown in Fig.6.17 (a) and (b). Specimen 'C-4PG50' failed by stud fracture, and there were no significant cracks observed during the loading. And Specimen 'C-9PG50' failed by the slab fracture following the beam yielded. It is notable in Fig. 6.15 that the SFRCC slab of Specimen 'C-9PG50' deformed seriously than that of Specimen 'C-4PG50'. Figure 6.18 illustrates the load resisting mechanism of the new beam-column connection. The boundary condition of the SFRCC slab is actually unsymmetrical between top and bottom beam flange. When the beam flange took the compressive load (push hereinafter), the beam flange was restrained at the end of the SFRCC slab because of a larger sectional stiffness of the SFRCC slab. While when the beam flange took the tensile load (pull hereinafter), the beam flange was restrained at the section where the out most studs located. The reason is that the portion of SFRCC slab was pried out by the studs when the flange was pulled and then this portion of SFRCC slab could not follow the bending deformation of beam. Therefore, there always was some vertical separation (separation hereinafter) between the beam flange and the SFRCC slab, when the beam flange was pulled.

| (a) | (b) |

Fig. 6. 17 Failure of specimens: (a) stud fracture (Specimen 'C-4PG50');
(b) combination of slab fracture and beam yield (Specimen 'C-9PG50')

The two specimens exhibited similar behavior during the loading cycles up to 3% rad story drift. As shown in Fig. 6.19 (a) and (b), the horizontal slip (slip hereinafter) and vertical separation (separation hereinafter) between the beam flange and the SFRCC slab kept increasing as the load increased. The separation was 11 mm and 8 mm after the competition load of 3% story drift for Specimen 'C-4PG50' and Specimen 'C-9PG50', respectively. Specimen 'C-4PG50' failed by stud fractures in the first cycle of 3% rad story drift. According to the stain gauges data, the studs at the top flange of the West beam fractured first in the negative loading of the first 3% story drift loading cycle. Then the studs at the top flange of the East beam fractured in the positive loading of the second 3% story drift loading cycle. Several cracks formed at the surface of slab and from the root of the stud. However, these cracks did not propagate seriously, with the maximum crack width of 0.85 mm, till the specimen failed.
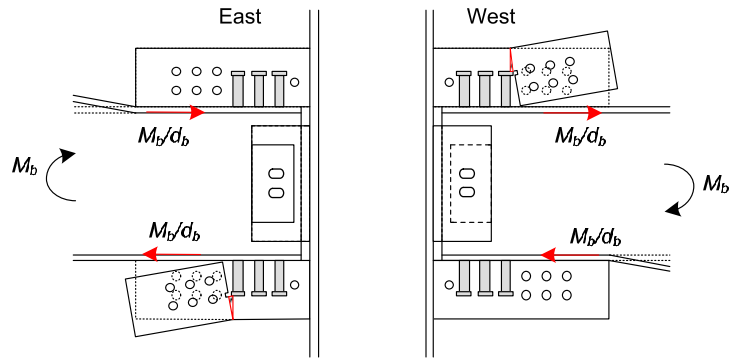
Fig. 6. 18 Exaggerated deformation of specimens

As observed in the test, the beam flange of Specimen 'C-9PG50' yielded (Fig. 6.19 (c)) in the first cycle of 4% story drift. Meanwhile there are several transverse cracks formed in the SFRCC slab. As shown in Fig. 6.19 (d), these transverse cracks were originated from the root of the studs, which was the same as the cracks observed in Specimen 'C-4PG50'. The transverse cracks at the bottom slab of the West beam widen to 10 mm at the negative loading of the first loading cycle of 6% story drift. Therefore, the SFRCC slab lost the capacity to transfer the beam load, and the West beam lost most of the strength. Then the transverse cracks at the bottom slab of the east beam widen to 15 mm at the positive loading of the second loading cycle of 6% story drift and East beam failed.
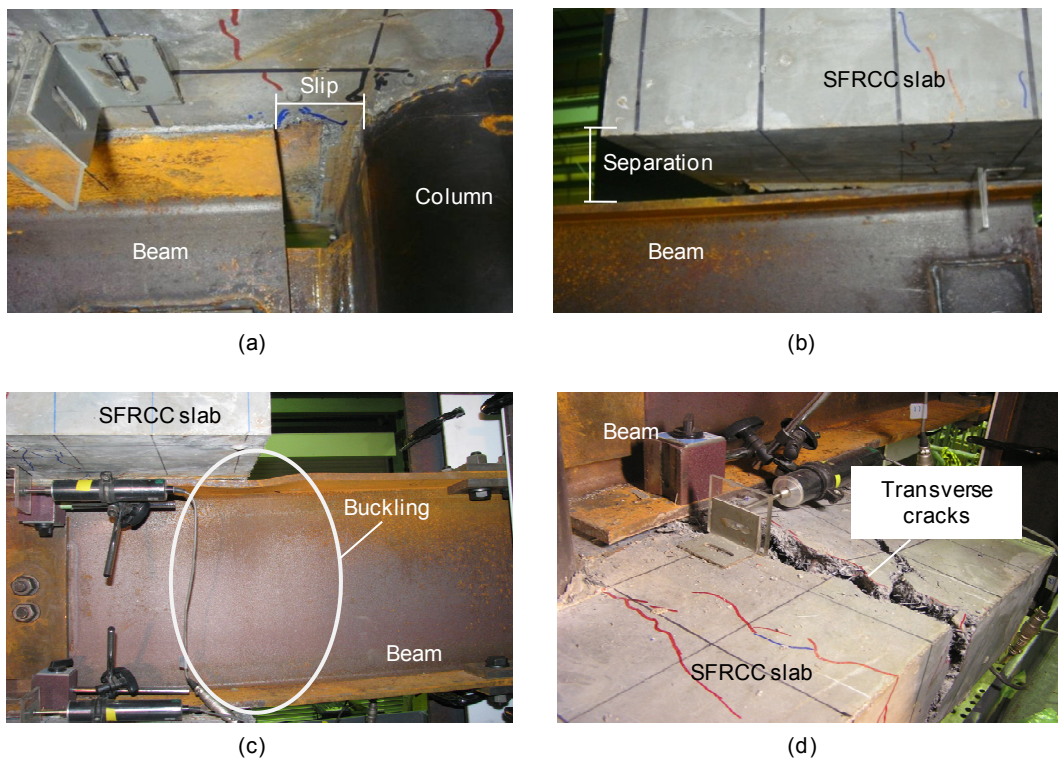

Fig. 6. 19 Experimental observation:
(a) slip between beam flange and SFRCC slab; (b) separation between slab and beam flange;
(c) local buckling of beam; and (d) transverse cracks of SFRCC slab

6.3.3   Behavior of headed studs

Specimen 'C-4PG50' has the same layout of studs as the push-out specimen '4PG50', whose detail was described in Chapter 5. The load per stud versus slip relationships of these two specimens are compared in Fig.6.20 (a). The abscissa is the measured slip between the beam flange and SFRCC slab (see Fig. 6.9 (b) for the measured location). The ordinate is the load taken by the individual stud. The load per stud for Specimen 'C-4PG50' is calculated by dividing the moment at the column face by the beam height and the number of studs. As discussed previously, the boundary conditions of the SFRCC slabs were different when the beam flange was pulled or pushed. Therefore, the load-slip relationship of the studs in Specimen 'C-4PG50' is shown with respect to the loading direction of the beam flange: push and pull. These two specimens, the connection specimen 'C-4PG50' and the push-out specimen '4PG50', both failed by stud fracture. However, the stud of Specimen 'C-4PG50' transferred larger load (242 kN) than the push-out specimen '4PG50' (192 kN). On the other hand, when the beam flange was pulled, the stud of Specimen 'C-4PG50' exhibited more ductile behavior, which is similar to the post-yield stud behavior of Specimen '4PG50'. As shown in Fig. 6.20(a), the stud of Specimen 'C-4PG50' reached the maximum strength earlier when the beam flange was pushed at a slip of around 1.5 mm. In contrast, when the beam flange was pulled, the studs reached the maximum strength at a slip of around 4.5 mm.
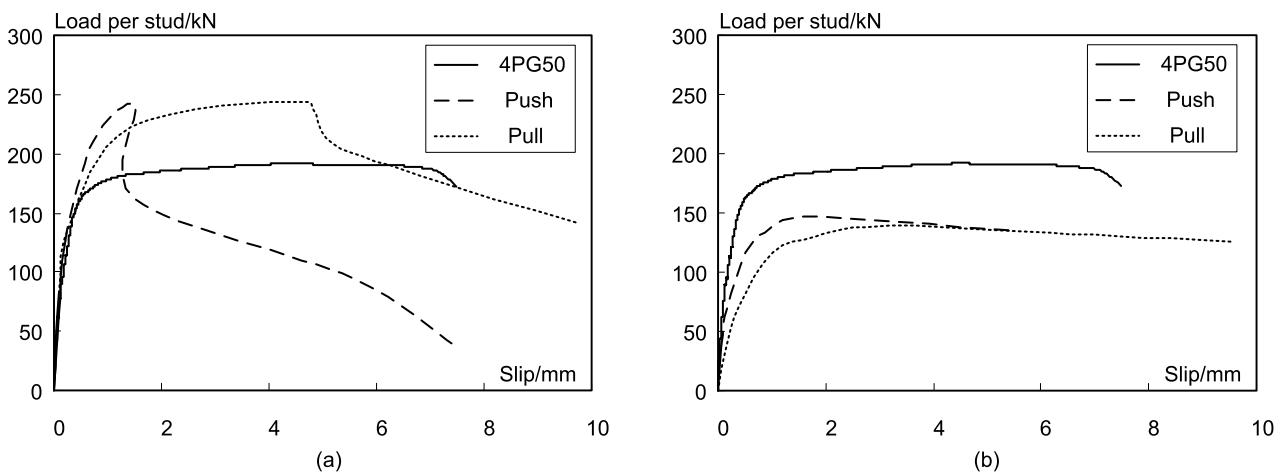

Fig. 6.20 Comparison of load-slip curves of stud: (a) Specimen 'C-4PG50'; (b) Specimen 'C-9PG50'

The difference in stud behavior is primarily caused by the different stress distribution of the stud. When the beam flange is pushed, the SFRCC slab is fully restricted at the column face because of the contribution of the portion of SFRCC slab at the other side. The deformation of the SFRCC slab is therefore slight. The studs embedded in the SFRCC slab therefore take shear force only. When the beam flange was pulled, the end of SFRCC slab is free. The SFRCC slab is deformed because of the pry out of the studs. The deformation of the SFRCC slab induces the moment to the studs. The studs therefore take both shear and tension force simultaneously. In the push-out test, the studs also take the shear and tension force simultaneously, because of the moment induced by the friction force at the end of slab. The tension force will reduce the shear resistance of the stud and increase the ductility of the stud behavior. According to the test results, the resisting force of studs measured from the

push-out test can be used directly to predict the transferred flange force by the studs in the new beam-column connection, as it provides a conservative estimate.

As shown in Fig. 6.20 (b), the studs of Specimen 'C-9PG50' show smaller maximum strengths than those of Specimen '4PG50'. Moreover, there is no sudden strength reduction occurred in the load-slip curves of Specimen '9-PG50'. It is further proved that the studs of Specimen 'C-9PG50' are intact and sufficient to transfer the beam load. The strength deterioration of the load-slip curves was caused primarily by the beam yielding and the slab failure instead of the stud fracture.

6.3.4 Effect of rebars

The distribution of strains along one rebar and the difference in strain between the rebars of Specimens 'C-4PG50' and 'C-9PG50' are investigated in this section. As previously mentioned, the rebars of the bottom slab were instrumented with strain gauges as illustrated in Fig. 6.10 (b). Strains were measured at six locations on the rebars. The strain gauges were oriented so that strains were measured along the axis of the rebars. The nomenclature used to identify the strain gauges was based on the location on the rebars. The layer of rebars arranged farther from the beam flange surface was identified as the top layer of rebars, and the strain gauges in this layer were classified using the label of "U".   There three rebar rings in each layer were identified using the labels of "A, B, C" from the most inner to the most outer. The three locations on the rebars were classified using label of "1, 2, 3" as shown in Fig. 6.10 (b). In addition, each strain gauge label was classified based on its location on the specimen relative to the laboratory (East and West). For example, the strain gauge of 'UAE1' was the strain gauge installed at the location 1 of the most inner rebars of the upper layer on the East side.

The typical measured strains of Specimens 'C-4PG50' and 'C-9PG50' are shown in Fig. 6.21. The measured rebars strain is positive during the loading, which indicates that the rebars take the tensile force during the loading. The rebars of Specimen 'C-9PG50' generally exhibited larger strains magnitude than those of Specimen 'C-4PG50'. The rebars ring which is close to the studs showed slightly (generally 10%) larger strains than the other two rebars rings at the same layer for each specimens. By comparing Fig. 6.21 (a) and (b) and Fig. 6.21 (c) and (d), it is notable that the three rebars rings located close to the beam flange showed 2 to 3 times larger strains than the others. It is coincided with the discussion of Chapter 5 that the rebars located near the root of studs took the largest resisting force than others.
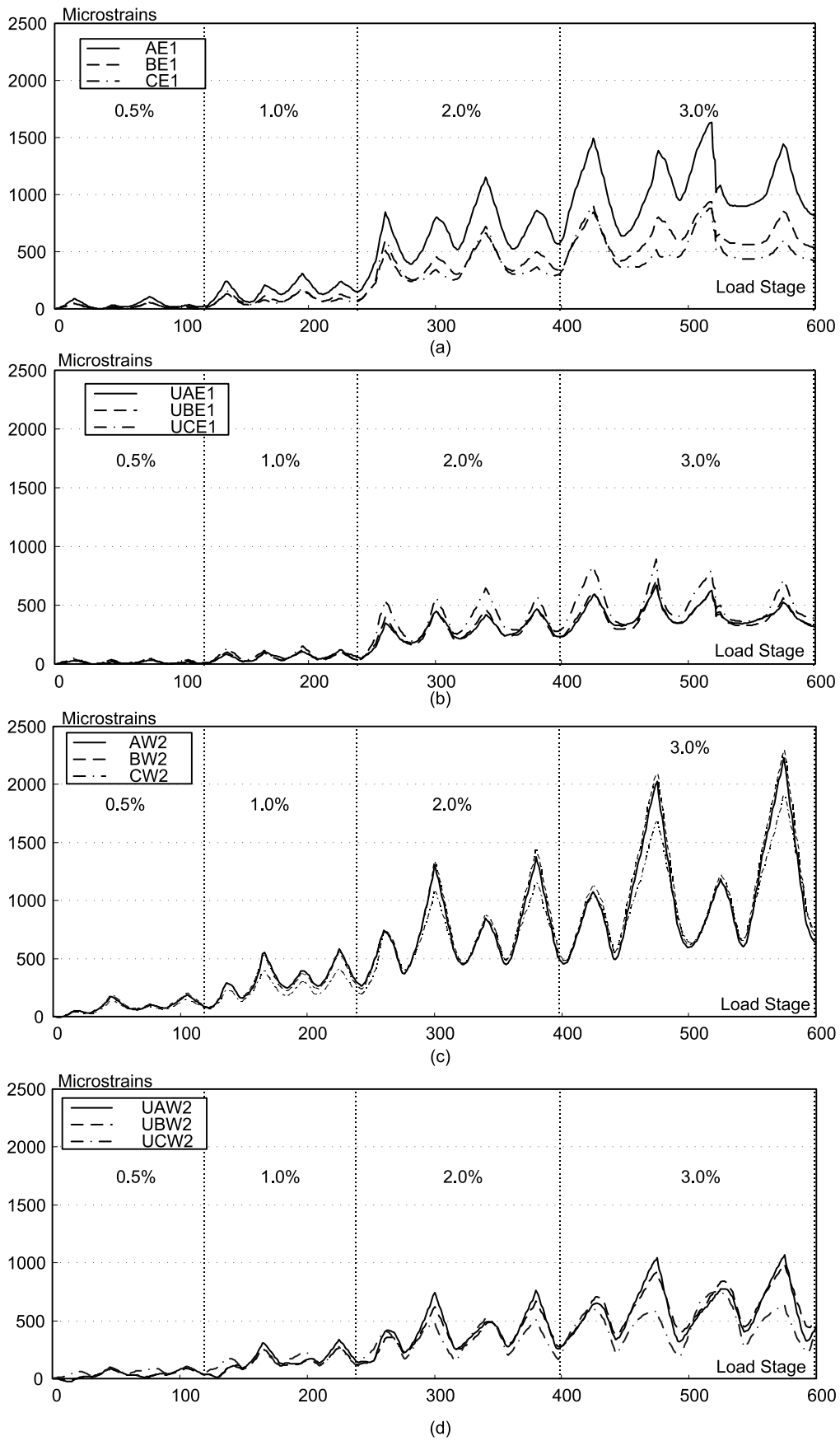
Fig. 6.21 Rebars strains: (a) bottom layer of Specimen 'C-4PG50'; (b) top layer of Specimen 'C-4PG50'; (c) bottom layer of Specimen 'C-9PG50'; and (d) top layer of Specimen 'C-9PG50'

It is notable that the rebar strains are smaller than the yield strain (2,000 $\mu\varepsilon$) up to 3% story drift angle. Therefore, the measured strain is used to estimate the resisting force of rebars using Eq. (6.2).

$$Force_{x,east/west} = \sum \varepsilon_{x,east/west} \cdot E \cdot A \tag{6.2}$$

Where, $Force_{x,east/west}$ is the total resisting force of rebars at one measured location on either the East or West side, E is the Young's Modulus of rebars, and A is section area of rebars.

It is assumed that the portion of rebars in the longitudinal direction took only the axial force. Therefore, the measured strain at location 3 was directly used to evaluate the amount of resisting force of the rebars. The calculated reisisting force of the rebars at the peak load at each drift level is ploted in Fig. 6.22. The rebars of both specimens showed almost the same resisting force up to 3% story drift, except the rebars on the West side of Specimen 'C-4PG50', which showed 40% smaller resisting force in the negative loading of 3% rad story drift. Reduction of resisting force occurred because the studs of the West beam of Specimen 'C-4PG50' fractured at that loading cycle and the beam flange load therefore was not transferred to the slab. According to this observation, it can be concluded that the new beam-column connection can transfer the same amount flange load regardless of the number of studs before the studs fractured.
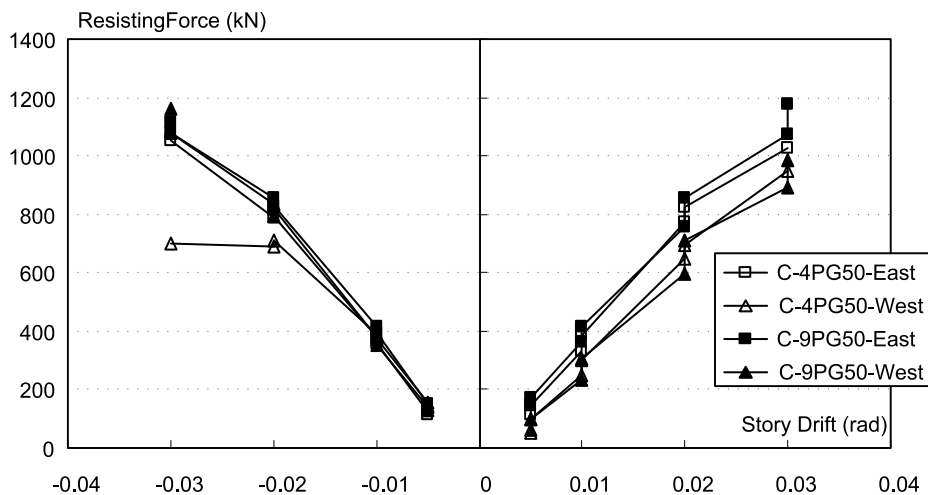

Fig. 6.22 Resisting force of rebars

Figure 6.23 showed the ratio of resisting force of rebars to the beam flange load. The ratio is calculated based on the Eq. (6.3).

$$\beta = \frac{Force_{x,east/west}}{Force_{lateral,east/west}} \tag{6.3}$$

Where, $Force_{lateral,east/west}$ is the flange load of each beam which is calculated by dividing the beam moment at the column face by the height of beam section. It is observed that the rebars transferred almost all the beam flange load at the story drift angle of 3%. It indicated that the amount of designed rebars is sufficient in this test.
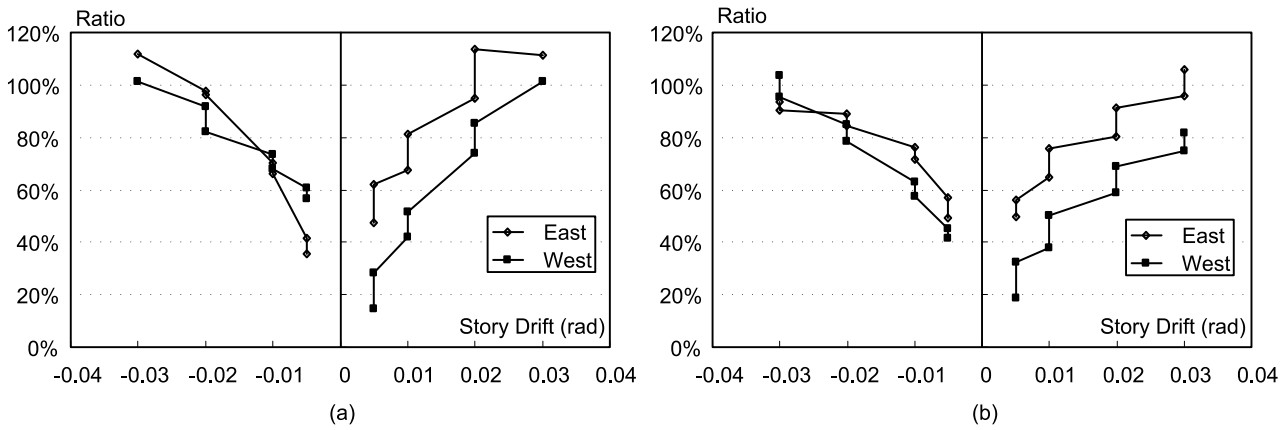
Fig. 6.23 Ratio of resisting force of rebars to beam flange load:
(a) Specimen 'C-4PG50'; (b) Specimen 'C-9PG50'

As aforementioned, the rebars in the transverse direction, perpendicular to the beam direction, were designed to prevent the split cracks caused by the studs. Here, the ratio between the resisting force of rebars at location 1 and location 3 (see Fig. 6.10 (b) for the location) is calculated by Eq. (6.4).

$$\alpha = \frac{Force_{1,east/west}}{Force_{3,east/west}}$$

(6.4)

When $\alpha > 1$, the rebars at location 1 take more resisting force than location 3, which means local deformation occurred at location 1; while when $\alpha < 1$, there is no local deformation occurred at location 1.
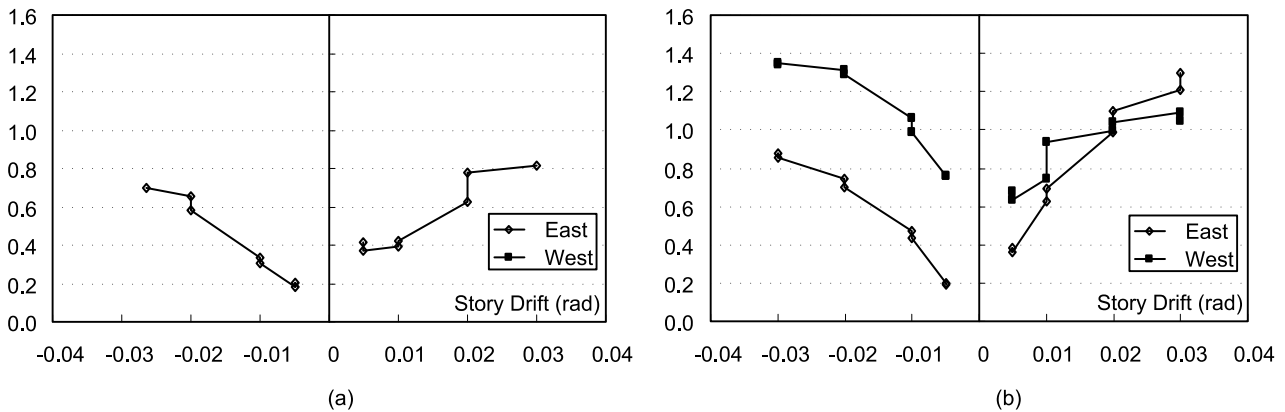

Fig. 6.24 Ratio of resisting force of rebars between location 1 and location3:
(a) Specimen 'C-4PG50'; (b) Specimen 'C-9PG50'

The ratio at each drift level is plotted in Fig. 6.24. Since some strain gauge at location 1 of Specimen 'C-4PG50' was broken during the test, only the ratio of the East side is shown. It is notable that for Specimen 'C-4PG50' rebars at location 1 always take smaller force than location 3. The primary reason is that the split crack is not significant in Specimen 'C-4PG50'. Contribution of rebars in front of the studs is slight. For Specimen 'C-9PG50', the value α of the rebars on the East is larger than unity after 2% story drift in the positive loading. While in the negative loading, rebars at location 1

always take smaller force than location 3. Such a mechanism is illustrated in Fig. 6.25. During the positive loading, the bottom beam flange on the East was pulled and the one on the West was pushed, therefore the rebars in front of the studs along the transferred load direction, location 1 on the East, would have worked to prevent the split cracks, while the rebars rear to the studs would not. The same phenomenon was observed for the West side rebars of Specimen 'C-9PG50'. The experimental observation proved that the design concept of rebars was rational.
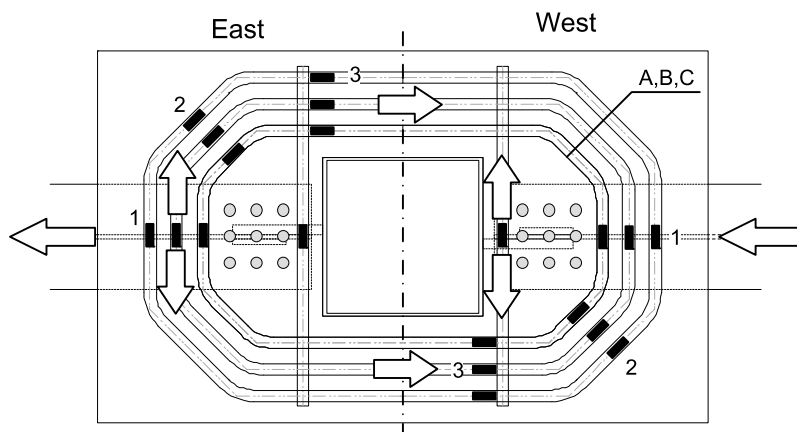

Fig. 6.25 Resisting force flow of rebars in positive loading

6.4 Conclusions

To examine the constructability, seismic performance and failure mechanism of the new beam-column connections, two full scale cruciform connection specimens were tested under horizontal cyclic loading. According to the test results, the new beam-column connection was found to be a promising connection for seismic design of ductile steel moment frames. Major findings obtained from the tests are as follows:

(1) Both specimens failed as the designed failure mode. The specimen with four studs (Specimen 'C-4PG50') failed by stud fracture, while the specimen with nine studs (Specimen 'C-9PG50') failed by beam yielding followed by slab fracture. The specimen failed by beam yielding exhibited fatter hysteretic curves than the other specimen.

(2) The number of studs showed minimal effect on the elastic stiffness. The two specimens showed almost the same elastic stiffness with a difference of 5%. In addition, the measured elastic stiffness agreed with the theoretical elastic stiffness well with a difference not greater than 10%.

(3) The experimental results revealed that the new beam-column connection has a potential to assure the formation of plastic hinges in the beam and achieve large energy dissipation and ductile behavior. In terms of the energy dissipation, the new beam-column connection showed the same value as the conventional beam-column connection up to 0.01 rad.

(4) Because of the presence of secondary bending moment, the studs of Specimen 'C-4PG50' showed 1.27 times larger strength and more brittle behavior in comparison of Specimen '4PG50', the push-out test specimens with four studs for each beam flange. From the test results, the resisting force

of studs measured from the push-out test could directly be used to predict the transferred flange force by the studs in the new beam-column connection.

(5) Rebars in the longitudinal direction, along the beam direction, were arranged to resist the tensile load in the SFRCC slab. While rebars in the transverse direction, perpendicular to the beam direction, were arranged to prevent split cracks caused by the studs. Such a resisting mechanism was proved based on the strain data glued on rebars. The rebars located closest to the root of studs resist the largest force than others. It coincides with the observation of Chapter 5.

6.5 Future Research

In this chapter, workability of the new beam-column connection was experimentally proved. Based on this study, the new beam-column connection was found to sustain similar stiffness (5% difference) as the theoretical stiffness of the corresponding rigid connected beam-column connection. However, contribution of the SFRCC slab to the elastic stiffness was not taken in full account. The new beam-column connection is designed to fail by beam yielding at the end of the SFRCC slab. A strong SFRCC slab and sufficient number of studs are needed to guarantee the failure mode. Studs should be arranged by considering not only the group effect but also the different loading condition, such as pure shear loading versus combined shear and tension loading. To develop a reasonable stiffness and strength evaluation procedure for the new beam-column connection, further work, both experimental and numerical, are needed.

REFERENCES

[6.1]   Architectural Institute of Japan (AIJ). (1995). Reconnaissance Rep. on Damage to Steel Building Structures Observed from the 1995 Hyogoken Nanbu Earthquake, Kinki Branch, Osaka (in Japanese).

[6.2]   Architectural Institute of Japan (AIJ). (1996). Japanese architectural standard specification: JASS 6 steel work, Tokyo (in Japanese).

[6.3]   Architectural Institute of Japan (AIJ). (2006). Recommendations for design of connections in steel structures, Tokyo (in Japanese).

[6.4]   Federal Emergency Management Agency (FEMA). (2000). Recommended seismic design criteria for new steel moment-frame buildings. FEMA350, Washington, D.C.

[6.5]   Kaneko Y., Mihashi H., Kirikoshi K., and Abe T. (2001). "New Application Field of Steel Fiber Reinforced Cementitious Composites – Experiment on column-beam joint in steel structures." *Journal of architecture and building science*, Vol. 116, No.1481, 119-122.

[6.6]   Kaneko Y., Mihashi H., Kirikoshi K., and Abe T. (2002). "Simple Column-Beam Joint of Steel Structures Employing Steel Fiber Reinforced Cementitious Composite: Experimental verification on structural performance of joint." *Journal of structural and construction engineering* (Transactions of AIJ), No.558, 219-225.

[6.7]   Nakashima, M., Inoue, K., and Tada, M., (1998). "Classification of damage to steel

buildings observed in the 1995 Hyogoken-Nanbu earthquake." *Eng. Struct.*, 20(4-6), 271-281.

[6.8]   Suita, K., Nakashima, M., and Engelhardt, M. D. (2000). "Comparison of seismic capacity between post-Northridge and post-Kobe beam-to-column connections." *Proc. 3rd Int. Conf. on Behavior of Steel Struct. In Seismic Area* (*STESSA 2000*), Montreal, 271-278.

[6.9]   Suita Keiichiro, Kitamura Yukiko, and Hashida Isao. (2009). "Seismic performance and retrofit of beam-to-column connection for early high-rise buildings." *Journal of structural and construction engineering, Transactions of AIJ*, 74 (636), 367-374.

[6.10]   Youssef, N.F.G., Bonowitz, D., and Gross, J. L. (1995). "A survey of steel moment resisting frame buildings affected by the 1994 Northridge earthquake." NISTIR 5625, National Institute of Standards and Technology, Gaithersburg, Md.

CHAPTER 7

Summary and Conclusions

Steel moment resisting frames are commonly used in seismic regions. During the 1995 Hyogoken-Nanbu (Kobe) earthquake and the 1994 Northridge earthquake, a large number of steel frames buildings developed cracks and brittle fracture in welded beam -column connections and some buildings suffered fracture of anchor bolts at column base connections. The fractures at welded beam-column connections were partly attributed to weld defects and insufficient deposition. How to ensure weld quality has been a key issue since that time. Because of the elongation of anchor bolts, the behavior of column bases is characterized by severely pinched hysteresis that is low in energy dissipation. How to increase the energy dissipation of such column bases is an issue. To overcome the difficulty in the weld quality assurance and enhance the plastic deformation of column base connections, it is desirable to develop new ductile connections. Recently a variety of construction materials have been developed to supplement conventional concrete and steel, steel fiber reinforced cementitous composites (SFRCC) is one of the advanced concrete. It shows not only high strength but also larger ductility relative to conventional concrete. The application of SFRCC so far is limited to precast elements. In this study, two connections (shallowly embedded column bases and the new beam-column connections), in which SFRCC slab is applied, are proposed.

The shallowly embedded column base is the exposed column base covered by a relatively thin slab, whose thickness is not greater than two times of the column width. In this column base connection, the covering slab is expected to provide larger resisting strength and dissipate more energy. The seismic behavior of the shallowly embedded column base was tested in cyclic loading condition. The effects of the slab thickness, slab shape, and rebar on the elastic stiffness, maximum strength, and energy dissipation were investigated. Design procedures of the elastic stiffness and maximum strength were developed as well. Furthermore, a numerical model was developed to generalize the behavior of shallowly embedded column bases.

The new beam-column connection is proposed aimed at solving the difficulty in the weld quality assurance. In the new beam-column connection, the portion of the slab around the column is cast in SFRCC. The SFRCC slab is applied on both the top and bottom beam flange by which welding between the column and beam flange is avoided completely. The headed studs are densely welded on the beam flange to transfer the beam force to the SFRCC slab. In this connection, the beam hinge is expected to form at the end of the SFRCC slab. In this study, workability of the new beam-column connection is investigated based on a series of cyclic loading test. The effect of the number of headed

studs to the elastic stiffness, maximum strength, and energy dissipation are also investigated.

This dissertation consists of seven chapters. Chapter 1 is the introduction, including the background and objectives of the dissertation. Chapters 2 and 3 deal with the experimental and numerical studies on the seismic behavior of shallowly embedded column bases with conventional concrete slab and design information is provided. Chapters 4 addresses the experimental and numerical investigations on the seismic behavior of shallowly embedded column bases with SFRCC slab. As a prelude of Chapter 6, Chapter 5 presents the stud behavior in solid SFRCC based on the test and numerical analysis. Chapter 6 presents the experimental investigations on the seismic behavior of the proposed new beam-column connection using headed stud connectors and SFRCC slab.

Test on Shallowly Embedded Column Base with Conventional Concrete Slab

A series of quasi-static cyclic loading tests of steel column bases were conducted to investigate how the floor slab would contribute to the seismic performance of column bases. Major test variables were the thickness, the shape of the floor slab, and the horizontal rebars. Major observations obtained from this study are as follows.

(1) The elastic stiffness, maximum strength, and dissipated energy were improved by the presence of the floor slab. The elastic stiffness of the shallowly embedded column base specimens was about 1.1 times and 1.5 times for the 100 mm and 200 mm thick floor slabs, respectively. For the same thickness slab, neither the slab shape nor the horizontal rebars contributed to the improvement of elastic stiffness.

(2) Configuration (thickness and shape) of the floor slab influenced the maximum strength significantly. The presence of horizontal rebars further increased the maximum strength. Compared with the baseline exposed column base specimen, the maximum increase was around 2.0 times for the specimen featured with both the thickest slab and horizontal rebars.

(3) The deformation capacity was improved by the installation of horizontal rebars. Strength deterioration due to punching shear failure of the floor slab started at around a drift angle of 0.03 rad. Because of the presence of horizontal rebars, the strengthened specimens sustained 90% of the maximum strength until the drift angle reached 0.06 rad.

(4) The punching shear failure in the floor slab was the main failure mode of the shallowly embedded column base. However, the failure mode was converted to the column local buckling mode when the strength of the column base became larger than the full-plastic moment of the column.

(5) Considering the performance and the volume of concrete, the shallowly embedded column base having elevated foundation shape is recommended in practice. The elastic stiffness, maximum strength and dissipated energy increased 1.5, 2.0, and 2.7 times as compared with that of the corresponding exposed column base.

(6) Using the plasticity theory applied to the punching shear failure on the uplifted side of the floor slab and the compressive failure on the compressive side of the floor slab, the maximum strength can be estimated with reasonable accuracy regardless of the thickness and geometrical condition of the floor slab. The evaluated results show no more than 20% errors compared with the corresponding test results.

(7)   Using the elasticity theory applied to the same model adopted for the strength evaluation, the elastic stiffness can be estimated with reasonable accuracy regardless of the geometric condition of the floor slab and presence of rebars. The evaluated results show no more than 15% errors compared with the corresponding test results.

Numerical Analysis of Shallowly Embedded Column Base with Conventional Concrete Slab

To enhance the understanding of the test results shown in Chapter 2, extensive numerical analysis was carried out. The numerical model was developed to simulate the cyclic behavior of specimens by incorporating a contact model between the base plate and anchor bolts and adopting a concrete damage plasticity model.

(1)   The slip of hysteresis curves of the test specimens was successfully reproduced by adopting contact interaction between the head of anchor bolts and base plate. By using the concrete damage plastic model, the cyclic behavior of concrete was simulated reasonably.

(2)   The maximum strength and elastic stiffness from the numerical results agreed with the test results with the difference not greater than 15%. Punching failure regions of the slab were successfully estimated from the analysis.

Furthermore, the behavior of shallowly embedded column bases was generalized through a series of parametric analysis. Investigation was given to the effects of three parameters, i.e. the thickness of concrete slab, the number of anchor bolts, and axial force ratio. Moreover, a design procedure to estimate the elastic stiffness and strength proposed in Chapter 2 was calibrated against the analytical results. Several conclusions can be drawn from the results.

(1)   The elastic stiffness is mainly affected by the slab thickness and axial force ratio. The number of anchor bolts has a minimal effect on the elastic stiffness with an increase of 10% when the number increases from 4 to 12.

(2)   The maximum strength is influenced by the slab thickness, the number of anchor bolts, and axial force ratio. Among these three parameters, the slab thickness shows the most significant effect on the maximum strength.

(3)   The design procedure to estimate the elastic stiffness proposed in Chapter 2 is calibrated against the analysis results. The difference between the prediction and analysis is at most around 20%. To simplify the evaluation of the elastic stiffness, the elastic stiffness is suggested to be a fraction of the elastic stiffness of the corresponding embedded column base.

(4)   The design procedure to estimate the maximum strength proposed in Chapter 2 is calibrated against the analytical results. The proposed evaluation was conservative in comparison with the analytical results. The difference between the prediction and analysis ranges from 10% to 30%.

Test on Shallowly Embedded Column Base with SFRCC Slab

A series of tests were conducted for shallowly embedded steel column bases with SFRCC floor slab. Major findings obtained from the tests are summarized as follows:

(1)   The elastic stiffness, maximum strength and energy dissipation of shallowly embedded column bases were improved by 40%, 70%, and 70%, respectively, by using SFRCC instead of

conventional concrete in the presence of the floor slab but without horizontal rebars.

(2)   With horizontal rebars, the maximum strength was further improved by 15% to 30%, and the strength deteriorated more gradually. As a result, energy dissipation of reinforced SFRCC specimens increased to about two times. The improvement was achieved even when the rebars were closely arranged and covered with SFRCC of a small thickness.

(3)   Contribution of high strength rebars to the performance was primarily toward the improvement of ductility, because the rebars yielded after large deformation. On the contrary, application of large size normal strength rebars was more effective to improve both the maximum strength and energy dissipation.

The experimental study provided fundamental information on the behavior of shallowly embedded column bases featured with SFRCC floor slab. A separate numerical study using FEM was conducted to reproduce the test results and quantify the effects of various parameters such as the slab thickness and rebars on the elastic stiffness and maximum strength.

(1)   By the application of the damaged plasticity model, the cyclic behavior of SFRCC is simulated reasonably.

(2)   The maximum strength and stiffness obtained from the analyses agree with the test results within a 20% difference. The failure region is also estimated successfully from the analysis.

(3)   The elastic stiffness of shallowly embedded column bases is essentially controlled by the slab thickness. A simplified equation is proposed to assess the elastic stiffness as a fraction of the corresponding elastic stiffness of fully embedded column bases.

(4)   Considering the material characteristics of SFRCC, the proposed equation to evaluate the maximum strength is revised for SFRCC slabs. The contribution in the tensile behavior is included in the revised evaluation of the punching resistance portion. The revised equation provides values within 20% errors with respect to the analytical results.

Push-out Test on Shear Stud Connectors in Solid SFRCC Slab

A series of push-out tests was conducted on four specimens with SFRCC with multiple studs arranged in small intervals. The results suggested that the application of SFRCC, which has a large tensile strength and ductility, promises larger shear forces transferred through stud connectors allocated in a small area. Major findings obtained from the tests are summarized as follows:

(1)   One headed stud connector embedded in solid SFRCC slab can transfer the load that 15% larger than the evaluated strength by AIJ and AISC specification. Compared with the headed stud connectors embedded in the normal concrete slab, the headed stud connectors embedded in SFRCC slab exhibited a larger slip strength and resisting load. It is primarily because of the larger material properties of SFRCC, i.e. a larger Young's Modulus.

(2)   The ultimate load per stud was reduced to 90%, when the longitudinal spacing of studs was 50 mm. The reduction occurred because of the overlap of bearing region in front of the studs. The transverse spacing of studs in an interval of 50 mm has no significant effect on the shear capacity of studs.

(3)   The shear capacity of studs was also controlled by the slab bearing capacity. An appropriate

amount of rebar is needed to strengthen the slab to guarantee the stud fracture occurred prior to the slab failure.

Finite element models were developed to simulate the behavior of headed stud connectors in solid SFRCC slab. The model took into account the nonlinear material properties. The numerical results agreed reasonably with the results obtained from the experimental results. Furthermore, three series of parametric analyses were conducted, and the following observations were drawn.

(1) For the model with two studs aligned longitudinally with only 50 mm spacing, the strength is smaller than other models with larger longitudinal spacing. In this model, the two crushed regions of the slab around the studs merge each other.

(2) The length of uncrushed portion of the slab directly in front of the studs varies only little when two studs are aligned transversely, thus the shear capacity of stud remain the same with the decrease in transverse spacing.

(3) The transverse rebar is likely to be very effective to improve the shear stud capacity because of the prevention of split cracks in the slab. The rebar closer to the root of the stud are most effective.

Beam-Column Connection of Steel Structures Using SFRCC

To examine the constructability, seismic performance and failure mechanism of the new beam-column connections, two full scale cruciform connection specimens were tested under horizontal cyclic loading. According to the test results, the new beam-column connection was found to be a promising connection for seismic design of ductile steel moment frames. Major findings obtained from the tests are as follows:

(1) Both specimens failed as the designed failure mode. The specimen with four studs (Specimen 'C-4PG50') failed by stud fracture, while the specimen with nine studs (Specimen 'C-9PG50') failed by beam yielding followed by slab fracture. The specimen failed by beam yielding exhibited fatter hysteretic curves than the other specimen.

(2) The number of studs showed minimal effect on the elastic stiffness. The two specimens showed almost the same elastic stiffness with a difference of 5%. In addition, the measured elastic stiffness agreed with the theoretical elastic stiffness well with a difference not greater than 10%.

(3) The experimental results revealed that the new beam-column connection has a potential to assure the formation of plastic hinges in the beam and achieve large energy dissipation and ductile behavior. In terms of the energy dissipation, the new beam-column connection showed the same value as the conventional beam-column connection up to 0.01 rad.

(4) Because of the presence of secondary bending moment, the studs of Specimen 'C-4PG50' showed 1.27 times larger strength and more brittle behavior in comparison of Specimen '4PG50', the push-out test specimens with four studs for each beam flange. From the test results, the resisting force of studs measured from the push-out test could directly be used to predict the transferred flange force by the studs in the new beam-column connection.

(5) Rebars in the longitudinal direction, along the beam direction, were arranged to resist the tensile load in the SFRCC slab. While rebars in the transverse direction, perpendicular to the beam direction, were arranged to prevent split cracks caused by the studs. Such a resisting mechanism was

proved based on the strain data glued on rebars. The rebars located closest to the root of studs resist the largest force than others. It coincides with the observation of Chapter 5.

ACKNOWLEDGEMENTS